Solid State Phase Transformations in Medium Manganese Steels

Farahani, Hussein

DOI
10.4233/uuid:26f3b0db-4c77-4564-8a59-a802fff39028

Publication date
2018

Document Version
Final published version

Citation (APA)
Farahani, H. (2018). *Solid State Phase Transformations in Medium Manganese Steels*. [Dissertation (TU Delft), Delft University of Technology]. https://doi.org/10.4233/uuid:26f3b0db-4c77-4564-8a59-a802fff39028

Solid State Phase Transformations in Medium Manganese Steels

Hussein FARAHANI

Novel Aerospace Materials group, Faculty of Aerospace Engineering,

Delft University of Technology

Solid State Phase Transformations in Medium Manganese Steels

Dissertation

for the purpose of obtaining the degree of doctor
at Delft University of Technology
by the authority of the Rector Magnificus prof. dr. ir. T.H.J.J. van der Hagen

chair of the Board for Doctorates
to be defended publicly on
Tuesday 11 December 2018 at 12:30 pm

by

Hussein FARAHANI

Master of Science in Computational Materials Science,
Technical University Bergakademie Freiberg, Germany

Born in Tehran, Iran.

This dissertation has been approved by the

Promotores:	Prof. dr. ir. S. van der Zwaag Prof. dr. W. Xu

Composition of the doctoral committee:

Rector Magnificus,	Chairman
Prof. dr. ir. S. van der Zwaag	Delft University of Technology, promotor
Prof. dr. W. Xu	Delft University of Technology Northeastern University, China, promotor

Independent Members:

Prof. dr. E. Gamsjäger	Montanuniversität Leoben, Austria
Dr. D. Huin	ArcelorMittal Global R&D Maizières, France
Dr.ir. S. E. Offerman	Delft University of Technology
Prof. dr. M. Perez	Universite de Lyon, France
Prof. dr. ir. R. H. Petrov	Delft University of Technology

Reserve Member:

Prof. dr. C. Pappas	Delft University of Technology

The research described in this thesis was carried out in the Novel Aerospace Materials group, Department of Aerospace Structures and Materials, Faculty of Aerospace Engineering.

Keywords: Steel, Phase Transformation, Interface
Printed by: Ipskamp Printing (www.ipskampprinting.nl/)

ISBN 978-94-028-1308-1

Author email: H.Farahani@tudelft.nl / hnf191@gmail.com

to *Farideh* ♥

and my parents

Summary

Steels are still, and probably will remain in future, the primary choice for applications as structural materials. This is not only because of the reasonable ratios of properties over production costs, but also owing to the versatile properties realisable via variety of microstructures achieved by controlling the solid-state phase transformations between austenite and ferrite phases in steels. The noticeable improvements in the properties of advanced high strength steels since the invention, have led to development of three generation of these steels. A sustainable continuous improvement in developing new grades of steels, requires more and deeper understanding of the effect of macroscopically controllable parameters, such as overall composition and temperature variations, on the rate of nucleation and migration of interfaces during solid-state phase transformations.

In this PhD thesis, experimental and modelling approaches are developed and employed to study the effect of alloying elements, such as Mn and C, on migration behavior of interfaces during solid state phase transformations at high and low temperatures. To this aim, the first five chapters of this thesis are dedicated to study austenite to ferrite phase transformation at high intercritical temperatures. In **Chapter 2**, the effect of Mn and Si and initial microstructure on the fraction of austenite during intercritical isothermal annealing are investigated with experimental and modelling approaches. This study highlights the key role of Mn partioning mode on the overall rate of transformations. However, the rate of the isothermal transformations through conventional methods is influenced by the concurrent nucleation and growth phenomena. In order to separate these two phenomena, the recently developed cyclic partial phase transformation approach, where the effect of nucleation during phase transformations are proved to be negligible, is used in the subsequent investigations. By means of this approach, the effect of interstitial elements on the

partitioning of Mn during austenite-ferrite phase transformation is studied in **Chapter 3**. This study shows that Mn interaction with the transformation interfaces occurs even in interstitial free Fe-0.5Mn alloy. The segregation of Mn to the interfaces is increased by presence of interstitial elements of C and N and significantly slows down migration of interfaces during cyclic experiments. It is also found that C promotes more Mn partioning in an Fe-C-Mn alloy compared to that of Fe-N-Mn alloy.

In order to gain better insight into the Mn segregation to transformation interfaces as a function of composition and temperature, a systematic set of computational and experimental cyclic partial phase transformations in low to medium Mn steels are designed and implemented. The results of this study, presented in **Chapter 4**, reveal a critical Mn concentration of 1.5 to 2 mass% at which Mn partitioning mode during the transformation significantly changes. The controlled segregation of Mn to the interfaces achieved via transitions in Mn partioning mode can be used to temporarily suspend further transformations during subsequent cooling. This approach is successfully employed to prevent microstructural band formation in a micro-chemically banded Fe-C-Mn-Si steel in **Chapter 5**. The origin of the suppression of band formation either by means of fast cooling or a cyclic partial phase transformation is investigated in detail and could be linked to the effect of local Mn partitioning on the effective austenite-ferrite interface mobility.

In **Chapter 6**, the sophisticated technique of in-situ high temperature electron back scattered diffraction is used to directly observe and analyse migration behavior of austenite-ferrite interfaces in a medium Mn steel during cyclic experiment. This study is coupled with 3D phase field simulations to better understand the in-situ 2D observations in the context of the 3D transformation events taking place below the surface. The trajectories of selected characteristic interfaces are analysed in detail and individual interfaces are found not to necessarily follow the overall response of the material to temperature variations. The reasons for observed scattered behavior of individual interfaces are discussed considering the local conditions in the vicinity of interfaces on its motion, as well as the misleading effects of 2D observations of processes essentially taking place in 3D.

After studying austenite-ferrite transformations at high temperatures, the last two chapters of this thesis are dedicated to study the isothermal bainite formation at low temperatures.

The results of a direct high temperature laser scanning confocal microscopy of isothermal bainite formation in a Fe-0.2C-1.5Mn-2.0Cr alloy are presented in **Chapter 7**. Evolution of isothermal bainite in terms of nucleation and growth phenomena at different temperatures is monitored in-situ and the kinetics of both nucleation and growth of the bainitic plates are analysed quantitatively. Grain boundary nucleation is observed to be the dominant nucleation mode at all transformation temperatures. The rate of nucleation is found to vary markedly between different austenite grains. The temperature dependence of the average bainite nucleation rate is in qualitative agreement with the classical nucleation theory. Analysis of plate growth reveals that the lengthening rates of bainite plates differs strongly between different grains. However, the lengthening rates do not seem to be related to the type of nucleation site. Analysis of the temperature dependence of the growth rate shows that the lengthening rates at high temperatures are in line with a diffusional model when a growth barrier of 400 J/mol is considered.

Finally, in **Chapter 8**, an extended Gibbs Energy Balance model is introduced for predicting the effect of alloying elements on the degree of incomplete austenite to bainite transformation in low carbon steels. This model makes use of an additive approach to calculate the coupled effect of substitutional alloying elements on the fraction of bainitic ferrite after the incomplete transformation in multicomponent steels. The model predicts significant effects of Mn and Mo and negligible effect of Si levels on the fraction of bainitic ferrite. This is attributed to the high value of dissipation of Gibbs energy caused by interfacial diffusion of Mn and Mo and low values caused by Si diffusion. The model predictions for quaternary Fe-C-Mn-Si system are comparable with the experimentally measured values of bainite fraction. For the Fe-C-Mn-Mo system, the agreement is less accurate, and the accuracy decreases with increasing Mo content, which is attributed a substantial carbide formation but interaction effects between Mn and Mo or a temperature dependent binding energy cannot be ruled out.

Samenvatting

Staal is en blijft ook in de toekomst het preferente materiaal voor constructieve toepassingen. Dit is niet alleen vanwege de gunstige verhouding van prestaties tegen materiaalkosten maar ook omdat de eigenschappen van staal zich zo makkelijk laten sturen door een veelvoud van microstructuren die door vaste-stof fasetransformaties bij het afkoelen vanuit de austeniet-fase verkregen kunnen worden. De belangrijke veranderingen hebben geleid tot drie nieuwe generaties van staal als basis materiaal voor de dragende constructies in passagiers- en vracht wagens. Een verdere ontwikkeling van deze moderne staaltypen vereist een nog beter inzicht in de effecten van temperatuur en staalsamenstelling op de kiem- en groeisnelheid van de fasen die ontstaan bij afkoeling van hoge temperatuur.

In dit proefschrift worden nieuwe experimentele methoden en theoretische modellen gepresenteerd die de effecten van legeringselementen zoals koolstof en mangaan, op de snelheid van austeniet-ferriet grensvlakken bij hoge en lage temperaturen beter trachten te beschrijven. De eerste vijf hoofdstukken gaan over het grensvlakgedrag bij hoge, zogenaamde interkritische, temperaturen. **Hoofstuk 2** beschrijft het onderzoek naar het effect van Mn en Si en uitgangsmicrostructuur op de hoeveelheid austeniet die gevormd wordt bij een gegeven gloeitemperatuur. Deze metingen laat duidelijk de invloed van het Mn gehalte op het uiteindelijke resultaat zien. In bovenstaande experimenten speelden zowel nucleatie van nieuwe korrels als groei van bestaande korrels een rol. Dit was echter niet het geval in de experimenten in **Hoofstuk 3** waarbij cyclische gedeeltelijke transformaties gebruikt werden om de nog onbekende effecten van koolstof en stikstof alsmede het ontbreken van interstitiële legeringselementen op de snelheid van het austeniet-ferriet grensvlak te bestuderen. Gebleken is dat de interstitiële legeringselementen de snelheid behoorlijk vertragen en dat koolstof een sterker effect heeft dan stikstof.

Om het effect van Mangaan herverdeling aan het grensvlak op de transformatiesnelheid beter te beschrijven zijn experimenten en berekeningen uitgevoerd aan vergelijkbare staalsoorten met verschillend Mn gehalte die onderwerpen werden aan cyclische gedeeltelijke transformaties. De resultaten zijn beschreven in **Hoofdstuk 4** en laten zien dat het gedrag in belangrijke mate verandert bij een Mn gehalte van 1.5-2.0 gewichts %. De inzichten die verkregen zijn hoe de lokale Mn herverdelingen aan het grensvlak de beweeglijkheid ervan sterk kunnen terugbrengen, zijn gebruikt in het onderzoek zoals beschreven in **Hoofdstuk 5**. In dit hoofdstuk wordt laten zien hoe door slim gekozen cyclische transformaties de ongewenste ferriet-perliet bandvorming ook bij lage afkoelsnelheden onderdrukt kan worden. De verkregen resultaten worden vergeleken met die van conventionele experimenten waarin bandvorming alleen onderdrukt kan worden door verhoging van de afkoelsnelheid.

In **Hoofdstuk 6** wordt de geavanceerde ‘high temperature electron back scattering diffraction’ (HT-EBSED) techniek gebruikt om de verplaatsing van individuele austeniet-ferriet grensvlakken tijdens cyclische gedeeltelijke fasetransformaties rechtstreeks en in-situ waar te nemen. Deze experimentele studie is aangevuld met 3D ‘phase field’ simulaties om de waarnemingen aan het 2D grensvlak beter te kunnen relateren aan hun eigenlijke 3D karakter van de transformatie die zich grotendeels afspeelt onder het observatievlak. Individuele grensvlakken zijn met hoge precisie geregistreerd en de daarop losgelaten analyse laat zien dat het gedrag van individuele grensvlakken sterk kan verschillen van het gemiddelde grensvlakgedrag zoals dat uit dilatometrische metingen gedestilleerd kan worden. De oorzaak van de afwijking ligt meestal aan lokale omstandigheden of aan het feit dat processen in 3D de-facto aan een 2D oppervlak waargenomen worden.

De laatste twee hoofdstukken van dit proefschrift zijn gewijd aan de vorming van bainiet zoals dat bij een lagere transformatietemperatuur plaatsvindt. De resultaten van in-situ waarnemingen van bainietvorming in een legering Fe-0.2C-1.5Mn-2.0Cr zijn beschreven in **Hoofdstuk 7**. Uit de in-situ waarnemingen bij verschillende temperaturen kon zowel het nucleatie- als het groei-gedrag bepaald worden. Nucleatie op de korrelgrens bleek de belangrijkste verschijningsvorm van nieuwe korrels te zijn, waarbij de nucleatiesnelheid sterk per korrel bleek te kunnen verschillen. De temperatuurafhankelijkheid van de nucleatie bleek in overeenstemming te zijn met de klassieke theorieën. Analyse van de groeisnelheid liet zien dat deze sterk varieerde maar dat er geen relatie tussen groeisnelheid en moment van nucleatie aan te tonen was. Analyse van de groeisnelheid in de langsrichting van de bainietplaten liet zien dat die overeenkwam met theoretische voorspellingen in geval de energetische barrière voor groei 400 J/mol zou bedragen.

Tot slot wordt in **Hoofdstuk 8** een uitgebreide versie van het 'Gibbs Energy Balance' model voor het verklaren van de samenstellingsafhankelijkheid van de incomplete bainietvorming gepresenteerd. Dit model is gebaseerd op een additieve bijdrage van de verschillende legeringselementen. Het model voorspelt dat Mn en Mo een sterk effect hebben maar dat de invloed van Si verwaarloosbaar is. Het verschil wordt toegeschreven aan het grote verschil in bindingsenergie van de genoemde legeringselementen met het bewegende grensvlak. De voorspellingen voor het Fe-C-Mn-Si systeem zijn in goede overeenstemming met de experimentele resultaten. De overeenkomst voor het Fe-C-Mn-Mo systeem is minder goed en wordt slechter bij hoger Mo gehalte. Deze toenemende afwijking wordt toegeschreven aan mogelijke carbide vorming maar het is ook mogelijk dat een temperatuurafhankelijke interactie tussen Mo en Mn een rol speelt.

Contents

List of Figures

List of Tables

Chapter 1 **Introduction**

The possibility of realizing a wide range of mechanical and other properties in multicomponent alloys is directly connected to that fact that metallic materials in general and steels in particular can have many different microstructures for a given chemical composition by tailoring the successive liquid to solid and solid to solid phase transformations. While virtually all actual transformations proceed via nucleation and growth processes, overall it is the velocity of the interfaces between the transient phases present during thermal processing which determine the ultimate microstructure and hence the ultimate properties.

1.1 Importance of Phase Transformations in Steels

In steels, the solid-state phase transformations between face entered cubic (FCC) crystalline phase of austenite and body cantered cubic (BCC) crystalline phase of ferrite are by a great degree controlled by the rate of nucleation and the migration velocity of interfaces during phase transformations. The history of research and development in steels is full of challenges to understand and regulate the effect of macroscopically controllable parameters, such as overall composition and temperature variations, on solid state phase transformations. Earlier research efforts over the past two decades have led to three generations of advanced high strength steels (AHSS) each with different microstructures and compositions and properties: The first generation of AHSS includes dual phase (DP), transformation induced plasticity (TRIP), complex-phase (CP) and martensitic (MART) steels with a high fraction of allotriomorphic ferrite or ferrite-like phases. The second generation of AHSS, includes twinning induced plasticity (TWIP), Al-rich lightweight steels (L-IP®) and shear band strengthened steels (SIP) and contain a large fraction of metastable austenite as a result of their Mn concentration being up to 20 mass%. The third generation AHSS with better strength-ductility combinations at lower costs [1–4] includes the so-called medium Mn steels [5–11] to which the steels to be researched in this thesis belong. The attractive mechanical properties of these steels are due to their multi-phase microstructures with sizeable fractions of retained austenite. Intercritical annealing treatments at isothermal bainite transformation temperatures form the basis for the desired multi-phase bainite-austenite microstructures in these steels. Controlling the amount, morphology and stability of retained austenite as well as that of the other microstructural components is a goal not only of academic but also of significant industrial interest, since the austenite-bainite microstructure formed during intercritical annealing determines the mechanical properties of the steel [12–16].

Manganese is the key alloying element in development of the 3rd Gen of AHHS. Studying the partitioning behavior of Mn at interfaces solely and also in presence of other alloying elements and their effects on the kinetics of ferrite and bainite formation requires separation of the effects on the simultaneous nucleation of new grains and their growth behavior [17–25]. Approaching this goal, requires sophisticated experimental techniques and alternative thermal routes to be able to separately investigate effects of Mn at transformation interfaces during ferrite and bainite formation.

1.2 Thesis Structure and Scope

The main scope of this thesis is to study the effect of substitutional (in particular Mn) and interstitial (in particular C) alloying elements both by experimental and modelling approaches on migration behavior of interfaces during solid state phase transformations at high and low temperatures. The approaches are exclusively designed to elucidate role of interfaces in overall transformation kinetics.

In **Chapter 2**, the effects of Mn and Si concentration and the isothermal intercritical holding temperature on the austenite to ferrite and the martensite to austenite phase transformations are studied for a series of Fe-C-Mn-Si steels. The experimental observations are compared to predictions by the Local Equilibrium model [26], illuminating importance of the initial microstructure on the kinetics of phase transformations.

In **Chapter 3**, the effect of interstitial elements on the partitioning of Mn at migrating transformation interfaces during austenite-ferrite phase transformation is studied using the cyclic partial phase transformation concept [27]. In this study the transformation kinetics of the base Fe-C-0.5 Mn alloy, the same alloy after a decarburization treatment and the same alloy after a decarburization and re-nitriding treatment is determined and analysed.

Chapter 4 presents results of a systematic set of computational and experimental cyclic partial phase transformations in low to medium Mn steels revealing a critical Mn concentration at which Mn partitioning at moving austenite-ferrite interfaces can be used to temporarily suspend further transformation during subsequent cooling.

Using the insights achieved in the preceding systematic studies, in **Chapter 5** a novel approach using the cyclic partial phase transformation concept is developed and successfully applied to prevent microstructural band formation in a micro-chemically banded Fe-C-Mn-Si steel. The origin of the suppression of band formation either by means of fast cooling or a cyclic partial phase transformation is investigated in detail and could be linked to the effect of local Mn partitioning on the effective austenite-ferrite interface mobility.

In **Chapter 6**, the migration behavior of austenite-ferrite interfaces in a medium Mn steel using sophisticated in-situ high-temperature EBSD mapping techniques is recorded and analysed. The experimental study of the migration of the austenite-ferrite interfaces during cyclic austenite-ferrite phase transformations is coupled with 3D phase field simulations to better understand the 2D EBSD observations in the context of the 3D transformation events taking place below the surface. The trajectories of selected characteristic interfaces are analysed in detail and yield insight into the effect of local conditions in the vicinity of interfaces on its motion, as well as the misleading effects of 2D observations of processes essentially taking place in 3D.

Direct high temperature laser scanning confocal microscopical observations of the isothermal bainite formation in a Fe-0.2C-1.5Mn-2.0Cr alloy are presented in **Chapter 7**. Evolution of isothermal bainite in terms of nucleation and growth phenomena at different temperatures is monitored in-situ and the kinetics of both nucleation and growth of the bainitic plates is analysed quantitatively.

Finally, in **Chapter 8**, an extended Gibbs Energy Balance model is introduced for predicting the effect of alloying elements on the degree of incomplete austenite to bainite transformation [28,29] in low carbon steels. This model makes use of an additive approach to calculate the coupled effect of substitutional alloying elements on the fraction of bainitic ferrite after the incomplete transformation in multicomponent steels. The model predictions are compared with the experimentally measured values of bainite fraction and levels of accuracy of the model predictions are discussed considering effects of carbide formation, possible interaction between elements partitioned at interfaces and a potential temperature dependence of binding energies at austenite-ferrite interfaces.

1.3 References

[1] C. Capdevila, J. Cornide, K. Tanaka, K. Nakanishi, E. Urones-Garrote, Kinetic transition during ferrite growth in Fe-C-Mn medium carbon steel, Metall. Mater. Trans. A Phys. Metall. Mater. Sci. 42 (2011) 3719–3728. doi:10.1007/s11661-011-0650-y.

[2] H. Luo, J. Shi, C. Wang, W. Cao, X. Sun, H. Dong, Experimental and numerical analysis on formation of stable austenite during the intercritical annealing of 5Mn steel, Acta Mater. 59 (2011) 4002–4014. doi:10.1016/j.actamat.2011.03.025.

[3] C. Wang, W. Cao, J. Shi, C. Huang, H. Dong, Deformation microstructures and strengthening mechanisms of an ultrafine grained duplex medium-Mn steel, Mater. Sci. Eng. A. 562 (2013) 89–95. doi:10.1016/j.msea.2012.11.044.

[4] R. Zhang, W.Q. Cao, Z.J. Peng, J. Shi, H. Dong, C.X. Huang, Intercritical rolling induced ultrafine microstructure and excellent mechanical properties of the medium-Mn steel, Mater. Sci. Eng. A. 583 (2013) 84–88. doi:10.1016/j.msea.2013.06.067.

[5] A. Grajcar, K. Radwański, H.J. Krztoń, Microstructural Analysis of a Thermomechanically Processed Si-Al TRIP Steel Characterized by EBSD and X-Ray

Techniques, Solid State Phenom. 203–204 (2013) 34–37. doi:10.4028/www.scientific.net/SSP.203-204.34.

[6] K. Radwański, A. Wrożyna, R. Kuziak, Role of the advanced microstructures characterization in modeling of mechanical properties of AHSS steels, Mater. Sci. Eng. A. 639 (2015) 567–574. doi:10.1016/J.MSEA.2015.05.071.

[7] H. Kamoutsi, E. Gioti, G.N. Haidemenopoulos, Z. Cai, H. Ding, Kinetics of Solute Partitioning During Intercritical Annealing of a Medium-Mn Steel, Metall. Mater. Trans. A. 46 (2015) 4841–4846. doi:10.1007/s11661-015-3118-7.

[8] K. Sugimoto, H. Tanino, J. Kobayashi, Impact Toughness of Medium-Mn Transformation-Induced Plasticity-Aided Steels, Steel Res. Int. 86 (2015) 1151–1160. doi:10.1002/srin.201400585.

[9] S. Lee, K. Lee, B.C. De Cooman, Observation of the TWIP + TRIP Plasticity-Enhancement Mechanism in Al-Added 6 Wt Pct Medium Mn Steel, Metall. Mater. Trans. A. 46 (2015) 2356–2363. doi:10.1007/s11661-015-2854-z.

[10] C. Garcia-Mateo, T. Sourmail, F.G. Caballero, C. Capdevila, C. García de Andrés, New approach for the bainite start temperature calculation in steels, Mater. Sci. Technol. 21 (2005) 934–940. doi:10.1179/174328405X51622.

[11] H. Farahani, W. Xu, S. van der Zwaag, Prediction and Validation of the Austenite Phase Fraction upon Intercritical Annealing of Medium Mn Steels, Metall. Mater. Trans. A. 46 (2015) 4978–4985. doi:10.1007/s11661-015-3081-3.

[12] A. Arlazarov, M. Gouné, O. Bouaziz, A. Hazotte, G. Petitgand, P. Barges, Evolution of microstructure and mechanical properties of medium Mn steels during double annealing, Mater. Sci. Eng. A. 542 (2012) 31–39. doi:10.1016/j.msea.2012.02.024.

[13] J. Lee, S.S. Sohn, S. Hong, B.-C. Suh, S.-K. Kim, B.-J. Lee, N.J. Kim, S. Lee, Effects of Mn Addition on Tensile and Charpy Impact Properties in Austenitic Fe-Mn-C-Al-Based Steels for Cryogenic Applications, Metall. Mater. Trans. A. 45 (2014) 5419–5430. doi:10.1007/s11661-014-2513-9.

[14] S.S. Sohn, S. Lee, B.-J. Lee, J.-H. Kwak, Microstructural Developments and Tensile Properties of Lean Fe-Mn-Al-C Lightweight Steels, JOM. 66 (2014) 1857–1867. doi:10.1007/s11837-014-1128-3.

[15] J. Han, S.-J. Lee, J.-G. Jung, Y.-K. Lee, The effects of the initial martensite microstructure on the microstructure and tensile properties of intercritically annealed Fe–9Mn–0.05C steel, Acta Mater. 78 (2014) 369–377. doi:10.1016/j.actamat.2014.07.005.

[16] I. Gutierrez-Urrutia, D. Raabe, Influence of Al content and precipitation state on the mechanical behavior of austenitic high-Mn low-density steels, Scr. Mater. 68 (2013) 343–347. doi:10.1016/j.scriptamat.2012.08.038.

[17] O. Bouaziz, S. Allain, C.P. Scott, P. Cugy, D. Barbier, High manganese austenitic twinning induced plasticity steels: A review of the microstructure properties relationships, Curr. Opin. Solid State Mater. Sci. 15 (2011) 141–168. doi:10.1016/j.cossms.2011.04.002.

[18] B.C. De Cooman, Structure-properties relationship in TRIP steels containing carbide-free bainite, Curr. Opin. Solid State Mater. Sci. 8 (2004) 285–303. doi:10.1016/j.cossms.2004.10.002.

[19] Y.K. Lee, C. Choi, Driving force for γ→ε martensitic transformation and stacking fault energy of γ in Fe-Mn binary system, Metall. Mater. Trans. A. 31 (2000) 355–360. doi:10.1007/s11661-000-0271-3.

[20] S. Zaefferer, J. Ohlert, W. Bleck, A study of microstructure, transformation mechanisms and correlation between microstructure and mechanical properties of a low alloyed TRIP steel, Acta Mater. 52 (2004) 2765–2778. doi:10.1016/j.actamat.2004.02.044.

[21] E. De Moor, D.K. Matlock, J.G. Speer, M.J. Merwin, Austenite stabilization through manganese enrichment, Scr. Mater. 64 (2011) 185–188. doi:10.1016/J.SCRIPTAMAT.2010.09.040.

[22] S. Lee, S.-J. Lee, B.C. De Cooman, Austenite stability of ultrafine-grained transformation-induced plasticity steel with Mn partitioning, Scr. Mater. 65 (2011) 225–228. doi:10.1016/J.SCRIPTAMAT.2011.04.010.

[23] D.T. Pierce, D.R. Coughlin, D.L. Williamson, J. Kähkönen, A.J. Clarke, K.D. Clarke, J.G. Speer, E. De Moor, Quantitative investigation into the influence of temperature on carbide and austenite evolution during partitioning of a quenched and partitioned steel, Scr. Mater. 121 (2016) 5–9. doi:10.1016/J.SCRIPTAMAT.2016.04.027.

[24] F. HajyAkbary, J. Sietsma, G. Miyamoto, T. Furuhara, M.J. Santofimia, Interaction of carbon partitioning, carbide precipitation and bainite formation during the Q&P process in a low C steel, Acta Mater. 104 (2016) 72–83. doi:10.1016/j.actamat.2015.11.032.

[25] K.S. Choi, Z. Zhu, X. Sun, E. De Moor, M.D. Taylor, J.G. Speer, D.K. Matlock, Determination of carbon distributions in quenched and partitioned microstructures using nanoscale secondary ion mass spectroscopy, Scr. Mater. 104 (2015) 79–82. doi:10.1016/J.SCRIPTAMAT.2015.03.027.

[26] M. Hillert, Nature of local equilibrium at the interface in the growth of ferrite from alloyed austenite, Scr. Mater. 46 (2002) 447–453. doi:10.1016/S1359-6462(01)01257-X.

[27] H. Chen, S. van der Zwaag, An Overview of the Cyclic Partial Austenite-Ferrite Transformation Concept and Its Potential, Metall. Mater. Trans. A. (2016) 1–10. doi:10.1007/s11661-016-3826-7.

[28] H.I. Aaronson, W.T. Reynolds, G.R. Purdy, The incomplete transformation phenomenon in steel, Metall. Mater. Trans. A. 37 (2006) 1731–1745. doi:10.1007/s11661-006-0116-9.

[29] F.G. Caballero, C. Garcia-Mateo, M.J. Santofimia, M.K. Miller, C. García de Andrés, New experimental evidence on the incomplete transformation phenomenon in steel, Acta Mater. 57 (2009) 8–17. doi:10.1016/j.actamat.2008.08.041.

Chapter 2 **Effect of Mn and Si on Intercritical Ferrite and Austenite Formation**

This Chapter is based on

- H. Farahani, W. Xu, S. van der Zwaag, Prediction and Validation of the Austenite Phase Fraction upon Intercritical Annealing of Medium Mn Steels, Metallurgical and Materials Transactions A, Volume 46, Issue 11, 1 November 2015, Pages 4978-4985.

ABSTRACT

In this research the effects of Mn and Si concentration and that of the isothermal intercritical holding temperature on the austenite to ferrite (γ→α) and the martensite to austenite (α′→γ) phase transformations are studied for a series of Fe-C-Mn-Si steels with up to 7 mass% Mn. The model is based on the local equilibrium (LE) concept. The model predictions are compared to experimental observations. It is found that the austenite volume fraction at the end of intercritical annealing depends significantly on the initial microstructure. For Mn concentrations between 3 to 7 mass% the LE model is qualitatively correct. However, at higher Mn levels the discrepancy between the predicted austenite fractions and the experimental values increases, in particular for the α′→γ transformation. Intragrain nucleation is held responsible for the higher austenite fractions observed experimentally. Silicon is found have a much smaller effect on the kinetics of the intercritical annealing than Mn.

2.1 Introduction

The intercritical annealing treatment involves heating or cooling to and holding at a temperature between the Ae1 and the Ae3 temperature to obtain partial austenitization. The treatment is part of almost any process routes to create multiphase steels. The kinetics of the transformation from austenite to ferrite and vice versa during the intercritical annealing determines the austenite/ferrite fractions and eventually the mechanical properties. Hence the topic has been the subject of continued scientific interest as well as a key factor in the industrialization of multiphase steels [1–8]. It is therefore important to develop models for the kinetics and the final phase fractions during intercritical annealing. The models should be capable to handle different initial microstructures corresponding to different process routes and to capture the effects of key alloying elements such as C, Si and Mn [9,10].

It has been shown that in steels with a low concentration of Mn, the Mn enrichment at the moving austenite-ferrite interface is of crucial importance in determining the transformation kinetics [11–17]. Three main concepts have been formulated to describe the transformation between austenite and ferrite in the two-phase region: (i) Full equilibrium (FE) [18] in which all alloying elements redistribute till equilibrium is reached everywhere in system. In the case of FE, the fraction of ferrite or austenite in the intercritical region is fixed at a given temperature, irrespective of the starting microstructure. (ii) paraequilibrium (PE) [19,20] in which it is assumed that the phase transformation can proceed without any redistribution of the substitutional alloying element M (M = Mn, Si, Mo, etc.) and only the Carbon redistributes such that the chemical potential of carbon across any austenite-ferrite interface is constant. At a certain temperature, there is only one PE tie-line, which means that the PE fraction of ferrite or austenite is also fixed at that specific temperature. (iii) Local equilibrium (LE) [21,22]: In the LE model, the interface is assumed to migrate under full LE with partitioning of both C and M. Due to the large difference in the diffusivities of C and M, there are two different transformation modes: (a) local equilibrium with negligible partitioning (NPLE) mode. In this mode, the concentration of M in ferrite is the same as that in austenite, but there is a M spike in front of the migrating interface as a result of the assumed LE condition. The transformation rate is effectively controlled by carbon diffusion and is relatively fast; and (b) local equilibrium with partitioning (PLE) mode, in which the carbon gradient in austenite is negligible, while that of M is large. In this mode, the transformation rate is governed by the rate of M partitioning and is extremely sluggish. Depending on the composition of a material, the transformation could start in NPLE mode and then proceed in the PLE mode. In practice, the point at which the transformation mode switches from NPLE to PLE is regarded as the termination of the transformation [13–15,23–29]. For modest annealing times, the final phase fractions obtained after annealing correspond to the phase fraction achieved in PLE mode [16,30–32]. A similar halting criterion has been formulated in a recent model for a grain growth model involving boundary loading by impurities [33].

Medium and high Mn steels have drawn much attention in recent years in the development of the 3rd generation advanced high strength steels, combining excellent mechanical properties and reasonable material and production costs [25,30,34,35]. These steels are generally subjected to intercritical annealing so as to redistribute the Mn and to tailor the amount, morphology and stability of the retained austenite after the final cooling [36–40]. For higher Mn concentrations, the transition point from NPLE to PLE during the intercritical annealing, starting from different initial microstructures may differ significantly. Hence the transition conditions are crucial in determining the final microstructure (and the mechanical behavior) in the medium Mn steels [35,39–43].

In a previous study [16] for low Mn steels (Mn levels up to 1.5mass%), it was shown that the LE model provides the more accurate predictions of austenite fractions (f_γ) after the intercritical heat treatment starting from different initial microstructures, while FE and PE models failed to deliver satisfactory estimates. In the current study, the LE model is employed to study the effects of Mn and Si additions on the NPLE to PLE transition during the intercritical annealing, for both the austenite to ferrite ($\gamma \rightarrow \alpha$) and the martensite to austenite ($\alpha' \rightarrow \gamma$) transformations, for steels with up to 7 mass% Mn. The model predictions are compared to experimental metallographic data on samples subjected to well defined heat treatments.

2.2 Modelling and Experimental procedures

The LE and FE models were applied to simulate the $\gamma\rightarrow\alpha$ and the $\alpha'\rightarrow\gamma$ transformations in a series of four Fe-C-Mn-Si alloys with compositions listed in Table 1, at different intercritical annealing temperatures of 933 K (660 ℃), 953 K (680 ℃) and 973 K (700 ℃). While earlier studies in the literature [13,14,16,24,28,44,45] focused on Mn levels up to 3 mass%, in this study Mn levels up to 7 mass% are examined both computationally and experimentally. The corresponding Ae1 and Ae3 temperatures were calculated by Thermo-Calc coupled to the TCFe7 database. The values calculated for each steel are also listed in Table 1. The transformation kinetics simulations were performed using the DICTRA software linked to the TCFE7 and MOB2 databases [46,47]. Unless stated otherwise, a 1D geometry representing an austenite grain size of 50 µm was used in the simulations. To test the effect of cell size on the transformation behavior, the simulations were also executed using different cell sizes. The $\alpha'\rightarrow\gamma$ transformation is also modelled assuming the same highly simplified planar geometry for the interface between the martensite and the austenite. In Fig. 2.1, sketches of the initial simulation setups (an austenitic starting state or a martensitic starting state respectively) for the two transformations scenario are shown. The martensite can be modelled by the ferrite phase in DICTRA by imposing the appropriate concentrations and (ferritic) diffusion coefficients. The simulation studies focused only on intercritical annealing conditions. For all simulations the transformation time was fixed at 104 s.

Table 2.1 - Nominal composition of studied alloys with calculated A1 and A3 temperatures by Thermo-Calc.

Nominal composition in mass%					Calculated temperatures by Thermo-Calc	
Index	C	Mn	Si	Fe	Ae1	Ae3
A	0.1	3.0	0	bal.	878 K (605 ℃)	1050 K (777 ℃)
B	0.2	5.0	0	bal.	818 K (545 ℃)	991 K (718 ℃)
C	0.2	5.0	1.6	bal.	823 K (550 ℃)	1015 K (742 ℃)
D	0.2	7.0	1.6	bal.	673 K (400 ℃)	968 K (695 ℃)

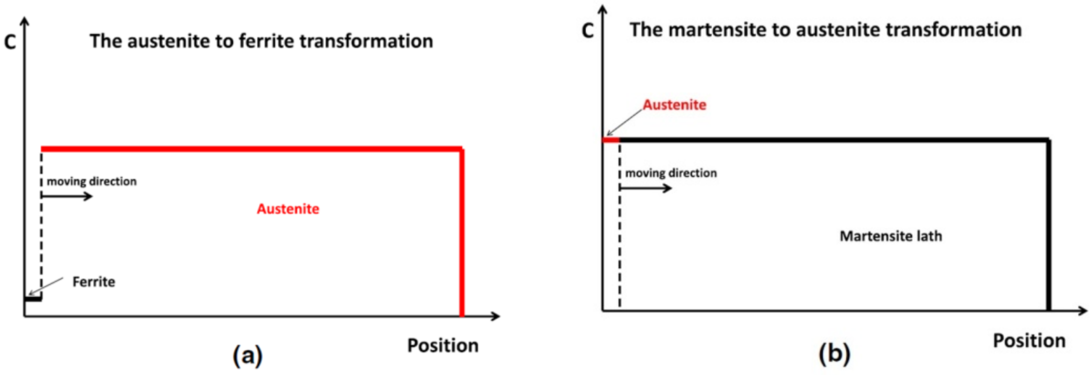

Fig. 2.1 - Sketch of simulation setup for (a) the austenite-to-ferrite transformation, and (b) the martensite-to-austenite transformation.

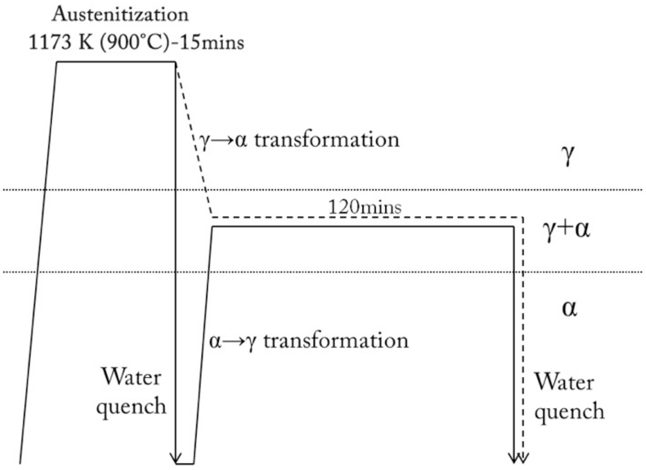

Fig. 2.2 - Heat treatment diagram illustrating two different transformation routes.

Real metallurgical experiments were also preformed to validate the model predictions. In the experiments, the specimens were subjected to heat treatment schemes as illustrated in Fig. 2.2. For the martensite to austenite transformation, the specimen was isothermally held at 1173 K (900 ℃) for 900 s, followed by water quench with cooling rate of ~75 K/s, to obtain a full martensitic structure, and subsequently heated to the intercritical regime at a heating rate of ~15 K/s and kept at the intended temperature for 7200 s. For the austenite to ferrite transformation, the specimen was austenitized at 1173 K (900 ℃) for 900 s and cooled in the furnace with a cooling rate of ~0.5 K/s then isothermally kept in the two-phase region for 7200 s. Both heat treatment routes were terminated with water quenching at the end of the intercritical annealing. The phase fractions were obtained by quantitative metallography based on optical micrographs after Nital etching.

2.3 Results

In Fig. 2.3, the austenite fractions as a function of time as predicted by LE model during the isothermal holding at 933 K (660 °C), for either the $\gamma \to \alpha$ (Fig. 2.3a) and the $\alpha' \to \gamma$ (Fig. 2.3b) transformations are presented for the four alloys studied. The LE model predicts that the kinetics depends on the initial microstructure, while the FE predictions for each of the alloys studied are transformation path independent. The LE model predicts that no transformation, i.e. $f_\alpha \approx 0$ occurs in case of an austenitic starting state. Interestingly, however, for all alloys the LE model predicts that the $\alpha' \to \gamma$ transformation progresses significantly. As can be seen in Fig. 2.3b, there is a primary fast mode in the kinetics of $\alpha' \to \gamma$ transformation during the first 10 s followed by a rather sluggish increase in γ fraction (NPLE/PLE transition). This interesting phenomenon implies that the NPLE/PLE transition point strongly depends on the transformation path and the alloy composition, as was also observed for the lower Mn levels [16]. According to LE model, when the concentration of Mn in ferrite is the same as in the austenite and the transformation is controlled by C diffusion in initial phase only and the process is fast. Since the diffusivity of C in ferrite is much higher than that in austenite, the $\alpha' \to \gamma$ transformation rate is significantly faster than the $\gamma \to \alpha$ phase transformation. Furthermore, differences in the NPLE/PLE transition of four alloys reveals effects of Mn and Si in the $\alpha' \to \gamma$ transformation, as shown in Fig. 2.3b. An increase in the Mn content, results in an earlier NPLE/PLE transition and a higher final austenite fraction for a fixed intercritical annealing temperature. In addition, the presence of concentration spike of substitutional alloying elements at the interface in composition profiles in low transformation rate confirms the transition in kinetics of the phase transformation [15,24,28,45]. A comparison of the red and blue transformation curves shows that changes in the Si level only have a small effect on the transformation behavior.

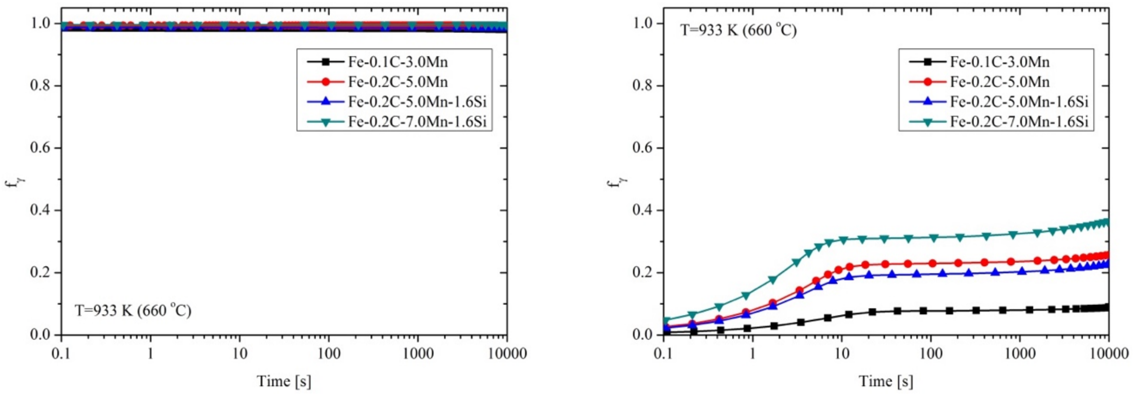

(a) (b)

Fig. 2.3 - Austenite fraction as a function of heating time in the intercritical zone predicted by LE modelling for a) austenite to ferrite and b) martensite to austenite transformation at T=933 K (660 °C).

As stated earlier, real metallurgical isothermal transformation experiments were performed in order to validate the LE model predictions. In Fig. 2.4, the typical microstructures of the sample A (0.1 mass% C & 3.0 mass% Mn) quenched from the γ→α and α′→γ phase transformations, after annealing for 7200 s at T=933 K (660 ℃), are presented. The micrographs show that only a very small fraction of austenite transformed into grain boundary ferrite during the γ→α transformation. In the experiments the average prior austenite grain size was found to be ~50 µm. As mentioned above, simulations were done assuming a variety of cell sizes from 10 to 100 µm. Fig. 2.5 a-d illustrates the effect of cell size on the transformations kinetics in different alloys at T=933 K (660 ℃) for both γ→α and the α′→γ transformations. Changing the simulation cell size from 50 µm to 100 µm does not have a noticeable impact on the kinetics of γ→α transformation. However, for all alloys the kinetics in the α′→γ transformation is significantly affected when reducing the simulation cell size from 50 µm to 10 µm, as the kinetic transition from fast carbon controlled to slow alloying element-controlled growth (NPLE/PLE transition) depends on cell size. Thus, the value of f_γ at the end of simulation time, approximately halves by halving the cell size. To highlight only the effect of composition and initial microstructure on the transformation the cell size in the α′→γ simulation is taken the same as for the γ→α transformation, i.e. 50 µm. The effect of simulation cell size will be re-addressed when comparing the experimental results to the model predictions.

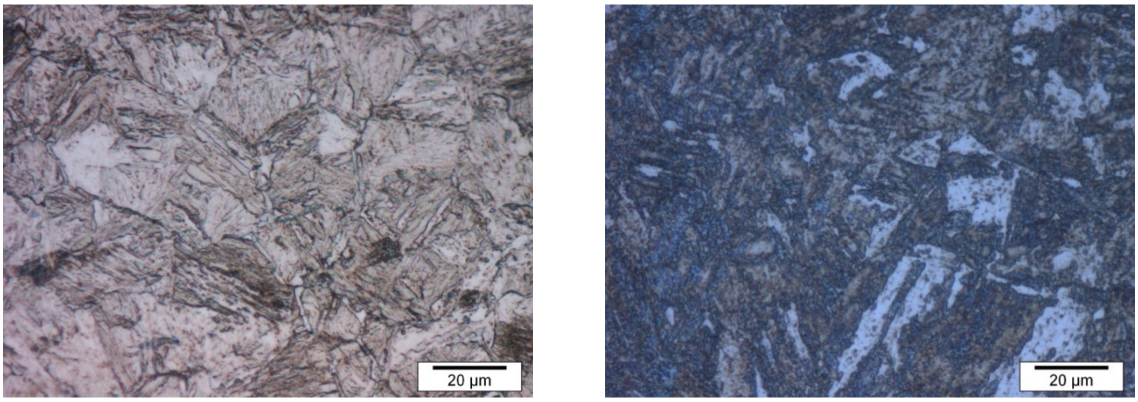

(a) (b)

Fig. 2.4 - The typical microstructures of the Fe-0.1C-3.0Mn alloy sample quenched after (a) the austenite to ferrite transformation and (b) martensite to austenite transformation at T= 933 K (660 °C). The annealing time is 7200 s.

Fig. 2.6 shows the fractions of austenite as predicted by the LE model, the FE model and the experimental results for both $\gamma \rightarrow \alpha$ and the $\alpha' \rightarrow \gamma$ transformations for all studied alloys at T=933, 953 and 973 K (660, 680 and 700 °C). The experimental values at 973 K (700 °C) are not plotted in this figure because of the high uncertainty in the quantification of the phase fractions due to the fine mixture of two phases and the lower optical contrast difference. As seen in Fig. 2.6a, the LE model predictions in Fe-0.1C-3.0Mn system are in good agreement with experimental values. The FE model predicted austenite fraction is not reached at any of the temperatures studied, irrespective of the starting microstructure. For Mn concentrations beyond 3 mass%, the data in Fig. 2.6 b-d, show that the final austenite fractions in the $\gamma \rightarrow \alpha$ transformation are well predicted by the LE model. However, the differences between simulations and experiments for $\alpha' \rightarrow \gamma$ transformation become larger at higher Mn and Si levels. The LE model underestimates the experimental austenite fractions. This observation is in agreement with Enomoto's earlier results [48]. Comparison of Fig. 2.6 b-c confirms the systematic effect of Si on reducing austenite formation. It is worth noting that according to Fig. 2.6 the experimental values of f_γ in $\alpha' \rightarrow \gamma$ phase transformation get closer to the full equilibrium predictions upon increasing Mn content. This phenomenon can be attributed to the availability of large number of nucleation sites in the initial martensitic microstructure and the late occurrence of the NPLE/PLE transition.

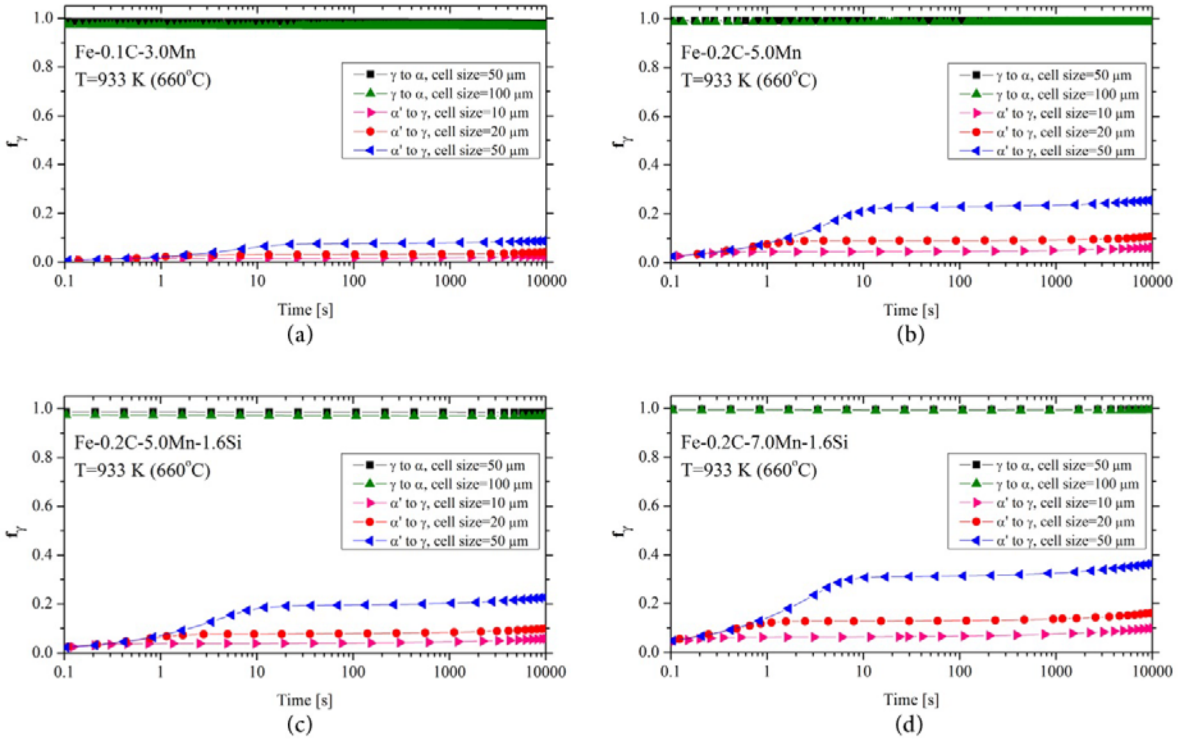

Fig. 2.5 - The effect of cell size on the simulated kinetics of phase transformations in a) Fe-0.1C-3.0Mn, b) Fe-0.2C-5.0Mn, c) Fe-0.2C-5.0Mn-1.6Si and d) Fe-0.2C-7.0Mn-1.6Si.

2.4 Discussion

We first focus on the results obtained at a fixed temperature of T=933 K (660 ℃). The isothermal sections of the Fe-C-Mn phase diagram, without and with 1.6mass% Si, created by Thermo-Calc coupled to the TCFe7 database are shown in Fig. 2.7. According to [43] and [49], in the case of ferrite formation (Fig. 2.7a and Fig. 2.7c) the boundaries between PLE region (shown in green colour) and NPLE region (shown in pink colour) runs between the intersection of the α/(α + γ) phase boundary with the axis of the Mn content and the intersection of the γ/(α + γ) phase boundary with the axis of the C content. For the austenite formation (Fig. 2.7b and Fig. 2.7d) the PLE/NPLE boundary can be described by the curve connecting the intersection of the γ/(α+γ) phase boundary with the axis of the Mn content to the intersection of α/(α+γ) phase boundary with the axis of the C content. The points indicated by A, B, C and D in Fig. 2.7 a-d refer to the alloys specified in Table 1. For all

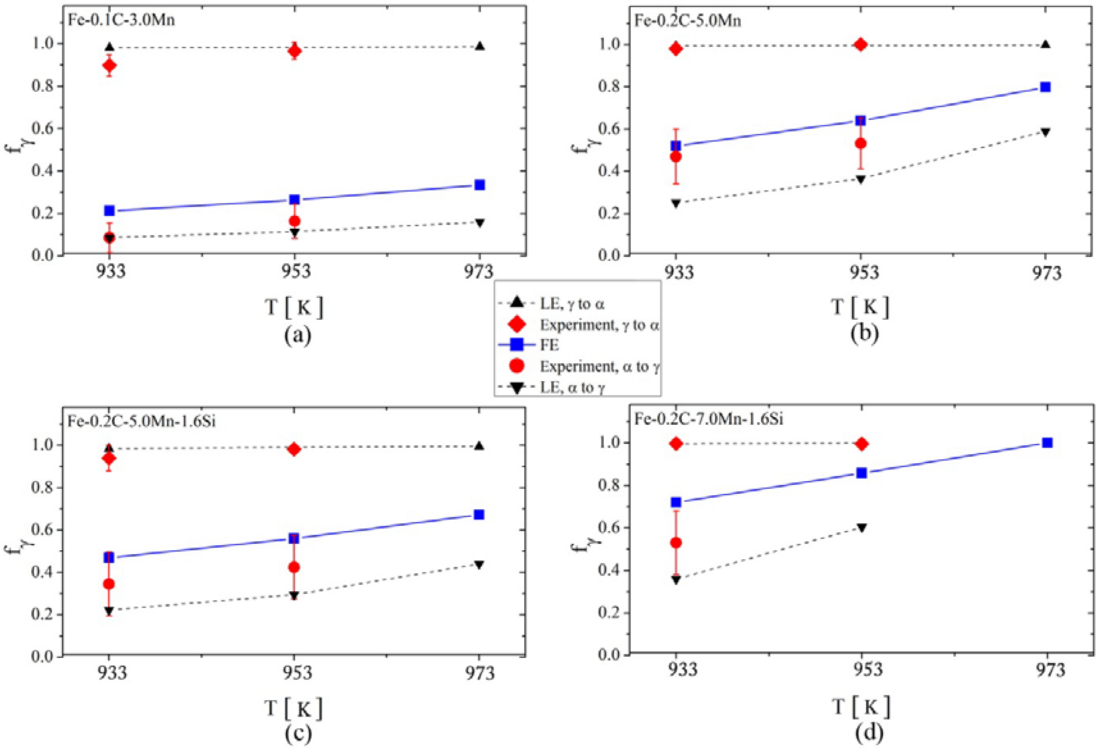

Fig. 2.6 - Experimental and modelling results of austenite fraction in a) Fe-0.1C-3.0Mn, b) Fe-0.2C-5.0Mn, c) Fe-0.2C-5.0Mn-1.6Si and d) Fe-0.2C-7.0Mn-1.6Si.

four alloys, ferrite growth from austenite starts in the PLE mode. Hence both C and Mn (and Si in the case of Fe-0.2C-5.0Mn-1.6Si and Fe-0.2C-7.0Mn-1.6Si alloys) redistribute into the untransformed austenite according to the PLE iso-activity (so called tie-lines) indicated by blue lines in Fig. 2.7a and Fig. 2.7c. The tie-lines in PLE mode region are obtained when the chemical potentials of each component are equal in both γ and α phases. Since both substitutional alloying elements have significantly lower diffusion coefficients than C, the ferrite growth rate is sluggish and is controlled by partioning of Mn (and Si) [50]. As shown in Fig. 2.7b and Fig. 2.7d, the austenite formation from ferrite for the four alloys starts under NPLE mode and continues with C depletion in the untransformed ferrite according to the horizontal blue tie-lines. Carbon is redistributed to keep the chemical potentials equal in each phase and Mn has the same concentration both in γ and α and has unequal chemical potentials in both phases. When the composition of ferrite reaches the NPLE/PLE boundary, the austenite growth mode switches to the PLE mode. Albeit the

$\alpha' \rightarrow \gamma$ transformation starts in NPLE mode, Mn and Si concentration profiles also develop across the interface at prolonged isothermal holding time [43,51]. The transformation stops well before the full equilibrium condition is reached. These observations are in good agreement with the Dictra simulations shown in Fig. 2.3 a-b.

Fig. 2.8 summarizes the model and experimental results for the four alloys studied. It is clear that that Mn and Si content directly affect the Ae1 and Ae3 temperatures and thus the full equilibrium fractions of ferrite or austenite at the fixed temperature of 933 K (660 ℃). As reported in [52–54] nucleation of austenite not only occurs at the grain boundaries but also at interfaces of α/α and α/carbides. This simultaneous nucleation on the carbides is not taken into account in the 1D model. It is worth noting that formation of cementite, which is neglected in the modelling part, affects the experimental value of f_γ. Although Si is known to retard the cementite formation, however, it does not completely suppress the precipitation and cementite will appear after a long annealing times [55,56].

It is worth noting that considering the observed effect of simulation cell size on the predicted value of f_γ, it is clear that varying the cell size does not affect the overall trend of predicted fractions for both $\gamma \rightarrow \alpha$ and the $\alpha' \rightarrow \gamma$ transformations. In the current analysis, the cell length of $\alpha' \rightarrow \gamma$ is taken the same as the $\gamma \rightarrow \alpha$ transformation, i.e. 50 µm. Using the lath width for the $\alpha' \rightarrow \gamma$ transformation might be an alternative, however, due to the continuous recovery of martensite and low angle lath boundaries at such high temperature, capturing the effect of a transient initial effective computational cell size is complex and outside the scope of the present study.

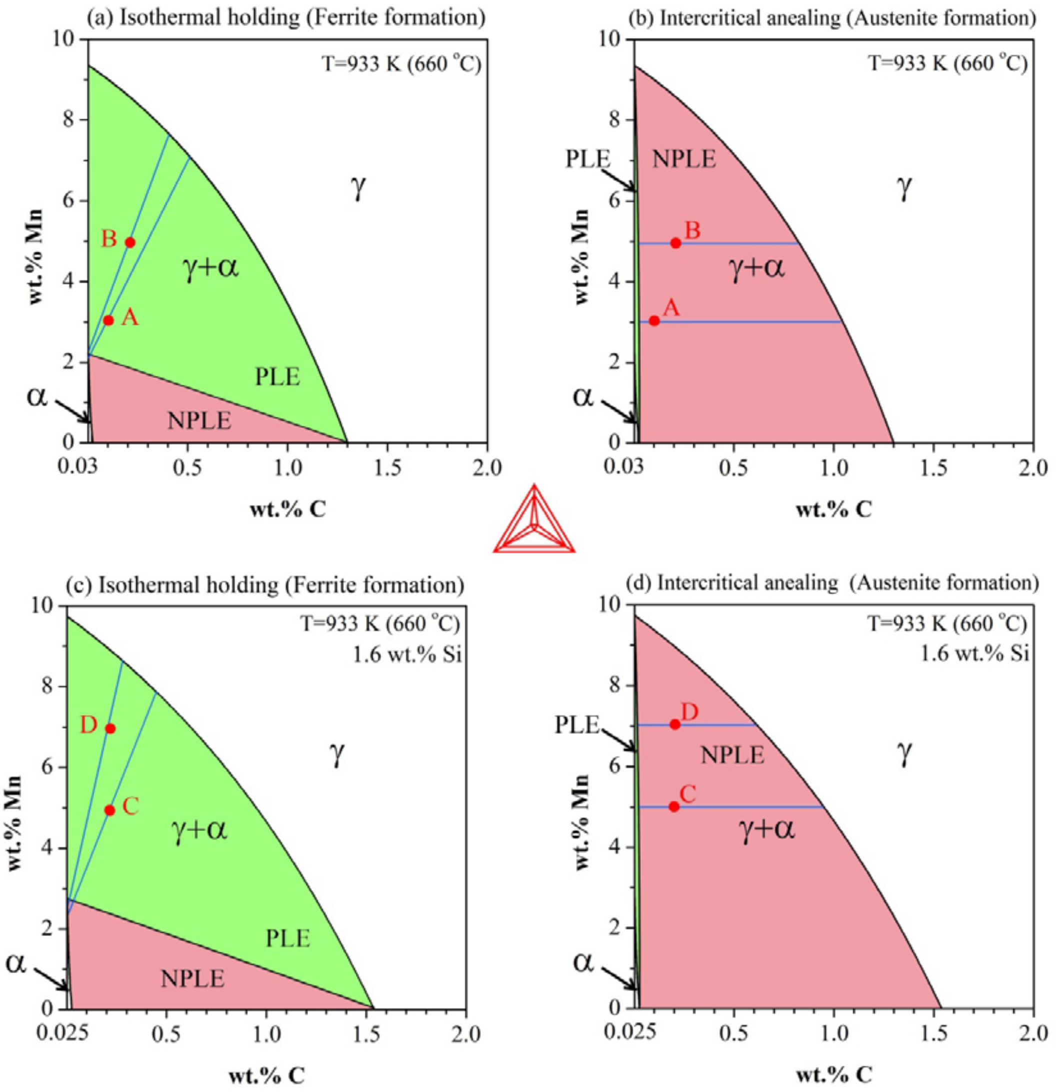

Fig. 2.7 - Isothermal section of an equilibrium phase diagram showing boundary of PLE/NPLE at T= 933 K (660℃) in (a) ferrite and (b) austeniteformations in C-Mn steel, and (c) ferrite and (d) austenite formations in C-Mn steel with 1.6mass% Si.

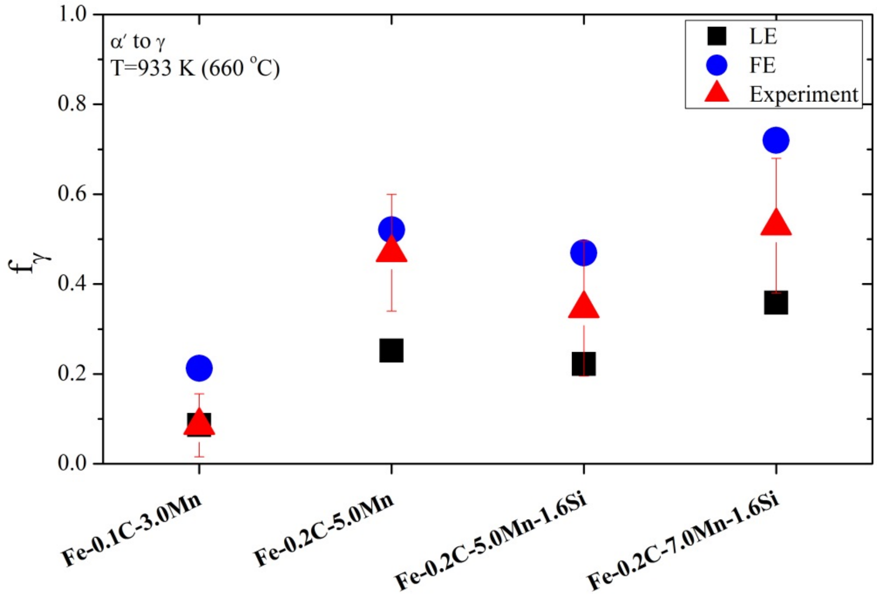

Fig. 2.8 - Heat treatment diagram illustrating martensite to austenite phase transformation at T=933 K (660℃).

2.5 Conclusions

In this study the effect of initial microstructure and isothermal holding temperature in the intercritical zone was studied experimentally and theoretically for a series of steels with Mn content up to 7mass%. The following results are obtained:

1. There is a significant difference in the transformation rate between the γ→α and α′→γ transformations.

2. For the alloy compositions and temperatures considered here, the γ→α transformation starts in PLE mode and the ferrite growth rate is constrained by the redistribution of Mn and Si. However, in the case of the α′→γ transformation, the austenite growth starts in the NPLE mode and shifts to PLE by depletion of C in the martensitic ferrite matrix.

3. For Mn levels between 3 to 7 mass% the LE model is qualitatively correct but does not predict the austenite fraction in α′→γ transformation with high enough accuracy.

4. For the higher Mn level steels, the additional intragranular nucleation of austenite during $\alpha' \rightarrow \gamma$ transformation increases the $f\gamma$ at the end of the intercritical holding stage of 104 s, which is not captured by 1D geometry of LE model.

2.6 References

[1] R. Ding, D. Tang, A. Zhao, A novel design to enhance the amount of retained austenite and mechanical properties in low-alloyed steel, Scr. Mater. 88 (2014) 21–24. doi:10.1016/J.SCRIPTAMAT.2014.06.014.

[2] E. Gamsjäger, J. Svoboda, F.D. Fischer, Austenite-to-ferrite phase transformation in low-alloyed steels, Comput. Mater. Sci. 32 (2005) 360–369. doi:10.1016/J.COMMATSCI.2004.09.031.

[3] A.T.W. Kempen, F. Sommer, E.J. Mittemeijer, The kinetics of the austenite–ferrite phase transformation of Fe-Mn: differential thermal analysis during cooling, Acta Mater. 50 (2002) 3545–3555. doi:10.1016/S1359-6454(02)00149-0.

[4] J.J. Wits, T.A. Kop, Y. van Leeuwen, J. Seitsma, S. van der Zwaag, A study on the austenite-to-ferrite phase transformation in binary substitutional iron alloys, Mater. Sci. Eng. A. 283 (2000) 234–241. doi:10.1016/S0921-5093(00)00735-8.

[5] G.P. Krielaart, J. Sietsma, S. van der Zwaag, Ferrite formation in Fe-C alloys during austenite decomposition under non-equilibrium interface conditions, Mater. Sci. Eng. A. 237 (1997) 216–223. doi:10.1016/S0921-5093(97)00365-1.

[6] C.-S. Oh, H.N. Han, C.G. Lee, T.-H. Lee, S.-J. Kim, Dilatometric analysis on phase transformations of intercritical annealing of Fe−Mn−Si and Fe−Mn−Si−Cu low carbon TRIP steels, Met. Mater. Int. 10 (2004) 399–406. doi:10.1007/BF03027339.

[7] S. Lee, B.C. De Cooman, On the Selection of the Optimal Intercritical Annealing Temperature for Medium Mn TRIP Steel, Metall. Mater. Trans. A. 44 (2013) 5018–5024. doi:10.1007/s11661-013-1860-2.

[8] E. Emadoddin, A. Akbarzadeh, G. Daneshi, Effect of intercritical annealing on retained austenite characterization in textured TRIP-assisted steel sheet, Mater. Charact. 57 (2006) 408–413. doi:10.1016/J.MATCHAR.2006.04.006.

[9] G.N. Haidemenopoulos, N. Aravas, I. Bellas, Kinetics of strain-induced transformation of dispersed austenite in low-alloy TRIP steels, Mater. Sci. Eng. A. 615 (2014) 416–423. doi:10.1016/j.msea.2014.07.099.

[10] A.I. Katsamas, A.N. Vasilakos, G.N. Haidemenopoulos, Simulation of intercritical annealing in low-alloy TRIP steels, Steel Res. 71 (2000) 351–356. doi:10.1002/srin.200001328.

[11] H.S. Zurob, C.R. Hutchinson, A. Béché, G.R. Purdy, Y.J.M. Bréchet, A transition from local equilibrium to paraequilibrium kinetics for ferrite growth in Fe–C–Mn: A possible role of interfacial segregation, Acta Mater. 56 (2008) 2203–2211. doi:10.1016/j.actamat.2008.01.016.

[12] H.S. Zurob, C.R. Hutchinson, Y. Bréchet, H. Seyedrezai, G.R. Purdy, Kinetic transitions during non-partitioned ferrite growth in Fe–C–X alloys, Acta Mater. 57 (2009) 2781–2792. doi:10.1016/j.actamat.2009.02.029.

[13] H. Chen, S. van der Zwaag, Analysis of ferrite growth retardation induced by local Mn enrichment in austenite created by prior interface passages, Acta Mater. 61 (2013) 1338–1349. doi:10.1016/j.actamat.2012.11.011.

[14] H. Chen, S. van der Zwaag, A general mixed-mode model for the austenite-to-ferrite transformation kinetics in Fe–C–M alloys, Acta Mater. 72 (2014) 1–12. doi:10.1016/j.actamat.2014.03.034.

[15] H. Chen, S. van der Zwaag, Predicting the Effect of Mo, Ni, and Si on the Bainitic Stasis, Metall. Mater. Trans. A. 45 (2014) 3429–3437. doi:10.1007/s11661-014-2262-9.

[16] H. Chen, X. Xu, W. Xu, S. van der Zwaag, Predicting the Austenite Fraction After Intercritical Annealing in Lean Steels as a Function of the Initial Microstructure, Metall. Mater. Trans. A. 45 (2014) 1675–1679. doi:10.1007/s11661-014-2186-4.

[17] C.R. Hutchinson, A. Fuchsmann, H.S. Zurob, Y. Brechet, A novel experimental approach to identifying kinetic transitions in solid state phase transformations, Scr. Mater. 50 (2004) 285–290. doi:10.1016/J.SCRIPTAMAT.2003.09.051.

[18] M. Hillert, J. Ågren, On the definitions of paraequilibrium and orthoequilibrium, Scr. Mater. 50 (2004) 697–699. doi:10.1016/j.scriptamat.2003.11.020.

[19] M.P. Hillert, Internal Report, Swedish Inst, Met. Res., Stock. Sweden. (1953).

[20] A. Hultgren, Isothermal transformation of austenite, Trans. Am. Soc. Met. 39 (1947) 915–1005.

[21] D.E. Coates, Diffusion-controlled precipitate growth in ternary systems I, Metall. Trans. 3 (1972) 1203–1212. doi:10.1007/BF02642453.

[22] D.E. Coates, Diffusion controlled precipitate growth in ternary systems: II, Metall. Trans. 4 (1973) 1077–1086. doi:10.1007/BF02645611.

[23] E. Gamsjäger, H. Chen, S. van der Zwaag, Application of the cyclic phase transformation concept for determining the effective austenite/ferrite interface mobility, Comput. Mater. Sci. 83 (2014) 92–100. doi:10.1016/J.COMMATSCI.2013.10.036.

[24] H. Chen, K. Zhu, L. Zhao, S. Van Der Zwaag, Analysis of transformation stasis during the isothermal bainitic ferrite formation in Fe-C-Mn and Fe-C-Mn-Si alloys, Acta Mater. 61 (2013) 5458–5468. doi:10.1016/j.actamat.2013.05.034.

[25] C. Capdevila, J. Cornide, K. Tanaka, K. Nakanishi, E. Urones-Garrote, Kinetic transition during ferrite growth in Fe-C-Mn medium carbon steel, Metall. Mater. Trans. A Phys. Metall. Mater. Sci. 42 (2011) 3719–3728. doi:10.1007/s11661-011-0650-y.

[26] G. Sheng, Z.-G. Yang, A calculation of partitional local equilibrium/negligible partitional local equilibrium boundaries in Fe–C–X systems, Mater. Lett. 62 (2008) 1933–1936. doi:10.1016/J.MATLET.2007.10.060.

[27] H.S. Zurob, D. Panahi, C.R. Hutchinson, Y. Brechet, G.R. Purdy, Self-Consistent Model for Planar Ferrite Growth in Fe-C-X Alloys, Metall. Mater. Trans. A. 44 (2013) 3456–3471. doi:10.1007/s11661-012-1479-8.

[28] H. Chen, B. Appolaire, S. van der Zwaag, Application of cyclic partial phase transformations for identifying kinetic transitions during solid-state phase transformations: Experiments and modeling, Acta Mater. 59 (2011) 6751–6760. doi:10.1016/j.actamat.2011.07.033.

[29] H. Chen, W. Xu, M. Goune, S. van der Zwaag, Application of the stagnant stage concept for monitoring Mn partitioning at the austenite-ferrite interface in the intercritical region for Fe–Mn–C alloys, Philos. Mag. Lett. 92 (2012) 547–555. doi:10.1080/09500839.2012.700124.

[30] H. Luo, J. Shi, C. Wang, W. Cao, X. Sun, H. Dong, Experimental and numerical analysis on formation of stable austenite during the intercritical annealing of 5Mn steel, Acta Mater. 59 (2011) 4002–4014. doi:10.1016/j.actamat.2011.03.025.

[31] J. Ågren, Computer simulations of the austenite/ferrite diffusional transformations in low alloyed steels, Acta Metall. 30 (1982) 841–851. doi:10.1016/0001-6160(82)90082-7.

[32] R. Wei, M. Enomoto, R. Hadian, H.S. Zurob, G.R. Purdy, Growth of austenite from as-quenched martensite during intercritical annealing in an Fe–0.1C–3Mn–1.5Si alloy, Acta Mater. 61 (2013) 697–707. doi:10.1016/J.ACTAMAT.2012.10.019.

[33] E. Hersent, K. Marthinsen, E. Nes, On the Effect of Atoms in Solid Solution on Grain Growth Kinetics, Metall. Mater. Trans. A. 45 (2014) 4882–4890. doi:10.1007/s11661-014-2459-y.

[34] C. Wang, W. Cao, J. Shi, C. Huang, H. Dong, Deformation microstructures and strengthening mechanisms of an ultrafine grained duplex medium-Mn steel, Mater. Sci. Eng. A. 562 (2013) 89–95. doi:10.1016/j.msea.2012.11.044.

[35] R. Zhang, W.Q. Cao, Z.J. Peng, J. Shi, H. Dong, C.X. Huang, Intercritical rolling induced ultrafine microstructure and excellent mechanical properties of the medium-Mn steel, Mater. Sci. Eng. A. 583 (2013) 84–88. doi:10.1016/j.msea.2013.06.067.

[36] A. Arlazarov, M. Gouné, O. Bouaziz, A. Hazotte, G. Petitgand, P. Barges, Evolution of microstructure and mechanical properties of medium Mn steels during double annealing, Mater. Sci. Eng. A. 542 (2012) 31–39. doi:10.1016/j.msea.2012.02.024.

[37] J. Lee, S.S. Sohn, S. Hong, B.-C. Suh, S.-K. Kim, B.-J. Lee, N.J. Kim, S. Lee, Effects of Mn Addition on Tensile and Charpy Impact Properties in Austenitic Fe-Mn-C-Al-Based Steels for Cryogenic Applications, Metall. Mater. Trans. A. 45 (2014) 5419–5430. doi:10.1007/s11661-014-2513-9.

[38] S.S. Sohn, S. Lee, B.-J. Lee, J.-H. Kwak, Microstructural Developments and Tensile Properties of Lean Fe-Mn-Al-C Lightweight Steels, JOM. 66 (2014) 1857–1867. doi:10.1007/s11837-014-1128-3.

[39] J. Han, S.-J. Lee, J.-G. Jung, Y.-K. Lee, The effects of the initial martensite microstructure on the microstructure and tensile properties of intercritically annealed Fe–9Mn–0.05C steel, Acta Mater. 78 (2014) 369–377. doi:10.1016/j.actamat.2014.07.005.

[40] I. Gutierrez-Urrutia, D. Raabe, Influence of Al content and precipitation state on the mechanical behavior of austenitic high-Mn low-density steels, Scr. Mater. 68 (2013) 343–347. doi:10.1016/j.scriptamat.2012.08.038.

[41] H. Guo, G.R. Purdy, M. Enomoto, H.I. Aaronson, Kinetic transitions and substititional solute (Mn) fields associated with later stages of ferrite growth in Fe-C-Mn-Si, Metall. Mater. Trans. A. 37 (2006) 1721–1729. doi:10.1007/s11661-006-0115-x.

[42] H. Guo, M. Enomoto, Effects of Substitutional Solute Accumulation at α/γ Boundaries on the Growth of Ferrite in Low Carbon Steels, Metall. Mater. Trans. A. 38 (2007) 1152–1161. doi:10.1007/s11661-007-9139-0.

[43] N. Nakada, K. Mizutani, T. Tsuchiyama, S. Takaki, Difference in transformation behavior between ferrite and austenite formations in medium manganese steel, Acta Mater. 65 (2014) 251–258. doi:10.1016/j.actamat.2013.10.067.

[44] H. Chen, S. van der Zwaag, Indirect evidence for the existence of the Mn partitioning spike during the austenite to ferrite transformation, Philos. Mag. Lett. 92 (2012). doi:10.1080/09500839.2011.634840.

[45] H. Chen, R. Kuziak, S. van der Zwaag, Experimental Evidence of the Effect of Alloying Additions on the Stagnant Stage Length During Cyclic Partial Phase Transformations, Metall. Mater. Trans. A. 44 (2013) 5617–5621. doi:10.1007/s11661-013-2040-0.

[46] J.O. Andersson, T. Helander, L. Höglund, P. Shi, B. Sundman, Thermo-Calc & DICTRA, computational tools for materials science, Calphad. 26 (2002) 273–312. doi:10.1016/S0364-5916(02)00037-8.

[47] A. Borgenstam, A. Engström, L. Höglund, J. Ågren, DICTRA, a tool for simulation of diffusional transformations in alloys, J. Phase Equilibria. 21 (2000) 269–280. doi:10.1361/105497100770340057.

[48] M. ENOMOTO, Comparison of alloy element partition behavior and growth kinetics of proeutectoid ferrite in Fe-C-X alloys with diffusion growth theory., Trans. Iron Steel Inst. Japan. 28 (1988) 826–835. doi:10.2355/isijinternational1966.28.826.

[49] C. Atkinson, T. Akbay, R.C. Reed, Theory for reaustenitisation from ferrite/cementite mixtures in Fe-C-X steels, Acta Metall. Mater. 43 (1995) 2013–2031. doi:10.1016/0956-7151(94)00366-P.

[50] Z.-Q. Liu, G. Miyamoto, Z.-G. Yang, T. Furuhara, Direct measurement of carbon enrichment during austenite to ferrite transformation in hypoeutectoid Fe–2Mn–C alloys, Acta Mater. 61 (2013) 3120–3129. doi:10.1016/j.actamat.2013.02.003.

[51] G.-H. Zhang, Y.-U. Heo, E.-J. Song, D.-W. Suh, Kinetic transition during the growth of proeutectoid ferrite in Fe-C-Mn-Si quaternary steel, Met. Mater. Int. 19 (2013) 153–158. doi:10.1007/s12540-013-2003-4.

[52] J. Huang, W.J. Poole, M. Militzer, Austenite formation during intercritical annealing, Metall. Mater. Trans. A. 35 (2004) 3363–3375. doi:10.1007/s11661-004-0173-x.

[53] C.I. Garcia, A.J. Deardo, Formation of austenite in 1.5 pct Mn steels, Metall. Trans. A. 12 (1981) 521–530. doi:10.1007/BF02648551.

[54] J. Lis, A. Lis, Kinetics of the austenite formation during intercritical annealing, J. Achiev. Mater. Manuf. Eng. 26 (2008) 195–198.

[55] E. Kozeschnik, H.K.D.H. Bhadeshia, Influence of silicon on cementite precipitation in steels, Mater. Sci. Technol. 24 (2013) 343–347. doi:10.1179/174328408X275973.

[56] B. Kim, C. Celada, D. San Martín, T. Sourmail, P.E.J. Rivera-Díaz-del-Castillo, The effect of silicon on the nanoprecipitation of cementite, Acta Mater. 61 (2013) 6983–6992. doi:10.1016/j.actamat.2013.08.012.

Chapter 3 Effect of C and N and their Absence on the Kinetics of Austenite-Ferrite Phase Transformations in Fe-0.5Mn alloy

This Chapter is based on

- H. Farahani, H. Zurob, C.R. Hutchinson S. van der Zwaag, Effect of C and N and their absence on the kinetics of austenite-ferrite phase transformations in Fe-0.5Mn alloy, *Acta Materialia*, Volume 150, 15 May 2018, Pages 224-235

ABSTRACT

Investigating the partitioning effect of substitutional and interstitial elements on the migration of transformation interfaces during austenite-ferrite phase transformation in steels with the conventional experimental method is extremely challenging due to interaction between the solute atoms and the transformation interfaces. Additionally, the simultaneous nucleation of new phases during phase transformations limits the accuracy of extracted growth rates from experimental kinetics measurements of phase fractions. In a novel experimental approach, the cyclic partial phase transformation concept is used to avoid the effect of nucleation on total kinetics of phase transformations. In this study, a Fe-0.5Mn alloy in the presence and absence of interstitial C and N additions is subjected to different cyclic transformation routes to examine the possible interaction between solute atoms and migrating interfaces. The experimental results are in semi-quantitative agreement with modelling predictions made by the local equilibrium approach and provide indirect evidence of Mn partitioning at austenite/ferrite interface in absence of any interstitial elements. It is also confirmed that the presence of interstitial elements promotes Mn

interaction with the interface, whereas N promotes more Mn partitioning at transformation interface compared to C.

3.1 Introduction

The precipitation of ferrite during austenite decomposition is a key step in the microstructure evolution of many important steel grades. The transformation kinetics in Fe-X-Y systems is complicated by the large difference in the diffusion rates of the interstitial elements, Y= C, N and the substitutional elements, X = Mn, Ni, Si, Mo…etc., along with the possible interactions of the elements with the transformation interfaces [1].

In a given industrial condition, ferrite formation may occur with or without partitioning of the substitutional alloying element between phases [2–5]. This leads to complex situations in which the kinetics of phase transformation in a Fe-X-Y steels can be controlled by the short-range or long-range or interfacial diffusion of substitutional and interstitial elements. This is not say, however, that these effects can be simply assumed separated. In many conditions, the interaction of substitutional element with the transformation interfaces strongly influences [6,7] or is influenced [8] by concentration of interstitial elements at the interface.

Several experimental and theoretical attempts have been conducted to capture effect of substitutional (especially Mn) and interstitial solutes (especially C and N) on the interface migration during austenite to ferrite phase transformation. In a simple approach, the individual effect of solutes on the austenite to ferrite phase transformation can be studied separately in binary Fe-C, Fe-N and Fe-Mn systems. On top of theoretical differences between effects of C and N in Fe-based alloys predicted by atomistic simulations [9,10], it has been experimentally shown that [11–13] in Fe-N system with low nitrogen, austenite to ferrite transformation occurs massively and the interface velocity is independent of the cooling rate, while in Fe-C system the transition from interface controlled to diffusion controlled regimes delimits transformation kinetics. In the Fe-Mn system, the austenite to ferrite transformation occurs massively with a large change in strain energy caused by misfit between the two phases. All these data provide useful basics to explain characteristic effects of each individual element on a migrating austenite/ferrite interface. However, a simple combination of these findings fails in making accurate predictions for ternary Fe-X-Mn systems, suggesting a potential role of interatomic interactions between solutes at interfaces.

In another approach, the effects can be studied by conducting austenite to ferrite phase transformation experiments in series of Fe-C-Mn and Fe-N-Mn ternary steels. In this regard, a series of recent experimental studies on ferrite growth during controlled decarburizing and denitriding [14], [15] have suggested interfacial segregation of Mn in presence of C, but no sign of interfacial segregation of Mn in Fe-N-Mn. These findings, based on analysis of the growth kinetic data, is consistent with the preceding accepted perception [8,16–18] that the presence of interstitial elements influences the tendency of the substitutional alloying element to segregate to the interface. However, the very slow and continuous ferrite growth in decarburizing and denitriding condition is quite different from the conventional ferrite precipitation reaction in which ferrite passes from fast transformation to a stasis regime [19,20], makes generalization of these findings difficult.

In parallel to experiment, theoretical works also confirm the importance of the interaction of solute elements at the interfaces. Recent ab-inito calculations by *Wicaksono* et al. [21] confirm strong attractive interaction between C and Mn in bulk bcc iron at the atomistic scale. This is in agreement with the study on ferrite transformation stasis by Sun et al. [22] using a coupled solute drag model, stating that repulsive or attractive interaction between interstitial and substitutional elements can directly influence the interfacial behaviour of substitutional elements. As an example, Si interaction with a migrating austenite/ferrite interface in a Fe-C-Y steel can be very different in the presence or absence of Mn [23].

Underlining the effect of solutes on migrating austenite/ferrite interfaces, one should remember that the experimentally measured kinetics of austenite to ferrite transformation is a product of both nucleation and growth. Addition of substitutional elements to Fe-C and Fe-N binary steels have a strong effect on the nucleation kinetics [24,25]. In recent years, development of the Cyclic Partial Phase Transformation (CPPT) concept, made it possible to study the effect of alloying elements on migration of the austenite/ferrite interface without the complications associated with concurrent nucleation [26–28]. In a CPPT experiment, the temperature is cycled inside the intercritical zone where both austenite and ferrite phases are present at all times. The CPPT concept has been successfully used to study, both experimentally and theoretically, the effect of substitutional elements, especially Mn, on the migration rate of austenite/ferrite interfaces. A stagnant stage, during which the growth of ferrite (or austenite) is significantly delayed, is found in Fe-C-Mn alloys, while no stagnant stage is observed in Fe-C alloys. While the reported increasing magnitude of the growth retardation with increasing concentration of substitutional elements (i.e. Mn or Ni) is attributed to strong partitioning behavior of substitutional elements at transformation interfaces [29], the role of interstitial elements on the partitioning behavior of substitutional elements is still unknown.

The approach of changing the bulk interstitial solute content in order to evaluate the effect of the X-Y interaction is not easily adapted to phase interfaces. Instead, in this study we have used CPPT concept to examine this possible interaction in an Fe-0.5Mn alloy in the presence and absence of interstitial C and N additions. The kinetics measurement in Fe-C-Mn, Fe-Mn and Fe-N-Mn systems will open windows to better understand the extent to which the presence of Mn at the interface is dictated by the Mn-interface interaction as opposed to the interaction of Mn with the interstitial elements present at the interface.

3.2 Decarburization and Nitriding experiments

An Fe-0.1C-0.5Mn steel was selected as the starting alloy for this study. In order to prepare interstitial free alloys, hollow cylindrical samples with length of 10 mm, diameter of 5 mm and thickness of 1 mm were subject to controlled decarburization to produce the binary Fe-0.5Mn alloy. The ternary Fe-N-Mn alloys were then produced using controlled nitriding of the Fe-0.5Mn binary. The full details for these processes are given by Guo et al [14]. The exact composition of the alloys used in this study are shown in Table 3.1. While we intended to make the nitrogen concentration equal to the original carbon concentration, we did not succeed, but as explained in the next section we could compensate for the difference in concentration level by adjusting the temperature ranges over which to cycle.

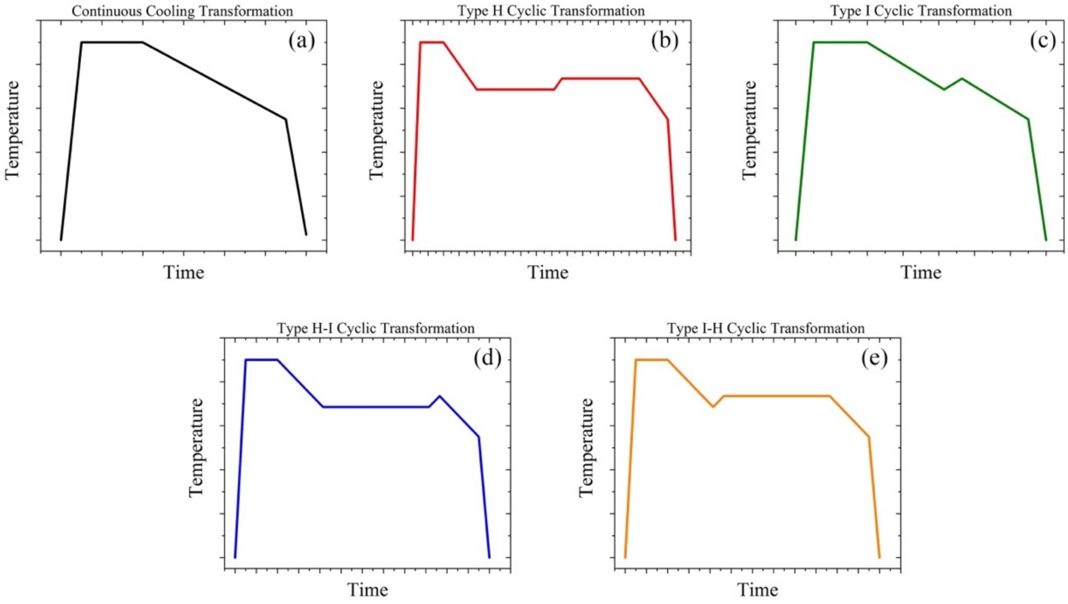

Fig. 3.1- Different applied experimental thermal routes.

3.3 The cyclic heat treatments

All heat treatments were performed using a Bähr DIL 805A/D/T Quenching Dilatometer. Two thermocouples, spaced 4 mm apart, were attached to the specimen to measure the temperature difference in the sample precisely. All the specimens were heated with a rate of 10 K/s to 1173 K (900 °C) and kept for 300 s (5 min) to ensure full austenitization. The samples were then subjected to different Cyclic Partial Phase Transformation (CPPT) routes and Continuous Cooling (CC) experiments with cooling (or heating) rates of 1 K/s as shown in Fig. 3.1, with the exact treatment temperatures indicated in Table 3.1 for each alloy.

In a continuous cooling (CC) experiment (Fig. 3.1a), the sample is cooled at a constant rate of 1 K/s from the austenitization temperature to a temperature below the A_1 transition temperature. During cooling, the kinetics of austenite to ferrite phase transformation is controlled via concurrent nucleation and growth events, in consort with continuous segregation of Mn at the newly formed austenite/ferrite interfaces and redistribution of interstitial element in the remaining austenite. In a type H CPPT experiment, as shown in Fig. 3.1b, the sample is continuously cooled to T_1, below A_3 and inside the intercritical region, kept isothermally for 20 min, leading to a mixture of austenite and ferrite with the formation of Mn spike at the interfaces and redistribution of interstitial elements (C or N) around the interface resulting in a minimal compositional gradient. Then, the temperature is increased to T_2, still inside the austenite/ferrite two phase region, and again kept isothermally for 20 minutes to give enough time for Mn interaction with the interface and redistribution of interstitial elements before final cooling to room temperature. In type I CPPT experiment (Fig. 3.1c), temperature is cycled between T_1 and T_2, but immediate changes in temperature after reaching T_1 and T_2 are used in order to limit the time available for the redistribution of interstitial elements. Type H-I and I-H (Fig. 3.1d and Fig. 3.1e) cyclic experiments are designed to generate a spike of Mn at the interface, with controlled redistribution of the interstitial element only at T_1 or T_2, through one isothermal holding stage at T_1 or T_2, and sudden changes in temperature after reaching T_2 or T_1, respectively.

Table 3.1. Compositions of the alloys used in the experiments.

Alloy name	Exact Composition (all in mass%)	T1	T2
Fe-0.1C-0.5Mn	Fe-0.0848C-0.47Mn	1048 K (775 °C)	1098 K (825 °C)
Fe-0.5Mn	Fe-0.01C-0.47Mn	1133 K (860 °C)	1158 K (885 °C)
Fe-0.3N-0.5Mn	Fe-0.27N-0.47Mn	958 K (685 °C)	1008 K (735 °C)

One of the subtle aspects of the experimental work concerns the stability of the Fe-N-Mn solution against decomposition into ferrite and nitrogen gas. In order to avoid decomposition during the present experiments, it was necessary to work with dilute N contents. The Fe-N-Mn samples were also coated using gold sputtering to prevent possible nitrogen bubble formation during thermal experiments in the dilatometer [30]. The microstructure of all of the samples were checked before and after the experiments to confirm the reliability of the experimental results. In each case, the experiments were performed at least twice to ensure the reproducibility of the results. The microstructures after the experiments were checked to make sure the amount of possible decarburization or denitriding during experiments was negligible.

3.4 Modelling Details

Simulations of cyclic phase transformations and continuous cooling experiments are performed in different composition sets of Fe-C-Mn, Fe-Mn and Fe-N-Mn systems. For all simulations a 1-D geometry with a size of 25 μm is assumed to represent austenite grain size of 50 μm. Simulations are carried out using the DICTRA software linked to TCFE7 and MOB2 databases. For each composition, the Ae_1 and Ae_3 temperatures are calculated with Thermo-Calc software [31]. The cyclic transformation temperatures, T_1 and T_2, are selected as $T_1 = \frac{(Ae_3+Ae_1)}{2} - \Delta T/2$ and $T_2 = \frac{(Ae_3+Ae_1)}{2} + \Delta T/2$, where $\Delta T = 50\ K$ for Fe-C-Mn and Fe-N-Mn systems and $\Delta T = 25\ K$ for Fe-Mn system.

3.5 Results

In this section, the results of the dilatometry experiments and LE modelling for all three systems subjected to different thermal routes are presented. For better comparisons in all of the dilatation graphs, the Y axis displays the absolute difference between recorded dilatation at temperature T and total dilatation at austenitization temperature of 1173 K (900 °C). Results of modelling are illustrated in graphs of 'superposed interface position' vs temperature and are plotted next to experimental results. In order to direct comparison of the modelling and experimental graphs, the interface position in modelling graphs are modified by applying the effect of thermal expansion/contraction with a constant coefficient of thermal expansion of 0.2 μm/K for both austenite and ferrite.

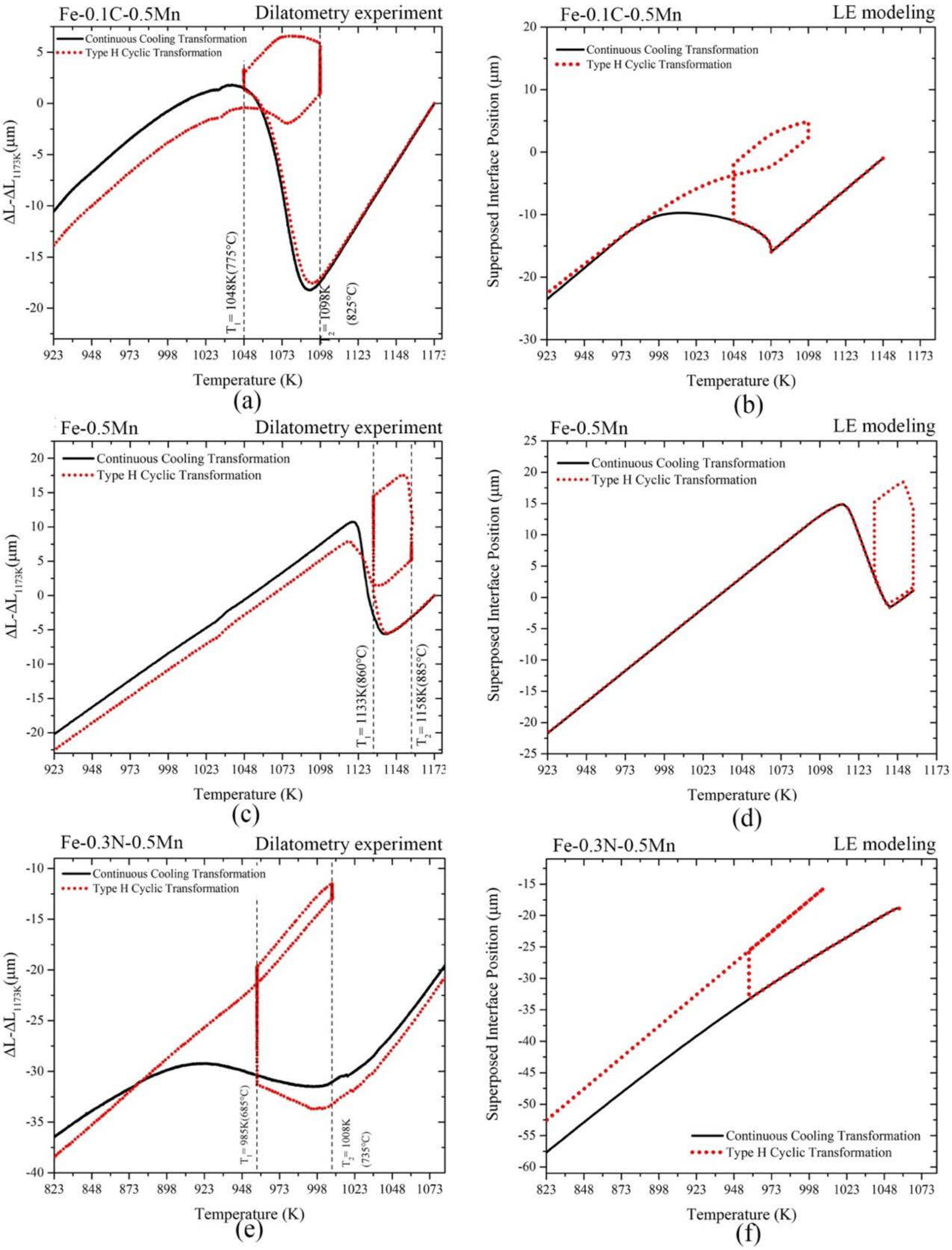

Fig. 3.2-Experimental dilation curves and modelling results for CC transformation vs type H CPPT in Fe-0.1C-0.5Mn, Fe-0.5Mn and Fe-0.3N-0.5Mn alloys.

Fig. 3.2 shows the experimental and modelling results for CC and type H CPPT routes in Fe-0.1C-0.5Mn, Fe-0.5Mn and Fe-0.3N-0.5Mn alloys. The experimental CC curve in Fe-0.1C-0.5Mn alloy (Fig. 3.2a) indicates a steady austenite to ferrite phase transformation, while the dilatation curve for the type H CPPT route between T_1=1048 K (775 °C) and T_2=1098 K (825 °C) shows different distinct stages of phase transformation. In this route, austenite to ferrite phase transformation starts during cooling and continues during the isothermal holding stage (20 minutes) at T_1=1048 K (775 °C). By heating from T_1 up to about 1073 K (800 °C), the so-called 'stagnant stage' [27] starts, during which a linear thermal expansion is observed and no phase transformation or austenite/ferrite interface migration occurs. Upon further heating, the nonlinear contraction is the signature of the 'direct transformation stage' during which ferrite transforms partially to austenite. After isothermal ferrite to austenite transformation in the course of holding at T_2=1098 K (825 °C) for 20 min, the linear contraction during cooling from 1098 K (825 °C) to about 1073 K (800 °C) indicates a stagnant stage in ferrite formation followed by direct austenite to ferrite transformation stage upon further cooling. The corresponding results of LE modelling in the Fe-0.1C-0.5Mn alloy are shown in Fig. 3.2b. Analogous to the experiments, the CC curve in Fig. 3.2b displays a smooth growth for ferrite with slightly different onset temperature compared to the experimental curve. The isothermal direct transformation stage, stagnant stage and non-isothermal transformation stage, which are observed during the type H CPPT experiment are all well captured by the LE model. The length of the stagnant stage, during which the austenite/ferrite interface in the model does not move in spite of temperature variation, is predicted to be 25 K, in close agreement with the corresponding experimental observation.

The experimental dilatation and modelling of CC and type H CPPT curves for the binary Fe-0.5Mn alloy are shown in Fig. 3.2c and Fig. 3.2d, respectively. Similar to the carbon containing system, both the experimental and simulated CC curves show steady austenite to ferrite phase transformation during cooling. Regardless of the absence of interstitial elements in this alloy, the experimental type H CPPT curve displays stagnant stages in both austenite to ferrite and ferrite to austenite phase transformations after isothermal holdings at

T_1=1133 K (860 °C) and T_2=1158 K (865 °C) with an approximate length of 20 K, which is well-captured by the interface position model in Fig. 3.2d.

For the Fe-0.3N-0.5Mn alloy, the austenite to ferrite phase transformation during continuous cooling is similar to that observed in the other two alloys as shown in Fig. 3.2e. A number of differences are observed, however, in the type H cyclic curve between T_1=958 K (685 °C) and T_2=1008 K (735 °C) in the nitrided system compared to the other two systems. The length of stagnant stages in ferrite to austenite (during heating) and austenite to ferrite (during second cooling) transformations are substantially different. In type H CPPT curve, the austenite to ferrite transformation is inactive for heating up to about 45 K. However, the linear contraction of the specimen for more than 180K during cooling cycle after the isothermal stage at T_2, indicates to a very long stagnant stage for ferrite formation in the second cooling cycle.

As with the experimental dilatation curves, the modelling results in Fe-0.3N-0.5Mn shown in Fig. 3.2f, are also quite different from the other two alloys. While the CC curve predicts a smooth ferrite growth during continuous cooling, in type H CPPT after the first isothermal holding at T_1, the interface remains immobile during heating and isothermal holding at T_2. The prediction of an immobile interface during heating and isothermal holding differs from the experimentally observed direct isothermal transformation stage at T_2. Upon final cooling down to 823 K (550 °C), the LE model predicts no interface motion, consistent with the experimental observation in Fig. 3.2e.

The results of type I vs type H CPPT experiments and modelling for the three alloys are shown in Fig. 3.3. The dilatation curves for the Fe-0.1C-0.5Mn alloy in Fig. 3.3a show slightly different behavior of the alloy when subjected to type I cyclic treatments. In the type I curve, at the onset of heating from T_1 in the first cycle, the nonlinear expansion for about 10 K points to continuation of austenite to ferrite transformation, notwithstanding heating of the sample; this part is referred as ‘inverse transformation stage’. The subsequent linear expansion and nonlinear contraction by further heating to T_2, are signatures of the ferrite to austenite stagnant stage and the direct transformation stage, respectively. Unlike heating, no inverse transformation stage is observed after an immediate change in temperature, as the linear contraction during cooling indicates a stagnant stage followed by nonlinear expansion due to austenite to ferrite transformation upon further cooling. In the modelling results of type I (Fig. 3.3b), the interface migration into the austenite region in spite of the temperature increase points to the inverse transformation stage. This is followed by a stagnant stage, occurring during the cooling cycle with a similar length to type H.

In the type I experimental curve for Fe-0.5Mn alloy (Fig. 3.3c), the respective expansion and contraction curves for heating and cooling cycles between T_1 and T_2 appear linear, but not perfectly parallel. This indicates a very short and negligible inverse transformation stage at the onset of heating/cooling cycles. The corresponding modelling curve in Fig. 3.3d successfully captures the experimental stagnant stage as well as the very short inverse transformation stage which is distinguishable by backward interface migration in the modelling results.

For the Fe-0.3N-0.5Mn alloy, according to the observed nonlinear dilatation curves of the type I CPPT in Fig. 3.3e, the inverse transformation stage expands for the whole length of heating cycle. The short linear contraction of about 10K after immediate change in the temperature regime corresponds to the stagnant stage followed by a short nonlinear stage promoted by negligible austenite to ferrite transformation and linear contraction in the final cooling. In the simulated curve for type I CPPT (Fig. 3.3f), the interface sluggishly moves into the austenite region during heating and becomes immobile after that. This interface migration manner is comparable to the slow inverse transformation stages observed in the experiment.

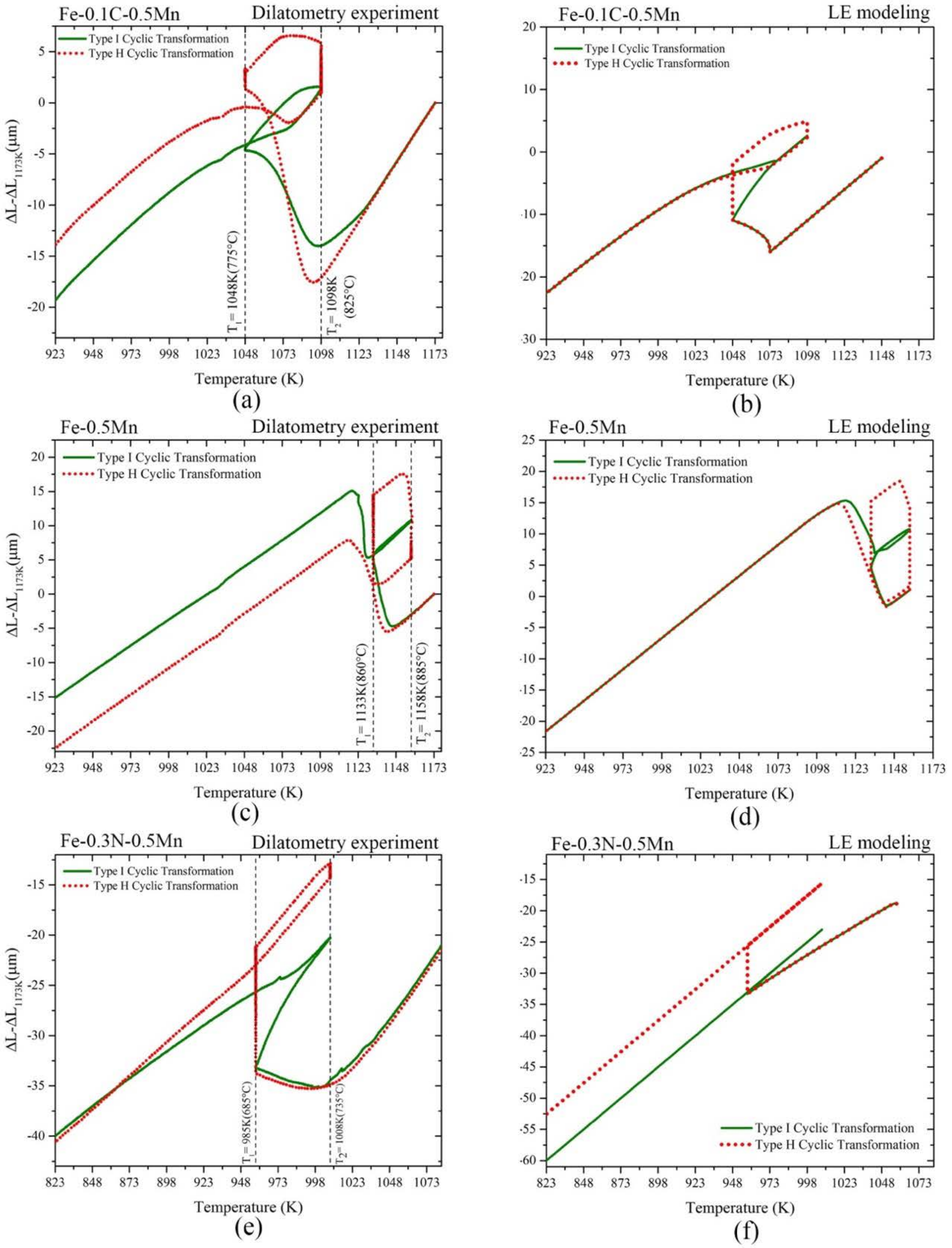

Fig. 3.3- Experimental dilation curves and modelling results for type I vs type H CPPT in Fe-0.1C-0.5Mn, Fe-0.5Mn and Fe-0.3N-0.5Mn alloys.

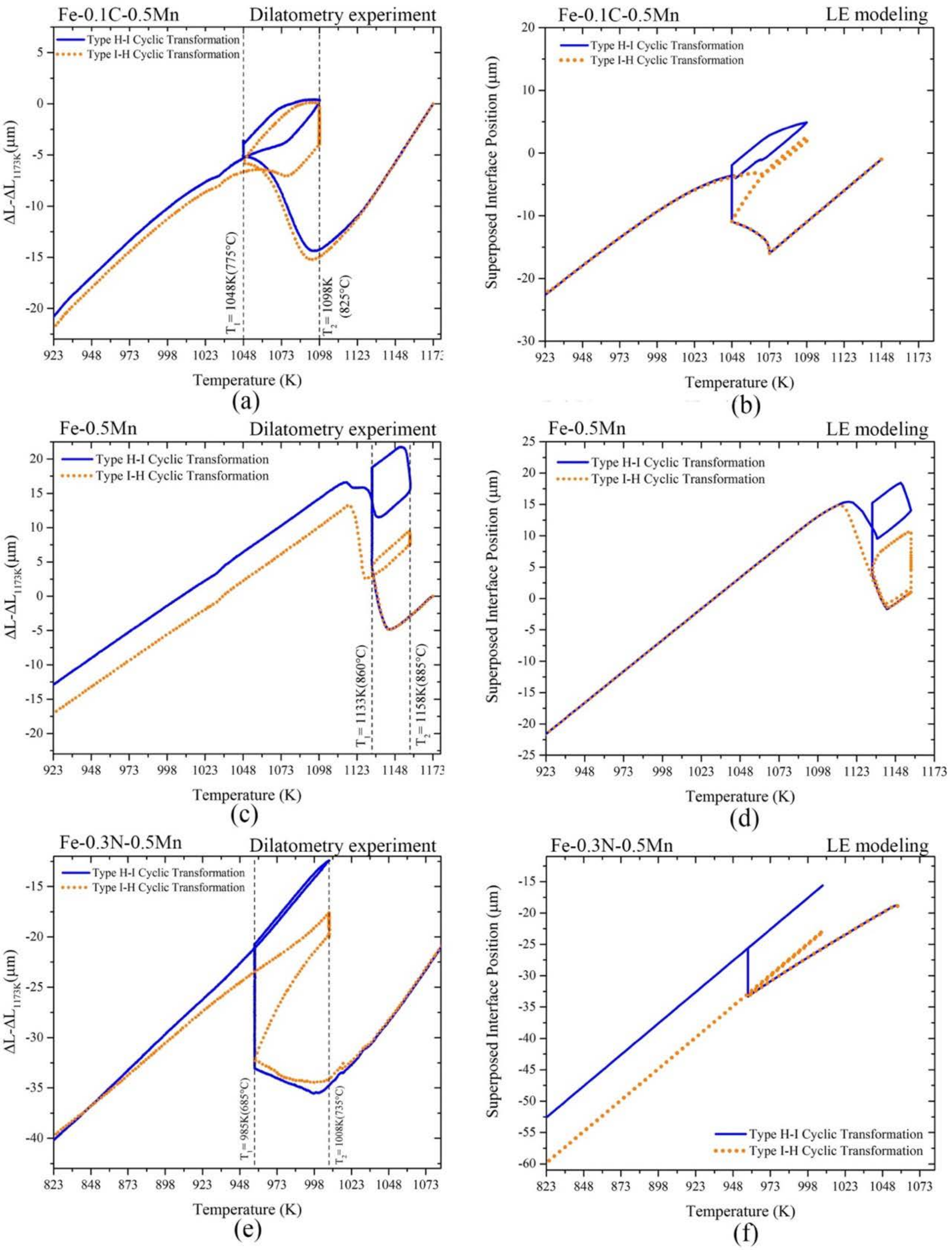

Fig. 3.4- Experimental dilation curves and modelling results for type H-I vs type I-H CPPT in Fe-0.1C-0.5Mn, Fe-0.5Mn and Fe-0.3N-0.5Mn alloys.

The experimental and modelling curves for H-I and I-H CPPT routes are shown in Fig. 3.4. As expected for the Fe-0.1C-0.5Mn alloy (Fig. 3.4a), in type H-I during the first isothermal holding and heating cycle, the dilatation curve points to an isothermal transformation stage, a stagnant stage and a direct transformation stage similar to the type H curve. The cooling curve is similar to type I and displays austenite to ferrite stagnant stage and direct transformation stages. In type I-H curve, a short nonlinear expansion due to the inverse austenite to ferrite transformation is also found at the onset of the heating stage, similar to type I, followed by stagnant stage. The dilatation behavior of the specimen during the rest of the thermal cycle is identical to the one subjected to type H cyclic experiment. The type H-I modelling curve (Fig. 3.4b), captures well the experimentally observed stages during heating. However, in the cooling cycle after the stagnant stage, there is an abrupt change in interface velocity during its migration into the austenite region, which could be caused by interaction with the residual Mn spike formed at the end of the isothermal heating stage at T_1. The smooth interface migration in type I-H curve, demonstrates the inverse transformation, stagnant stage and direct transformation stages.

Analogous to the Fe-0.1C-0.5Mn alloy, the dilatation curves for type H-I and I-H CPPT experiments in the Fe-0.5Mn alloy (Fig. 3.4c), exhibit mixed behavior in heating/cooling corresponding to type H and type I, with a stagnant stage of 20 K and negligible inverse transformation stage. The modelling results for Fe-0.5Mn alloy (Fig. 3.4d) nicely capture the experimentally observed transformation features in dilatation curves; similar to type I, the very short inverse transformation stages in type I-H CPPT curves is discernible by backward interface migration in the modelling results.

In Fe-0.3N-0.5Mn alloy (Fig. 3.4e), the dilatation curve for the type H-I CPPT route, is analogues to the type H curve, but without a direct isothermal transformation stage at T_2. During holding at T_2 in type I-H experiment, a new stage of ‘isothermal inverse transformation’ is observed corresponding to the continued austenite to ferrite phase transformation, notwithstanding the 50K rise in the temperature and 20 minutes of isothermal holding. The LE model results for type H-I and I-H CPPT routes (Fig. 3.4f), are very similar to the predictions for type H and type I routes. In addition, no isothermal inverse transformation stage at T_2 is predicted in the type I-H route.

In summary, the dilatation curves for the Fe-0.1C-0.5Mn alloy show four different transformation stages. The length of the stagnant stage in both austenite and ferrite formation is about 25 K. The inverse transformation stage is observed for about 10 K. The stagnant stage, with a length of 20 K, is still observed in the decarburized Fe-0.5Mn alloy. The dilatation behavior in the Fe-0.3N-0.5Mn alloy is quite different, with longer stagnant stages both in heating and cooling cycles, as well as protracted inverse transformation stages.

3.6 Discussion

The differences in the observed behavior between the different CPPT routes and continuous cooling experiments in the three Fe-0.1C-0.5Mn, Fe-0.5Mn and Fe-0.3N-0.5Mn systems are semi-quantitatively captured by LE model. Thus, it is expected that the features observed by experiments can be explained by analysing the results of the LE model.

The profile of Mn and interstitial elements (C or N) after cyclic experiments at T_1 before the final cooling for all of the thermal routes are shown in Fig. 3.5a-f. It can be seen that the profiles in type H show a spike of Mn at the interface, zig-zag partitioning of Mn at the former position of the interface after the second isothermal holding at T_2, a broadened bulge of Mn at former position of interface after first isothermal holding at T_1 and redistribution of interstitial alloying element around the interface. In type H-I, the profiles show a spike of Mn at the interface, the broadened bulge of Mn at former position of interface formed after first isothermal holding at T_1 and redistribution of interstitial alloying element around the interface. In type I, the profiles simply contain a spike of Mn at the interface and redistribution of interstitial alloying element around the interface. Finally, in type I-H, in addition to the spike of Mn at the interface and the zig-zag partitioning of Mn at the former position of the interface after the second isothermal holding at T_2, the profiles show redistribution of the interstitial alloying element around the interface.

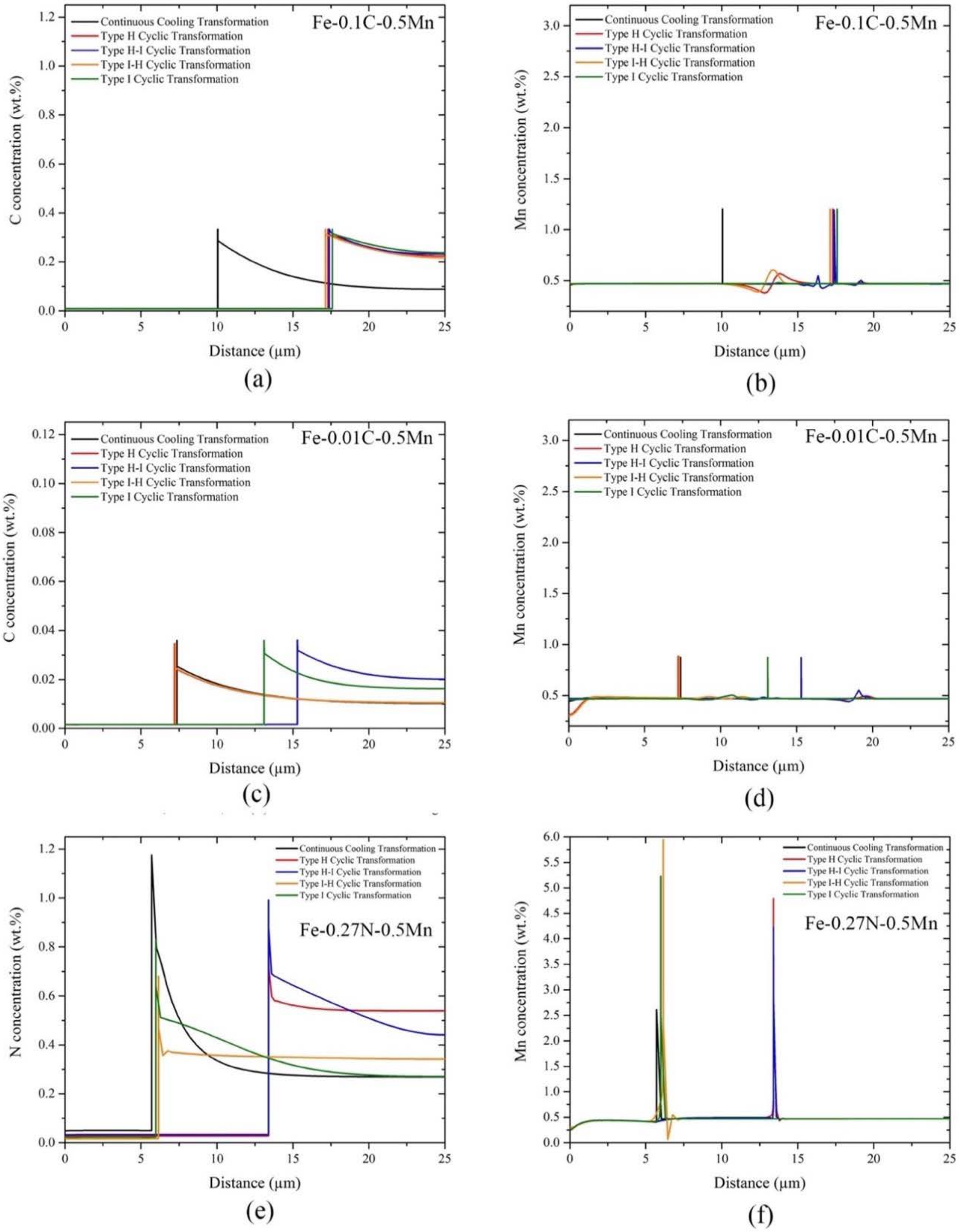

(a) (b)

(c) (d)

(e) (f)

Fig. 3.5- Profiles of Mn and C/N before the final cooling at T1 in LE modelling of different thermal routes.

The non-equilibrium transformation stage during heating in type I experiment is attributed to the incomplete redistribution of interstitial elements around the interface before subsequent variation of the temperature. In the Fe-0.1C-0.5Mn and Fe-0.5Mn systems, as a result of the relatively fast diffusion of carbon in austenite [32] and low carbon content, the length of the non-equilibrium transformation stage is very short. In the Fe-0.3N-0.5Mn alloy, the length of the non-equilibrium transformation stage is longer due to the slower diffusion of nitrogen in austenite [33] and associated decrease in the extent of nitrogen redistributed in type I cyclic route.

The stagnant stage during cyclic transformation is attributed to the spike of Mn at the interface as described by the local equilibrium partitioning model. The more partitioning of Mn at the interface, longer the stagnant stage is. Isothermal holding during cyclic transformation promotes partitioning of Mn at the interface and builds up a higher spike. This explains why the stagnant stage in the type I experiments is slightly shorter than that in type H experiments. In case of Fe-0.3N-0.5Mn alloy, the spike of Mn formed at the interface at the end of isothermal holding at T_1 in type H and type H-I is strong enough to hold the interface pinned until the end of cooling part. Thus, no ferrite growth is observed after first isothermal holding in Fig. 3.2f and Fig. 3.4f.

The difference between the length of the stagnant stage in Fe-C-Mn, Fe-Mn and Fe-N-Mn alloys under CPPT experiments appears to support that Mn partitioning around the austenite/ferrite interface is affected by the presence of interstitial elements. According to the LE model, partitioning of Mn at the interface is controlled by equilibrium tie-lines. In order to better compare the partitioning behavior of C/N and Mn at the austenite/ferrite interface, it is valuable to study the evolution of interfacial concentrations of the solutes during cyclic transformation. Fig. 3.6a shows the interfacial concentration of C and Mn on the austenitic side of interface during type H cyclic experiment in Fe-0.1C-0.5Mn alloy projected on the isothermal sections of the Fe-C-Mn phase diagram at three critical temperatures. The time, temperature and interface position corresponding to each combination of interfacial C and Mn concentrations are shown in Fig. 3.6b and Fig. 3.6c. The migration of the interface during the isothermal direct transformation stages at

T_1=1048 K (775 °C) and T_2=1098 K (825 °C), shown by C_1 to C_2 and C_4 to C_5, are accompanied by slight changes in the interfacial concentrations of both C and Mn along the austenitic boundary of the phase diagram at T_1 and T_2. The stagnant stages shown by C_2 to C_3 and C_5 to C_6, correspond to substantial changes of the Mn concentration at the interface. During the non-isothermal direct transformation stages of C_3 to C_4 and C_6 to C_7, the Mn concentrations are almost unchanged, and the interface migration is accompanied by a considerable change in the interfacial concentration of C. The information in Fig. 3.6a suggests that in the Fe-C-Mn alloy the stagnant stage proceeds under to the partitioning local equilibrium (PLE) condition and transformation stages proceed under the negligible-partitioning local equilibrium (NPLE) condition.

The projected interfacial concentrations of N and Mn for type H CPPT experiment in Fe-0.3N-0.5Mn and corresponding time, temperatures and interface positions are shown in Fig. 3.6 d-f. Similar to Fe-C-Mn system, the kinetics of the transformation stage (N_1 to N_2) and stagnant stages (N_2 to N_3, N_3 to N_4 and N_4 to N_5) in the Fe-N-Mn system are explainable by transitions between interface migration under PLE and NPLE thermodynamic conditions. In this system, unlike the Fe-C-Mn system, the transitions in the interfacial concentration of elements on the austenitic side of interface during heating from T_1 to T_2 and cooling from T_2 to T_1 occurs only in one step of substantial variations in concentrations of both N and Mn, which corresponds to the PLE thermodynamic condition. As it can be seen in the isothermal sections of the phase diagrams in Fig. 3.6, thermodynamic equilibrium between the austenite and ferrite phases in the Fe-N-Mn system forms with higher interfacial concentrations of N and Mn than C and Mn in Fe-C-Mn. In other words, nitrogen stimulates partitioning of Mn and the build-up of an interfacial spike, more than C during the isothermal austenite to ferrite phase transformation at T_1. This implies that more Mn partitioning is required for the back migration of the interface, as well as the N partitioning to satisfy the LE condition at the interface. For the applied heating rate which is the same in both Fe-C-Mn and Fe-N-Mn systems, before the N has diffused enough to make the interface move under NPLE condition, the sample temperature has already reached the inversion temperature T_2 and a new equilibrium with lower interfacial Mn concentration was established at the interface which requires even more partitioning of Mn. The PLE thermodynamic condition observed in the cooling part from T_2 to T_1 can also be explained in such a way. This suggests that the thermodynamic transitions from NPLE to PLE in Fe-N-Mn system similar to those in Fe-C-Mn are expected to occur if very low heating and cooling rates are applied during the cyclic experiment.

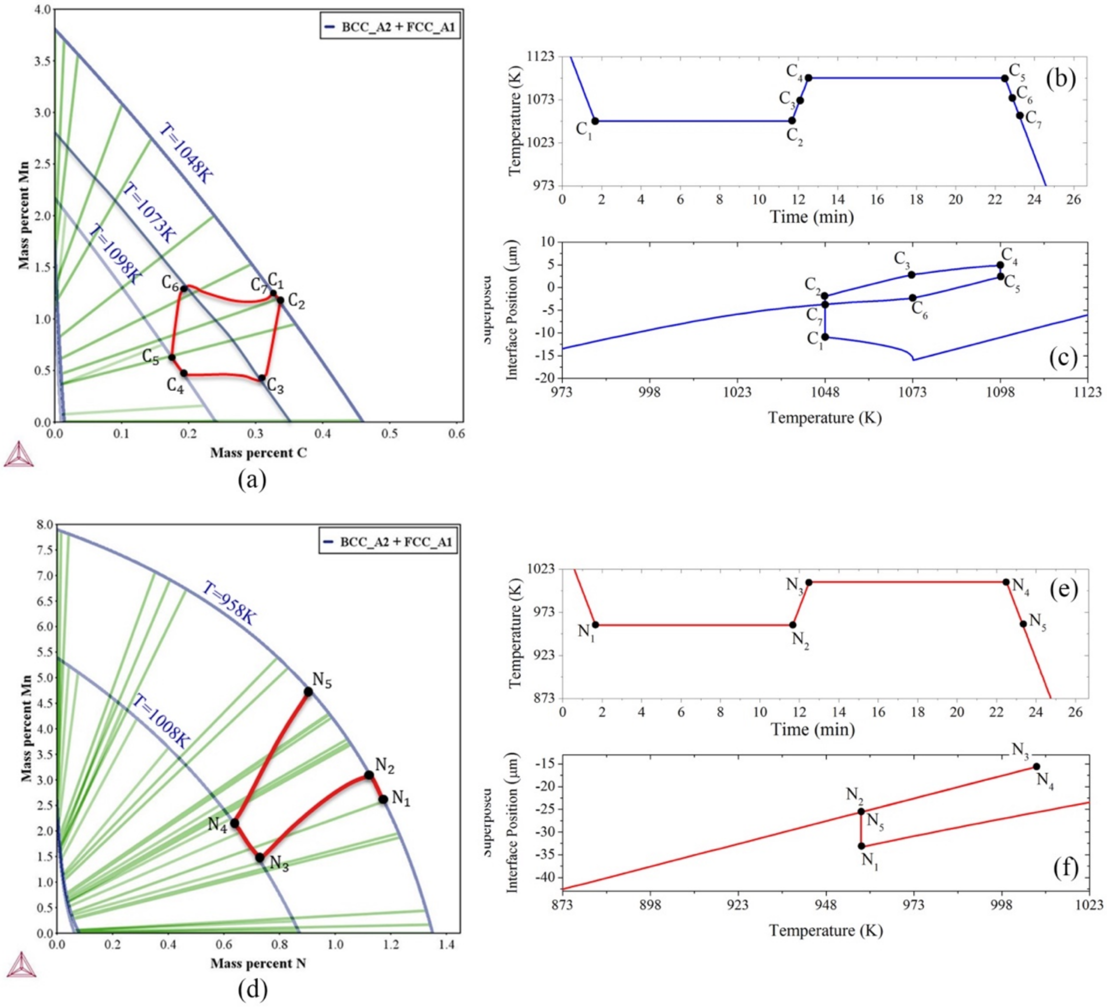

Fig. 3.6– a) Isothermal section of Fe-C-Mn phase diagram, b) applied thermal route, c) LE model results of type H CPPT in Fe-0.1C-0.5Mn alloy, d) Isothermal section of Fe-N-Mn phase diagram, e) applied thermal route, f) LE model results of type H CPPT in Fe-0.3N-0.5Mn alloy.

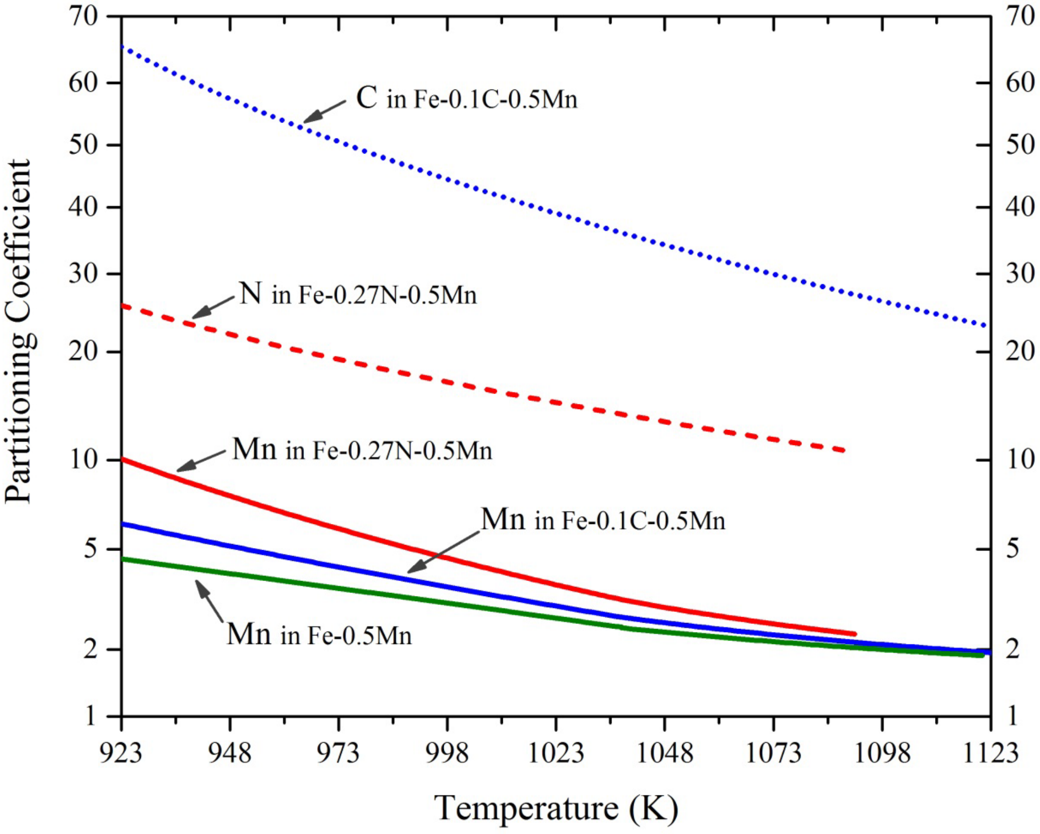

Fig. 3.7– Partitioning coefficient of C, N and Mn in different systems.

The inverse transformation stage during CPPT experiments shows up if the partitioning of the interstitial elements around the interface does not disappear prior to the rapid alternation of temperature regime and the interface continues its migration in a wrong direction. In order to better understand the differences in solute partitioning in the F-C-Mn, Fe-Mn and F-N-Mn systems at different temperatures it is useful to examine at the equilibrium partitioning coefficients shown in Fig. 3.7. These coefficients were defined as

$X^{\gamma}_{equilibrium}/X^{\alpha}_{equilibrium}$, where X is mole fraction of each alloying element. The partitioning coefficient of Mn is higher in the Fe-N-Mn system than it is in the Fe-C-Mn system. As a result, ferrite formation under equilibrium conditions in the Fe-N-Mn system requires more partitioning of Mn than ferrite formation in Fe-C-Mn at similar temperatures. Nitrogen partitions less than carbon during austenite decomposition, however, its lower diffusivity promotes the longer inverse transformation stages observed in type I cyclic experiments. Mn in the Fe-Mn binary system has the lowest partitioning coefficient suggesting that Mn tends to partition even in an interstitial-free system, but its partitioning is promoted in the presence of interstitial elements. The stagnant stage of 20K in Fe-0.5Mn alloy indirectly endorses that Mn interaction with the migrating interface in interstitial-free binary system should be substantial. This suggests, in contrast to other reports [13,34–36], that the kinetics of austenite to ferrite transformation in Fe-X systems alloyed with substitutional elements is a mixed-mode and controlled also by diffusion [37]. The analysis of partitioning coefficient of alloying elements in above indicates that experimental observations in this study for the base composition used with 0.5 mass% Mn are well explainable just with considering effect of C and N on the equilibrium thermodynamic partitioning of Mn between ferrite and austenite phases. However, we should emphasize that this does not mean that for other Mn contents, or in multi-component alloys (such as Fe-C-Mn-Si), or slower interface velocities (such as during decarburization reactions), an interaction between the C/Mn at the interface is not important to consider.

In our study, CPPT experiments provide indirect evidence for noticeable Mn partitioning at the austenite/ferrite interface in Fe-C/N-Mn systems. The difference between stagnant stages in type H cyclic experiments can only be explained by different partitioning behavior of Mn in the presence and absence of different interstitial elements. However, a counter argument opposing this can arise from selection of different critical temperatures for CPPT experiments in different systems. In order to remove the effect of temperature, further investigation on the effect of C and N and their absence on the length of stagnant stage at different temperatures is performed through systematic simulation of type H CPPT experiment using the LE model in Fe-xC-0.5Mn (Fig. 3.8a) and Fe-xN-0.5Mn (Fig. 3.8b) systems (x=0.01 to 0.4 mass%). As it can be seen in Fig. 8c, the stagnant stage, or as explained above spike of Mn, appears also in the interstitial-free system of Fe-0.5Mn and higher concentration of interstitial elements leads to a longer stagnant stage. In addition, nitrogen clearly creates a longer stagnant stage than the equivalent C containing system. As a final point, it is worth noting that the length of the stagnant stage predicted by LE model in Fig. 3.8c is quite comparable with the experimentally measured values in Fig. 3.2 to Fig. 3.4. This suggests that the concentration of interstitial elements can be estimated indirectly by measuring the length of stagnant stage.

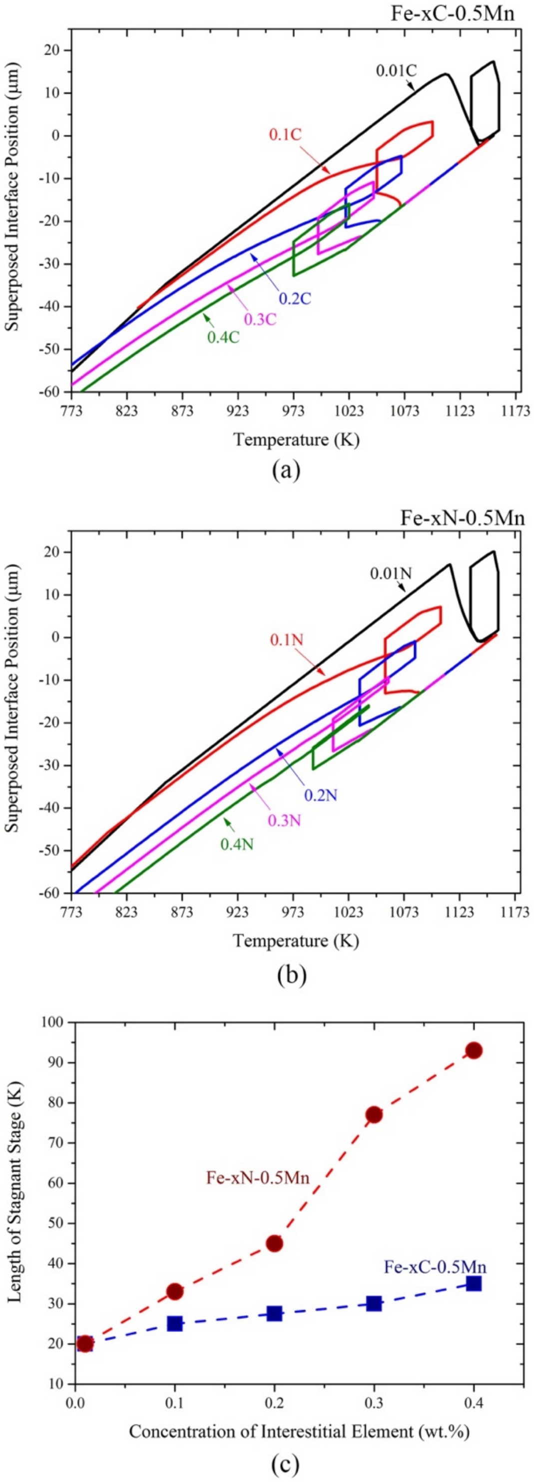

Fig. 3.8- Results of systematic type H CPPT simulations in a) Fe-C-Mn and b) Fe-N-Mn system, c) length of stagnant stage during type H CPPT in Fe-C-Mn and Fe-N-Mn systems.

3.7 Conclusions

In our study, cyclic partial phase transformation experiments have been successfully used to study the effect of interstitial elements (carbon and nitrogen) and their absence on the partitioning behavior of Mn in a Fe-0.5Mn steel. The results of experiments and local equilibrium modelling are comparable and confirm

1. Indirect evidence of Mn partitioning at austenite/ferrite interface in absence of interstitial elements,

2. Nitrogen promotes Mn partitioning at interface more than carbon, and

3. Local equilibrium model can semi-quantitatively capture the experimental observations in cyclic experiments.

3.8 References

[1] M. Gouné, F. Danoix, J. Ågren, Y. Bréchet, C.R. Hutchinson, M. Militzer, G. Purdy, S. van der Zwaag, H. Zurob, Overview of the current issues in austenite to ferrite transformation and the role of migrating interfaces therein for low alloyed steels, Mater. Sci. Eng. R Reports. 92 (2015) 1–38. doi:10.1016/j.mser.2015.03.001.

[2] D.E. Coates, Diffusion controlled precipitate growth in ternary systems: II, Metall. Trans. 4 (1973) 1077–1086. doi:10.1007/BF02645611.

[3] D.E. Coates, Diffusion-controlled precipitate growth in ternary systems I, Metall. Trans. 3 (1972) 1203–1212. doi:10.1007/BF02642453.

[4] M. Hillert, J. Ågren, On the definitions of paraequilibrium and orthoequilibrium, Scr. Mater. 50 (2004) 697–699. doi:10.1016/j.scriptamat.2003.11.020.

[5] M. Hillert, J. Odqvist, J. Ågren, Interface conditions during diffusion-controlled phase transformations, Scr. Mater. 50 (2004) 547–550. doi:10.1016/j.scriptamat.2003.10.027.

[6] H.S. Zurob, C.R. Hutchinson, Y. Bréchet, H. Seyedrezai, G.R. Purdy, Kinetic transitions during non-partitioned ferrite growth in Fe–C–X alloys, Acta Mater. 57 (2009) 2781–2792. doi:10.1016/j.actamat.2009.02.029.

[7] H.S. Zurob, C.R. Hutchinson, A. Béché, G.R. Purdy, Y.J.M. Bréchet, A transition from local equilibrium to paraequilibrium kinetics for ferrite growth in Fe–C–Mn: A possible role of interfacial segregation, Acta Mater. 56 (2008) 2203–2211. doi:10.1016/j.actamat.2008.01.016.

[8] M. Enomoto, Influence of solute drag on the growth of proeutectoid ferrite in Fe–C–Mn alloy, Acta Mater. 47 (1999) 3533–3540. doi:10.1016/S1359-6454(99)00232-3.

[9] V.G. Gavriljuk, J. Rawers, B.D. Shanina, H. Berns, Nitrogen and Carbon in Austenitic and Martensitic Steels: Atomic Interactions and Structural Stability, Mater. Sci. Forum. 426-432 (2003) 943–950. doi:10.4028/www.scientific.net/MSF.426-432.943.

[10] V.G. Gavriljuk, Austenite and martensite in nitrogen-, carbon- and hydrogen-containing iron alloys: Similarities and differences, Mater. Sci. Eng. A. 438 (2006) 75–79. doi:10.1016/j.msea.2006.01.097.

[11] Y. Liu, F. Sommer, E.J. Mittemeijer, Abnormal Austenite-Ferrite Transformation Kinetics of Ultra-Low-Nitrogen Fe-N Alloy, Metall. Mater. Trans. A. 39 (2008) 2306–2318. doi:10.1007/s11661-008-9601-7.

[12] N.K. Balliger, R.W.K. Honeycombe, The effect of nitrogen on precipitation and transformation kinetics in vanadium steels, Metall. Trans. A. 11 (1980). doi:10.1007/BF02654566.

[13] A.T.W. Kempen, F. Sommer, E.J. Mittemeijer, The kinetics of the austenite–ferrite phase transformation of Fe-Mn: differential thermal analysis during cooling, Acta Mater. 50 (2002) 3545–3555. doi:10.1016/S1359-6454(02)00149-0.

[14] M. Guo, D. Panahi, H. Van Landeghem, C.R. Hutchinson, G. Purdy, H.S. Zurob, A Comparison of Ferrite Growth Kinetics under Denitriding and Decarburizing Conditions, Metall. Mater. Trans. A. 46 (2015) 2449–2454. doi:10.1007/s11661-015-2851-2.

[15] H.P. Van Landeghem, B. Langelier, D. Panahi, G.R. Purdy, C.R. Hutchinson, G.A. Botton, H.S. Zurob, Solute Segregation During Ferrite Growth: Solute/Interphase and Substitutional/Interstitial Interactions, JOM. 68 (2016) 1329–1334. doi:10.1007/s11837-016-1852-y.

[16] Y. Yogo, K. Tanaka, H. Ikehata, N. Iwata, K. Nakanishi, T. Ishikawa, Calculation for grain growth rate of carbon steels by solute drag model considering segregation effect of each substitutional element, Mater. Sci. Technol. 27 (2011) 1593–1698. doi:10.1179/1743284710Y.0000000016.

[17] G. Purdy, J. Ågren, A. Borgenstam, Y. Bréchet, M. Enomoto, T. Furuhara, E. Gamsjager, M. Gouné, M. Hillert, C. Hutchinson, M. Militzer, H. Zurob, ALEMI: A Ten-

Year History of Discussions of Alloying-Element Interactions with Migrating Interfaces, Metall. Mater. Trans. A. 42 (2011) 3703–3718. doi:10.1007/s11661-011-0766-0.

[18] Z. Dai, X. Wang, J. He, Z. Yang, C. Zhang, H. Chen, Effect of Interfacial Mn Partitioning on Carbon Partitioning and Interface Migration During the Quenching and Partitioning Process, Metall. Mater. Trans. A. 48 (2017) 3168–3174. doi:10.1007/s11661-017-4121-y.

[19] H. Chen, S. van der Zwaag, The Effect of Interfacial Element Partitioning on Ferrite and Bainite Formation, JOM. 68 (2016) 1320–1328. doi:10.1007/s11837-016-1848-7.

[20] M. Hillert, Nature of local equilibrium at the interface in the growth of ferrite from alloyed austenite, Scr. Mater. 46 (2002) 447–453. doi:10.1016/S1359-6462(01)01257-X.

[21] A.T. Wicaksono, M. Militzer, Interaction of C and Mn in a ∑3 grain boundary of bcc iron, IOP Conf. Ser. Mater. Sci. Eng. 219 (2017) 012044. doi:10.1088/1757-899X/219/1/012044.

[22] W.W. Sun, H.S. Zurob, C.R. Hutchinson, Coupled solute drag and transformation stasis during ferrite formation in Fe-C-Mn-Mo, Acta Mater. 139 (2017) 62–74. doi:10.1016/J.ACTAMAT.2017.08.010.

[23] C. Qiu, H.S. Zurob, C.R. Hutchinson, The coupled solute drag effect during ferrite growth in Fe–C–Mn–Si alloys using controlled decarburization, Acta Mater. 100 (2015) 333–343. http://www.sciencedirect.com/science/article/pii/S1359645415006527 (accessed September 25, 2017).

[24] M. Enomoto, H.I. Aaronson, Nucleation kinetics of proeutectoid ferrite at austenite grain boundaries in Fe-C-X alloys, Metall. Trans. A. 17 (1986) 1385–1397. doi:10.1007/BF02650120.

[25] S.E. Offerman, N.H. van Dijk, J. Sietsma, S. Grigull, E.M. Lauridsen, L. Margulies, H.F. Poulsen, M.T. Rekveldt, S. van der Zwaag, Grain Nucleation and Growth During Phase Transformations, Science. 298 (2002) 1003–1005. doi:10.1126/science.1076681.

[26] H. Chen, S. van der Zwaag, An Overview of the Cyclic Partial Austenite-Ferrite Transformation Concept and Its Potential, Metall. Mater. Trans. A. (2016) 1–10. doi:10.1007/s11661-016-3826-7.

[27] H. Chen, B. Appolaire, S. van der Zwaag, Application of cyclic partial phase transformations for identifying kinetic transitions during solid-state phase transformations: Experiments and modeling, Acta Mater. 59 (2011) 6751–6760. doi:10.1016/j.actamat.2011.07.033.

[28] H. Chen, S. van der Zwaag, Analysis of ferrite growth retardation induced by local Mn enrichment in austenite created by prior interface passages, Acta Mater. 61 (2013) 1338–1349. doi:10.1016/j.actamat.2012.11.011.

[29] H. Chen, Cyclic Partial Phase Transformations In Low Alloyed Steels: Modeling and Experiments, Delft University of Technology, 2013. doi:10.4233/UUID:66975E4A-4B2D-4933-95C5-F180B6605882.

[30] A.G. Svyazhin, J. Siwka, Z. Skuza, A. Hutny, Gas blow-holes forming in nitrogen iron alloys and steels during their crystallization, in: Mater. Sci. Forum, 1999.

[31] J.-O. Andersson, T. Helander, L. Höglund, P. Shi, B. Sundman, Thermo-Calc & DICTRA, computational tools for materials science, Calphad. 26 (2002) 273–312. doi:10.1016/S0364-5916(02)00037-8.

[32] K. Nakajima, M. Apel, I. Steinbach, The role of carbon diffusion in ferrite on the kinetics of cooperative growth of pearlite: A multi-phase field study, Acta Mater. 54 (2006) 3665–3672. doi:10.1016/j.actamat.2006.03.050.

[33] S. Mändl, F. Scholze, H. Neumann, B. Rauschenbach, Nitrogen diffusivity in expanded austenite, Surf. Coatings Technol. 174-175 (2003) 1191–1195. doi:10.1016/S0257-8972(03)00454-7.

[34] J. Hamada, M. Enomoto, T. Fujishiro, T. Akatsuka, In-Situ Observation of the Growth of Massive Ferrite in Very Low-Carbon Fe-Mn and Ni Alloys, Metall. Mater. Trans. A. 45 (2014) 3781–3789. doi:10.1007/s11661-014-2336-8.

[35] J.J. Wits, T.A. Kop, Y. van Leeuwen, J. Seitsma, S. van der Zwaag, A study on the austenite-to-ferrite phase transformation in binary substitutional iron alloys, Mater. Sci. Eng. A. 283 (2000) 234–241. doi:10.1016/S0921-5093(00)00735-8.

[36] G.P. Krielaart, S. van der Zwaag, Kinetics of γ→α phase transformation in Fe-Mn alloys containing low manganese, Mater. Sci. Technol. 14 (1998) 10–18. doi:10.1179/mst.1998.14.1.10.

[37] M. Enomoto, X.L. Wan, In Situ Observation of Austenite Growth During Continuous Heating in Very-Low-Carbon Fe-Mn and Ni Alloys, Metall. Mater. Trans. A. 48 (2017) 1572–1580. doi:10.1007/s11661-017-3961-9.

Chapter 4 Analysis of Mn Partioning Mode in cyclic partial phase transformation in Fe-0.1C-xMn alloys as a function of the Mn concentration

This Chapter is based on

- H. Farahani, W. Xu, S. van der Zwaag, Determination of mode switching in cyclic partial phase transformation in Fe-0.1C-xMn alloys as a function of the Mn concentration, submitted to JOM.

ABSTRACT

Controlling the kinetics of austenite decomposition by controlled partitioning of alloying elements, in particular C and Manganese, is the key factor for optimizing the microstructures of advanced high strength steels. In this study, a systematic set of computational and experimental cyclic partial phase transformations in low to medium manganese steels revealed a critical manganese concentration at which manganese partitioning at moving austenite-ferrite interfaces can be used to temporarily suspend further transformation during subsequent cooling. Most interestingly, this critical concentration only become visible in case of reversed partial transformations in the intercritical regime.

4.1 Introduction

The attractive combination of a high tensile strength with good formability in advanced high strength steels (AHSS) is the result of tailored microstructures achieved by controlling the kinetics of the austenite decomposition [1–5]. The third AHSS generation, the so-called medium Mn steels, are compositionally relatively simple C-Mn steels having a multi-phase microstructures in combination with a high volume fraction of retained austenite [6–8]. The amount and stability of the austenite phase can be regulated by an overall compositional optimization and adjusting the temperature and time of intercritical annealing treatment which directly affects the C/Mn partitioning [9–17]. Understanding the partitioning behavior of alloying elements, specially Mn, for conventional and alternative thermal cycles is a key requirement for the control of the austenite ferrite phase transformations kinetics in medium Mn steels [18–21].

Recently, the 'Cyclic Partial Phase Transformation' (CPPT) approach has been introduced as an novel intercritical annealing route revealing the partitioning behavior of interstitial and substitutional alloying elements at transformation interfaces during austenite to ferrite and ferrite to austenite phase transformations [22,23]. In the typical CPPT thermal route, the temperature is cycled between two temperatures in the intercritical region, such that both austenite and ferrite phases are present at all times and additional nucleation of either ferrite or austenite is proved to be absent. The observed complex transformation kinetics during CPPT experiments in low (< 0.5 mass%) Mn steels and medium Mn steels can be completely explained by considering local partitioning of Mn at the mobile interfaces [24]. As the kinetics of cyclic phase transformations in steels with higher Mn levels (up to 5 mass%) has been observed to be rather different from that of steels with lower Mn levels [25], it is interesting to get more insight into the origin of these differences and to determine the role of the Mn partitioning on the transitions in the transformation kinetics. To this aim, the present work focusses on the transformation kinetics during and immediately after the cyclic transformation cycle as a function of the Mn concentration.

The work presented here involves both computational simulations and complementary dilatometry experiments.

4.2 Modelling Details

The Local Equilibrium (LE) model was used to simulate cyclic partial phase transformations in a series of alloys with compositions Fe-0.1C-xMn (x = 0.1 to 3.0 mass%, details shown in Table 4.1). In the LE model, interfacial concentrations of C and Mn in ferrite and austenite phases are selected on the basis of an assumed equal chemical potential for each phase across the interface. The current simulations were made using Dictra (linked to TCFE7 and MOB2 databases [26]) and assumed a 1D-geometry with a size of 25 μm presumed to represent austenite grain size of 50 μm. Using this geometry, all the important transitions in local interface velocity as a function of the (complex) thermal history can be captured and transformation curves in all aspects are comparable to those obtained in dilatometry experiments [23,27,28].

Table 4.1.The cyclic transformation temperatures of T1 and T2 and the equilibrium fraction of ferrite predicted by Thermo-Calc [29] for all the simulated composition systems.

Alloy tag	Composition (all in mass%)	T1	f_{eq}^{α} at T1	T2	f_{eq}^{α} at T2
0.1Mn	Fe-0.1C-0.1Mn	1063 K (790 °C)	0.75	1113 K (840 °C)	0.44
0.25Mn	Fe-0.1C-0.25Mn	1058 K (785 °C)	0.74	1108 K (835 °C)	0.43
0.5Mn	Fe-0.1C-0.50Mn	1048 K (775 °C)	0.70	1098 K (825 °C)	0.43
1Mn	Fe-0.1C-1.0Mn	1033 K (760 °C)	0.73	1083 K (810 °C)	0.4
1.5Mn	Fe-0.1C-1.5Mn	1018 K (745 °C)	0.70	1068 K (795 °C)	0.38
2Mn	Fe-0.1C-2.0Mn	1003 K (730 °C)	0.69	1053 K (780 °C)	0.36
2.5Mn	Fe-0.1C-2.5Mn	988 K (715 °C)	0.67	1038 K (765 °C)	0.34
3Mn	Fe-0.1C-3.0Mn	973 K (700 °C)	0.65	1023 K (750 °C)	0.32

Simulations are done for three thermal routes shown schematically in Fig. 4.1 a-c. The actual simulations start from point A (shown Fig. 4.1) where a fully austenitic microstructure is present. All subsequent cooling or heating rates (CR) are 1 K/s. In the CPPT route (Fig. 4.1a), the temperature is cycled between T1 and T2 and held at each temperature for 1200 s (20 min) and then cooled further to room temperature. In the continuous cooling (CC) route (Fig. 4.1b), the temperature is decreased continuously from T2. In the isothermal holding+cooling (IC) route (Fig. 4.1c) after cooling from T2 to T1, the temperature is held constant for a time equal to the total intercritical holding time in the CPPT route and then the temperature is decreased continuously. The T1 and T2 temperatures in the cyclic transformations for each composition are selected taking into account the corresponding Ae1 and Ae3 temperatures calculated with Thermo-Calc [29] and imposing the requirement of a fixed cycling range ΔT=T2-T1=50 K and comparable equilibrium fractions of ferrite (f_{eq}^{α}) at T1 and T2 for all compositions. The selected T1 and T2 values and the equilibrium fractions as predicted by Thermo-Calc are listed in Table 4.1 against the sample code.

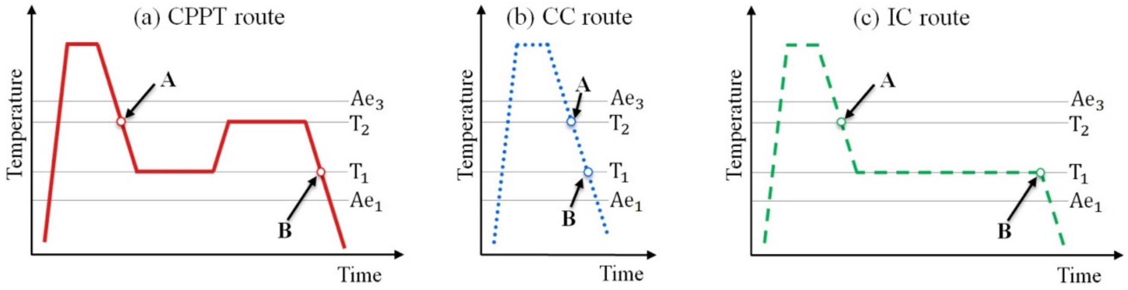

Fig. 4.1- Schematics of typical (a) cyclic Partial Phase Transformation (CPPT), (b) Continuous Cooling (CC) and (c) Isothermal holding and cooling (IC) thermal routes. “A” marks the condition to start the simulations and “B” marks the condition for which the calculated Mn profiles are presented in Fig. 4.3.

4.3 Results and Discussion

Fig. 4.2 a-h show the simulation results for the CPPT (solid lines), CC (dotted lines) and IC (dashed lines) thermal routes for compositions Fe-0.1C-xMn (x = 0.1 to 3.0 mass%), respectively. The results of the simulations are presented as graphs of interface position versus temperature. Given the 1D nature of the model, the position of the interface represents the ferrite fraction present (with an interface position of 25 μm corresponding to 100% ferrite). For the cooling rate applied the CC curves for all the compositions below 2 mass% Mn show ample and smooth migration of the interface but only minute amounts of interface migration for higher Mn concentrations indicating significantly less formation of intercritical ferrite.

The IC curves in Fig 2 a-h show variations in the interface migration behavior with increasing Mn concentration in a similar trend to that of the CC curves. While for systems with Mn content below 2 mass% a significant ferrite formation during the isothermal holding stage is predicted, for higher Mn content the total fraction of isothermally formed ferrite reduces significantly. More importantly, for all Mn concentrations the migration of interface at the end of the isothermal holding step picks up as soon as the final cooling starts and the behavior resembles that of the CC curves for that particular alloy.

For the CPPT curves, a rather different behavior as a function of the Mn concentration is predicted. For Mn concentrations below 0.5 mass% (Fig. 4.1 a-b), a very short so-called ‘stagnant stage’ [23] is observed during which only minimal austenite-ferrite interface migration is predicted to occur. The CPPT curves following the cyclic treatment show a continued migration of the interface when the final cooling below the T1 temperature starts and a behavior is observed which resembles that for CC and IC treatments.For systems with Mn concentrations from 0.5 to 1.5 mass% (Fig. 4.2 c-e), a clear stagnant stage both in the austenite to ferrite and the ferrite to austenite transformations can be distinguished in the CPPT curves [23]. For the 0.5Mn and 1Mn systems, the stagnant stage in the ferrite formation when cooling form, the T2 temperature finishes before the lower cycling temperature T1 and the interface continues to migrate smoothly during final cooling from T1 similar to the CC and IC curves. In a different way for the 1.5Mn system, the stagnant stage in ferrite formation continues until below T1, generating a ´post cyclic stagnant stage´ in the interface migration which is absent in the corresponding curves of the CC and IC routes. For systems with Mn concentration above 2 mass% (Fig. 4.2 f-h), the CPPT curves show primarily stagnant stages, and the isothermal direct formation of ferrite or austenite is negligible. Furthermore, for 2Mn and 2.5Mn systems the austenite to ferrite phase transformation during final cooling from T1 is fully suppressed to well below the T1 temperature. For the 3Mn system, migration of the interface during both CPPT, CC and IC thermal routes is minimal and the marginal differences between curves for all three thermal routes predict formation of negligible amounts of ferrite when subjected to either of the three thermal routes.

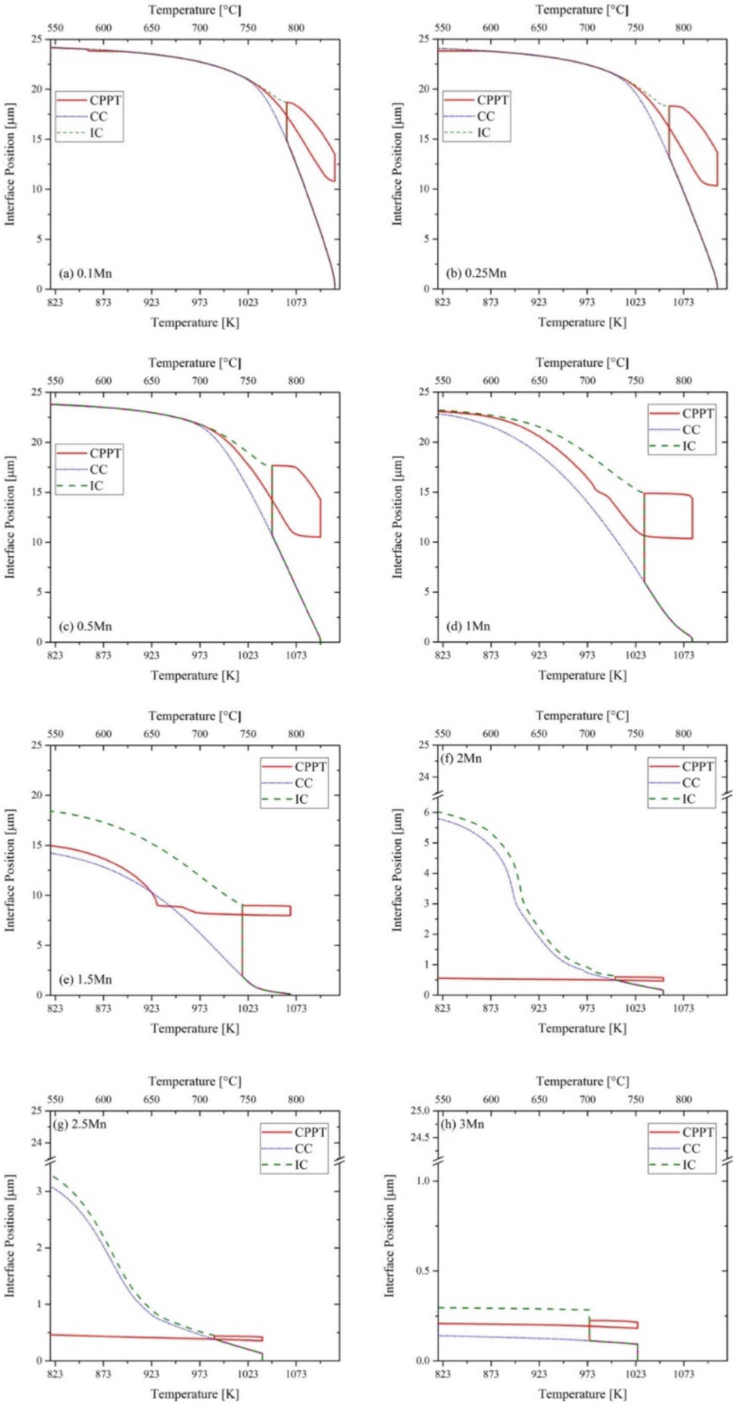

Fig. 4.2- Simulation results of CPPT (solid lines), CC (dotted lines) and IC (dashed lines) thermal routes using the LE model in systems of (a) 0.1Mn,(b) 0.25Mn, (c) 0.5Mn, (d) 1Mn, (e) 1.5Mn, (f) 2Mn, (g) 2.5Mn and (h) 3Mn.

The observed transitions in cyclic behavior of the simulated systems can be explained by considering the decisive effect of local Mn concentrations on the transformation kinetics. Fig. 4.3 a-h shows the local Mn profile in relevant regions near the moving austenite-ferrite interface for all of the simulated systems at T1 during cooling after the CPPT, CC and IC treatments (point B in Fig. 4.1 a-c). The differences in the Mn profile can explain well the kinematic features in the interface migration behavior by considering the transition from negligible-partitioning local equilibrium (NPLE) to partitioning local equilibrium (PLE) mode at transformation interfaces [1,23,30,31]. The Mn concentration profiles after the CC and IC treatments show a Mn spike at interface position as a result the LE condition at the interface. The position of these Mn spikes is consistent with the positions of the interface in the corresponding curves in Fig. 4.2. For all nominal Mn concentrations, the Mn profile at T1 at the end of the CPPT treatment is quite different from the profiles after CC and IC routes.

After the CPPT treatment, the systems with Mn concentration up to 1.5 mass% (Fig. 4.3 a-e) show a profile Mn profile with a ‘zig-zag’ shape attributed to the LE condition at the interface marking the ferrite to austenite phase transformation during isothermal holding at T2, a Mn spike marking the interface position for the austenite to ferrite transformation during final cooling similar to that for the CC and IC curves, and finally an expanded spike as a result of the LE condition at interface during isothermal austenite to ferrite phase transformation at T1 after the first cooling stage (these features are best demonstrated in Fig. 4.3d).

In systems with a Mn content below 0.5 mass%, the partitioning of Mn at interface is too insignificant to cause any detectable disturbance in the interface motion and phase transformation kinetics in the three CPPT, CC and IC routes proceeding under the NPLE mode [32]. For the 0.5Mn and 1Mn systems, the spikes of Mn formed at T1 and T2 are moderately strong and cause stagnant stages in austenite to ferrite and ferrite to austenite transformations in the CPPT route. However, the interface can still move under NPLE condition after passing the existing Mn spike.

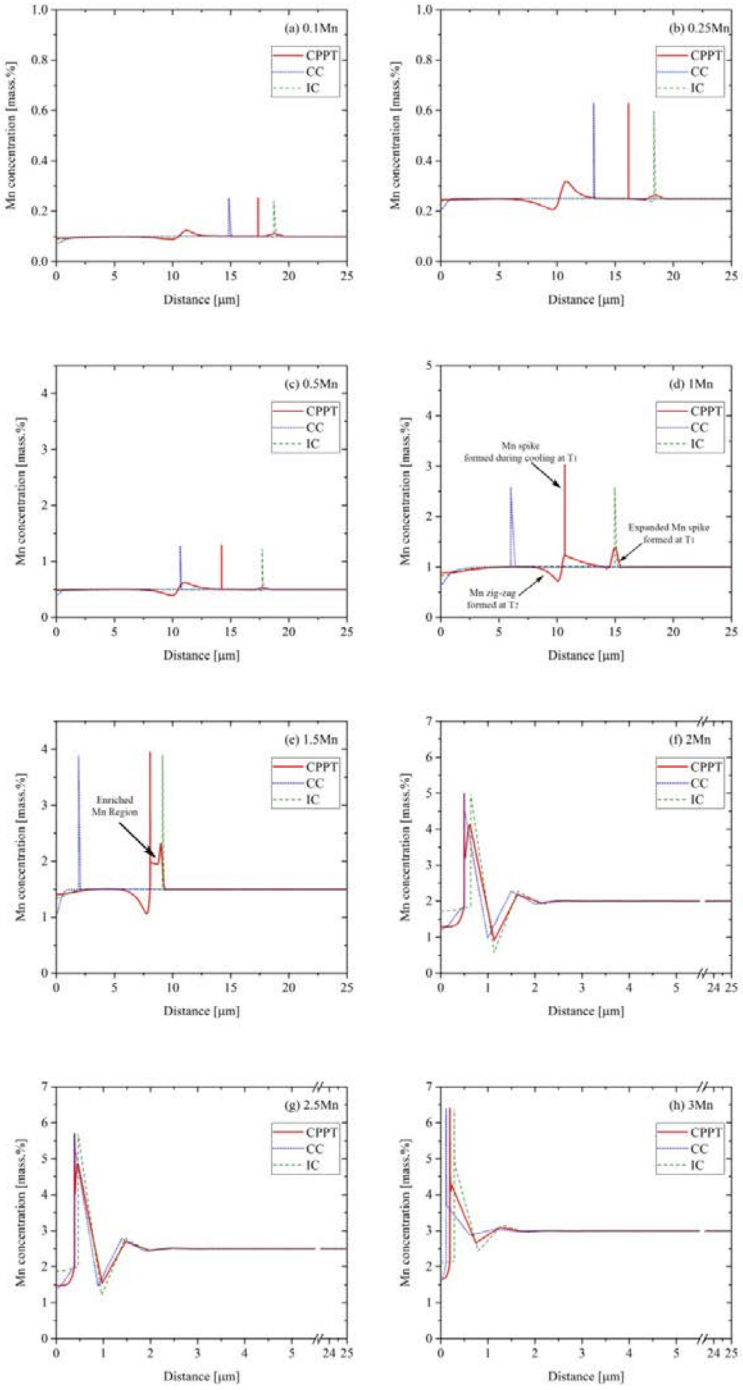

Fig. 4.3- Mn profile after simulation of CPPT (solid lines), CC (dotted lines) and IC (dashed lines) thermal routes (point B in Fig. 4.1) using the LE model in systems of (a) 0.1Mn,(b) 0.25Mn, (c) 0.5Mn, (d) 1Mn, (e) 1.5Mn, (f) 2Mn, (g) 2.5Mn and (h) 3Mn.

In the 1.5Mn system, the pinning effect of Mn spike partly limits the back migration of the interface during austenite reversion at T2, such that the existing expanded Mn spike formed at T1 and the zig-zag profile formed at T2 overlap and create an enriched Mn region (shown in Fig. 4.3e), leading to a local increase of the effective Mn concentration. Passage of the interface (during the final cooling stage from T1) through this locally enriched Mn region requires severe partitioning of Mn at the interface (similar to the PLE mode) and consequently causes the post cyclic stagnation in ferrite formation. As there no such Mn spikes are created in the CC and IC treatments, the kinetic curves show no stagnation upon final cooling.

For the systems with 2 mass% Mn and more (Fig. 4.3 f-h), the phase transformations involve full Mn partitioning at the (slowly moving) interfaces (PLE mode). Due to the severe pinning effect of the Mn spike formed at interface and the marginal migration of the interface during CPPT, the three aforementioned peaks in the Mn profile (as observed in lower Mn systems after CPPT) virtually overlap and are no more distinguishable. Thus, the Mn profile after CPPT is very similar to that of the CC and IC routes, but only in the CPPT, final cooling starts with the interface positioned behind the very narrow but highly enriched Mn region that can seriously halt the migration of the interface during final cooling after the CPPT route.

Table 4.2. Composition of the alloys used for CPPT and CC experiments.

Alloy tag	Composition (all in mass%)
0.15Mn	Fe-0.023C-0.17Mn
0.25Mn	Fe-0.095C-0.25Mn
0.5Mn	Fe-0.0848C-0.47Mn
1Mn	Fe-0.095-1.1Mn
1.5Mn	Fe-0.061C-1.52Mn
2Mn	Fe-0.135C-2.058Mn
2.5Mn	Fe-0.06C-2.4Mn

3Mn	Fe-0.1C-3.0Mn

The predicted stagnation in ferrite formation in lean Mn steels with Mn concentrations around 1.0-1.5 wt% Mn during stages of the CPPT treatment has been confirmed experimentally using dilatometry [33] and in-situ confocal microscopy [34]. However, in order to assess the predicted trends in the transformation kinetics for the three thermal treatments as a function of the Mn concentration, a series of ternary alloys with different Mn concentrations close to those used in the computational experiments, listed in Table 2, were collected. A Bähr DIL 805A/D/T Quenching Dilatomer was used to measure the longitudinal dilatation of the specimens (typically 10 mm length and 4 mm diameter), using the same thermal routes as used in the LE simulations. All specimens were heated with a rate of 10 K/s to 1273 K (1000 °C) and kept for 300 s (5 min) to ensure full austenitization. Then the samples were subjected to the CC, IC and CPPT thermal routes with a constant rate of 1 K/s under vacuum condition with a maximum pressure of 5×10-4 mbar. Fresh samples were used for each different thermal route. For alloys with a Mn concentration below 2 mass%, the CPPT route was performed using isothermal intercritical holdings of 1200 s (20 min) similar to the simulations. For alloys with Mn levels above 2 mass%, the cyclic treatments were done with isothermal holding at T1 for 86400 s (24 h) and at T2 for 7200 s (2 h) to compensate for the very slow rate of nucleation and to reach a starting ferrite fraction comparable to that in the simulations.

Fig. 4.4 a-h show the measured longitudinal dilatation curves for the experiments using the CC (dotted lines), IC (dashed lines) and the CPPT (solid lines) thermal routes. The CC dilatation curves for all Mn concentrations indicate steady austenite decomposition, while the dilatation curves for the IC and CPPT routes show distinctly different behavior depending on the Mn concentration. It is worth mentioning that the stagnant stages in the experimental dilatation curves can be identified by the linear contraction or expansion of the specimens during cooling or heating.

The observed experimental transformation curves as plotted Fig. 4.4. are all in very good agreement with their respective predictions made by the LE model. In line with the simulations, the experimental CPPT curves for 0.15Mn, 0.25Mn, 0.5Mn and 1Mn alloys (Fig. 4.4 a-d) show direct transformation and stagnant stages with lengths up to 50 K during the thermal cycles. For these alloys no post cyclic stagnation in the ferrite formation after the cyclic treatment is observed. The IC curves in these alloys indicate significant ferrite formation during isothermal holding. The minor non-linearity in the IC dilatation curves during the final cooling are an indication of the transformation of the small austenite fraction present after isothermal holding.

For the 1.5Mn alloy (Fig. 4.4e), the IC curve shows significant ferrite formation both during isothermal holding and final cooling. In the CPPT curve, the isothermal direct ferrite formation and austenite reversion stages during the isothermal holdings at T1 and T2, respectively, are easily identified. The predicted post cyclic stagnant stage in the ferrite formation is clearly present in the experimental CPPT curve where after the austenite reversion at T2 the ferrite formation is suppressed for about 40 K of cooling below T1 (when compared to the CC curve). This stage is obviously absent in the experimental CC and IC curves.

For the alloys with 2 mass% of Mn and higher (Fig. 4.4 f-h), due to extended isothermal holding times in the CPPT and IC routes, the austenite decomposition starts at higher temperatures compared to the CC routes. As predicted by the simulations, the cyclic partial phase transformations in these alloys proceed with only slight isothermal transformations during holdings at T1 and T2 temperatures. In the 2Mn and 2.5Mn alloys, the CPPT treatment causes a post cyclic stagnant stage in austenite decomposition during cooling below T1 for about 25 K (when compared to the corresponding CC curves). Although ferrite, and therefor austenite-ferrite interfaces are present at the end of both the CPPT and the IC routes, the post cyclic stagnant stage is only observed after CPPT route and is absent in the samples subjected to the IC route. In the 3Mn alloy, showing a very good agreement with the predictions by the LE model, it is clear that the CPPT treatment has virtually no effect on the transformation kinetics during final cooling which proceeds in a similar manner in the CC, IC and CPPT treated samples.

The experimental results in above put forward a critical Mn concentration range from about 1.5 to 2.5 mass% in which formation of the intercritical and post-intercritical ferrite can be suppressed significantly via austenite reversion through the cyclic treatment. The CPPT treatment in these range of composition can locally increase the effective Mn concentration and enhance stabilization of retained austenite with suppression of further intercritical ferrite formation.

Comparing the experimental and computationally simulated CPPT curves for 1.5Mn, 2Mn and 2.5Mn systems, a difference in the length (i.e. duration) of the post cyclic stagnant stage is observed. While the simulations predict stronger suppression of ferrite formation after CPPT for higher Mn contents, in the physical experiments, notwithstanding the extended time for ferrite nucleation in 2Mn and 2.5Mn alloys, the post cyclic stagnant stages in these alloys are shorter than the one observed in the 1.5Mn alloy. The difference arises from the lower fraction of intercritical ferrite (and consequently less number of available interfaces) formed during the first isothermal holding at T1 in the in 2Mn and 2.5Mn alloys compared to the 1.5Mn alloy.

It is worth noting that, although for the composition range of Mn higher than 2 mass%, the cyclic transformation behavior can be initiated by providing extended time for nucleation of ferrite at higher temperatures (i.e. lower undercoolings), we also could have opted for selecting lower critical T1 and T2 temperatures for the cyclic treatment. However, when calculating the bainite start temperature for this range of composition using $Bs(K) = 907.95 - 193.1C + 02.4C2 - 31.2Mn + 10.36 \ln(d\gamma)$ [35] (where the C and Mn compositions are in mass% and $d\gamma$ is the austenite grain size in μm), a high probability of bainite formation during cyclic treatment at the lower transformation temperatures is predicted. Since the kinetics and mechanism of bainite formation in these alloys are controversial and different from those of the proeutectoid ferrite [36,37], the occurrence of bainite formation in the CPPT treatment would complicate the interpretation of the dilatometry curves in relation to the degree of austenite reversion.

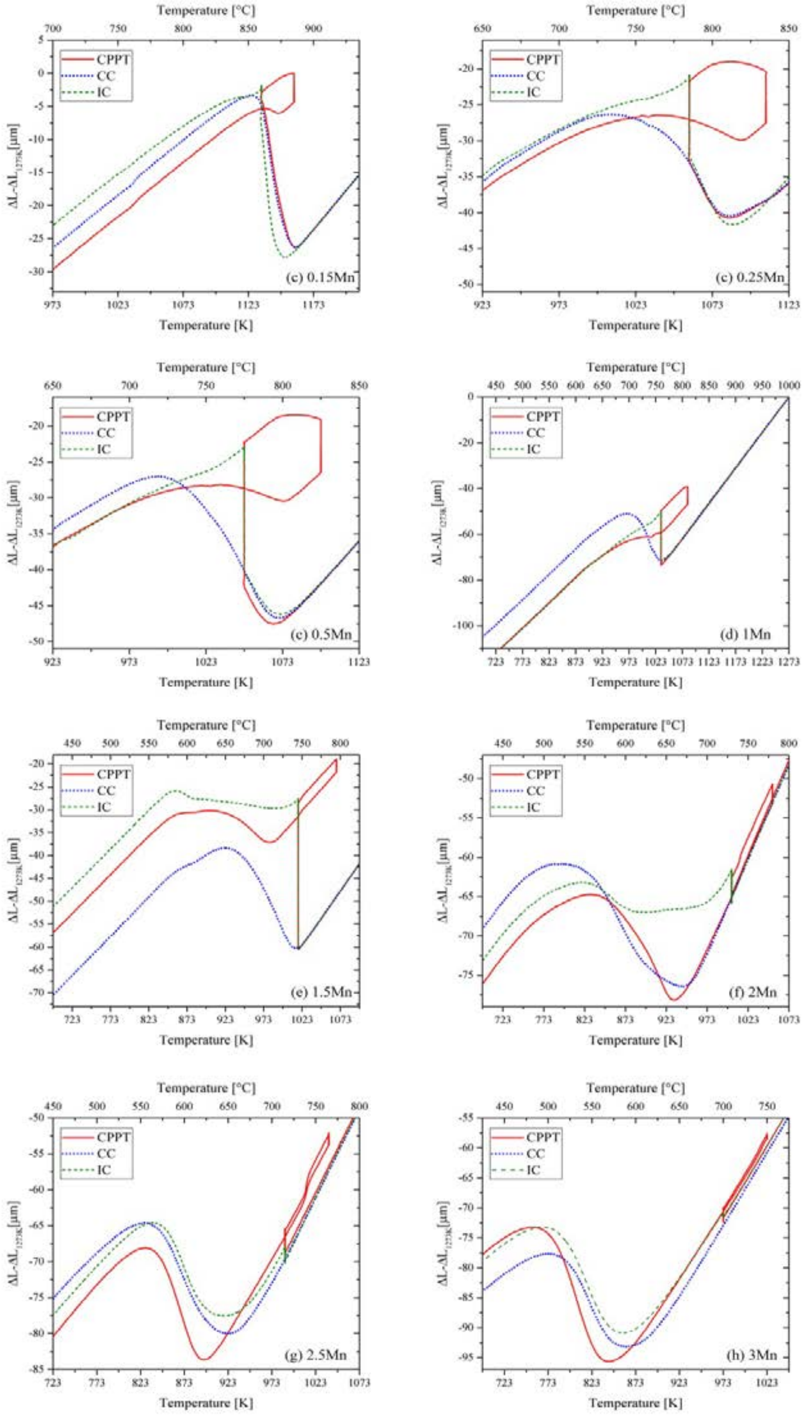

Fig. 4.4- Experimental dilatation results of CPPT (solid lines), CC (dotted lines) and IC (dashed lines) thermal routes in alloys with (a) 0.15Mn, (b) 0.25Mn, (c) 0.5Mn, (d) 1Mn, (e) 1.5Mn, (f) 2Mn, (g) 2.5Mn and (h) 3Mn.

4.4 Conclusions

In summary, the systematic simulations of the cyclic partial phase transformations using the LE model revealed a critical Mn concentration range of 1.5 to 2.5 mass% in which the CPPT treatment can locally increase the effective Mn concentration in regions near the moving austenite-ferrite interface. This process suppresses ferrite formation via controlled mode switching in the interfacial Mn partitioning and creates a post cyclic stagnant stage. This stage is absent in the CC and IC thermal routes as there is no reversion stage. The systematic experiments on the alloys subjected to the CPPT route are in well agreement with the LE model predictions and confirm the predicted critical Mn concentration range from 1.5 to 2.5 mass% of Mn.

4.5 References

[1] C. Capdevila, J. Cornide, K. Tanaka, K. Nakanishi, E. Urones-Garrote, Kinetic transition during ferrite growth in Fe-C-Mn medium carbon steel, Metall. Mater. Trans. A Phys. Metall. Mater. Sci. 42 (2011) 3719–3728. doi:10.1007/s11661-011-0650-y.

[2] H. Luo, J. Shi, C. Wang, W. Cao, X. Sun, H. Dong, Experimental and numerical analysis on formation of stable austenite during the intercritical annealing of 5Mn steel, Acta Mater. 59 (2011) 4002–4014. doi:10.1016/j.actamat.2011.03.025.

[3] C. Wang, W. Cao, J. Shi, C. Huang, H. Dong, Deformation microstructures and strengthening mechanisms of an ultrafine grained duplex medium-Mn steel, Mater. Sci. Eng. A. 562 (2013) 89–95. doi:10.1016/j.msea.2012.11.044.

[4] R. Zhang, W.Q. Cao, Z.J. Peng, J. Shi, H. Dong, C.X. Huang, Intercritical rolling induced ultrafine microstructure and excellent mechanical properties of the medium-Mn steel, Mater. Sci. Eng. A. 583 (2013) 84–88. doi:10.1016/j.msea.2013.06.067.

[5] W.W. Sun, Y.X. Wu, S.C. Yang, C.R. Hutchinson, Advanced high strength steel (AHSS) development through chemical patterning of austenite, Scr. Mater. 146 (2018) 60–63. doi:10.1016/J.SCRIPTAMAT.2017.11.007.

[6] J. Shi, X. Sun, M. Wang, W. Hui, H. Dong, W. Cao, Enhanced work-hardening behavior and mechanical properties in ultrafine-grained steels with large-fractioned metastable austenite, Scr. Mater. 63 (2010) 815–818. doi:10.1016/J.SCRIPTAMAT.2010.06.023.

[7] R. Ding, D. Tang, A. Zhao, A novel design to enhance the amount of retained austenite and mechanical properties in low-alloyed steel, Scr. Mater. 88 (2014) 21–24. doi:10.1016/J.SCRIPTAMAT.2014.06.014.

[8] J. Hu, L.-X. Du, G.-S. Sun, H. Xie, R.D.K. Misra, The determining role of reversed austenite in enhancing toughness of a novel ultra-low carbon medium manganese high strength steel, Scr. Mater. 104 (2015) 87–90. doi:10.1016/J.SCRIPTAMAT.2015.04.009.

[9] O. Bouaziz, S. Allain, C.P. Scott, P. Cugy, D. Barbier, High manganese austenitic twinning induced plasticity steels: A review of the microstructure properties relationships, Curr. Opin. Solid State Mater. Sci. 15 (2011) 141–168. doi:10.1016/j.cossms.2011.04.002.

[10] B.C. De Cooman, Structure-properties relationship in TRIP steels containing carbide-free bainite, Curr. Opin. Solid State Mater. Sci. 8 (2004) 285–303. doi:10.1016/j.cossms.2004.10.002.

[11] Y.K. Lee, C. Choi, Driving force for $\gamma \rightarrow \varepsilon$ martensitic transformation and stacking fault energy of γ in Fe-Mn binary system, Metall. Mater. Trans. A. 31 (2000) 355–360. doi:10.1007/s11661-000-0271-3.

[12] S. Zaefferer, J. Ohlert, W. Bleck, A study of microstructure, transformation mechanisms and correlation between microstructure and mechanical properties of a low alloyed TRIP steel, Acta Mater. 52 (2004) 2765–2778. doi:10.1016/j.actamat.2004.02.044.

[13] E. De Moor, D.K. Matlock, J.G. Speer, M.J. Merwin, Austenite stabilization through manganese enrichment, Scr. Mater. 64 (2011) 185–188. doi:10.1016/J.SCRIPTAMAT.2010.09.040.

[14] S. Lee, S.-J. Lee, B.C. De Cooman, Austenite stability of ultrafine-grained transformation-induced plasticity steel with Mn partitioning, Scr. Mater. 65 (2011) 225–228. doi:10.1016/J.SCRIPTAMAT.2011.04.010.

[15] D.T. Pierce, D.R. Coughlin, D.L. Williamson, J. Kähkönen, A.J. Clarke, K.D. Clarke, J.G. Speer, E. De Moor, Quantitative investigation into the influence of temperature on carbide and austenite evolution during partitioning of a quenched and partitioned steel, Scr. Mater. 121 (2016) 5–9. doi:10.1016/J.SCRIPTAMAT.2016.04.027.

[16] F. HajyAkbary, J. Sietsma, G. Miyamoto, T. Furuhara, M.J. Santofimia, Interaction of carbon partitioning, carbide precipitation and bainite formation during the Q&P process in a low C steel, Acta Mater. 104 (2016) 72–83. doi:10.1016/j.actamat.2015.11.032.

[17] K.S. Choi, Z. Zhu, X. Sun, E. De Moor, M.D. Taylor, J.G. Speer, D.K. Matlock, Determination of carbon distributions in quenched and partitioned microstructures using

nanoscale secondary ion mass spectroscopy, Scr. Mater. 104 (2015) 79–82. doi:10.1016/J.SCRIPTAMAT.2015.03.027.

[18] J. Zhu, R. Ding, J. He, Z. Yang, C. Zhang, H. Chen, A cyclic austenite reversion treatment for stabilizing austenite in the medium manganese steels, Scr. Mater. 136 (2017) 6–10. doi:https://doi.org/10.1016/j.scriptamat.2017.03.038.

[19] Z.-D. Li, G. Miyamoto, Z.-G. Yang, T. Furuhara, Kinetics of Reverse Transformation from Pearlite to Austenite in an Fe-0.6 Mass pct C Alloy and the Effects of Alloying Elements, Metall. Mater. Trans. A. 42 (2011) 1586–1596. doi:10.1007/s11661-010-0560-4.

[20] Z. Dai, R. Ding, Z. Yang, C. Zhang, H. Chen, Elucidating the effect of Mn partitioning on interface migration and carbon partitioning during Quenching and Partitioning of the Fe-C-Mn-Si steels: Modeling and experiments, Acta Mater. 144 (2018) 666–678. doi:10.1016/J.ACTAMAT.2017.11.025.

[21] M. Gouné, F. Danoix, S. Allain, O. Bouaziz, Unambiguous carbon partitioning from martensite to austenite in Fe–C–Ni alloys during quenching and partitioning, Scr. Mater. 68 (2013) 1004–1007. doi:10.1016/J.SCRIPTAMAT.2013.02.058.

[22] H. Chen, S. van der Zwaag, An Overview of the Cyclic Partial Austenite-Ferrite Transformation Concept and Its Potential, Metall. Mater. Trans. A. (2016) 1–10. doi:10.1007/s11661-016-3826-7.

[23] H. Chen, B. Appolaire, S. van der Zwaag, Application of cyclic partial phase transformations for identifying kinetic transitions during solid-state phase transformations: Experiments and modeling, Acta Mater. 59 (2011) 6751–6760. doi:10.1016/j.actamat.2011.07.033.

[24] H. Chen, S. van der Zwaag, Analysis of ferrite growth retardation induced by local Mn enrichment in austenite created by prior interface passages, Acta Mater. 61 (2013) 1338–1349. doi:10.1016/j.actamat.2012.11.011.

[25] M.-I. Tzini, P. Sarafoglou, A. Stieben, G. Haidemenopoulos, W. Bleck, Austenite Evolution and Solute Partitioning during Thermal Cycling in the Intercritical Range of a Medium-Mn Steel, Steel Res. Int. 87 (2016) 1686–1693. doi:10.1002/srin.201600050.

[26] A. Borgenstam, A. Engström, L. Höglund, J. Ågren, DICTRA, a tool for simulation of diffusional transformations in alloys, J. Phase Equilibria. 21 (2000) 269–280. doi:10.1361/105497100770340057.

[27] H. Chen, S. van der Zwaag, Simulation of the stagnant stage during the austenite to ferrite transformation in cyclic partial phase transformations, in: TMP 2012-4th Int. Conf. Thermomechanical Process. Steels, Sheffield, 2012.

https://www.scopus.com/inward/record.uri?eid=2-s2.0-84896857966&partnerID=40&md5=d4171b55b98da128d515948f88138611.

[28] H. Chen, S. van der Zwaag, Application of the cyclic phase transformation concept for investigating growth kinetics of solid-state partitioning phase transformations, Comput. Mater. Sci. 49 (2010) 801–813. doi:10.1016/J.COMMATSCI.2010.06.026.

[29] J.O. Andersson, T. Helander, L. Höglund, P. Shi, B. Sundman, Thermo-Calc & DICTRA, computational tools for materials science, Calphad. 26 (2002) 273–312. doi:10.1016/S0364-5916(02)00037-8.

[30] H. Chen, W. Xu, M. Goune, S. van der Zwaag, Application of the stagnant stage concept for monitoring Mn partitioning at the austenite-ferrite interface in the intercritical region for Fe–Mn–C alloys, Philos. Mag. Lett. 92 (2012) 547–555. doi:10.1080/09500839.2012.700124.

[31] H. Farahani, W. Xu, S. van der Zwaag, Prediction and Validation of the Austenite Phase Fraction upon Intercritical Annealing of Medium Mn Steels, Metall. Mater. Trans. A. 46 (2015) 4978–4985. doi:10.1007/s11661-015-3081-3.

[32] M. Hillert, Nature of local equilibrium at the interface in the growth of ferrite from alloyed austenite, Scr. Mater. 46 (2002) 447–453. doi:10.1016/S1359-6462(01)01257-X.

[33] H. Chen, R. Kuziak, S. van der Zwaag, Experimental Evidence of the Effect of Alloying Additions on the Stagnant Stage Length During Cyclic Partial Phase Transformations, Metall. Mater. Trans. A. 44 (2013) 5617–5621. doi:10.1007/s11661-013-2040-0.

[34] H. Chen, E. Gamsjäger, S. Schider, H. Khanbareh, S. van der Zwaag, In situ observation of austenite–ferrite interface migration in a lean Mn steel during cyclic partial phase transformations, Acta Mater. 61 (2013) 2414–2424. doi:10.1016/j.actamat.2013.01.013.

[35] S. Kang, S. Yoon, S.-J. Lee, Prediction of Bainite Start Temperature in Alloy Steels with Different Grain Sizes, ISIJ Int. 54 (2014) 997–999. doi:10.2355/isijinternational.54.997.

[36] L.C.D. Fielding, The Bainite Controversy, Mater. Sci. Technol. 29 (2013) 383–399. doi:10.1179/1743284712Y.0000000157.

[37] H.I. Aaronson, M.G. Hall, A history of the controversy over the roles of shear and diffusion in plate formation aboveM d and a comparison of the atomic mechanisms of these processes, Metall. Mater. Trans. A. 25 (1994) 1797–1819. doi:10.1007/BF02649030.

Chapter 5 **Controlling Band Formation via Designated Segregation of Mn**

This Chapter is based on

- H. Farahani, W. Xu, S. van der Zwaag, A Novel Approach for Controlling the Band Formation in Medium Mn Steels, *Metallurgical and Materials Transactions A*, Volume 49, Issue 6, 1 June 2018, Pages 1998-2010.

ABSTRACT

Formation of the microstructural ferrite/pearlite bands in medium Mn steels is an undesirable phenomenon commonly addressed through fast cooling treatments. In this study, a novel approach using the cyclic partial phase transformation concept is applied successfully to prevent microstructural band formation in a micro-chemically banded Fe-C-Mn-Si steel. The effectiveness of the new approach is assessed using the ASTM E1268-01 standard. The cyclic intercritical treatments lead to formation of isotropic microstructures even for cooling rates far below the critical one determined in conventional continuous cooling. In contrast, isothermal intercritical experiments have no effect on the critical cooling rate to suppress microstructural band formation. The origin of the suppression of band formation either by means of fast cooling or a cyclic partial phase transformation is investigated in detail. Theoretical modelling and microstructural observations confirm that band formation is suppressed only if the intercritical annealing treatment leads to partial reversion of the austenite-ferrite interfaces. The resulting interfacial Mn enrichment is responsible for suppression of the band formation upon final cooling at low cooling rates.

5.1 Introduction

The formation of ferrite/pearlite microstructural bands in hot rolled low alloy steels has been one of the main challenges in the development of medium Mn steels for low weight automotive applications [1–3]. The presence of the ferrite/pearlite microstructural banding leads to an undesirable reduction of the mechanical properties perpendicular to the rolling direction [4–10]. The band formation is the result of significant partitioning of alloying elements during solidification which generally cannot be undone sufficiently during the solid-state homogenization treatments preceding the hot-rolling and subsequent thermomechanical processing steps. Not surprisingly, the topic of band formation and its relation to the imposed thermal trajectory when cooling down from the hot rolling temperature has been researched for more than 50 years [11–16].

In micro-chemically banded Fe-C-Mn-Si steels, the spatial variation of substitutional alloying element concentrations locally reduces (in regions with high levels of austenite forming elements such as Mn) or raises (in regions with high levels of ferrite forming elements such as Si) the A_3 transition temperature. Upon cooling from the austenite, the ferrite starts to nucleate in regions with a high A_3 transition temperature as the required undercooling for ferrite nucleation is reached there first. With the formation of the early ferrite, C is injected into the remaining neighbouring austenite with a higher Mn content, reducing the local A_3 transition temperature even more. Upon further cooling, the composition in these remaining austenitic regions reaches eutectoid levels and the austenite decomposition continues with pearlite formation in a banded arrangement [17]. Hence, formation of the ferrite/pearlite microstructural bands is a matter of balancing nucleation and growth during austenite decomposition [5,18]. In a standard approach, formation of microstructural bands can be suppressed via fast cooling after hot rolling. The severe undercooling from austenitization temperature results in simultaneous nucleation of ferrite in both rich and poor Mn containing regions. Although fast cooling prevents band formation, but it leads to formation of ferrite with a fine average grain size and a higher hardness and yield strength which is not always desirable.

Recently, the ‘Cyclic Partial Phase Transformation’ (CPPT) approach has been proposed as an scientifically interesting intercritical annealing route to investigate the effect of alloying elements on interface migration kinetics [19,20]. In a CPPT experiment, the temperature is cycled between two temperatures inside the austenite-ferrite two-phase regime such that both austenite and ferrite phases are present at all times. The CPPT experiments demonstrate a clear retardation of the final ferrite growth as a result of local Mn enrichment due to the back and forth migration of the austenite-ferrite interfaces more or less following the same trajectory [21]. In a more recent approach, the cyclic treatments is successfully used as a novel route to stabilize austenite in a medium Mn steel down to room temperature [22].

The present work introduces a new approach for controlled suppression of ferrite/pearlite band formation in a medium Mn steel using the CPPT approach and making use of the controlled Mn partitioning at moving austenite-ferrite interfaces. The approach led to a considerable lowering of the minimum cooling rate required to prevent band formation. The unique observation of perfectly aligned pearlite rims around ferrite grains is a clear evidence of the impact of local Mn enrichment at halted interfaces.

5.2 Experimental Details

In this study, a commercial hot rolled Fe-0.17C-1.47Mn-1.48Si (all concentrations in mass pct.) steel grade is subjected to different thermal treatments. Solid cylindrical samples for dilatometric experiments with a diameter of 5.0 mm and length of 10.0 mm were wire-cut with the axis of the cylinder parallel to the rolling direction. Qualitative energy dispersive spectroscopy (EDS) across the rolling direction in the samples was done confirming micro-chemical banding of both Mn and Si. All thermal processing was done using a Bähr DIL 805A/D/T Quenching dilatometer. As samples containing micro-chemical bands show different dilatation signals parallel and perpendicular to the rolling direction [23] the dilatation of the specimens was measured in both the longitudinal and lateral direction. The samples were aligned such that the rolling plane was perpendicular to the direction in which the lateral expansion was measured. All experiments were done in vacuum with a pressure of 5×10^{-4} mbar. Two thermocouples spaced 4 mm apart were spot welded to the samples to ascertain that the thermal gradient along the sample was less than 3 K. All samples were heated with a rate of 10 K/s and fully austenitized at 1273 K (1000 °C) for 300 s (5 min) and then subjected to either Continuous Cooling (CC) experiments with different cooling rates (CR) from 20 K/s to 0.17 K/s (10 K/min) or to different Cyclic Partial Phase Transformation (CPPT) routes. The samples were cut in the longitudinal direction and polished and etched with a 2 percent *Nital* etchant and subsequently evaluated using conventional light and scanning electron microscopical methods. The micro-segregation of C, Mn and Si was determined using a *Jeol JXA* 8900R microprobe instrument fitted with appropriate wavelength dispersive spectrometers.

5.3 Results

First, the results of cooling rate experiments on the ferrite/pearlite band formation during continuous cooling (CC) experiments are presented. Fig. 5.1 a-b show the dilatation curves in longitudinal and lateral directions for continuous cooling experiments with cooling rates (CR) of 20, 10, 5, 4, 3, 2, 1, 0.5 and 0.17 K/s (10 K/min), respectively. In these graphs the dilatation with respect to the dilatation at the end of the austenitization treatment is plotted. The increase in length during cooling reflects decomposition of austenite. For low cooling rates the dilatation curves indicate a two- step process of ferrite formation followed by pearlite formation, while at higher cooling rates a two-step ferrite-bainite/martensite reaction is observed. The difference between the ferrite nucleation start temperature (T_s) and transformation end temperature (T_e) increases significantly with increasing cooling rate. For example, in the curve of CR=1 K/s, austenite decomposition starts at T_s=1040 K (767 °C) and finishes at T_e=896 K (623 °C), while for CR=10 K/s, T_s= 982 K (709 °C) and T_e=625 K (352 °C). A comparison of the dilatation curves parallel and perpendicular to the sample (i.e. to the rolling direction) shows that at relatively low cooling rates the dilatation due to the pearlite formation is much more significant in the lateral dilatation curves than in the axial dilation curves. Earlier work [23] has shown that such a difference in the relative dilatation due to the pearlite formation is a clear sign of band formation. At higher cooling rates, the axial and radial dilatation curves become more equal, indicative of a more isotropic microstructure.

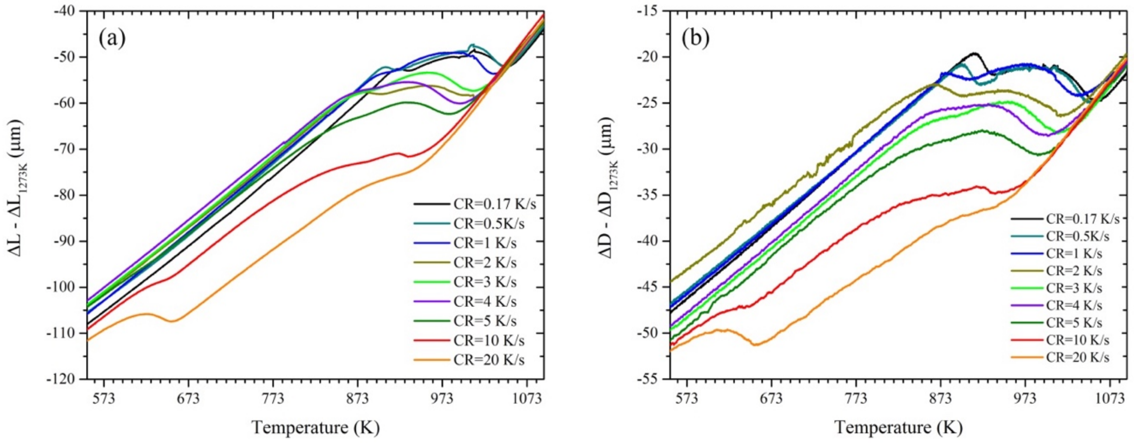

Fig. 5.1- Dilatation curves achieved in CC experiments in a) longitudinal direction and b) lateral direction.

Fig. 5.2 a-i show the microstructures achieved after CC experiments with different cooling rates. For low cooling rates of 0.17, 0.5 and 1 K/s, the microstructures in Fig. 5.2 g-i display well developed ferrite/pearlite bands parallel to the rolling direction. The pearlitic regions are the dark phase in these figures. The ferrite and pearlite grains are formed in rows with a spacing of ~50 μm. For samples subjected to cooling rates of 2, 3 and 4 K/s, ferritic/pearlitic microstructures are observed (Fig. 5.2 d-f), but the microstructural components are more randomly distributed with no noticeable sign of preferential band formation. The microstructures of samples after CC experiments with a cooling rates of 5, 10 and 20 K/s in Fig. 5.2 a-c consist of ferrite, pearlite and bainite or martensite phases [24] (and possibly fractions of retained austenite); all phases are distributed homogeneously across the microstructure. These micrographs demonstrate that for this alloy and linear cooling a cooling rate of 2 K/s is the critical rate below which the resulting microstructure shows fully banded characteristics with distinct rows of ferrite and pearlite formed. Banding can only be avoided with cooling rates equal or higher than 2 K/s.

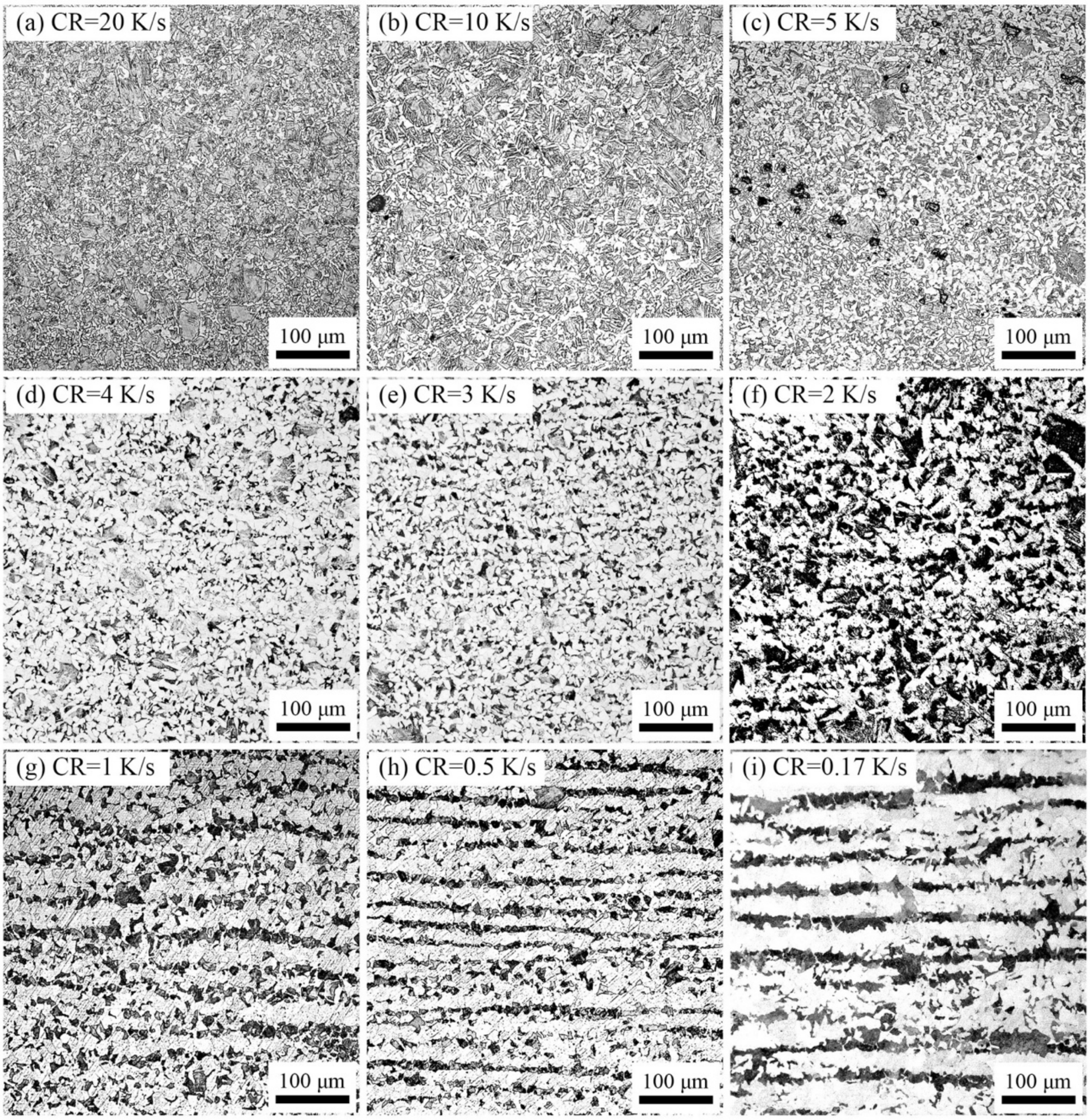

Fig. 5.2-Microstructure after continuous cooling experiments with different cooling rates of a) 20 K/s, b) 10 K/s, c) 5 K/s, d) 4 K/s, e) 3 K/s, f) 2 K/s, g) 1 K/s, h) 0.5 K/s, and i) 0.17 K/s (10 K/min).

The dilatation curves for CC experiments in longitudinal (Fig. 5.3a) and lateral (Fig. 5.3b) directions for a band forming (CR=0.5 K/s) and a non-band forming (CR=5 K/s) condition respectively are in line with the microstructural observations in Fig. 5.2. In the dilatation curve for a cooling rate of 0.5 K/s, the lateral expansion due to pearlite formation, between 900-920 K (627-647 °C), is noticeably more pronounced than the axial dilatation over this temperature domain, while for CR=5 K/s, the relative contributions of the second dilatation peak are comparable for both sets of data.

As explained above, in order to avoid ferrite/pearlite band formation in a CC experiment, cooling faster than the critical cooling rate of 2 K/s is essential. In the next section, new routes of intercritical annealing using the CPPT approach are explained and the results are presented.

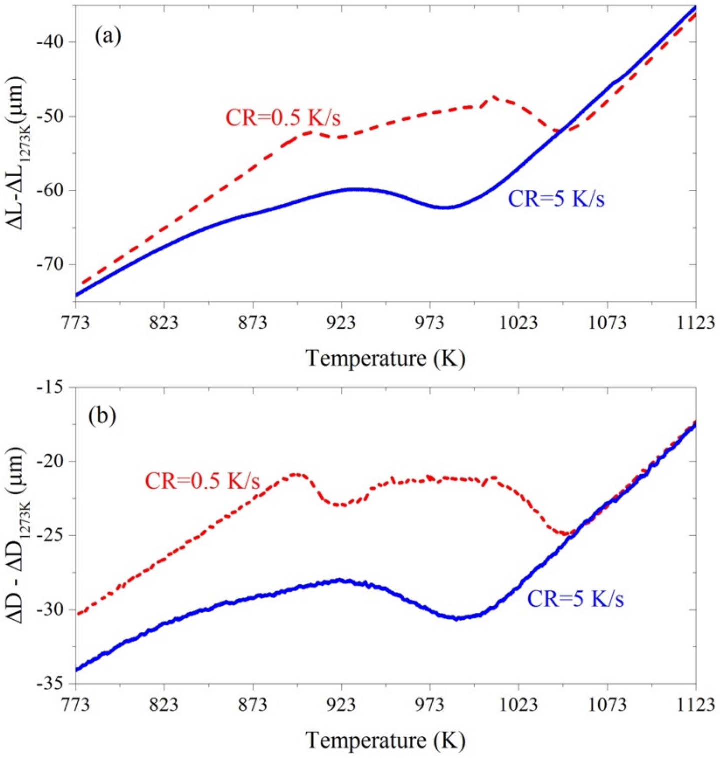

Fig. 5.3-Comparision between dilatation curves achieved by continuous cooling experiment with rate of 0.5 K/s (leading to band formation) and 5 K/s (no band formation) in a) longitudinal and b) lateral direction.

Fig. 5.4 a-d show different applied intercritical annealing routes with cooling/heating rates of 0.17 K/s (10 K/min) as well as the CC route with the same CR (in red). In type H1 CPPT (Fig. 5.4a), after continuous cooling to T_1=998 K (725 °C), the sample is held isothermally for 20 min and then heated to T_2=1048 K (775 °C), held again isothermally for 20 min (total isothermal holding for 40 min), followed by cooling at 0.17 K/s to room temperature. In type H2 CPPT (Fig. 5.4b), the intercritical reheating-cooling cycle is imposed twice before final cooling down. In type I CPPT (Fig. 5.4c), after reaching T_1, the temperature is increased gradually to T_2 such that the reheating time is equivalent to the total isothermal holding and heating times in type H1, i.e. 40 min. Finally, in the isothermal experiment

(Fig. 5.4d), after cooling from the austenitization temperature, the sample is held isothermally at 1048 K (775 °C) for 40 min, prior to final cooling down at the usual cooling rate.

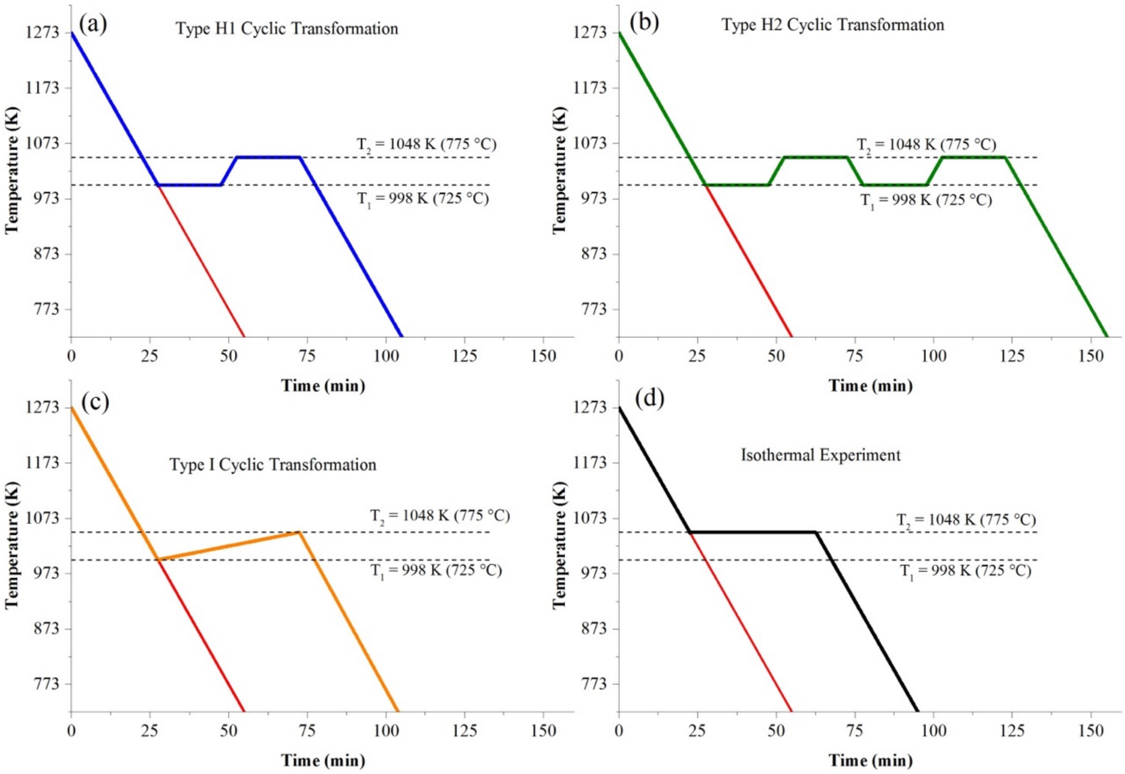

Fig. 5.4-The CC experiment with CR=0.17 K/s versus different intercritical annealing routes of a) type H1 CPPT, b) type H2 CPPT, c) type I CPPT and d) isothermal experiment.

In Fig.5, the longitudinal dilatation curves for each of the intercritical annealing experiments described above are presented and compared to those of the corresponding CC experiment. In the type H1 CPPT experiment (Fig. 5.5a), after reaching T_1=998 K (725 °C), ferrite formation continues isothermally, and there is a linear increase in sample length due to heating after isothermal holding. The sudden jump in the sample length at around T=1010 K (737 °C), both in cyclic and CC curves is an artefact and is due to a change in the magnetic properties of the alloy upon reaching the Curie temperature [25–27]. The linear increase in the sample length during heating after isothermal holding in the CPPT curve corresponds to the so-called ‘stagnant stage’ during which the transformation is suppressed due to pinning effect of segregated Mn atoms at austenite-ferrite interfaces

[19,20]. Upon reaching T_2=1048 K (775 °C), ferrite to austenite back transformation starts to occur isothermally. In the final cooling stage, first the sample shrinks linearly down to T≈973 K (700 °C) and then after a non-linear decreasing stage, the dilatation curve shows a delayed increase in the length at T≈923 K (650 °C) reflecting the delay in the final ferrite/pearlite formation. It is worth to point out that the pearlite formation in type H1 CPPT finishes at T_e≈898 K (625 °C), whereas in the CC experiment the pearlite formation finishes at a significantly higher temperature of T_e≈910 K (637 °C).

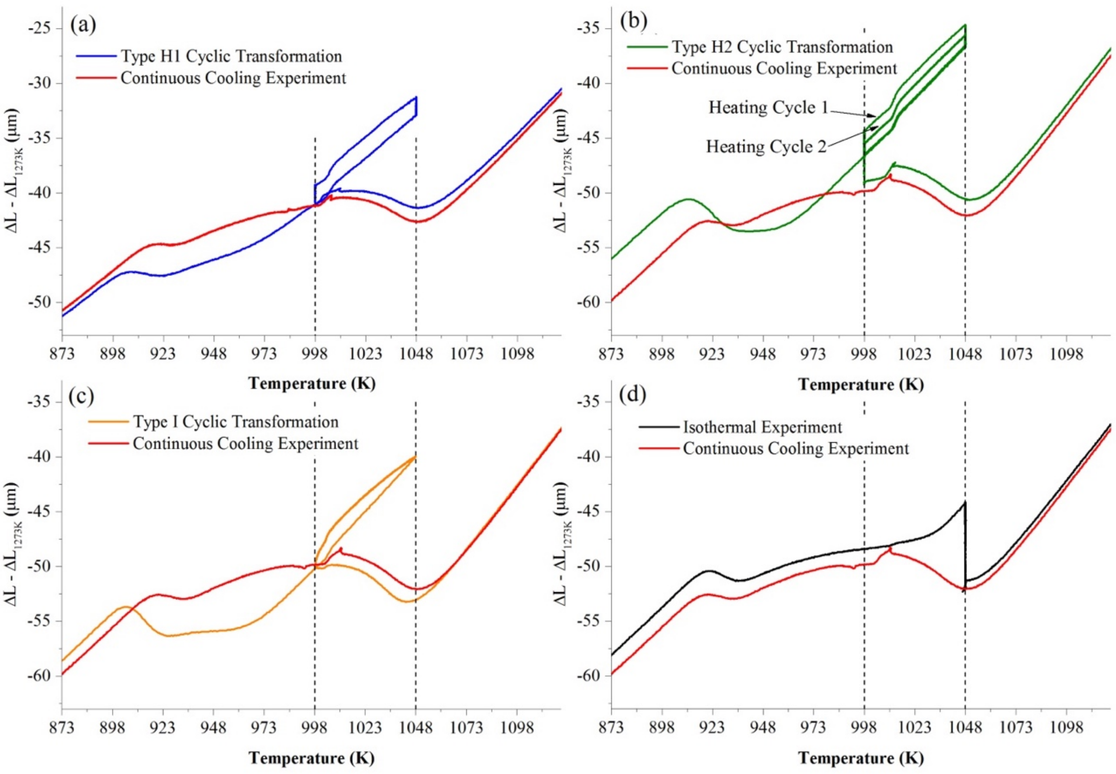

Fig. 5.5- Dilatation curves after different a) type H1, b) type H2, c) type I CPPT and d) isothermal experiment compared to continuous cooling curve with CR=0.17 K/s.

The dilatation behavior for the type H2 CPPT experiment, Fig. 5.5b, is similar to that for type H1 but linear contraction corresponding to the stagnant stage in austenite decomposition during final cooling continues down to T≈960 K (687 °C) instead of T≈973 K (700 °C) measured in the type H1 route. In type I CPPT (Fig. 5.5c), after reaching T_1, despite the increase in temperature and the expected decrease in length due to ferrite to austenite transformation, the sample length increases non-linearly for about 15 K. This stage is called ‘inverse transformation’ and is explained by non-equilibrium condition around the austenite-ferrite interface due to incomplete redistribution of C atoms after sudden change in the temperature regime [19,20]. After the inverse transformation stage, the stagnant stage starts and continues during cooling similar to that of type H1 and H2 CPPT routes. Finally, in the isothermal experiment (Fig. 5.5d), the austenite to ferrite transformation proceeds isothermally and upon further cooling the dilatation behavior is analogous to that of the CC curve with no sign of delayed austenite decomposition during final cooling.

The observed differences between the dilatation behavior after the various intercritical annealing treatments and the continuous cooling experiment with the same CR are reflected in the radically different final microstructures shown in Fig. 5.6. The microstructure after type H1 CPPT (Fig. 5.6a), has no significant evidence of ferrite/pearlite band formation notwithstanding its final cooling rate (0.17 K/s) being well below the critical cooling rate of 2 K/s determined by CC experiment. Similarly, treatments of the type H2 (Fig. 5.6b), and I (Fig. 5.6c) lead to non-banded microstructures. These microstructures consist of homogenously distributed ferrite and pearlite grains, despite the applied low cooling rate. In contrast, the microstructure of isothermal experiment (Fig. 5.6d) still shows significant broad bands of ferrite/pearlite parallel to the rolling direction.

Having presented the effectiveness of CPPT treatment in suppression of the band formation at a final cooling rate of 0.17 K/s, the intercritical type H1 treatment has also been applied but with higher final cooling rates of 0.5 and 1K/s. Fig. 5.7a and Fig. 5.7c show the longitudinal dilatation curve for type H1 CPPT with CR=0.5 and 1 K/s, respectively. In these figures, the corresponding CC curves are also plotted. In both cyclic experiments, the ferrite formation after the cyclic experiment is significantly retarded compared to that in the CC experiment. The corresponding microstructures in Fig. 5.7b and Fig. 5.7d, show that band formation is more reduced after the type H1 cyclic experiment with CR=0.5 K/s compared to the CR=1 K/s. This gives an impression that CPPT experiment with lower CR is more effective in controlling the band formation, while in the CC experiments banding is reduced as a result of the higher cooling rate.

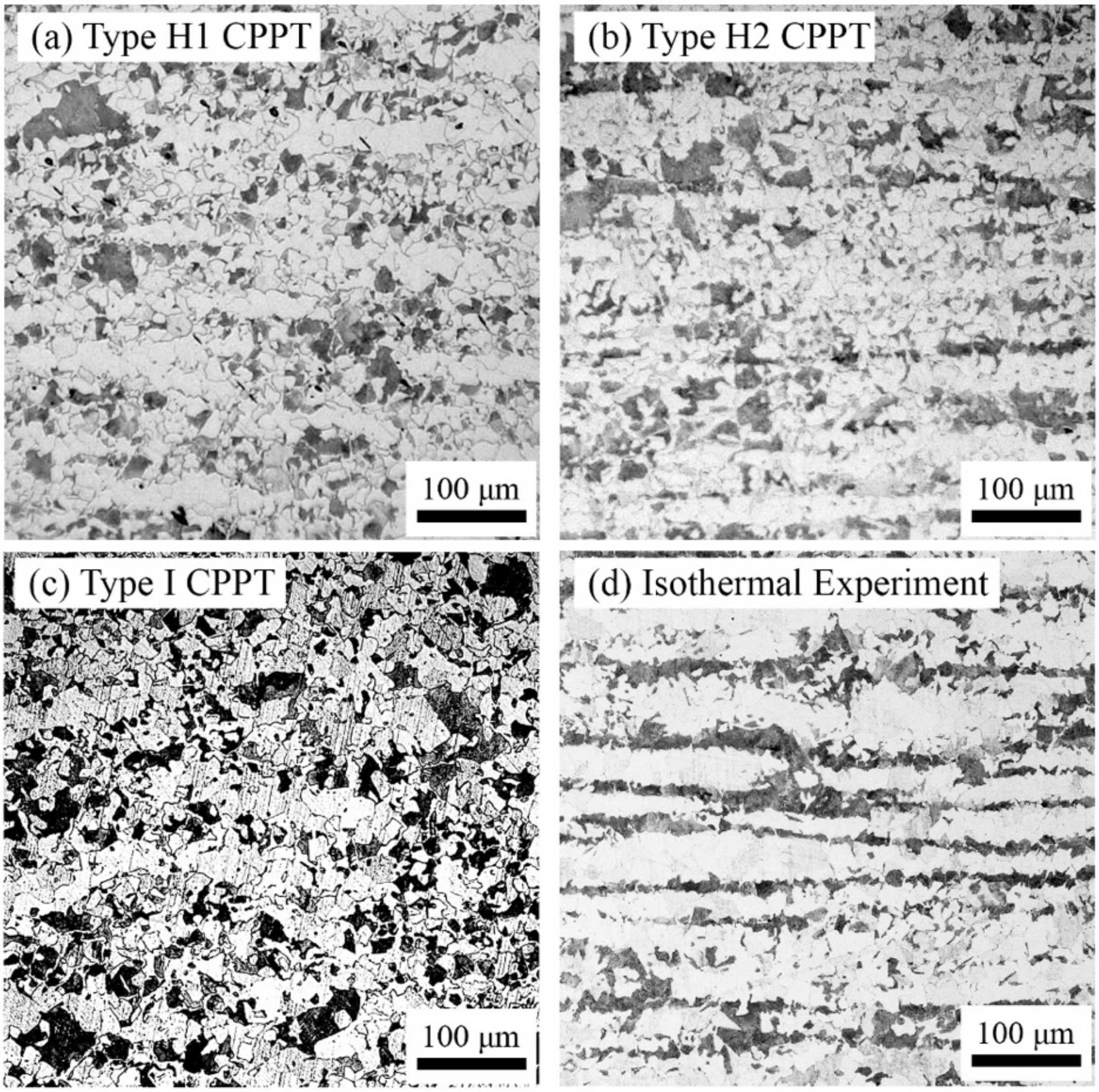

Fig. 5.6- Microstructures after different intercritical annealing routes of a) type H1 CPPT, b) type H2 CPPT, c) type I CPPT and d) isothermal experiment all with CR = 0.17 K/s.

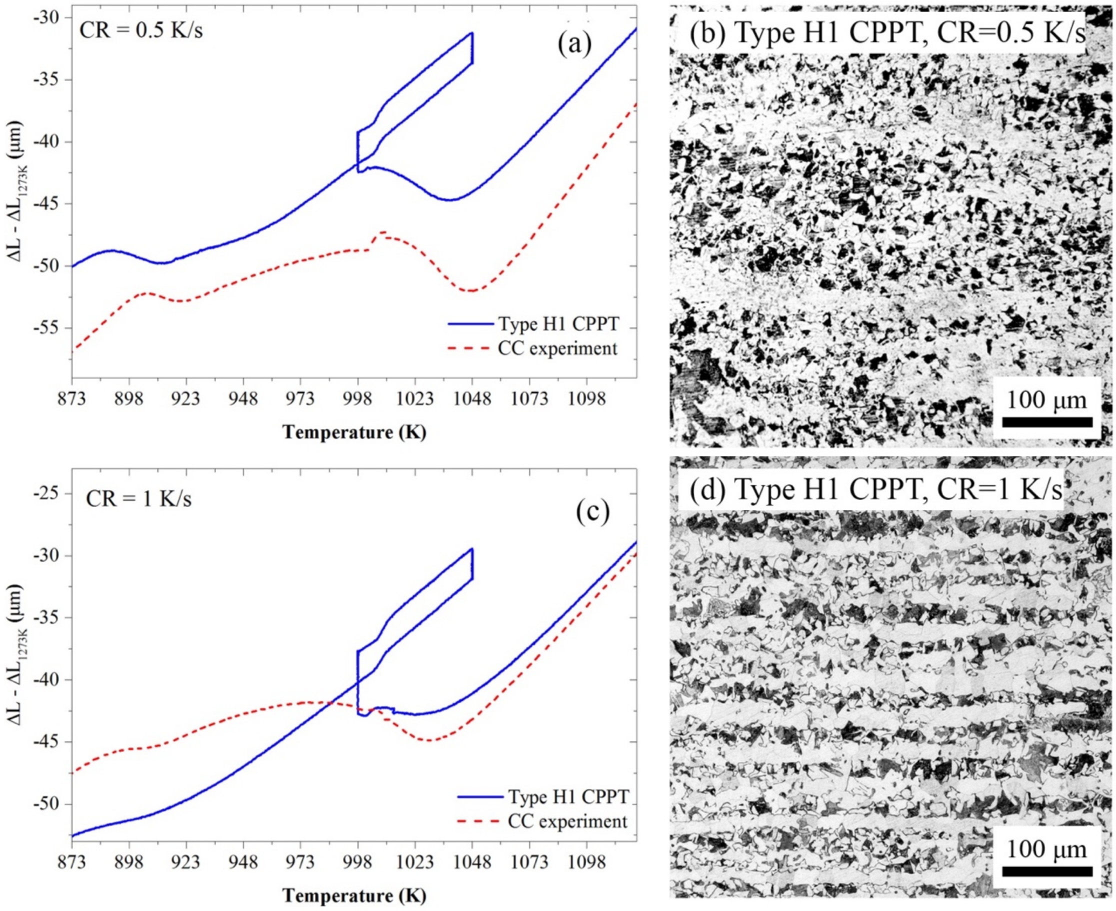

Fig. 5.7- a) longitudinal dilatation curves for type H1 CPPT experiments with CR=0.5 and 1 K/s, b) microstructure after type H1 CPPT with CR=0.5 K/s, c) lateral dilatation curves for type H1 CPPT experiments with CR=0.5 and 1 K/s and d) microstructure after type H1 CPPT with CR=1 K/s.

The extent of ferrite/pearlite banding can be quantified by the anisotropy index (AI) as defined in the industrial ASTM E1268-01 standard [28]. In this standard method the degree of banded or oriented microstructures is quantified using statistical measurements on the morphological appearance of certain microstructural features. AI values close to 1 belong to samples which do not exhibit banding and AI values bigger than 1 indicate microstructures showing increasingly noticeable band formation levels. Fig. 5.8 shows the AI values for all microstructures created via intercritical annealing routes or CC experiments as a function of the applied cooling rate. The error bars in AI refer to the standard deviation in the measurements. Continuous cooling with rates equal or higher than 2 K/s lead to fully isotropic microstructures i.e. AI values equal to 1. The degree of banding increases extensively with decreasing cooling rates, to an anisotropy index of 6 for a CC experiment with CR=0.17 K/s. All CPPT experiments with a slow cooling rate of 0.17 K/s show isotropic microstructures with an AI value <1. In the type H1 CPPT experiment, the anisotropy index increases with increasing cooling rate. For CR=1 K/s, there is no difference between AI values achieved from microstructures after cyclic treatment (Fig. 5.7d) and continuous cooling (Fig. 5.2g). The AI value of microstructure after the isothermal experiment is about 4, displaying minor band formation.

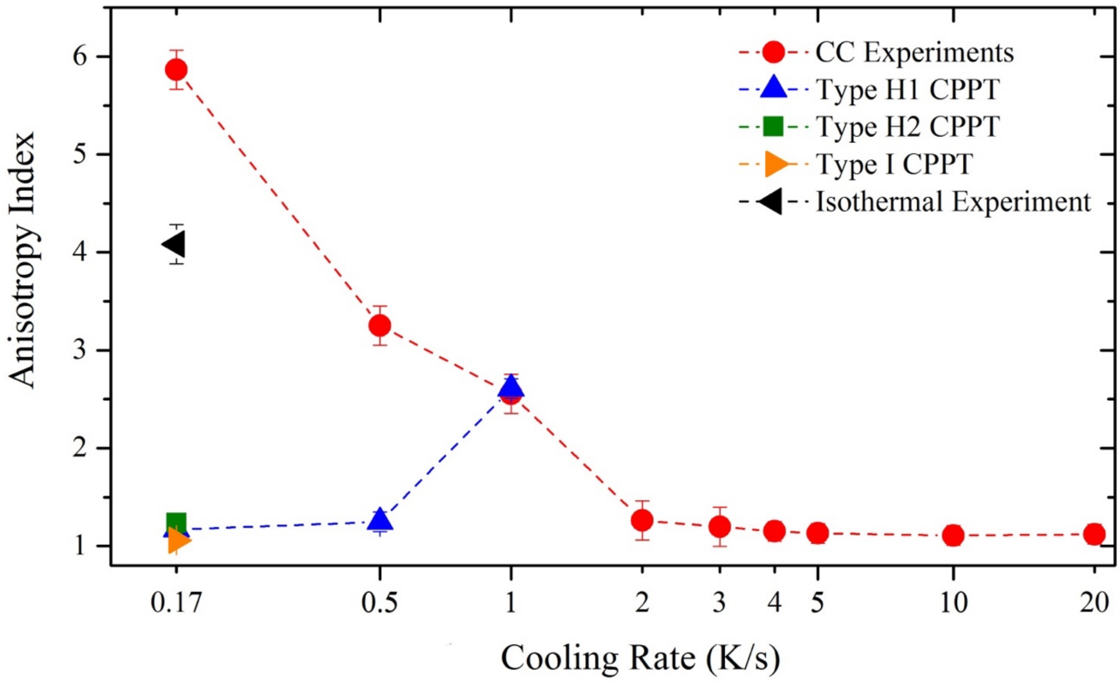

Fig. 5.8- Standard anisotropy index for all the microstructures after different intercritical annealing and CC experiments versus the applied cooling rates.

5.4 Discussion

As shown above, the CPPT treatments with low cooling rates effectively suppress band formation, even at a final cooling rate well below the critical cooling rate determined for continuous cooling. The effect is well reflected in the ASTM E1268-01AI index. However, to analyse the band formation in even more detail a new parameter of ‘band formation index’ is defined similar to the one used for dielectrophoretically aligned PZT particles in a polymer matrix [29]. To this aim, the micrographs are first processed using the Matlab image processing toolbox [30]. The micrographs are transformed to binary images, and the sum of the darkness levels of all the pixels (having a dimension of 500×500 µm) in every horizontal row is determined and normalized to the total number of pixels in each row. Pixels with a high darkness level indicate pearlite while pixels with a low darkness level correspond to ferrite grains. Peaks in the resulting spectrum correspond to the band position and the magnitude of sum is a measure of the quality of the band. The intercolumnar distance between the peaks shows the lateral distance between the formed bands. Results of applying the band formation indexing process to the microstructures after different intercritical treatment routes of type H1 (with CR=0.17, 0.5 and 1 K/s), H2 and I CPPT, isothermal experiment (with CR=0.17 K/s) and corresponding CC experiments are presented in Fig. 5.9 a-f. The curves for microstructures after CC experiments with CR=0.17, 0.5 and 1 K/s in Fig. 5.9 a-c clearly show the peaks corresponding to the preferential nucleation and growth sites of pearlite grains in columns with a typical distance of 50µm. The reduction of ratio of peak heights over the average values with increasing cooling rates in these graphs indicates the more uniform distribution of phases after CC experiments with higher cooling rates in spite of presence of broad bands.

The curves for type H1 CPPT with CR=0.17 and 0.5 K/s (Fig. 5.9 a-b), are significantly smoothed with a substantial reduction of the relative peak heights, indicative of the more uniform microstructure. The hills in the band formation index indicate that there are still preferential locations for pearlite formation with the typical distance of 50µm. This indicates that Mn is still non-uniformly distributed along the microstructure, but for the cyclic annealing route the formation of pearlite in preferential columns is strongly suppressed. The distinct peaks in type H1 with CR=1 K/s curve in Fig. 5.9c are another indication of the anisotropic distribution of phases in microstructure after this treatment. As expected, the curves of band formation index for type H1, H2 and I CPPT routes with CR=0.17 K/s shown in Fig. 5.9 d-e are flattened, while the curve of band formation index for isothermal experiment in Fig. 5.9f clearly shows sharp separate peaks corresponding to diffusely banded and non-uniform microstructure.

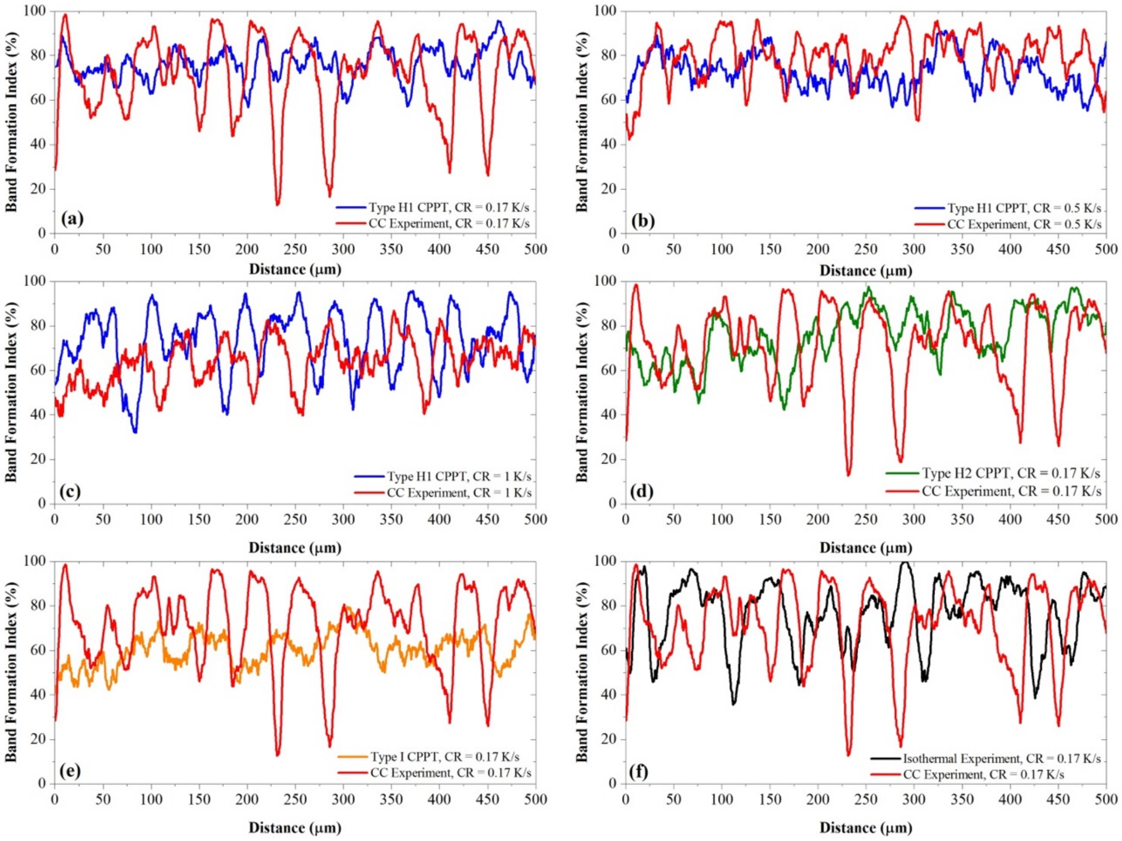

Fig. 5.9- Band formation index of microstructure versus the distance along the normal to the rolling direction after a) type H1 CPPT with CR=0.17 K/s, b) type H1 CPPT with CR=0.5 K/s, c) type H1 CPPT with CR=1 K/s, d) type H2 CPPT with CR=0.17 K/s, e) type I CPPT with CR=0.17 K/s and f) isothermal experiment with CR=0.17 K/s and the CC experiments with similar CR.

As suggested above, despite the suppression of band formation after a CPPT treatment, the original inhomogeneous banded Mn distribution leading to band formation under conventional linear cooling conditions should still be present even after the CPPT treatment as the CPPT treatment only leads to Mn redistribution on a very local scale. In order to demonstrate this, a two-step route as shown in Fig. 5.10a was designed where a fresh sample was first subjected to the type H1 treatment, cooled to room temperature and then re-austenitized and cooled continuously at the rate of 0.17 K/s. Fig. 5.10b shows the longitudinal dilatation curves recorded for the type H1 CPPT and subsequent CC experiment. The differences between type H1 CPPT and subsequent CC dilatations are similar to the ones in Fig. 5.5a in which cyclic treatment and CC experiments were done in two different samples. During the CC experiment, austenite decomposes continuously, while in CPPT route, the austenite decomposition is retarded. The microstructure after the CC experiment (on a sample having first undergone the type H treatment) in Fig. 5.10c, shows a clearly banded microstructure. This confirms that the starting non-homogenous distribution of Mn in the material is preserved during the type H1 CPPT treatment and hence re-occurrence of the ferrite/pearlite band formation occurs in the following CC experiment.

The continuous cooling experiments show that in the hot rolled alloy with micro-segregation of Mn and Si, formation of ferrite/pearlite bands during continuous cooling from austenitic temperature is a virtual function of the applied cooling rate. As shown concisely in Fig. 5.8, cooling with rates equal or higher than 2 K/s is essential to prevent the development of a banded microstructure. This is in agreement with earlier publications showing that even though the presence of micro-chemical segregation of Mn/Si is a prerequisite for band formation, it is the kinetics of the phase transformation, and in particular that of the ferrite, which controls the actual formation of the microstructural bands [5,18,31]. Pearlite grows much faster than the ferrite due to availability of higher driving force at lower transformation temperatures and with a shorter diffusion length as a result of the laminar pearlite structure [4,5,31]. The time available for the growth of the ferrite controls the carbon enrichment of the austenite and this, for non-isothermal conditions, controls the chance of nucleation of either ferrite or pearlite in the Mn rich and Mn poor regions. For slow cooling rates, ferrite nucleation starts preferentially in the Mn poor regions and the time for ferrite formation is long and the C partitions over relatively large distances. Hence, new ferrite nucleation will not occur in the Mn rich regions assisting continuous pearlite formation in these regions. In general, for differences less than 6-8 percent in ferrite nucleation rate, banding does not take place [5,32,33].

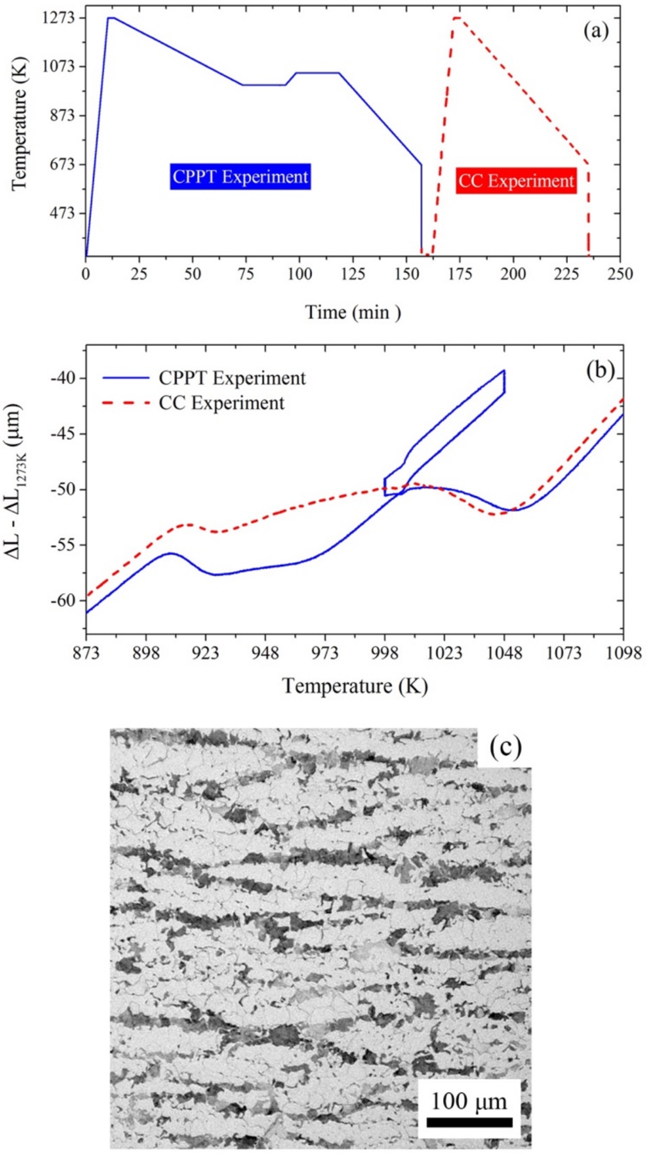

Fig. 5.10- a) Band recovery heat treatment route, b) dilatation curves achieved with CPPT and CC experiments and c) microstructure after the CC experiment.

Interestingly, the nucleation conditions of both ferrite and pearlite (or bainite/martensite), can be derived from the dilatometric curves. The onset of the pearlite is most easily distinguishable in the lateral dilatation curves [21]. The nucleation temperatures as a function of the cooling rate are shown in Fig. 5.11. The usual linear relationship between onset temperature and cooling rate [34] is obtained from this graph. Interestingly for this steel, the slope of the ferrite onset temperature does not change over the explored domain of cooling rated although the microstructure changes from a ferrite/pearlitic microstructure to a more pearlitic-bainitic/martensitic microstructure at around 10 K/s. Furthermore, the slope for the onset of the pearlite formation is equal to that of the ferrite onset temperature.

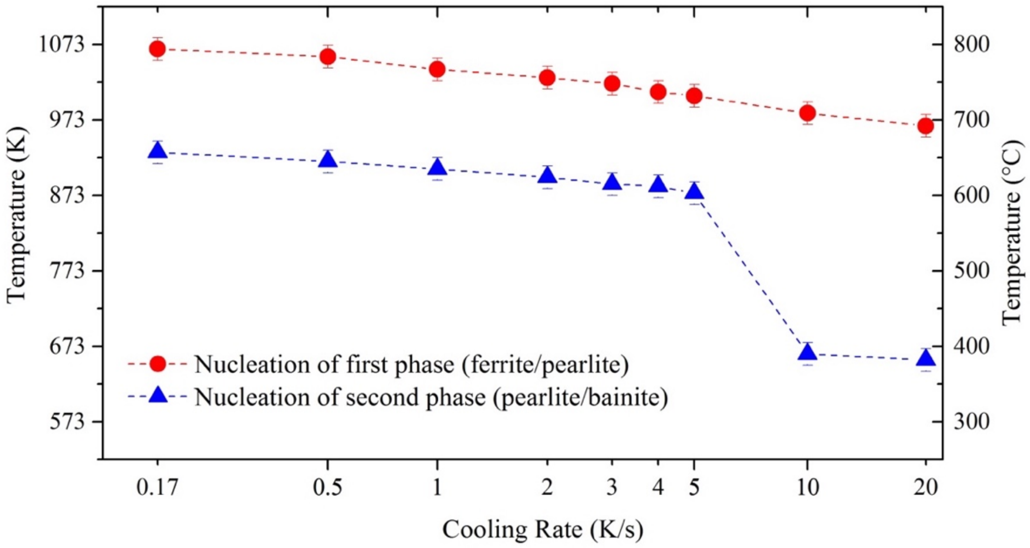

Fig. 5.11- Transformation onset of first phase (ferrite/pearlite) and second phase (pearlite/bainite/martensite) formation during continuous cooling.

The experimental observations clearly show that the band formation can be suppressed by some of the CPPT treatments (see Fig. 5.4), even for a low cooling rate of 0.17 K/s. The suppression is due to the ferrite formation being halted as a result of the local Mn enrichment at the moving austenite ferrite interface and the spike of Mn left behind as a result of the cycling process. As the transformation is halted there is less carbon enrichment and new ferrite formation can take place during the final cooling down. Thus, new ferrite formation can take place in the higher Mn regions and band formation is suppressed.

Fig. 5.12 shows the total time spent on ferrite formation during cooling derived from dilatometry experiments versus the anisotropy index of the resulted microstructure after different CPPT and continuous cooling experiments. As explained above, in the presence of microchemical banding, isotropic microstructure with AI values close to 1 can only be achieved by continuous cooling with major time-constraint for ferrite formation achievable only through high cooling rates. In contrast, the CPPT treatments make formation of fully isotropic microstructures possible in case of long cooling down times.

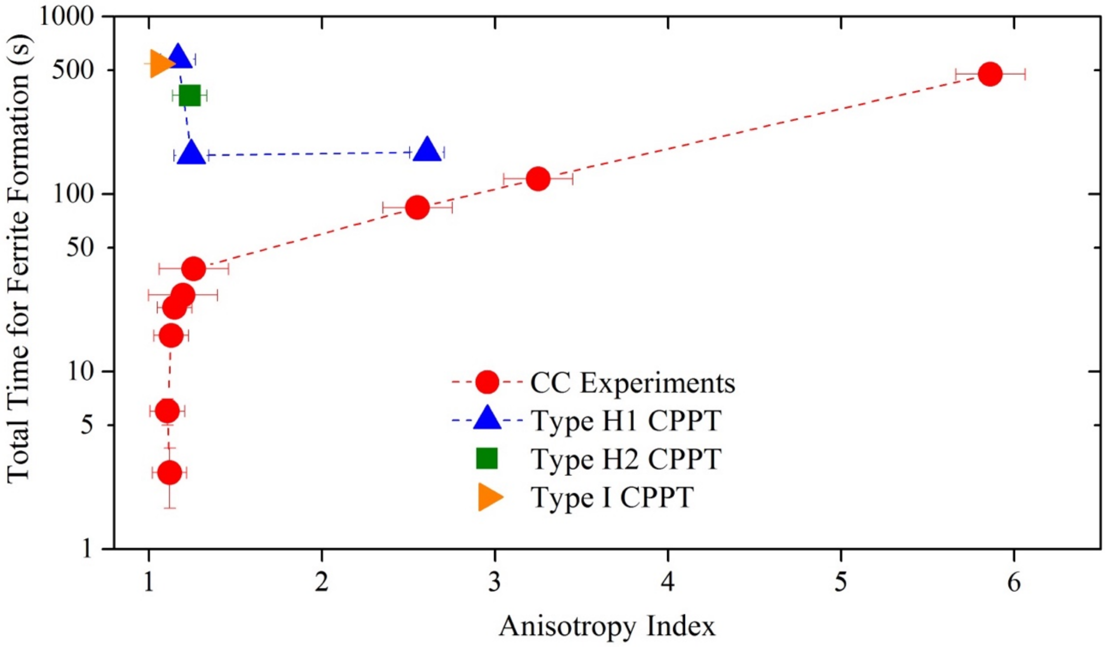

Fig. 5.12- Total time spent on ferrite formation in logarithmic scale versus the anisotropy index of the resulted microstructure after different thermal treatments.

As concisely shown in Fig. 5.8, the values of AI very close to 1 for type H1, H2 and I CPPT routes with CR=0.17 K/s indicate that a CPPT route such as that of type H in which the austenite-ferrite interface is forced to reverse its propagation direction, provides the conditions required for suppression of band formation.

In order to computationally investigate the effect of CPPT in controlling band formation, a Local Equilibrium (LE) thermodynamic model is used in a 1-D geometry with a size of 25 μm. Simulations of type H1 CPPT and CC experiments are performed with CR=0.17 K/s using the DICTRA software linked to TCFE7 and MOB2 databases [35], with the nominal composition set to Fe-0.17C-1.47Mn-1.48Si (all in mass pct.). Fig. 5.13a shows the position of austenite-ferrite interface versus the transformation temperature achieved using LE model for both cyclic and CC experiments. In this graph, the position of the interface represents the fraction of formed ferrite. In agreement with the experimental results, the model predicts that during CC experiment the interface migrates smoothly during cooling. However, after the CPPT experiment, the interface becomes quasi-immobile up to the moment of a high undercooling. Fig, 13b and 13c show the Mn and C profiles in the simulation cell at T_1=998 K (725 °C) just before the final cooling. In the CC curves, there is a narrow Mn spike at the position of interface with incomplete redistribution of C in the remaining austenite. In the CPPT curves, the Mn spike is widened, and carbon is firmly redistributed in the austenitic zone. During back transformation of ferrite to austenite in the reheating stage up to T_2, the interface leaves behind a spike of Mn in the austenite and due to diffusion of the Mn atoms, the spike starts to broaden and to form a narrow Mn enriched zone. During final cooling after the thermal cycle, the austenite-ferrite interface has to pass through this enriched zone leading to a stagnation in the interface motion and hence a stagnation of the ferrite growth [21,36]. In continuous cooling from a fully austenitic state or after an interim isothermal treatment, this Mn spike at the interface also exists, but there is no reversion of interface and the austenite-ferrite interface does not have to transverse a previously Mn-enriched and now interface motion retarding zone.

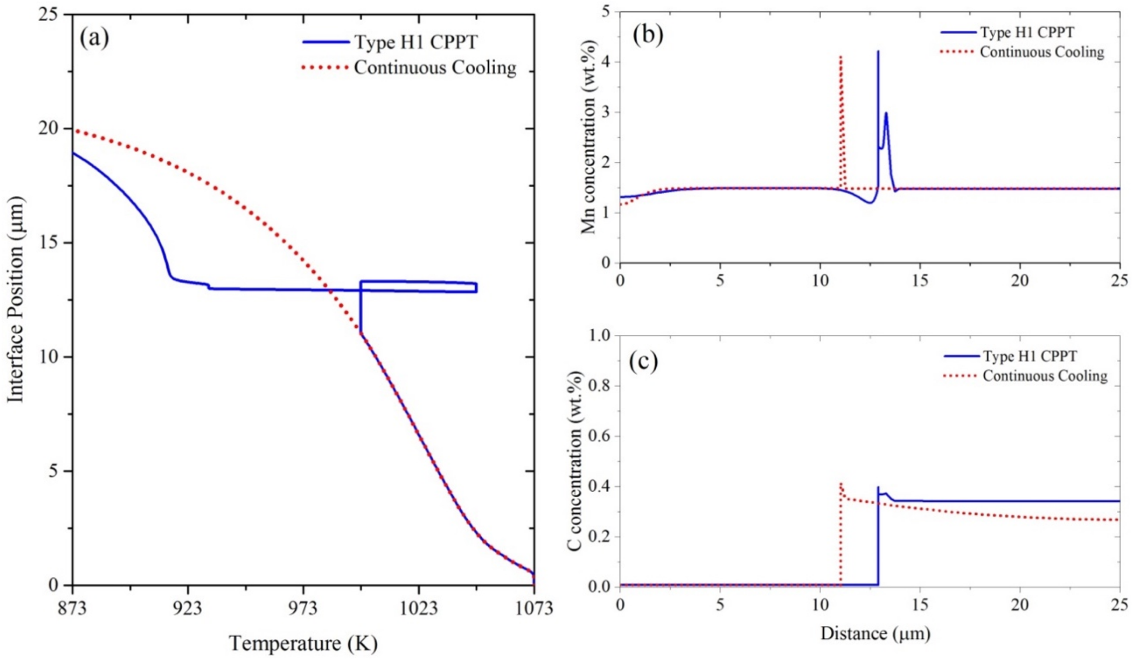

Fig. 5.13-Results of LE model prediction of type H1 CPPT and CC experiments with CR=0.17 K/s, a) interface position versus temperature, b) Mn profile and c) C profile. The ferrite region is at the left side of interface in Mn and carbon profile.

Fig. 5.14a shows a SEM micrograph of the microstructure after type H1 CPPT displaying a non-banded mixture of ferrite and pearlite grains. The actual width of this micrograph is about 130 μm and includes three vertical microchemical bands of Mn. Five different microstructural components can be defined in this graph:

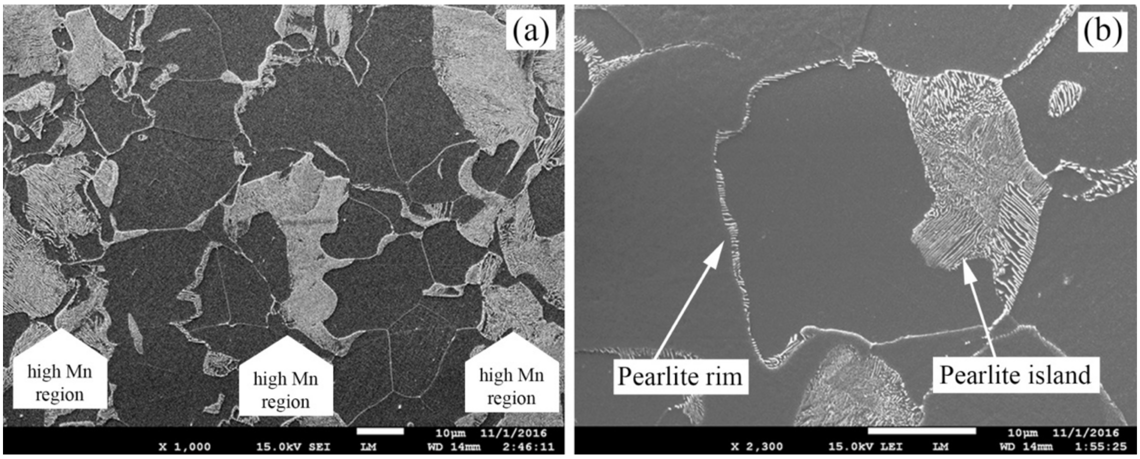

Fig. 5.14–SEM micrographs of after type H1 CPPT experiment with cooling rate of 0.17 K/s showing a) ferritic and pearlitic grains in high and low Mn regions and b) ferrite grain pearlite rim and pearlite island in a low Mn region.

i. Ferrite grains at lower Mn regions,

ii. Pearlite grains in high Mn regions,

iii. Pearlite rims in low Mn regions,

iv. Pearlite islands in low Mn regions,

v. Ferrite grains in high Mn regions.

In a fully banded structure, the first two components dominate the microstructure. Formation of the last three components can be linked to an interrupted band formation process as a result of the CPPT treatment. Fig. 5.14b shows a ferrite grain in a low Mn region with so called ‘pearlite rims’ perfectly aligned and decorating the ferrite grain and a ‘pearlitic island’ surrounded by different ferrite grains. The cementite lamella in the pearlite rim are more or less parallel all along the curved rim and indicates that the pearlite rim has a growth orientation relationship with the enclosed ferrite grain. As shown in Fig. 5.13b, with cyclic experiment a bump of residual Mn forms opposing the migrating ferrite interface. If the size of remaining austenite is big enough, no saturation of carbon occurs in the austenite. When the ferrite front reaches this locally enriched Mn, the interface is halted until further cooling provides sufficient driving force for the transformation, and the ferritic interface continues its growth in the form of pearlite. The thickness of ~3 μm of pearlite rims in Fig. 5.14b is in good agreement with the width of residual Mn bump in Fig. 5.13b predicted by the LE model.

In contrast, the pearlite islands consist of different growth orientations of cementite indicating that it has formed through several nucleation events. The pearlitic islands are small austenitic regions surrounded by growing ferrite fronts. As shown in Fig. 5.13c by modelling, the incomplete ferrite transformation during cyclic experiment provides time for full carbon rejection from ferritic zones into some of the remaining austenite. During final cooling, as a result of high carbon content, these zones reach eutectoid composition and transform into isolated pearlitic islands.

The ferritic zones inside high Mn regions are the result of austenite back-transformation during the cyclic experiments. Adjacent to ferrite grains formed in low Mn regions, new low carbon content austenite forms. During final cooling, the low carbon austenite region transforms into ferrite and prevents formation of continuous pearlite band in high Mn regions.

Fig. 5.15 shows the line profiles for C, Mn and Si, as measured with EPMA across a rimmed ferrite grain and into a pearlite grain in a low Mn region of the sample having received a type H1 CPPT treatment with CR=0.17 K/s. The qualitative profiles of alloying elements show that Si concentration does not differ across different phases and the ferrite grain has low concentration of both C and Mn. The pearlitic islands have a higher carbon content compared to the adjacent ferrite but have similar Mn concentration. The pearlite rims have both high C and high Mn concentrations. This confirms that pearlite rims are locally enriched Mn zones formed by residual Mn concentrations explained above.

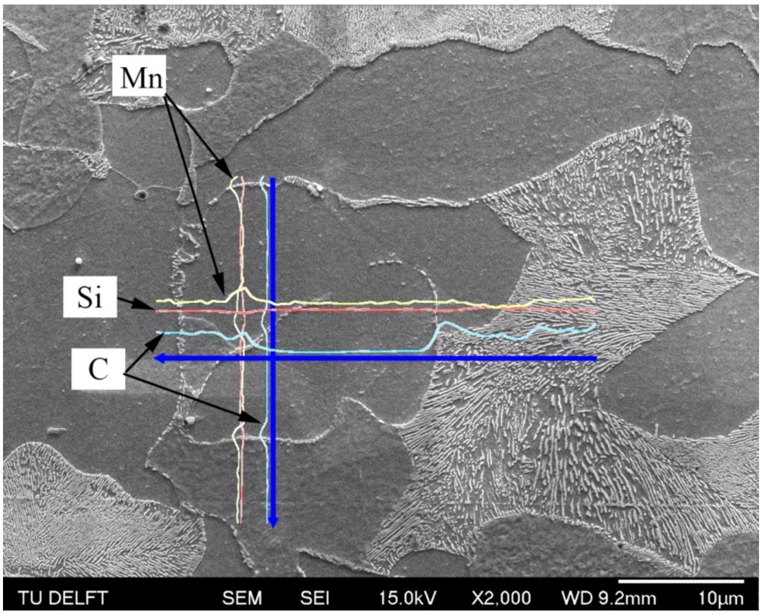

Fig. 5.15– EPMA measurements of composition after Type H1 CPPT experiment with CR=0.17 K/s, Carbon(=blue), Mn(yellow) and Si (dark red).

5.5 Conclusions

In this study, the effect of cooling rate on ferrite/pearlite band formation in a medium Mn alloy during continuous cooling experiments starting from the fully austenitic state is explored systematically. The experiments showed that for linear cooling band formation could only be suppressed by cooling at rates in excess of 2 K/s. However, when a cyclic partial phase transformation treatment in the intercritical domain was included in the final cooling down from the austenitic state, band formation was suppressed even at cooling rates as low as 0.17 K/s. Simple isothermal annealing in the intercritical region was found to have no effect on band formation tendency.

Based on all experiments it can be concluded that:

1. Suppression of band formation during continuous cooling will only occur when the ferrite nucleation is promoted over the ferrite formation by the application of a higher cooling rate.

2. In case of an interim cyclic partial phase transformation in the intercritical region the growth of the initially formed ferrite is significantly retarded such that new ferrite formation is made possible even in the case of a low cooling rate.

3. Controlled local enrichment of Mn at reversing austenite-ferrite interfaces during cyclic transformations is responsible for the suppression of ferrite growth leading to the prevention of ferrite/pearlite band formation even when a low cooling rate is applied.

4. The cyclic partial phase transformation can lead to the formation of perlite rims not encountered in conventionally cooled material.

5.6 References

[1] H. Song, S.S. Sohn, J.-H. Kwak, B.-J. Lee, S. Lee, Effect of Austenite Stability on Microstructural Evolution and Tensile Properties in Intercritically Annealed Medium-Mn Lightweight Steels, Metall. Mater. Trans. A. 47 (2016) 2674–2685. doi:10.1007/s11661-016-3433-7.

[2] A. Mayyas, A. Qattawi, M. Omar, D. Shan, Design for sustainability in automotive industry: A comprehensive review, Renew. Sustain. Energy Rev. 16 (2012) 1845–1862. doi:10.1016/j.rser.2012.01.012.

[3] R. Kuziak, R. Kawalla, S. Wanegler, Advanced high strength steels for automotive industry, Arch. Civ. Mech. Eng. 8 (2008) 103–117. doi:10.1016/S1644-9665(12)60197-6.

[4] S.W. Thompson, P.R. Howell, Factors influencing ferrite/pearlite banding and origin of large pearlite nodules in a hypoeutectoid plate steel, Mater. Sci. Technol. 8 (1992) 777–784. doi:10.1179/mst.1992.8.9.777.

[5] S.E. Offerman, N.H. van Dijk, M.T. Rekveldt, J. Sietsma, S. van der Zwaag, Ferrite/pearlite band formation in hot rolled medium carbon steel, Mater. Sci. Technol. 18 (2002) 297–303. doi:10.1179/026708301225000752.

[6] W. Xu, P.E.J. Rivera Díaz Del Castillo, S. van der Zwaag, Ferrite/Pearlite Band Prevention in Dual Phase and TRIP Steels: Model Development, ISIJ Int. 45 (2005) 380–387. doi:10.2355/isijinternational.45.380.

[7] R.A. Grange, Effect of microstructural banding in steel, Metall. Trans. 2 (1971) 417–426. doi:10.1007/BF02663328.

[8] R. Feng, S. Li, X. Zhu, Q. Ao, Microstructural characterization and formation mechanism of abnormal segregation band of hot rolled ferrite/pearlite steel, J. Alloys Compd. 646 (2015) 787–793. doi:10.1016/j.jallcom.2015.05.128.

[9] Y. Karimi, S. Hossein Nedjad, G. Miyamoto, H. Shirazi, T. Furuhara, Banding effects on the process of grain refinement by cold deformation and recrystallization of acicular C-Mn steel, Mater. Sci. Eng. A. 697 (2017) 1–7. doi:10.1016/j.msea.2017.05.006.

[10] F.G. Caballero, A. García-Junceda, C. Capdevila, C.G. De Andrés, Evolution of Microstructural Banding during the Manufacturing Process of Dual Phase Steels, Mater. Trans. 47 (2006) 2269–2276. doi:10.2320/matertrans.47.2269.

[11] J. Komenda, R. Sandström, Assessment of pearlite banding using automatic image analysis: application to hydrogen-induced cracking, Mater. Charact. 31 (1993) 143–153. doi:10.1016/1044-5803(93)90055-Z.

[12] F.A. Khalid, M. Farooque, A. Ul Haq, A.Q. Khan, Role of ferrite/pearlite banded structure and segregation on mechanical properties of microalloyed hot rolled steel, Mater. Sci. Technol. 15 (1999) 1209–1215. doi:10.1179/026708399101505121.

[13] R. Grossterlinden, R. Kawalla, U. Lotter, H. Pircher, Formation of pearlitic banded structures in ferritic-pearlitic steels, Steel Res. 63 (1992) 331–336. doi:10.1002/srin.199200529.

[14] J.S. Kirkaldy, J. von Destinon-Forstmann, R.J. Brigham, Simulation of Banding in Steels, Can. Metall. Q. 1 (1962) 59–81. doi:10.1179/cmq.1962.1.1.59.

[15] A. From, R. Sandström, Assessment of Banding in Steels by Using Advanced Image Analysis, Mater. Charact. 41 (1998) 11–26. doi:10.1016/S1044-5803(98)00019-9.

[16] K. Mukherjee, L.S. Thomas, C. Bos, D.K. Matlock, J.G. Speer, Modification of Banding in Dual-Phase Steels via Thermal Processing, Mater. Sci. Forum. 783–786 (2014) 1067–1072. doi:10.4028/www.scientific.net/MSF.783-786.1067.

[17] J.D. Verhoeven, A Review of Microsegregation Induced Banding Phenomena in Steels, J. Mater. Eng. Perform. 9 (2000) 286–296. doi:10.1361/105994900770345935.

[18] F.W. Y. Zhang, Y, H. Liu, X. Ruan, G. Li, L. Bai, Y.-L. Zhang, H.-Y. Liu, X.-J. Ruan, G.-Z. Li, L.-G. Bai, F.-M. Wang, Microsegregation behaviors of alloy elements and their effects on the formation of banded structure in pinion steels, Beijing Keji Daxue Xuebao/Journal Univ. Sci. Technol. Beijing. 31 (2009) 199–206.

[19] H. Chen, S. van der Zwaag, An Overview of the Cyclic Partial Austenite-Ferrite Transformation Concept and Its Potential, Metall. Mater. Trans. A. (2016) 1–10. doi:10.1007/s11661-016-3826-7.

[20] H. Chen, B. Appolaire, S. van der Zwaag, Application of cyclic partial phase transformations for identifying kinetic transitions during solid-state phase transformations: Experiments and modeling, Acta Mater. 59 (2011) 6751–6760. doi:10.1016/j.actamat.2011.07.033.

[21] H. Chen, S. van der Zwaag, Analysis of ferrite growth retardation induced by local Mn enrichment in austenite created by prior interface passages, Acta Mater. 61 (2013) 1338–1349. doi:10.1016/j.actamat.2012.11.011.

[22] J. Zhu, R. Ding, J. He, Z. Yang, C. Zhang, H. Chen, A cyclic austenite reversion treatment for stabilizing austenite in the medium manganese steels, Scr. Mater. 136 (2017) 6–10. doi:https://doi.org/10.1016/j.scriptamat.2017.03.038.

[23] T.A. Kop, J. Sietsma, S. van der Zwaag, Anisotropic dilatation behaviour during transformation of hot rolled steels showing banded structure, Mater. Sci. Technol. 17 (2001) 1569–1574. doi:10.1179/026708301101509629.

[24] S.M.C. van Bohemen, L. Morsdorf, Predicting the Ms temperature of steels with a thermodynamic based model including the effect of the prior austenite grain size, Acta Mater. 125 (2017) 401–415. doi:https://doi.org/10.1016/j.actamat.2016.12.029.

[25] A. Verma, M. Sundararaman, J.B. Singh, S.A. Nalawade, A new method for determining the curie temperature using a dilatometer, Meas. Sci. Technol. 21 (2010) 105106. doi:10.1088/0957-0233/21/10/105106.

[26] Y.. Liu, F. Sommer, E.. Mittemeijer, Calibration of the differential dilatometric measurement signal upon heating and cooling; thermal expansion of pure iron, Thermochim. Acta. 413 (2004) 215–225. doi:10.1016/J.TCA.2003.10.005.

[27] G. Mohapatra, F. Sommer, E.J. Mittemeijer, Calibration of a quenching and deformation differential dilatometer upon heating and cooling: Thermal expansion of Fe and Fe–Ni alloys, Thermochim. Acta. 453 (2007) 31–41. doi:10.1016/J.TCA.2006.11.007.

[28] ASTM E1268-01(2016), Standard Practice for Assessing the Degree of Banding or Orientation of Microstructures, (2016). doi:https://doi.org/10.1520/E1268-01R16.

[29] M.A. Gutiérrez, H. Khanbareh, S. van der Zwaag, Computational modeling of structure formation during dielectrophoresis in particulate composites, Comput. Mater. Sci. 112 (2016) 139–146. doi:10.1016/j.commatsci.2015.10.011.

[30] The Math Works Inc., MATLAB Image Processing Toolbox Realese 2015b; The Math Works Inc.: Natick, MA, USA, (2007). https://www.mathworks.com/products/image.html.

[31] J.A. Eckert, P.R. Howell, S.W. Thompson, Banding and the nature of large, irregular pearlite nodules in a hot-rolled low-alloy plate steel: A second report, J. Mater. Sci. 28 (1993) 4412–4420. doi:10.1007/BF01154950.

[32] P.E.J. Rivera Díaz Del Castillo, S. van der Zwaag, J. Sietsma, A model for ferrite/pearlite band formation and prevention in steels, Metall. Mater. Trans. A. 35 (2004) 425–433. doi:10.1007/s11661-004-0353-8.

[33] P.E.J. Rivera-Díaz-del-Castillo, S. van der Zwaag, Assuring Microstructural Homegeniety in Dual Phase and Trip Steels, Steel Res. Int. 75 (2004) 711–715. doi:10.1002/srin.200405832.

[34] H.K.D.H. Bhadeshia, Thermodynamic analysis of isothermal transformation diagrams, Met. Sci. 16 (1982) 159–166. doi:10.1179/030634582790427217.

[35] J.O. Andersson, T. Helander, L. Höglund, P. Shi, B. Sundman, Thermo-Calc & DICTRA, computational tools for materials science, Calphad. 26 (2002) 273–312. doi:10.1016/S0364-5916(02)00037-8.

[36] H. Chen, S. van der Zwaag, Indirect evidence for the existence of the Mn partitioning spike during the austenite to ferrite transformation, Philos. Mag. Lett. 92 (2012). doi:10.1080/09500839.2011.634840.

Chapter 6 A coupled in-situ high-temperature EBSD and 3D Phase Field study of the motion of austenite-ferrite interfaces

This Chapter is based on

- H. Farahani, G. Zijlstra c, M. G. Mecozzi, V. Ocelík, J. Th. M. De Hosson, S. van der Zwaag, In-situ high-temperature EBSD and 3D Phase Field studies of the austenite-ferrite transformation in a medium Mn steel, submitted to the Journal of Microscopy and Microanalysis.

ABSTRACT

In this research, in-situ high-temperature EBSD mapping is applied to record and analyse the migration of the α/γ interfaces during cyclic austenite-ferrite phase transformations in a lean medium manganese steel. The experimental study is supplemented with 3D phase field simulations to better understand the 2D EBSD observations in the context of the 3D transformation events taking place below the surface. The in-situ EBSD observations and phase field simulations show an overall transformation behavior qualitatively similar to that measured in dilatometry. The behavior and kinetics of individual austenite-ferrite interfaces during the transformation is found to show a wide scatter around the average interface behavior deduced on the basis of the macroscopic measurements. The trajectories of selected characteristic interfaces are analysed in detail and yield insight into the effect of local conditions in the vicinity of interfaces on its motion, as well as the misleading effects of 2D observations of processes taking place in 3D.

6.1 Introduction

The science of solid-state phase transformation in crystalline materials in general and in steels in particular has been a stimulating field of research for decades. The transformations of interest take place via migration of interfaces over relatively large distances at the micrometre scale and play a key role in the formation of transient and final microstructures. As many mechanical and physical properties of a material depend on its microstructure, it is of great importance to understand the parameters controlling the migration behavior of the interfaces between the parent and product phases [1–4].

In steels, the phase transformations from austenite (γ) to ferrite (α) and vice versa are controlled by migration of their interfaces [5] and this migration behavior can be used to control the final mechanical properties [6]. Excluding local topology effects, the interface migration behavior depends on the differences in crystal structure between both phases, the average chemical composition of the alloy but even more so the local chemical compositions at the interface and the transformation temperature [7,8]. Many models have been proposed to incorporate the effect of various parameters on the rate of interface migration during ferrous phase transformations as nicely summarized in a comprehensive review paper [9]. In such models, the phase transformation is modelled by reducing the actual interface to a mathematical surface characterized with multiple variables and parameters such as the interface thickness [10], trans-interface diffusivity [11], interface energy [12] and orientation relationship (OR) between two crystals in contact [13]. Yet, all these models explicitly or implicitly assume that the local interface movement is the same for each interface and does not vary along a particular interface, except near triple points.

The actual motion of real α/γ interfaces has been studied experimentally with different in-situ techniques such as optical microscopy (OM) [14–16], laser scanning confocal microscopy (LSCM) [17–20], scanning electron microscope (SEM)/electron backscattered diffraction (EBSD) [21–25] and transmission electron microscopy (TEM) [26–30]. Each of these techniques has its own advantages and drawbacks in accurately documenting the interface motion as a function of the imposed external parameters (such as temperature and composition) and the transient local conditions (such as triple junctions, neighbouring interfaces and grain boundaries and overall degree of transformation). Typical instrumental constraints are the spatial resolution, the imaging speed, the field of view and finally the possibility to measure the crystal structure and orientation of the phases in contact at the interface

With the recent advent of high-temperature EBSD techniques, in-situ SEM/EBSD emerges as a potentially useful technique for in-situ observation of the local dynamics during the microstructural evolution. Its ability to determine the crystal structure and relative orientation of the growing and shrinking grains of the transient parent and product phases [23,31,32] is a major advantage over the conventional high temperature (optical and electron) imaging techniques. Therefore, in-situ EBSD can yield quasi-continuous information on the motion of individual α/γ interfaces during the phase transformation, facilitating full quantification of the evolution of the crystallographic texture. However, temperature control can be difficult and the data analysis needs considering a possible intrusion of surface artefacts [33]. In general, the observed migration behavior of interfaces in 2D is strongly affected by the transformation behavior taking place just below the surface, i.e. it depends on the (truncated) 3D topology of the grains monitored on the free surface [34]. Hence, ‘medium-scale’ 3D modelling approaches using micromechanics or phase field simulation are recommended to be coupled to EBSD results in order to get a more complete insight into the processes responsible for the observed features at 2D interfaces [35].

The results of such EBSD experiments also depend on the nature of the transformation experiment itself. In conventional heating and cooling experiments, the phenomena to be observed are related to both nucleation and growth. The recently introduced cyclic partial phase transformation (CPPT) approach [36] provides a simple method to exclude the nucleation effects such that all observations are related to grain growth (and shrinkage) only. In a CPPT route, the temperature is cycled in such a manner that the α and γ phases both are present at all times and the transformation proceeds via back-and-forth migration of existing α/γ interfaces. Apart from the expected forward and backward migration of the interfaces, also so-called ‘stagnant stages’ have been observed during which the α→γ and γ→α interface migration is halted while a clear overall thermodynamic driving force for further transformation is present. The temporary pining of the α/γ interfaces is due to a built-up of enrichment in alloying elements, in particular Mn, in or near the migrating α/γ interfaces [37–41].

In the present work, in-situ high-temperature EBSD mapping is applied to directly observe the migration of the α/γ interfaces in a medium manganese steel during slow cyclic partial phase transformations. The behaviour of (segments of) individual moving interfaces is compared to the average interface behaviour of the α/γ interfaces during thermal cycling as derived from the corresponding dilatometric measurements. Furthermore, the experimental EBSD data are compared qualitatively to the results of 3D phase field simulations in order to examine the effect of the actual transformation directly below the surface on which the 2D observations are made.

6.2 Experimental Details

The material selected for this in-situ study is a hot-rolled medium Mn steel with a nominal composition of Fe-0.056C-2.0Mn (all in mass%). The same material has been used in other cyclic phase transformation studies using dilatometry and neutron depolarization and its cyclic transformation behavior in relation to Mn partitioning has been well documented (Chapter 4). Furthermore, for a steel of this composition the transformation conditions can be selected such that the motion and details of the interface can be captured well given the recording time per EBSD map and the dimensions of the field of view. The low carbon concentration in this steel was selected to minimize the effect of decarburization during thermal cycling in the SEM. In this experiment, the upper and lower transformation temperatures during cycling were 1168 and 1148 K (895 and 875 °C). The temperatures were selected on the basis of the preliminary EBSD observations and yielded an initial ferrite fraction at the start of the reversing heating cycle of about 80%.

The in-situ EBSD experiments were conducted in a *Tescan Lyra FEG/FIB* Dual beam microscope, equipped with an orientation imaging microscopy OIM system by EDAX including a *Hikari* super camera. Based on a trade-off between map size, spatial resolution (step size) and time resolution for dynamic observation of migration of phase boundaries, the EBSD images were recorded over a fixed representative area of 200×100 μm with a step-size of 1.0 μm using hexagonal grid. Under these conditions the recording of a single OIM map took 50 seconds.

Thermal treatment inside the microscope was performed with a *Kammrath & Weiss* heating module equipped with a ceramic resistance heater. A thin flat sample with dimensions of 10×5×0.5 mm and a finely polished surface was used. The temperature was controlled via thermocouples connected to the heating element just below the specimen. The vacuum in the SEM chamber was of the order of 9×10-3 Pa. The EBSD detector was shielded in between measurements to avoid thermal damage to the detector.

The acquisition moments for OIM maps during the thermal cycle are shown in Fig. 6.1, in which each point marks the collection of a new OIM map. The same 200×100 μm region was mapped in all measurements. The imposed thermal profile is that of a type H cyclic partial phase transformation [36], where the sample is held isothermally for some time at the upper and lower temperature during cycling. Such a profile gives the best change of measuring the direct transformation and the stagnant stage [36]. The time t = 0 s in Fig. 6.1 marks the start of the reheating stage after the prior intercritical holding treatment for 3000 s.

The EBSD data were collected by means of the TSL OIM Data Collection 7.3 software and OIM analysis was performed by TSL OIM Analysis v.7.3 software [42]. This procedure consists of a two-step data cleaning process starting with Grain Confidence Index Standardization (setting grain tolerance angle of 5°, minimum grain size of 5 pixels at multiple rows) followed by a Neighbour Orientation Correlation procedure (level 4, tolerance 5 and a minimal Confidence Index of 0.1). In the data cleaning treatment all data points with a confidence index value below 0.1 were ignored and are shown as white points in the OIM maps. The second cleaning treatment changed the orientation of less than 2% of the scanned points but the phase allocation of each data point remained unchanged.

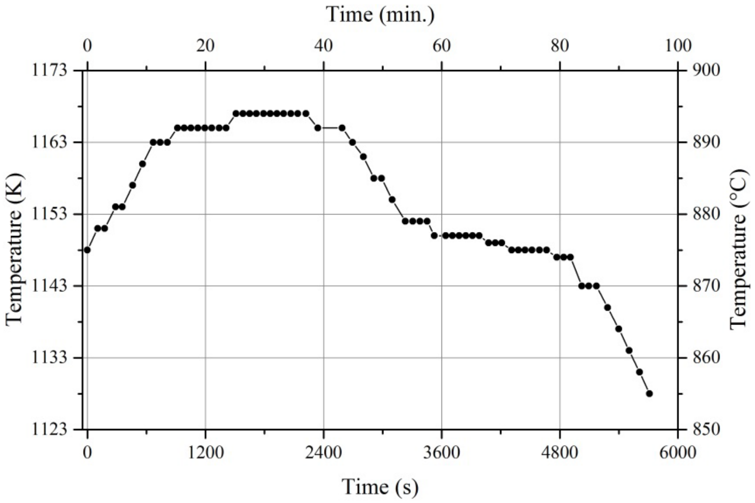

Fig. 6.1- Applied thermal route. Each point in the curve refers to an EBSD image recording.

Determination of motion of the phase fronts during α→γ and γ→α phase transformations was done by point-wise comparison of time-sequenced OIM phase maps, using an Matlab image analysis tool [43]. The tool identified the area swept by each interface in between two successive phase maps.

Finally, in this manuscript only one set of experiments is presented. However, based on a large number of less successful trial experiments we are convinced that the findings reported here are representative for the transformation behavior in this steel as far as the transformation details can be recorded with the EBSD technique.

6.3 Phase Field Model and simulation conditions

The MICRESS® software [44,45] was used to solve the phase field and diffusion equations and enabled prediction of the microstructure evolution and alloy element distribution in time and space. A full 3D austenitic microstructure created by a Voronoi construction was used as the starting microstructure in the phase field simulations. The calculation domain size was 45 × 45 × 45 µm3. The number of grains was adjusted to have an austenite grain size of 12 µm, i.e. the calculation domain contained 60 individual grains. The grid size employed was $\Delta x = 0.3$ µm. Periodic boundary conditions were set for all simulations. Crystallographic orientations were assigned to the parent austenite and newly formed ferrite grains and special misorientation boundaries with low energy and high mobility were defined. The initial 3D microstructure is shown in Fig. 6.2, which also contains the reconstructed image for a 2D cut; the grain colours in the 2D cut represent the different crystallographic orientations. The 3D simulation results have been visualized using the ParaView software [46]. The thermal route imposed in the simulation is time-wise identical to the one shown Fig. 6.1. However, different absolute temperatures were used to achieve a better fit between the phase field calculations and the accompanying experimental results. More details of the thermal route and fitting parameters used in the PF simulations are presented in section 6.5.

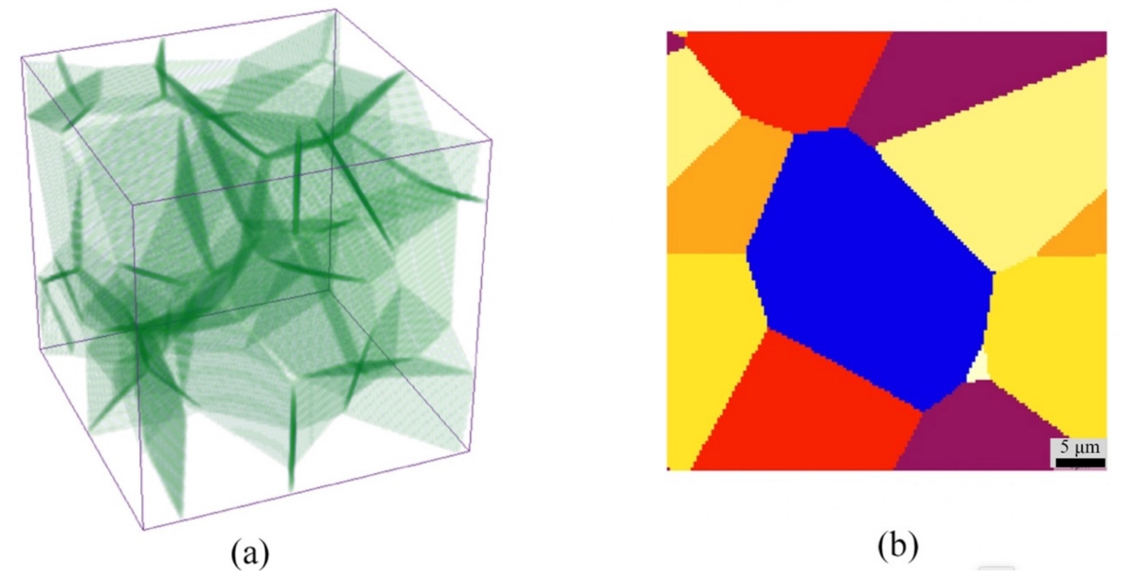

Fig. 6.2 Initial austenite microstructure in 3D simulations (a); 2D cut of a 3D microstructure (b); the grain colours in (b) represent the different crystallographic orientations.

6.4 Results of in-situ EBSD

In this section, the results of the HT EBSD measurements during thermal cycling are presented and discussed from various perspectives. The recorded OIM maps are collected in **Appendix A**, and for each map the time and temperature are reported.

In the following subsections, first, the results dealing with the overall behavior of the material are presented. Then, the behavior of (segments of) selected individual interphase boundaries are presented and discussed.

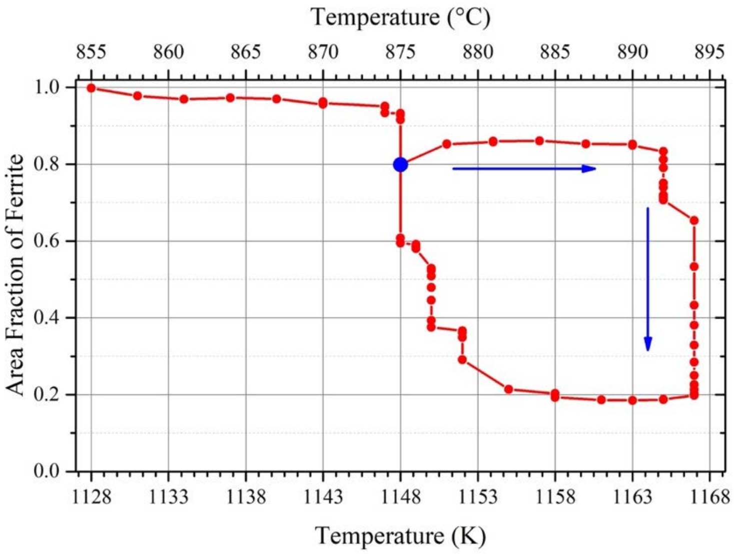

Fig. 6.3- EBSD measured ferrite fraction versus temperature during thermal cycling. The measurements start from the large blue data point and the curve is to be read clock-wise as shown by the blue arrows.

6.4.1 Overall transformation kinetics

The best impression of the overall transformation kinetics can be obtained by plotting the degree of transformation (i.e. the α fraction present) as a function of the temperature. Fig. 6.3 shows the areal α fraction derived from the OIM-maps as a function of the temperature over the thermal cycle. The measurements start from the large blue data point and the curve is to be read clock-wise (as indicated by the blue arrows in the figure). Upon slow heating from 1148 to 1166 K (875 to 893 °C) the ferrite fraction remains constant notwithstanding the imposed temperature rise, reflecting the so-called stagnant stage [36,47]. Upon further heating from 1166 to 1168 K (893 to 895 °C) and holding there, a normal quasi-isothermal transformation takes place and the α fraction decreases continuously. Upon subsequent cooling the ferrite fraction remains constant up to a temperature of 1155 K (882 °C), i.e. we entered another stagnant stage. Upon further cooling to 1148 K (875 °C), we observe a continuous growth of the α to more or less the initial ferrite fraction. Final cooling of the sample caused the remaining γ grains to slowly disappear (the post-cyclic retardation stage [48] and Chapter 4.) ultimately leading to a fully ferritic microstructure at 1128 K (855 °C).

The overall transformation behaviour during partial cyclic phase transformation as observed in EBSD is in good qualitative agreement with earlier CPPT studies using dilatometry, confocal microscopy and neutron depolarization and shows the known distinctive stages in the process (Chapter 4). These stages themselves are relatively well understood and can even be reproduced in a simple 1D model which takes into account substitutional alloying element partitioning at the moving α/γ interface [49].

Having established the overall validity of the EBSD experiment, it is now appropriate to turn to those rather unique features which cannot be made visible with any of the experimental techniques used so far. Hence, the next section focusses on the displacement characteristics of individual (segments of) interfaces both during the α→γ and the γ→α phase transformation.

6.4.2 Local displacement sequences of selected interfaces:

In this section, the displacement characteristics of 15 different α/γ interface segments are characterized in a chronological order of appearance and their migration behavior is analysed in terms of the local crystallographic characteristics as far as they can be derived from the EBSD data. These interface segments appeared and disappeared on the sample surface at different times (and temperatures) during the thermal cycle. Fig. 6.4 a-o show the displacement of each of the selected 15 interphases as a function of the temperature. By default, the starting position of each interface is set to zero; a positive displacement value means migration of the interface into the austenitic region (α growth) while a negative value means migration in the ferritic region (α shrinkage), respectively. Displacement values are measured in the direction perpendicular to the local interface boundary orientation (as seen in the 2D measurement). Comparison of the data in Fig. 6.3 and those in Fig. 6.4 makes it immediately clear that the behavior of a single interface can be rather different from the overall material behavior, as derived from the time dependence of the ferrite fraction. Over the temperature range 1148 to 1168 K (875 to 895 °C) according to Fig. 6.3 the ferrite fraction decreases, yet some local interface displacement measurements suggest local ferrite growth (Fig. 6.4 a-c), the ferrite fraction to remain constant (Fig. 6.4d) but of course some interfaces also suggest ferrite shrinkage (Fig. 6.4 e-f). As also been reported by others [50], the growth of the ferrite fraction does not mean that all ferrite grains grow equally and isotopically, as we assume in simple 1D models, but local competition results in interface segments growing at different speeds and sometimes even in different directions, in order to optimize the overall rate of global free energy minimization [51].

In order to analyse the migration behavior of characteristic interface segments (also contained in the video clip in the **Appendix A**), some EBSD images taken at successive stages of the heat treatment are selected and shown in Fig. 6.5 a-j. Each interface segment was allocated a unique identifier for the duration of its existence even though its character and growth direction may change. The behavior of these boundaries is analysed with respect to the measured orientation relationship and other properties in phase boundary. The character of each boundary segment grouped per subset of figures from Fig. 6.5 is listed in Table 6.1. It should be stated that characterization of the interphase boundaries via the orientation relationship of the crystals at the interface determined using the 2D EBSD does not necessarily fully reflect the orientation relation in 3D. However, this characterization is useful for a first-order assessment between different interfaces when comparing their behaviours in groups.

In the following subsections, the behavior of these different interphase boundary segments during the thermal cycle is analysed as completely as possible, without being able to comment on the local chemical composition at the moving interface, which, as all CPPT experiments have demonstrated, is crucial in controlling the average velocity.

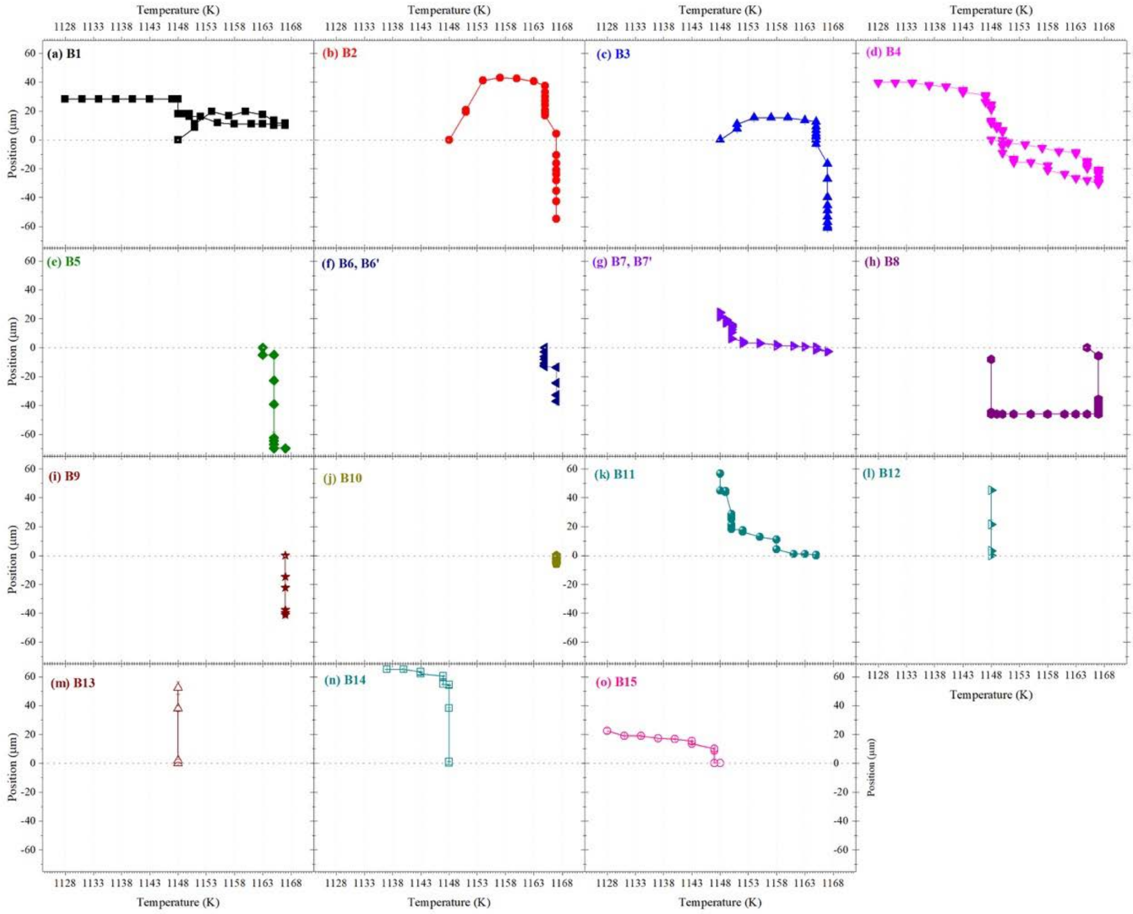

Fig. 6.4- Position of all fifteen tracked interfaces during the cyclic transformation vs temperature of a) B1, b) B2, c) B3, d) B4, e) B5, f) B6, g) B7, h) B8, i) B9, j) B10, k) B11, l) B12, m) B13, n) B14 and o) B15.

6.4.3 Local features observed during ferrite shrinkage

6.4.3.1 Migration of coherent (straight) interface segments

The interphase segments B1 and B7 are characterized as coherent interfaces with an OR close to the Nishiyama-Wasserman (NW) and Kurdjumov–Sachs (KS) OR, respectively [52]. Both interfaces have a limited migration during the γ growth stage (Fig. 6.4a and Fig. 6.4g). The inclination angle of the interface plane B1 and B7 with respect to the surface where the interface migration is analysed, was calculated to be equal to 123° and 170°, respectively. During the whole thermal cycle, the OR of B1, as measured, changes between NW and KS OR, with its misorientation angle varying about 3°. Compared to the other interface segments, B1 remains almost fully pinned until final cooling to 1128 K (855 °C). During the heating stage, the interface segment B7 is also very stable and barely moves. It is well accepted that mobility of an interface depends on the proximity of misorientation at the interface to an special the OR [53]. The existing OR at B1 and B7 can be held responsible for the observed low mobility during α shrinkage (γ growth).

6.4.3.2 Slow migrating incoherent (curved) interfaces segments

The B4 phase boundary segment is an incoherent interface with no special OR. This interface is quite stable and is preserved until almost the end of transformations (Fig. 6.5 a-j). At the start of the heating stage, while B1, B2 and B3 show slight migration toward the centre of the existing γ grain, B4 remains pinned upon heating from 1148 K (875 °C) to 1163 K (890 °C), and then migrates directly upon further heating to 1167 K (894 °C) and isothermal holding at this temperature.

The interphase boundaries B5, B6 and B7 appear more or less at the same time but migrate at different rates resulting in the formation of a γ grain with an elongated morphology. B5 and B6 are characterized as incoherent interfaces with no special OR. The calculated inclination angle of 170° at B7 means the corresponding γ grain, as indicated in Fig. 6.5d, is so shallow and the growth of B6 can be affected by topology of the γ grain beneath the surface [54–57].

6.4.4 Fast migrating incoherent (curved) interface segments

The B2 and B3 phase boundary segments have similar characteristics and are likely type ∑7 interfaces (Table 6.1). Upon heating the semi-straight B2 and B3 α/γ phase boundaries in Fig. 6.5b transform to two curved interfaces in Fig. 6.5c and Fig. 6.5d. During migration of these interfaces, the short area between B2 and B3 (B2/3) has a [0.69,0.52,0.49]36.3° character but is no longer of the ∑7 type.

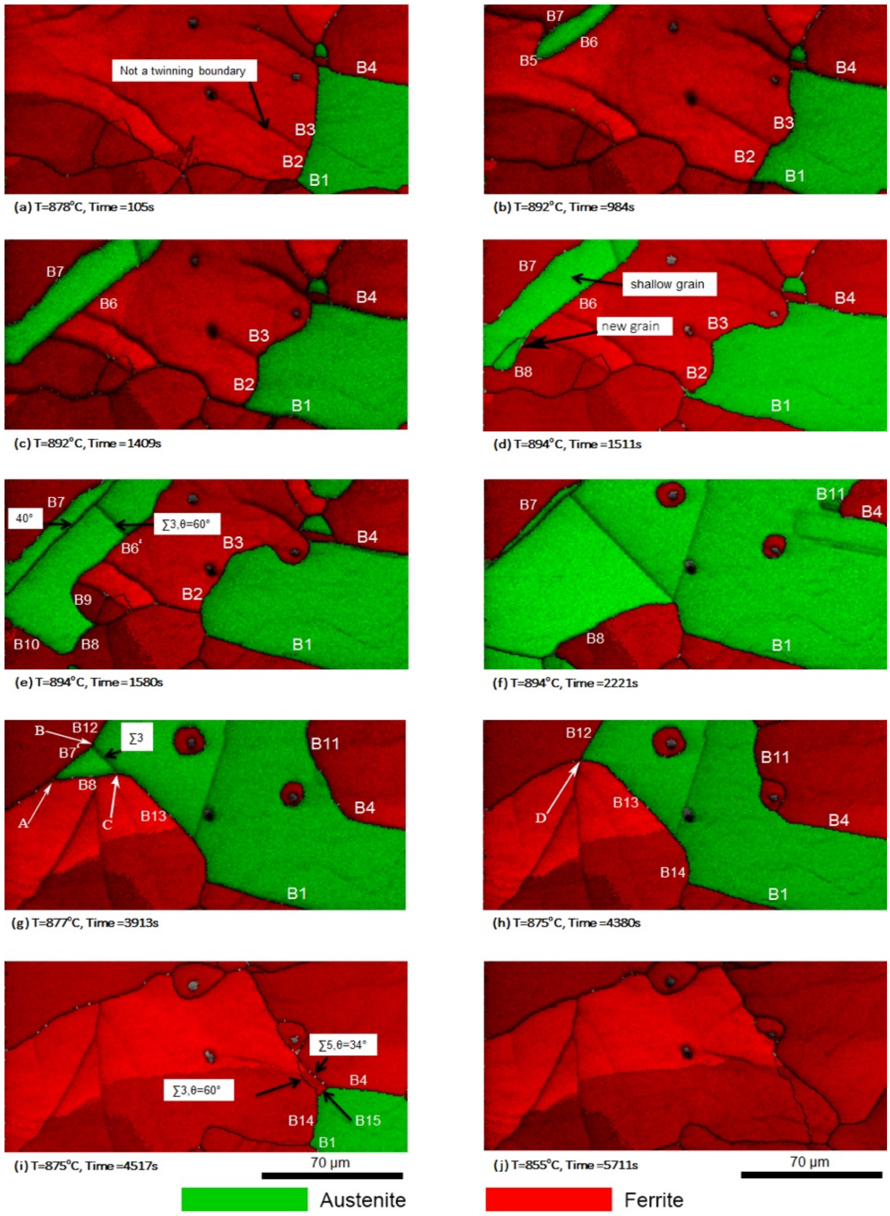

(a) T=878°C, Time=105s
(b) T=892°C, Time=984s
(c) T=892°C, Time=1409s
(d) T=894°C, Time=1511s
(e) T=894°C, Time=1580s
(f) T=894°C, Time=2221s
(g) T=877°C, Time=3913s
(h) T=875°C, Time=4380s
(i) T=875°C, Time=4517s
(j) T=855°C, Time=5711s

🟩 Austenite 🟥 Ferrite

Fig. 6.5- Selected in-situ EBSD phase maps showing different configurations of interphase boundaries during cyclic partial phase transformation during ferrite shrinkage (austenite growth) at a) T=1148 K (875 °C) , time=0 s, b) T=1151 K (878 °C) , time=105 s, c) T=1165 K (892 °C) , time=984 s, d) T=1165 K (892 °C) , time=1409 s, e) T=1167 K (894 °C) , time=1511 s, f) T=1167 K (894 °C) , time=1580 s and ferrite growth at g) T=1167 K (894 °C) , time=2221 s, h) T=1150 K (877 °C) , time=3913 s, i) T=1148 K (875 °C) , time=4380 s, j) T=1148 K (875 °C) , time=4517 s and k) T=1128 K (855 °C) , time=5711 s.

Table 6.1. Characters of phase boundaries corresponding to Fig. 6.5.

Transformation Stage	Phase Boundary	Average misorientation angle (°)	OR
Austenite Growth	B1	42.9	KS (with calculated 123° inclination angle of boundary plane)
	B2	36	
	B3	37.6	
	B4	52.3	
	B5	59	
	B6	55.8	
	B6’	23.9	
	B7	42.4	KS (with calculated 170° inclination angle of boundary plane)
	B8	29	
	B9	29	
	B10	48.3	
Ferrite Growth	B1	44.8	NW
	B4	52	
	B7’	35.6	
	B8	44.9	
	B11	53.7	
	B12	49.43	
	B13	56.2	
	B14	22.13	
	B15	54.2	

The aforementioned shallow γ grain (Fig. 6.5d) is separated from surrounding α grains by B5, B6 and B7. Upon heating from 1165 K (892 °C) to 1167 K (894 °C), a new γ grain (indicated in Fig. 6.5e) appears adjacent to the existing shallow γ grain. By isothermal holding, the new γ grain grows relatively fast, forming new α/γ interphase segments of B6’, which appears to be a separated segment from B6 with a new misorientation, B8, B9 and B10. These new interphase boundary segments are incoherent boundaries and migrate fast leading to considerable growth of the austenite fraction during isothermal holding at 1167 K (894 °C).

6.4.5 Local features observed during α growth

After isothermal holding, cooling starts with interphase boundaries B7, B8 at one side and B11 and B4 at the other side of the austenite grain (Fig. 6.5g). The γ→α phase transformation starts with the disappearance of the shallow γ grain, which results in a new incoherent interface segment B7’ without any special OR and the growth of α continues with the migration of B7’ and B8.

6.4.5.1 Neighbouring fast and slowly migrating incoherent interface segments

The interphase boundaries of B4 and B11 are thought-provoking phase boundaries, separating the same α and γ grains from each other, but at different angles (different habit planes). As shown in Table 6.1, both are incoherent interfaces. As shown in Fig. 6.5 g-j and Fig. 6.4 d-k, during cooling, the γ→α phase transformation finishes early at B11 while B4 is quite stable. The stability of B4, both during heating and cooling stages (the α→γ and γ→α phase transformations) suggests that B4 may have been pinned by local segregation of Mn to the interface during thermal cycling.

6.4.5.2 Geometry affected motion of interface segments

The special make up of B12 and B13 interphase boundary segments during cooling (α growth) can be seen in Fig. 6.5 h-i. As shown in Table 6.1, at start of the cooling stage both phase boundaries are incoherent. It seems that the γ→α phase transformations at B7’, B8, B12 and B13 boundaries are interconnected: As long as B7’ and B8 exist, migration of the

B12 and B13 boundaries are negligible; as soon as B7’ and B8 disappear, B12 and B13 become mobile, though their characters remain unchanged. This observation can be explained by taking into account the special geometrical arrangement of these interface segments.

The observed behavior of B12 and B13 boundaries before and after disappearance of B7’, B8 can be rationalized by considering the pinning effect triple junctions[58] :

According to the Gibbs definition of interface energy [59], at a constant temperature, T, and pressure, P, the interface tension is related to the interface energy as

$$F_k = \sigma_k + A\left(\frac{\partial\sigma_k}{\partial A}\right) + \Psi\left(\frac{\partial\sigma_k}{\partial\Psi}\right)\ [\frac{N}{m}], \text{(i)}$$

where F_k is the tension for unit length of interface k [N/m], σ_k is the interface energy [J/m^2], A is the interface area and Ψ is the misorientation angle at the interface. In case of a low interface velocity, the time required for reconstruction of the interface structure is negligible and the interface energy remains independent of the interface area, $\frac{d\sigma_k}{dA} = 0$. In addition, when there is no special OR at the solid-solid interface, the dependency of the interface energy to the misorientation angle is negligible, $\frac{\partial\sigma_k}{\partial\Psi} = 0$. Hence, at the given condition the interface energy per unit surface area can be numerically taken equal to surface tension per unit length of the boundary.

The schematics of the A, B, C and D triples junctions as indicated in Fig. 6.5 g-h are sketched in Fig. 6.6 a-b. At the moment of observation in Fig. 6.5 g-h, no special OR is seen in at B7’, B8, B12 and B13, hence for these interfaces the dependency of interface tension on OR in equation (i) can be neglected. By taking interfaces energies of $\sigma_{\alpha\gamma}$=0.85 J/m2, $\sigma_{\gamma\gamma}$=0.6 J/m2 [60], and $\sigma_{\alpha\alpha}$=1.11 J/m2 (in pure Fe) [61], the equilibrium of tensions between different interfaces at the junctions for each schematic configuration of triple junctions shown in Fig. 6.6 a-b can be calculated, assuming the triple junction plane being orthogonal to the surface with a similar radius of curvature for all the interfaces. According to the observed angles between interfaces at the mentioned triple junctions, calculation of the absolute values of drag per unit length for each configuration leads to F_A=1.06 N/m,

F_B=0.42 N/m, F_C=0.88 N/m and F_D=0.92 N/m in the directions shown inFig. 6.6. These calculations confirm that the balance of tensions in configuration of triple junctions A and D are favourable for γ→α phase transformation, while for triple junctions B and C the equilibrium drag force is against motion of these triple junctions toward γ→α phase transformation. Henceforth, in conditions of availability of low chemical driving force for γ→α phase transformation, the triple junctions A and D can accelerate motion of B7', B8 interface segments in Fig. 6.5g and B12, B13 interface segments in Fig. 6.5h; whereas the motion of B12 and B13 interphase boundaries adjacent to triple junctions B and C in Fig. 6.5g seem to be triple junction controlled [62,63].

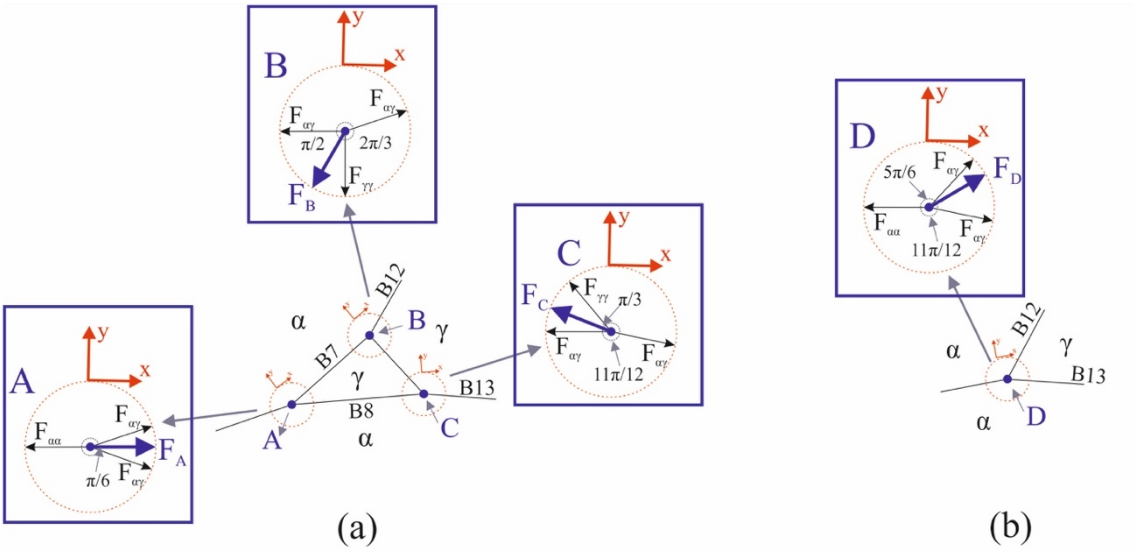

Fig. 6.6- Schematics of the triple junctions corresponding to configuration of interfaces and balance of interfacial tensions at a) triple junctions A, B and C and b) triple junction D as shown in Fig. 6.5 g-h. The FA, FB, FC and FA indicate the overall tension at the triple points A, B, C and D; the different insets show the area around the different triple points.

6.4.6 Final stage of α growth

The constitution of these phase boundaries at the final stage of cooling at 1148 K (875 °C) is shown in Fig. 6.5j. After isothermal holding at this temperature for about 205 s, migrations of B1, B4 and B14 phase boundary segments stop and these interface segments do not move further. Apart from B1, there is no special OR at B4 and B14. With further cooling to 1128 K (855 °C), a new α grain appears creating the B15 phase boundary segment adjacent to B4 and B14. While B1 is pinned and migration of B4 and B14 is negligible, the γ→α phase transformation finishes as a result of the smooth migration of B15 (Fig. 6.5k). The stable migration of B4 and B14 after this point can be explained by assuming compositional variations of Mn, or local enrichment of Mn in front of these interfaces existing from the previous heating cycle creating a post cyclic stagnant stage in α growth [48] and Chapter 4. As shown in Table 6.1, the misorientation angle in B15 is no different from that of B4, but the misorientation at grain boundary segments separating the α grain corresponding to B15 from its neighbours (Fig. 6.5j), suggest that B15 approaches the assumed local Mn-enriched zone from a different angle. Hence, the assumed Mn spike at B4 is ineffectual in pinning B15.

The mechanisms supposed responsible for the behavioural features of different interfaces are summarized in Table 6.2. The existence of special OR, or coherency of interfaces can be held responsible for stagnation of B1 and B7 (during heating). Compositional variations of elements can be held responsible for the stagnation at B4 during most stages of this long treatment. Finally, the pinning effect of triple junctions can be held responsible for the behavior observed in the pair of B7’, B8 and B12, B13.

6.4.7 Migration velocities of the interfaces

The migration rate of each identified phase boundary segment can be measured from the slope of the position of interfaces versus time. The measured growth rates of the different selected interfaces and the temperature profile versus time are shown in Fig. 6.7. The motion centre of the graphs in this figure denotes zero velocity, the upper side and the lower side of the graph denotes the measured migration velocities leading to α or γ growth, respectively. The growth rates of different boundaries are widely scattered and at many points the rates drop to zero. Such a behavior is similar to the jerky-type motion reported [64], however the number of boundaries studied in the present work is too limited to draw the same conclusion. The average migration rate of interface segments during the whole transformation, for both γ or α growth can be derived from Fig. 6.7. Comparison between average growth rates of α/γ interphase boundaries during their migrations show no major difference between averaged growth rates of interface segments during α growth, as calculated 0.057 µm/s, and γ growth as calculated 0.080 µm/s.

Table 6.2.- Summary of the experimentally observed features in the characterized interface segments.

Feature	Interface segments
Low velocity of coherent interfaces	B1, B7
High velocity of incoherent interfaces	B2, B3, B8, B9, B10
Geometry effect (Triple junction pinning effect)	B7’, B8 and B12, B13
Possible Mn pinning effect	B4

A unique feature of the in-situ EBSD measurement is the possibility to characterize and follow the misorientation angle of each identified interface segment during the cyclic treatment. Fig. 6.8 shows the misorientation angle of some interphase boundaries versus their migration velocity during ferrite or austenite growth. Analogous to findings in ref. [32], no clear correlation was found between the average migration velocity and the misorientation angle between the parent-daughter interphase boundaries.

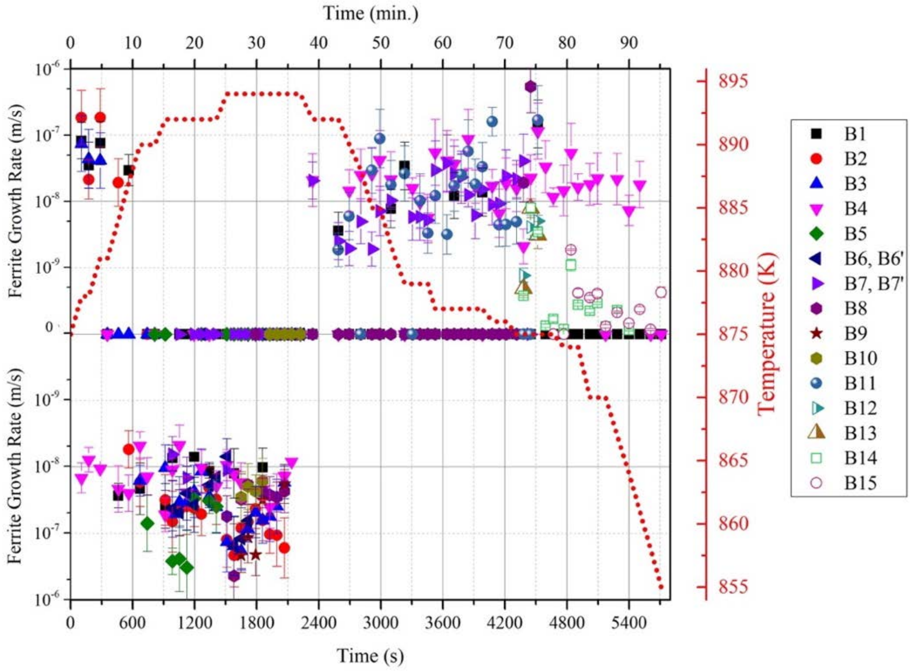

Fig. 6.7- Measured velocities of different boundaries and applied temperature versus time.

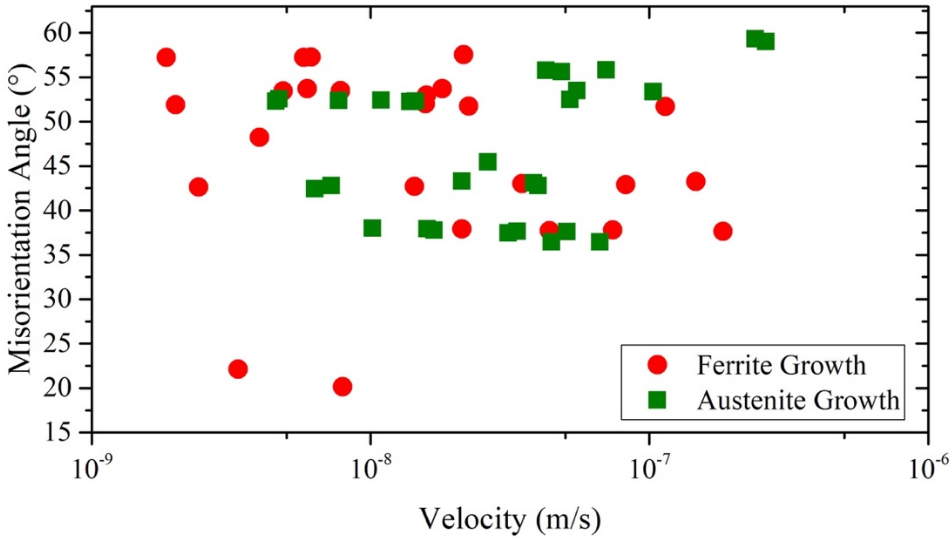

Fig. 6.8- Misorientation angle of interphase boundaries vs their migration velocity for growth of α and γ.

6.4.8 Post analysis of the surface

Given the long exposure time of the sample to the high intercritical annealing temperatures before and during the in-situ experiments in combination with the modest vacuum conditions, after the in-situ experiment, a cross-section of the sample perpendicular to the surface analysed in EBSD was made to check for anomalies due to surface decarburization, anomalous grain growth etc. Fig. 6.9 shows an EBSD map of the cross section of the specimen at room temperature subsequent to the in-situ HT observations. As observed, the important microstructural features at the free surface, i.e. the grain size and morphology of the grains are similar to those well below the sample surface studied, which suggests that the observations on the free surface are more or less representative for those in the bulk. While the bias is not very strong, the cross-sectional cut suggests that a slightly higher than expected number of grain boundaries intersects the original observation surface perpendicularly. This would imply that, certainly at later stages of the experiment, the EBSD observations are not too strongly affected by moving interphases intersecting the plane of observation at a shallow angle.

6.5 Phase Field simulation assisted interpretation of the experimental results

As described in the previous section, the highly diverse local behavior observed at different interface segments can be linked to different mechanisms including compositional variations across the interface, the coherency of the interfaces as well as topology and geometry effect caused by the 2D surface cut.

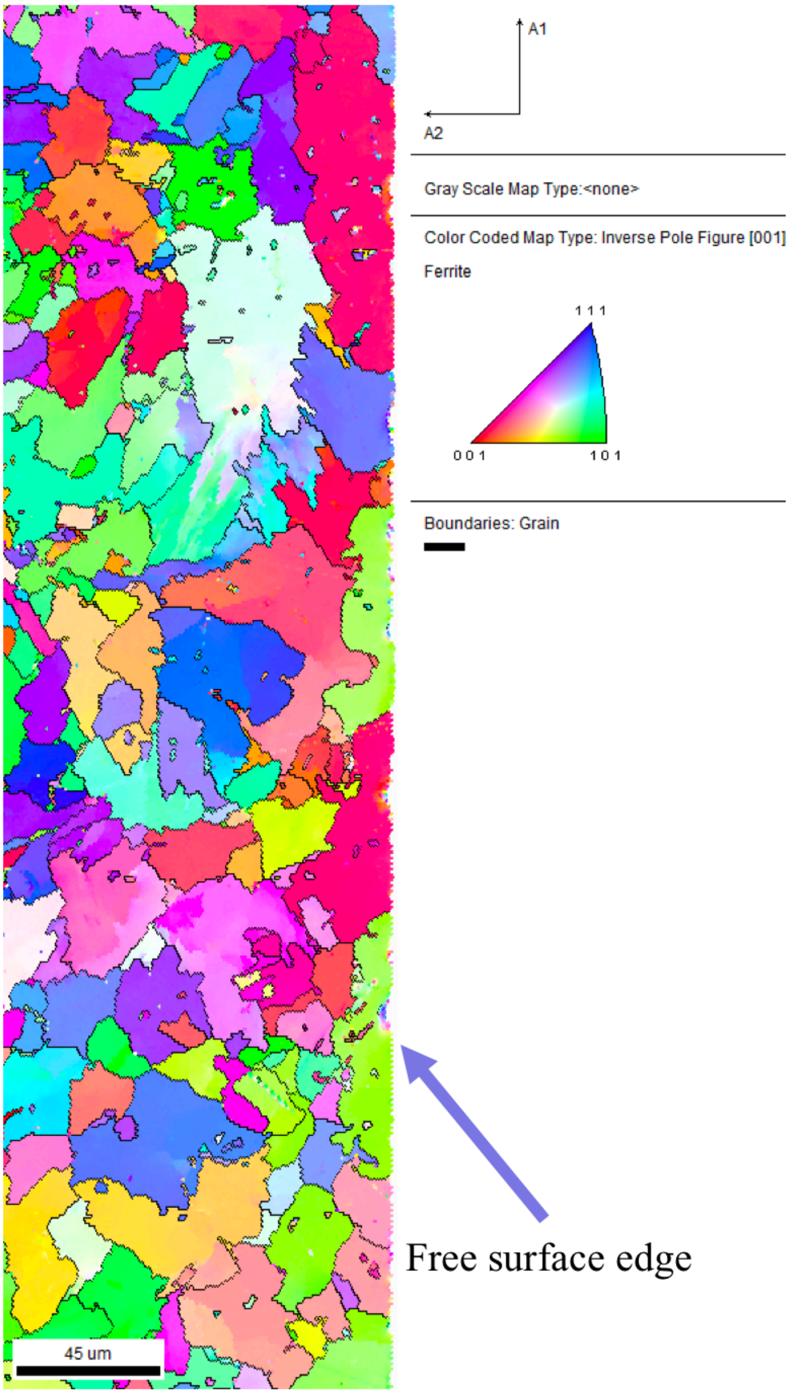

Fig. 6.9- The EBSD map of the cross section of the specimen after the HT in-situ stage.

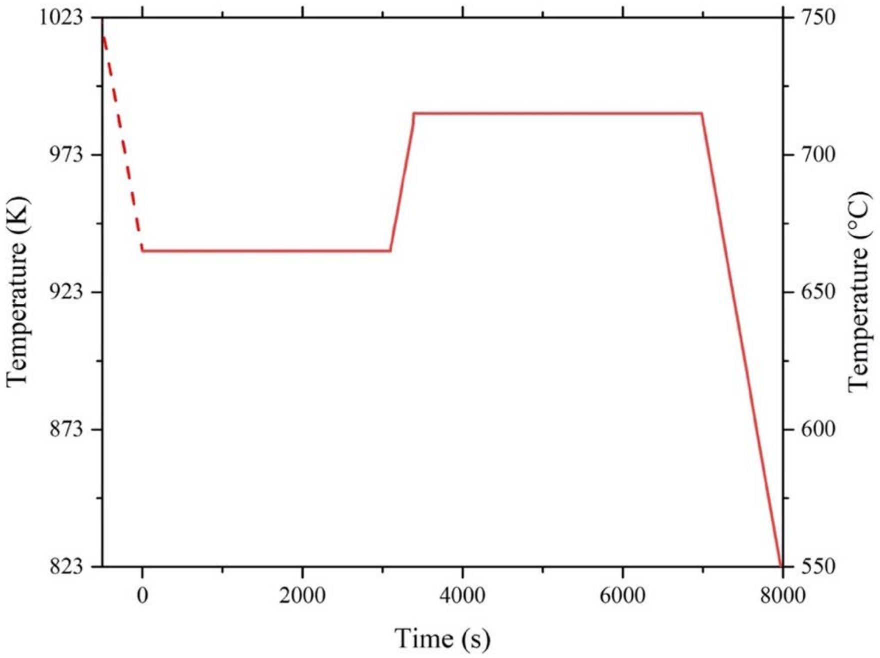

Fig. 6.10. The applied thermal route in the 3D phase Field simulation of CPPT treatment.

The thermal route imposed in the phase field simulations is a typical type H route (shown in Fig. 6.10) and starts with cooling an austenitic microstructure from T0 (1023 K), isothermal holding of the α/γ microstructure at T1 (938 K) for 20 min, heating to T2 (988 K) and isothermal holding at this temperature for 20 min and a final cooling stage with a rate of 0.17 K/s (10 K/min). In order to avoid effect of nucleation on the assessment, the analysis of the simulation results starts from the isothermal holding at T1, and the first cooling stage is shown in dotted line in Fig. 6.10. It is important to note that since the aim of using 3D PF simulation is to qualitatively investigate the effect of 2D cut surface on the observation of behavior of interfaces during partial γ→α and α→γ phase transformations, no quantitative consistency between the numeric details of the simulation condition and results of the experimental observations are targeted. In this regard, for achieving desired partial γ→α and α→γ phase transformation during the 3D PF simulations, the absolute temperatures of T1 and T2 were chosen to be different from those in the actual experiment.

In the next subsections, the characteristic behavior of the system and the displacement behaviours of some selected interfaces under CPPT as calculated by 3D phase field simulations are investigated.

6.5.1 Retraceable back and forth migration of the interfaces

The 3D video of migration of interfaces during the simulation is presented in **Appendix B**. Fig. 6.11 shows some selected 3D images of the microstructure during the simulation. These images alongside the supplementary video in **Appendix B** confirm retraceable back and forth migration of the interfaces observed in 3D PF simulation of the partial γ→α and α→γ phase transformations. This retractability phenomenon has not been observed in-situ EBSD experiments reported here, but earlier scanning laser confocal microscopy studies on a leaner steel [19] clearly suggested that some of interface pathways are retractable.

6.5.2 Local features in displacement of interface segments

In the EBSD data, different α/γ interface segments were observed to show different local displacement behavior upon temperature variations. Such behavior can also be observed in the PF simulation results when following local migration of interface segments at different 2D cuts. Fig. 6.12 a-c and Fig. 6.12 d-f show 2D migration behavior of two groups of selected interface segments at two different orthogonal cuts of the same 3D microstructure at different times during the conditions of overall α growth. While all the α/γ interface segments existing in the given orthogonal 2D cut no. 1 (Fig. 6.12 a-c) are observed to follow overall growth of α grains, only a few interface segments in cut no. 2 (Fig. 6.12 d-f) of the same microstructure migrate toward α growth and the rest of existing interfaces are stagnant and do not react to the change in the temperature regime. This shows that observation of the stagnation of the present interfaces in the 2D cut of a 3D microstructure can be due to by the inclination of the plane of observation, rather than to special local crystallographic or compositional conditions. The videos of these two figures are enclosed in **Appendix C** for further review.

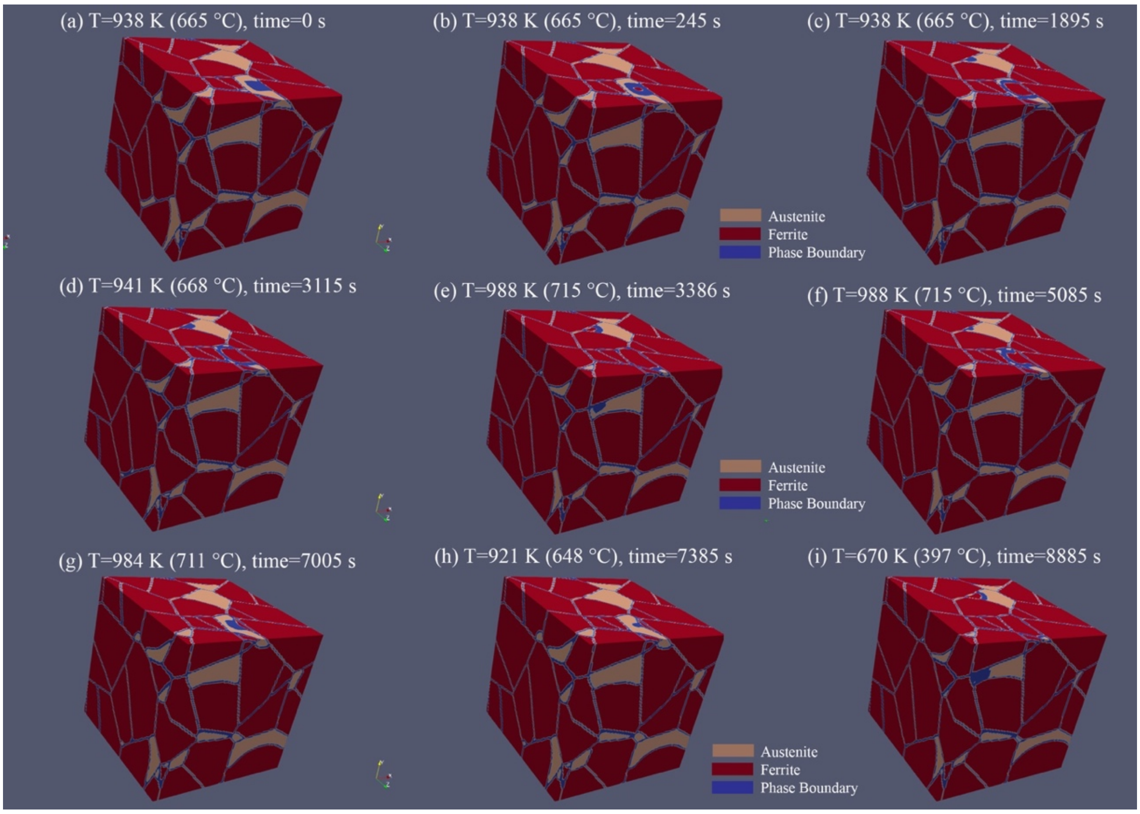

Fig. 6.11. Overall behavior of 3D material under simulation of CPPT treatment at different time/temperatures.

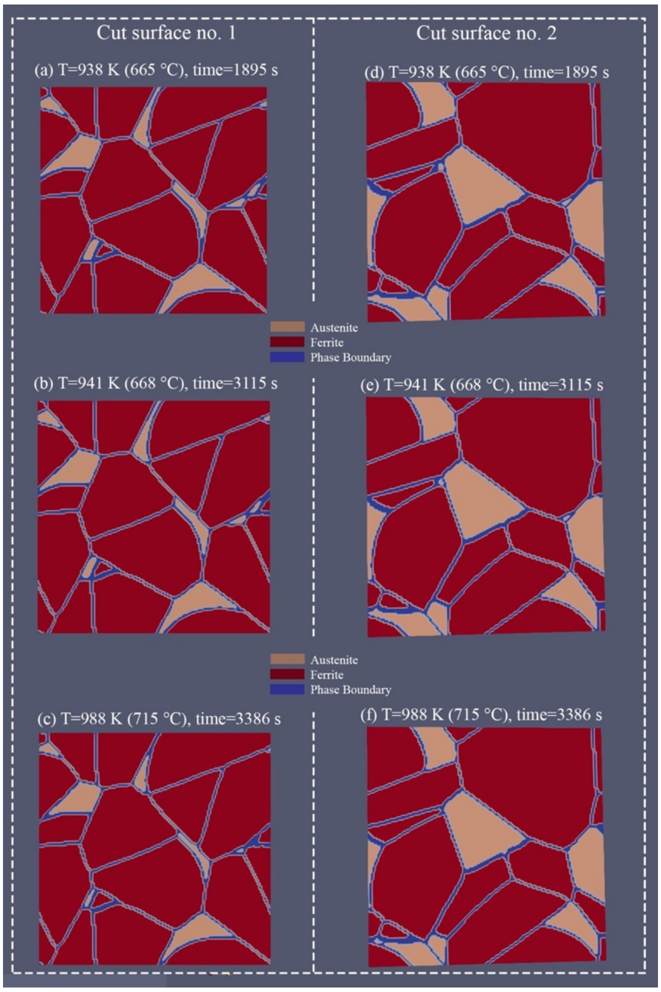

Fig. 6.12. Selected time/temperatures of two different 2D orthogonal cuts of the 3D simulation microstructure showing a), b) AND C) all migrating interfaces by change in temperature regime, and d), e) and f) migration of a few interfaces and stagnation in the other existing interfaces. The videos of these two figure groups are found in **Appendix C**.

6.5.3 Topology effect

The effect of 3D topology of the grains on the 2D observable local features of the transformation interfaces can lead to at least three different incorrect interpretations. First, Fig. 6.13 shows an example of how a 3D curved interface can appear as a semi-straight phase boundary segment in a 2D cut. The interface A in Fig. 6.13a appears as a straight segment in the given 2D surface cut. However, the same interface appears to be a 3D curved plane below the 2D cut surface in Fig. 6.13b. This effect resembles the situation of the B2 and B3 interphase boundary segments that were curved around two surface defects, while the other interface segments identified in the same in-situ EBSD maps were perceived as approximately straight lines.

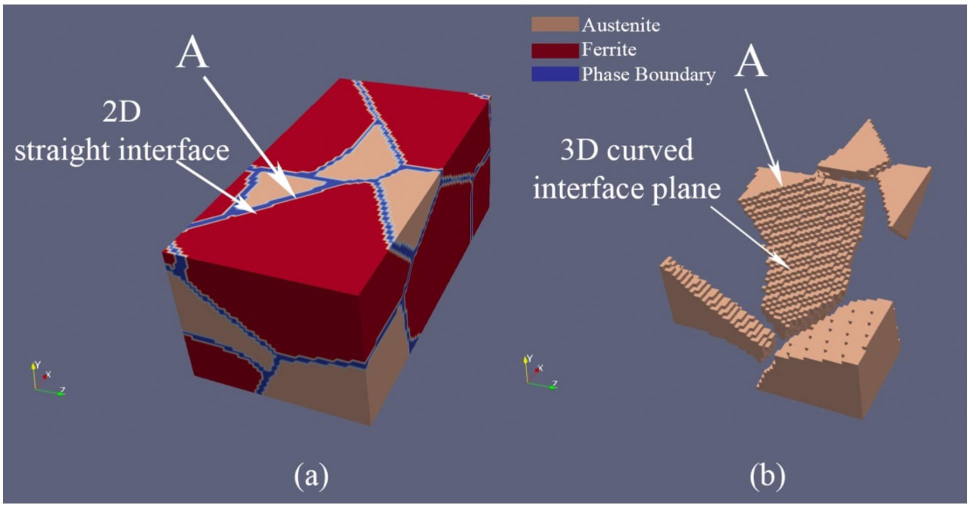

Fig. 6.13-Effect of topology of the grains on the apparent 2D curvature of the interfaces. a) an interface observed straight in 2D cut, b) the same interface area observed as a 3D curved plane when removing the ferrite phase.

The second case of misleading 2D information concerns the 2D recorded interface velocity. In the example shown in Fig. 6.14 a-b, the interface A as observed in the 2D cut surface appears to be immobile during the whole partial phase transformation cycle. However, when viewing the same grain from an orthogonal cut to that used to construct Fig. 6.14 a-b, displacements of the interface B on the other side the grain beneath the surface are clearly observable (Fig. 6.14 c-d). This confirms that the immobility of some interfaces at 2D does not necessarily mean stagnation in all of the interfaces in a particular 3D grain. This example is relevant for the correct interpretation of Fig. 6.4, where individual interfaces are observed not to necessarily follow the overall behavior of the material which is plotted in Fig. 6.3.

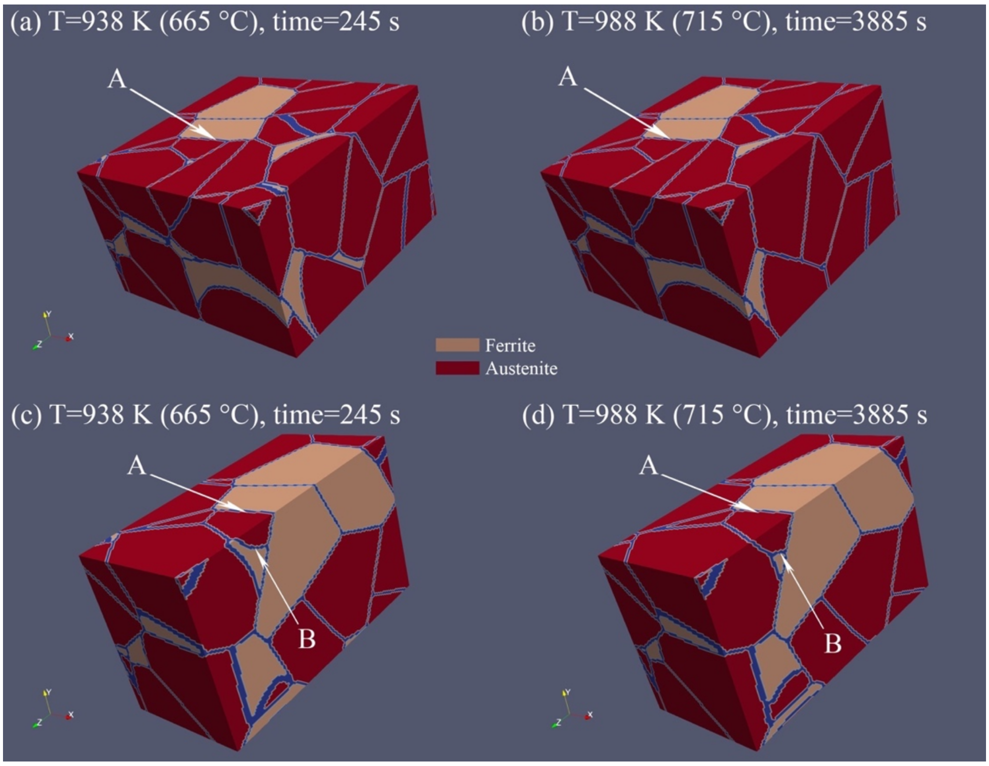

Fig. 6.14. Selected microstructures showing the effect of 3D topology of grains on apparent stagnation of interfaces at different time/temperatures.

Finally, the angle between the 2D surface cut and the 3D interface plan can also have effect on the apparent migration rate of the interface in 2D. Fig. 6.15 a-c show three 2D surface cuts of interface C (as indicated in the images) at different angles of Φ = 0, $\pi/4$ and $\pi/2$ corresponding to the interface plan in 3D, respectively. The average migration rate of the interface C during $\gamma\rightarrow\alpha$ phase transformation during the first isothermal holding stage measured at each of these planes is shown in Fig. 6.15d. The apparent velocities as measured in 2D are clearly different, while the actual velocity measured perpendicular to the interface is the same. This qualitative observation can provide a first order explanation for the large scatter observed in the experimentally measured growth rates of different interfaces via the EBSD maps shown in Fig. 6.7 and Fig. 6.8. Given the fact that at the end of the thermal cycle a large fraction of the grain boundaries appears to be more or less perpendicular to the plane of observation (Fig. 6.9), the effect of inclination angle may play a smaller role in the physical experiment than in the computer simulation.

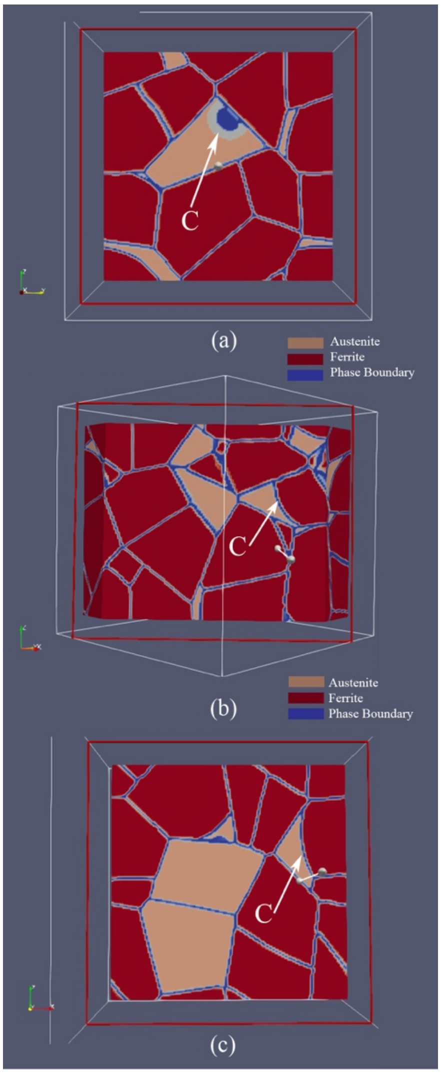
C
(a)
Austenite
Ferrite
Phase Boundary
C
(b)
Austenite
Ferrite
Phase Boundary
C
(c)

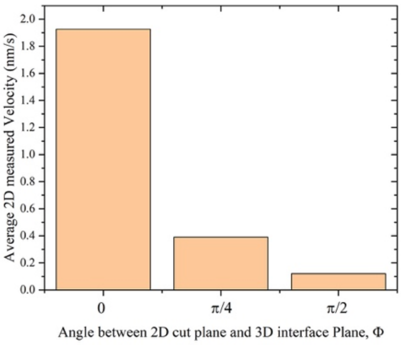
Average 2D measured Velocity (nm/s)
2.0
1.8
1.6
1.4
1.2
1.0
0.8
0.6
0.4
0.2
0.0
0
π/4
π/2
Angle between 2D cut plane and 3D interface Plane, Φ

(d)

Fig. 6.15. The 2D cut planes showing interface C at different angles of a) Φ = 0, b) Φ = π/4 and c) Φ = π/2. d) the average measured growth rate of interface C versus Φ.

6.5.4 Triple junction effect

Analysing the in-situ motion of the α/γ interface segments recorded via EBSD and reported in section 4, at least one case of interphase migration to be controlled by the balance of interfacial tensions at triple junctions was observed. This situation is schematically illustrated in Fig. 6.16a. However, no similar effect of the triple junctions was spotted in the phase field simulation and the interface segments around triple junctions were observed to preserve their configuration in the back and forth migrations during partial γ→α and α→γ phase transformations, as schematically shown in Fig. 6.16b. This difference between experimental observations and simulation results can arise from neglecting interfacial tensions around triple junctions in the simulations. As suggested in [65], inclusion of this effect in future phase field models could improve their accuracy in predicting microstructure evolution.

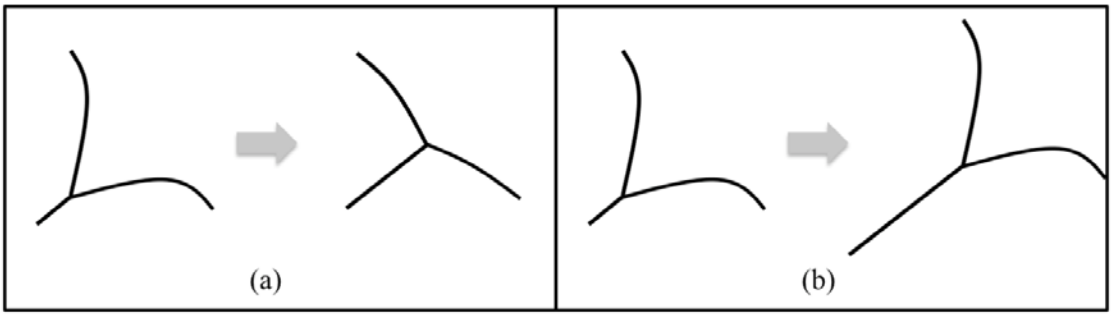

Fig. 6.16. a) Schematic of experimentally observed configuration of interfaces affected by triple junction pinning effect, b) schematic of configuration of interfaces observed in the simulation results.

6.6 Summary and Conclusions

In this study, in-situ high-temperature EBSD mapping is coupled with 3D phase field simulation to directly observe and analyse the migration of the α/γ interfaces during the cyclic partial phase transformations in a carbon-poor medium manganese steel. The experimentally observed phenomena are qualitatively compared to the 3D phase field simulations to examine the effect of the surface cut on 2D observation of 3D phase transformation phenomenon and the following conclusions has been achieved:

1. Individual interfaces as observed via in-situ EBSD do not necessarily follow the overall response of the material to temperature variations.

2. The behavioural features of different interfaces can be qualitatively explained bearing in mind local conditions at the interface, i.e. orientation relationship, topology of grains, geometrical configuration of the interfaces and the local concentration of alloying elements around the interface.

3. Motion of the coherent interfaces versus temperature variation was observed to be slower than that observed for incoherent interfaces.

4. No relationship between coherency of the interface and the likelihood of that interface showing immobility during the stagnant stage of the thermal cycle was observed.

5. No real difference was observed between average velocities of interfaces during partial γ→α and α→γ phase transformations. In addition, a relation between the misorientation angle and the interface velocity could not be established.

6. The scattered behavior as well as velocities of different interfaces versus temperature variations recorded via the in-situ EBSD maps are found to be comparatively explainable by the effect of 2D observation cut surface of the 3D phase transformation phenomena in the PF simulations, too.

7. The shape of α and γ grains as observed during the EBSD mapping changed during partial phase transformations. However, in the PF simulation the traceable back and forth migration of interphase boundaries led to grain shape preservation during the imposed CPPT treatment.

6.7 References

[1] G. Kostorz, ed., Phase Transformations in Materials, Wiley-VCH Verlag GmbH & Co. KGaA, Weinheim, FRG, 2001. doi:10.1002/352760264X.

[2] V. Raghavan, M. Cohen, Solid-State Phase Transformations, in: Chang. State, Springer US, Boston, MA, 1975: pp. 67–127. doi:10.1007/978-1-4757-1120-2_2.

[3] G. Gottstein, Solid State Phase Transformations, in: Phys. Found. Mater. Sci., Springer Berlin Heidelberg, Berlin, Heidelberg, 2004: pp. 389–422. doi:10.1007/978-3-662-09291-0_10.

[4] J.W. (John W. Christian, The theory of transformations in metals and alloys, Pergamon, 2002.

[5] G. Purdy, J. Ågren, A. Borgenstam, Y. Bréchet, M. Enomoto, T. Furuhara, E. Gamsjager, M. Gouné, M. Hillert, C. Hutchinson, M. Militzer, H. Zurob, ALEMI: A Ten-Year History of Discussions of Alloying-Element Interactions with Migrating Interfaces, Metall. Mater. Trans. A. 42 (2011) 3703–3718. doi:10.1007/s11661-011-0766-0.

[6] M. Ashby, Mapping the fracture properties of engineering materials, Philos. Mag. 93 (2013) 3878–3892. doi:10.1080/14786435.2013.794983.

[7] G.R. Purdy, The dynamics of transformation interfaces in steels—I. The ferrite-austenite interface in Fe-C-Mo alloys, Acta Metall. 26 (1978) 477–486. doi:10.1016/0001-6160(78)90173-6.

[8] G.R. Purdy, The dynamics of transformation interfaces in steels—II. Transformations in FE-C-MO alloys at intermediate temperatures, Acta Metall. 26 (1978) 487–498. doi:10.1016/0001-6160(78)90174-8.

[9] M. Gouné, F. Danoix, J. Ågren, Y. Bréchet, C.R. Hutchinson, M. Militzer, G. Purdy, S. van der Zwaag, H. Zurob, Overview of the current issues in austenite to ferrite transformation and the role of migrating interfaces therein for low alloyed steels, Mater. Sci. Eng. R Reports. 92 (2015) 1–38. doi:10.1016/j.mser.2015.03.001.

[10] J. Svoboda, E. Gamsjäger, F.D. Fischer, Y. Liu, E. Kozeschnik, Diffusion processes in a migrating interface: The thick-interface model, Acta Mater. 59 (2011) 4775–4786. doi:10.1016/J.ACTAMAT.2011.04.020.

[11] E. Gamsjäger, M. Rettenmayr, The kinetics of diffusive phase transformations in the light of trans-interface diffusion, Philos. Mag. 95 (2015) 2851–2865. doi:10.1080/14786435.2015.1078514.

[12] M. Militzer, J.J. Hoyt, N. Provatas, J. Rottler, C.W. Sinclair, H.S. Zurob, Multiscale Modeling of Phase Transformations in Steels, JOM. 66 (2014) 740–746. doi:10.1007/s11837-014-0919-x.

[13] R.C. Ecob, B. Ralph, A model of the equilibrium structure of F.C.C./B.C.C. interfaces, Acta Metall. 29 (1981) 1037–1046. doi:10.1016/0001-6160(81)90055-9.

[14] V.T. Witusiewicz, U. Hecht, S. Rex, M. Apel, In situ observation of microstructure evolution in low-melting Bi–In–Sn alloys by light microscopy, Acta Mater. 53 (2005) 3663–3669. doi:10.1016/J.ACTAMAT.2005.04.015.

[15] T. Watanabe, K. Obara, S. Tsurekawa, In-Situ Observations on Interphase Boundary Migration and Grain Growth during α/γ Phase Transformation in Iron Alloys, Mater. Sci. Forum. 467–470 (2004) 819–824. doi:10.4028/www.scientific.net/MSF.467-470.819.

[16] V.T. Witusiewicz, U. Hecht, S. Rex, In-situ observation of eutectic growth in Al-based alloys by light microscopy, J. Cryst. Growth. 372 (2013) 57–64. doi:10.1016/J.JCRYSGRO.2013.02.033.

[17] D. Phelan, N. Stanford, R. Dippenaar, In situ observations of Widmanstätten ferrite formation in a low-carbon steel, Mater. Sci. Eng. A. 407 (2005) 127–134. doi:10.1016/J.MSEA.2005.07.015.

[18] L. Cheng, K.M. Wu, X.L. Wan, R. Wei, In-situ observation on the growth of Widmanstätten sideplates in an Fe–C–Mn steel, Mater. Charact. 87 (2014) 86–94. https://www.sciencedirect.com/science/article/pii/S104458031300346X (accessed June 30, 2016).

[19] H. Chen, E. Gamsjäger, S. Schider, H. Khanbareh, S. van der Zwaag, In situ observation of austenite–ferrite interface migration in a lean Mn steel during cyclic partial phase transformations, Acta Mater. 61 (2013) 2414–2424. doi:10.1016/j.actamat.2013.01.013.

[20] S. Sainis, H. Farahani, E. Gamsjäger, S. van der Zwaag, An In-Situ LSCM Study on Bainite Formation in a Fe-0.2C-1.5Mn-2.0Cr Alloy, Metals (Basel). 8 (2018) 498. doi:10.3390/met8070498.

[21] G.G.E. Seward, D.J. Prior, J. Wheeler, S. Celotto, D.J.M. Halliday, R.S. Paden, M.R. Tye, High-temperature electron backscatter diffraction and scanning electron microscopy imaging techniques: In-situ investigations of dynamic processes, Scanning. 24 (2006) 232–240. doi:10.1002/sca.4950240503.

[22] S. van der Zwaag, E. Anselmino, A. Miroux, D.J. Prior, In-Situ SEM Observations of Moving Interfaces during Recrystallisation, Mater. Sci. Forum. 519–521 (2006) 1341–1348. doi:10.4028/www.scientific.net/MSF.519-521.1341.

[23] T. Fukino, S. Tsurekawa, In-Situ SEM/EBSD Observation of α/γ Phase Transformation in Fe-Ni Alloy, Mater. Trans. 49 (2008) 2770–2775. doi:10.2320/matertrans.MAW200824.

[24] T. Fukino, S. Tsurekawa, Y. Morizono, In-Situ Scanning Electron Microscopy/Electron Backscattered Diffraction Observation of Microstructural Evolution during α → γ Phase Transformation in Deformed Fe-Ni Alloy, Metall. Mater. Trans. A. 42 (2011) 587–593. doi:10.1007/s11661-010-0285-4.

[25] M. Enomoto, X.L. Wan, In Situ Observation of Austenite Growth During Continuous Heating in Very-Low-Carbon Fe-Mn and Ni Alloys, Metall. Mater. Trans. A. 48 (2017) 1572–1580. doi:10.1007/s11661-017-3961-9.

[26] M. Onink, F.D. Tichelaar, C.M. Brakman, E.J. Mittemeijer, S. van der Zwaag, An in situ hot stage transmission electron microscopy study of the decomposition of Fe-C austenites, J. Mater. Sci. 30 (1995) 6223–6234. doi:10.1007/BF00369670.

[27] J. Du, F. Mompiou, W.-Z. Zhang, In-situ TEM study of dislocation emission associated with austenite growth, Scr. Mater. 145 (2018) 62–66. doi:10.1016/J.SCRIPTAMAT.2017.10.014.

[28] F. Mompiou, J. Wu, W.-Z. Zhang, A Preliminary In-situ TEM Study of Martensite/Austenite Interface Migration in an Fe-20Ni-5.4Mn Alloy, Mater. Today Proc. 2 (2015) S651–S654. doi:10.1016/J.MATPR.2015.07.368.

[29] D. Guan, J. Nutter, J. Sharp, J. Gao, W. Mark Rainforth, Direct observation of precipitation along twin boundaries and dissolution in a magnesium alloy annealing at high temperature, Scr. Mater. 138 (2017) 39–43. doi:10.1016/J.SCRIPTAMAT.2017.05.015.

[30] J. Liu, C. Chen, Q. Feng, X. Fang, H. Wang, F. Liu, J. Lu, D. Raabe, Dislocation activities at the martensite phase transformation interface in metastable austenitic stainless steel: An in-situ TEM study, Mater. Sci. Eng. A. 703 (2017) 236–243. doi:10.1016/J.MSEA.2017.06.107.

[31] S.I. Wright, D.P. Field, M.M. Nowell, Impact of local texture on recrystallization and grain growth via in-situ EBSD, Mater. Sci. Forum. 495–497 (2005) 1121–1130. https://www.scopus.com/inward/record.uri?eid=2-s2.0-33751354041&partnerID=40&md5=ace510fd8eed6cb342affa8f82e474ef.

[32] G. Zijlstra, M.M.S.B. van Daalen, D.I. Di Vainchtein, V. Ocelík, Jt.J.T.M. De Hosson, Interphase boundary motion elucidated through in-situ high temperature electron

back-scatter diffraction, Mater. Des. 132 (2017) 138–147. https://ac.els-cdn.com/S0264127517306573/1-s2.0-S0264127517306573-main.pdf?_tid=815e5eaa-d03a-11e7-a556-00000aacb361&acdnat=1511433715_f40a5e9afeefcf6229b6111b79e59ead (accessed November 23, 2017).

[33] A.F. Gourgues-Lorenzon, Application of electron backscatter diffraction to the study of phase transformations, Int. Mater. Rev. 52 (2007) 65–128. doi:10.1179/174328007X160254.

[34] Y.B. Zhang, J.D. Budai, J.Z. Tischler, W. Liu, R. Xu, E.R. Homer, A. Godfrey, D. Juul Jensen, Boundary migration in a 3D deformed microstructure inside an opaque sample, Sci. Rep. 7 (2017) 4423. doi:10.1038/s41598-017-04087-9.

[35] A.-F. GOURGUES-LORENZON, Application of electron backscatter diffraction to the study of phase transformations: present and possible future, J. Microsc. 233 (2009) 460–473. doi:10.1111/j.1365-2818.2009.03130.x.

[36] H. Chen, S. van der Zwaag, An Overview of the Cyclic Partial Austenite-Ferrite Transformation Concept and Its Potential, Metall. Mater. Trans. A. (2016) 1–10. doi:10.1007/s11661-016-3826-7.

[37] J. Zhu, R. Ding, J. He, Z. Yang, C. Zhang, H. Chen, A cyclic austenite reversion treatment for stabilizing austenite in the medium manganese steels, Scr. Mater. 136 (2017) 6–10. doi:https://doi.org/10.1016/j.scriptamat.2017.03.038.

[38] H. Chen, S. van der Zwaag, Indirect evidence for the existence of the Mn partitioning spike during the austenite to ferrite transformation, Philos. Mag. Lett. 92 (2012). doi:10.1080/09500839.2011.634840.

[39] H. Chen, S. Van Der Zwaag, An experimental study of the stagnant stage in bainite phase transformations starting from austenite-bainite mixtures, in: TMP 2012 - 4th Int. Conf. Thermomechanical Process. Steels, Sheffield, UK, 10–12 September, 2012. https://www.scopus.com/record/display.uri?eid=2-s2.0-84896891374&origin=resultslist&sort=plf-f&src=s&sid=1946a7bc694969cb3dc997da6da11cd7&sot=autdocs&sdt=autdocs&sl=18&s=AU-ID%2857188745139%29&relpos=33&citeCnt=0&searchTerm= (accessed September 27, 2017).

[40] H. Chen, B. Appolaire, S. van der Zwaag, Application of cyclic partial phase transformations for identifying kinetic transitions during solid-state phase transformations: Experiments and modeling, Acta Mater. 59 (2011) 6751–6760. doi:10.1016/j.actamat.2011.07.033.

[41] H. Chen, Cyclic Partial Phase Transformations In Low Alloyed Steels: Modeling and Experiments, Delft University of Technology, 2013. doi:10.4233/uuid:66975e4a-4b2d-4933-95c5-f180b6605882.

[42] E. Inc., OIM AnalysisTM, (n.d.). http://www.edax.com/products/ebsd/oim-analysis.

[43] The Math Works Inc., MATLAB Image Processing Toolbox Realese 2015b; The Math Works Inc.: Natick, MA, USA, (2007). https://www.mathworks.com/products/image.html.

[44] MICRESS®, Software developed in ACCESS is an independent research center associated with the Technical University of Aachen, (n.d.). http://www.micress.de/.

[45] I. Steinbach, F. Pezzolla, A generalized field method for multiphase transformations using interface fields, Phys. D Nonlinear Phenom. 134 (1999) 385–393. doi:10.1016/S0167-2789(99)00129-3.

[46] U. Ayachit, The ParaView Guide: A Parallel Visualization Application, Kitware, Inc., USA, 2015.

[47] H. Chen, R. Kuziak, S. van der Zwaag, Experimental Evidence of the Effect of Alloying Additions on the Stagnant Stage Length During Cyclic Partial Phase Transformations, Metall. Mater. Trans. A. 44 (2013) 5617–5621. doi:10.1007/s11661-013-2040-0.

[48] H. Chen, S. van der Zwaag, Analysis of ferrite growth retardation induced by local Mn enrichment in austenite created by prior interface passages, Acta Mater. 61 (2013) 1338–1349. doi:10.1016/j.actamat.2012.11.011.

[49] M. Hillert, Nature of local equilibrium at the interface in the growth of ferrite from alloyed austenite, Scr. Mater. 46 (2002) 447–453. doi:10.1016/S1359-6462(01)01257-X.

[50] S.E.E. Offerman, Microstructures in 4D, Science (80-.). 305 (2004) 190–191. doi:10.1126/science.1100682.

[51] C. Bos, J. Sietsma, Application of the maximum driving force concept for solid-state partitioning phase transformations in multi-component systems, Acta Mater. 57 (2009) 136–144. doi:10.1016/J.ACTAMAT.2008.08.060.

[52] K. Verbeken, L. Barbé, D. Raabe, Evaluation of the Crystallographic Orientation Relationships between FCC and BCC Phases in TRIP Steels, ISIJ Int. 49 (2009) 1601–1609. doi:10.2355/isijinternational.49.1601.

[53] I. Lischewski, D.M. Kirch, A. Ziemons, G. Gottstein, Investigation of the $\alpha-\gamma-\alpha$ Phase Transformation in Steel: High-Temperature In Situ EBSD Measurements, Texture, Stress. Microstruct. 2008 (2008) 1–7. doi:10.1155/2008/294508.

[54] C. Wert, C. Zener, Interference of Growing Spherical Precipitate Particles, J. Appl. Phys. 21 (1950) 5–8. doi:10.1063/1.1699422.

[55] H. Chen, S. van der Zwaag, Modeling of soft impingement effect during solid-state partitioning phase transformations in binary alloys, J. Mater. Sci. 46 (2011) 1328–1336. doi:10.1007/s10853-010-4922-5.

[56] K. Fan, F. Liu, X.N. Liu, Y.X. Zhang, G.C. Yang, Y.H. Zhou, Modeling of isothermal solid-state precipitation using an analytical treatment of soft impingement, Acta Mater. 56 (2008) 4309–4318. doi:10.1016/J.ACTAMAT.2008.04.053.

[57] S.E. Offerman, N.H. van Dijk, J. Sietsma, E.M. Lauridsen, L. Margulies, S. Grigull, H.F. Poulsen, S. van der Zwaag, Solid-state phase transformations involving solute partitioning: modeling and measuring on the level of individual grains, Acta Mater. 52 (2004) 4757–4766. doi:10.1016/J.ACTAMAT.2004.06.030.

[58] G. Gottstein, L.S. Shvindlerman, Grain boundary junction engineering, Scr. Mater. 54 (2006) 1065–1070. doi:10.1016/J.SCRIPTAMAT.2005.11.057.

[59] P.-G. de Gennes, F. Brochard-Wyart, D. Quéré, Capillarity and Wetting Phenomena, Springer New York, New York, NY, 2004. doi:10.1007/978-0-387-21656-0.

[60] P. Clemm, J. Fisher, The influence of grain boundaries on the nucleation of secondary phases, Acta Metall. 3 (1955) 70–73. doi:10.1016/0001-6160(55)90014-6.

[61] S. Ratanaphan, D.L. Olmsted, V. V Bulatov, E.A. Holm, A.D. Rollett, G.S. Rohrer, Grain boundary energies in body-centered cubic metals, Acta Mater. 88 (2015) 346–354. doi:10.1016/j.actamat.2015.01.069.

[62] S. Hilgenfeldt, A.M. Kraynik, D.A. Reinelt, J.M. Sullivan, The structure of foam cells: Isotropic Plateau polyhedra, Europhys. Lett. 67 (2004) 484–490. doi:10.1209/epl/i2003-10295-7.

[63] G. Gottstein, V. Sursaeva, L.S. Shvindlerman, The Effect of Triple Junctions on Grain Boundary Motion and Grain Microstructure Evolution, Interface Sci. 7 (1999) 273–283. doi:10.1023/A:1008721426104.

[64] S.M. Yufatova, Y.G. Sindeyev, V.G. Gavrilyatchenko, E.G. Fesenko, Different kinetic types of phase transformation in lead titanate, Ferroelectrics. 26 (1980) 809–812. doi:10.1080/00150198008008177.

[65] E.A. Brener, G. Boussinot, C. Hüter, M. Fleck, D. Pilipenko, R. Spatschek, D.E. Temkin, Pattern formation during diffusional transformations in the presence of triple junctions and elastic effects, J. Phys. Condens. Matter. 21 (2009) 464106. doi:10.1088/0953-8984/21/46/464106.

Chapter 7 An in-situ LSCM study on the bainite formation

This Chapter is based on

- S. Sainis, H. Farahani, E. Gamsjäger, S. van der Zwaag, An in-situ LSCM study on bainite Formation in a Fe-0.2C-1.5Mn-2.0Cr Alloy, *Metals*, Volume 8, Issue 7, July 2018, Article number 498.

ABSTRACT

Direct microscopical observation of the isothermal bainite evolution in terms of nucleation events, the location of the nuclei as well their growth is very valuable for the refinement of models predicting the kinetics of bainite transformation. To this aim, the microstructural evolution in an Fe-0.2C-1.5Mn-2.0Cr alloy during isothermal bainite formation at temperatures between 723 K and 923 K is monitored in-situ using high temperature laser scanning confocal microscopy (LSCM). Both the nucleation and the growth kinetics of the bainitic plates are analysed quantitatively. Bainitic plates are observed to nucleate on three different types of locations in the grain: at austenitic grain boundaries, on newly formed bainite plates and at unspecific sites within the austenite grains. Grain boundary nucleation is observed to be the dominant nucleation mode at all transformation temperatures. The rate of nucleation is found to vary markedly between different austenite grains. The temperature dependence of the average bainite nucleation rate is in qualitative agreement with the classical nucleation theory. Analysis of plate growth reveals that also the lengthening rates of bainite plates differs strongly between different grains. However, the lengthening rates do not seem to be related to the type of nucleation site. Analysis of the temperature

dependence of the growth rate shows that the lengthening rates at high temperatures are in line with a diffusional model when a growth barrier of 400 J/mol is considered.

7.1 Introduction

The wish for better performing automobiles with improved fuel efficiency, low CO_2 emission, crashworthiness and rigidity has directed the automotive industry’s efforts towards the adoption of advanced high strength steels (AHSS) as the primary structural material. AHSS offer the opportunity to create cost effective and light-weight car body structures with improved crash worthiness [1–3]. The AHSS steels are compositionally relatively simple C-Mn based steels having rather different microstructures as a result of different complex multistep thermomechanical treatments. The first generation of AHSS (1st Gen AHSS) includes dual phase (DP), transformation induced plasticity (TRIP), complex-phase (CP) and martensitic (MART) steels with a high allotriomorphic ferrite fraction. The second generation of AHSS (2nd Gen AHSS) includes twinning induced plasticity (TWIP), Al-rich lightweight steels (L-IP®) and shear band strengthened steels (SIP) containing a mass fraction of Mn of about 20%. These 2nd Gen AHSS display significantly higher strength values compared to the 1st Gen AHSS. The third generation AHSS (3rd Gen AHSS) show even better strength-ductility combinations at lower costs [4–7]. Their attractive mechanical properties are due to the presence of a high volume fraction of retained austenite which is stabilized by increasing the Mn content [8–11]. The occurrence of high volume fractions of retained austenite in the microstructure is realised by specific thermal processing routes and fine tuning of the Mn concentration. A key feature of these multi-phase steels is their primarily bainitic microstructure containing retained austenite volume fractions between 10 and 30% [12] at overall Mn concentrations between 1.5 and 8 mass% [13–19]. The 3rd Gen AHSS family includes the so-called medium Mn steels, to which the steel to be researched in this publication belongs. Intercritical annealing treatments at isothermal bainite transformation temperatures form the basis for the desired multi-phase bainite-austenite microstructures. In view of its technological importance, significant research efforts have been made to tailor the amount, morphology and stability of retained austenite after cooling [20–24] in relation to the preceding bainite formation. Predicting the kinetics of the bainite transformation by means of numerical models is a goal not only of academic but also of significant industrial interest, since the austenite-bainite microstructure formed during intercritical annealing determines the mechanical properties of the steel.

The kinetics of bainite formation has been studied extensively for decades since the first observation of the microstructure by Davenport and Bain in 1930s [25,26]. Due to the wide temperature range in which such bainitic microstructures form, its transformation kinetics is a complex phenomenon consisting of coupled dissipative processes. It is thus a challenging task to describe and predict the transformation kinetics. Currently two schools of thought exist that provide different explanations for the physical mechanism through which bainite evolves and the topic has been under debate for many decades [27,28,37–44,29–36]. While it is not the purpose of this paper to enter into this controversy, the concepts of both models are considered to be relevant for the interpretation of our observations. The diffusional approach, first formulated by Aaronson [45] explains the formation of bainite as a ferrite ledge growth mechanism which involves reconstructive ferrite and cementite formation. The kinetics is governed by the movement of austenite-ferrite interface which depends on the interactions of constituent alloying elements in the iron lattice. The displacive school of thought, on the other hand, considers a diffusionless nucleation and growth of so called bainitic sub-units to be the crucial formation mode. Growth is assumed to occur by successive nucleation of new sub-units. The overall kinetics is thus controlled by nucleation events, since the growth of sub-units is a very fast process [46]. Both schools succeeded to model the overall transformation kinetics based on their own perception of the dominant bainite formation mechanism [46,47,56–59,48–55], without paying much attention to the actual microstructure evolution and its relation to the initial austenitic microstructure.

Given the importance of correctly modelling the austenite to bainitic ferrite transformation kinetics for designing suitable multiphase microstructures, in-situ methods are applied to observe evolution of microstructural features in real time. Conventional metallography is the classical method to investigate bainite formation, however, this technique can only be used to observe post mortem microstructures. While in-situ optical observations of metallurgical transformation reactions using conventional microscopy were already made in 1952 [60], in recent years in-situ high temperature laser scanning confocal microscopy (HT-LSCM) has been used preferentially [61–67] because of its high sensitivity to the out-of-plane distortions at moving interfaces.

Xu et al. [65] quantitatively analysed the austenite transformation rates by combining LSCM and dilatometry. *Kolmskog* et al. [62] also applied LSCM to directly observe isothermal bainite formation below the martensite start temperature. Dynamic LSCM imaging studies of the bainite evolution revealed a continuous lengthening of bainitic ferrite plates. *Wan* et al. [66] showed that the lengthening rate of the plates was constant with time irrespective of the nucleation location. *Hu* et al. [67] investigated the plate growth rates at low transformation temperatures in a super bainitic steel Fe-0.4C-2.81Mn-2.0Si (all in mass%) and also observed a constant lengthening rate. However, in contrast to the results presented in [64], they reported a dependency of the growth rates on the location of the nucleation site. Their study supported the diffusional growth hypothesis by semi-quantitatively validating their observations with the *Zener-Hillert* [68,69] and the *Trivedi* [70] model. *Tian* et al. [71] studied the same steel but under different isothermal temperatures and reported a decrease in lengthening rate with decreasing temperature.

However, the past studies have focussed only on quantifying the growth rate of bainitic plates but did not pay attention to the variation of the growth rate. Some studies reported a variance in growth rate nucleating at different locations in the microstructure [67,71]. However, the nucleation aspect in the evolution of bainitic ferrite has rarely been measured and analysed quantitatively. In this paper, in-situ LSCM at a framing rate of 15 Hz is applied to directly observe the bainite phase transformation process in a typical Fe-0.2C-1.5Mn-2.0Cr (all in mass%) alloy. The dynamics of the bainite formation process, within the spatial and temporal resolution limits of LSCM, is quantified using a combination of manual and computer aided image analysis techniques. This study reports on the bainitic nucleation and growth observed at different isothermal temperatures 723 K, 773 K, 823 K and 923 K (450 °C, 500 °C, 550 °C and 650 °C). Nucleation and growth of bainitic plates has been analysed quantitatively by distinguishing different nucleation sites and by comparing the bainite formation behaviour in different grains. This latter aspect has not been addressed in previous bainite formation studies reported in the literature.

7.2 Experimental procedure and microstructure measurement

The investigated material is an Fe-C-Mn-Cr alloy with the chemical composition listed in Table 7.1. Cold rolled cylindrical samples with a radius of 4 mm and a height of 5 mm were used in which the highly polished surface was perpendicular to the rolling direction.

In situ optical observation and recording of growing bainitic ferrite plates were done using a *Yonekura VL* 2000 DX HT-LSCM coupled with an *SVF 17 SP* mirror furnace. Details of the experimental set-up can be found in *Chen* et al. [72]. Images of a region in the centre of the sample (i.e. the thermally most homogeneous part of the sample) were video-recorded with a scanning frequency of 15Hz. The temperature was recorded by a thermocouple. The applied combinations of austenitising temperature and isothermal holding temperatures are listed in Table 7.1. The samples were typically austenitized for about 250 s and subsequently cooled from the austenitising temperature to the bainitic holding temperature with a recorded cooling rate of 10-20 K/s.

Table 7.1- Testing matrix containing the details of alloy composition and thermal treatments applied in situ optical recording.

Steel composition (mass%)			Austenitising Temperature	Isothermal treatment Temperature
C	Mn	Cr		
0.2	1.5	2.0	1223 K (950 °C)	723 K (450 °C)
			1233 K (960 °C)	773 K (500 °C)
			1233 K (960 °C)	823 K (550 °C)
			1373 K (1100 °C)	923 K (650 °C)

The time-temperature dependent microstructural changes observed by HT-LSCM measurements were analysed after selecting representative large austenite grains showing the formation of multiple bainite plates. The austenite grains could be distinguished because of light thermal grooving at their grain boundaries. MATLAB's image processing toolbox [73] (*imtool*) was used to isolate and quantify the bainite microstructure evolution from the recorded images, such as that shown in Fig. 7.1. Each pixel size corresponds to ~0.23 μm, which sets the resolution of the analysis. Although the real nucleus size must be much smaller than the minimal detectable feature dimension, the detection of the earliest features of a particular bainite plate at ~0.6μm recorded at this resolution is taken as the nucleation event. For analysing plate growth, temporal measurements of individual plates were performed to obtain plate growth rates using MATLAB's imtool. The lengthening rate of individual bainitic plates was determined by linear regression yielding typical high correlation coefficients ($R^2 > 0.95$) indicative of a constant growth rate within experimental accuracy. The plate growth rate (v) is then slope of the fitted line. In some cases, where overall linear fitting would not yield a good fit, linear fitting was done in sub-growth stages to get a good fit. For plates with distinct stages of growth, overall plate growth rate was calculated by averaging in the following way:

$$v = \sum_{i=1}^{n} \frac{v_i \Delta t_i}{\Delta t_i} \tag{7.1}$$

where v_i and Δt_i are the velocity and time period of stage *i*, respectively.

Complementary to HT-LSCM experiments, the bainite formation in this steel was also studied using a *Bähr DIL 805A/D* dilatometer. Although results of these two experimental approaches were qualitatively comparable, due to significant differences in the temperatures at which comparable macroscopic bainite formation rates were obtained, only the results of HT LSCM are presented. As discussed in [74], these differences can be caused by an uncertainty in the exact sample temperature in the LSCM and/or possible surface decarburization of the sample in the LSCM set-up.

7.3 Results

7.3.1 Nucleation

In this section quantitative results of the in-situ nucleation events of bainitic plates during austenite to bainite transformation as observed with HT-LSCM are presented. The bainite plates were observed to nucleate and grow during cooling as well as during the subsequent isothermal holding stage. Nucleation was found to take place a) at the grain boundary, b) in the grain interior at the side of a recently formed bainite plate and c) in the grain interior at a location not showing any specific feature. Characteristic examples are shown in Fig. 7.2. The occurrence of bainite formation on these specific locations has also been reported previously [67].

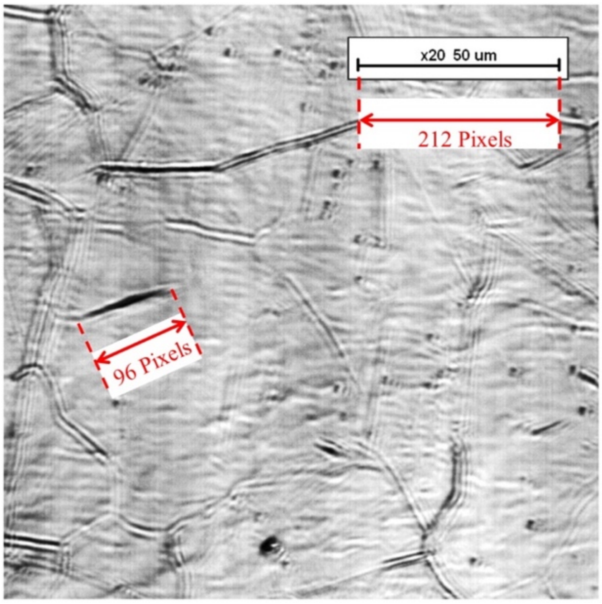

Fig. 7.1- Demonstration of MATLAB's image viewing toolbox imtool for estimating the μm equivalent of pixel measurement according to the scale bar and measuring length of ferrite plate (unit of measurement in pixels).

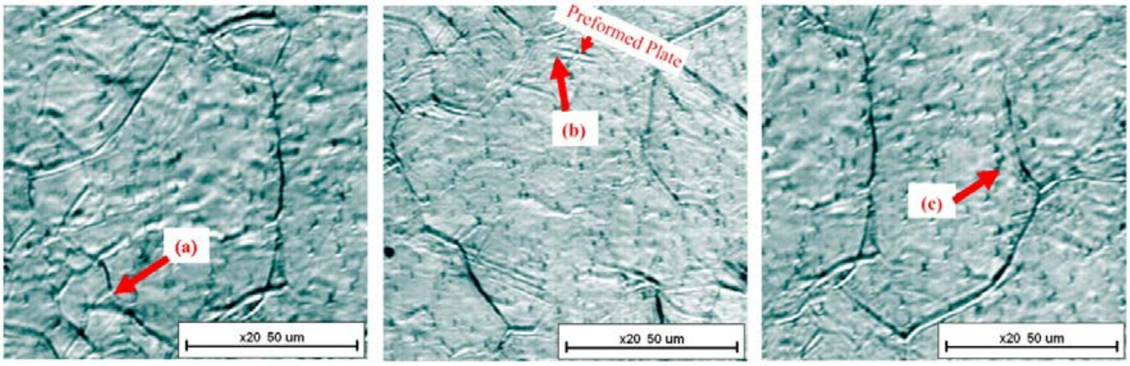

Fig. 7.2- Bainite plate nucleation observed on three distinct locations: (a) on grain boundaries (GB), (b) on preformed bainite (OP) and (c) within the grain (IN).

In our data analysis each nucleation event is characterized by its type of the nucleation site, the moment of first observation (the apparent nucleation time), the actual temperature and finally by the (numbered) grain in which nucleation occurs. The quantitative data concerning the nucleation events as observed in four separate samples of the same steel transformed at different isothermal holding treatments at 723 K, 773 K, 823 K and 923 K (450 °C, 500 °C, 550 °C and 650 °C) are presented in Fig. 7.3, Fig. 7.4, Fig. 7.5 and Fig. 7.6, respectively. The austenitising temperatures used for each transformation temperature are listed in Table 7.1. For further view, the video of isothermal bainite formation at T= 723 K (450 °C) can be found in **Appendix D**. The austenisation time was kept constant at 250 s. The bainite formation relevant part of the time- temperature profile is presented in Fig. 7.3, Fig. 7.4, Fig. 7.5 and Fig. 7.6. The time marked ‘zero’ in each graph refers to the time at which the isothermal temperature is reached first. Different symbols have been used to indicate the three distinct types of nucleation sites:

i. nucleation on grain boundary (●)

ii. nucleation on the surface of an existing bainite plate (■)

iii. nucleation occurring inside the austenitic grain (▲).

No bainite nucleation was observed prior to the shortest indicated time and no further bainite formation was observed after the longest indicated time in each figure.

Bainitic ferrite plates were observed to nucleate predominantly on grain boundaries during the onset of the transformation. As the transformation proceeds, new plates are also observed to nucleate on previously formed ones. It was observed that some new plates emerged from within the matrix, i.e. without any microstructural ‘reason’ in a few cases. They have been indexed as 'internal'. All of these so-called ‘internal nucleation events’ took place near an existing plate or near a grain boundary. It is thus very likely that such a plate may have nucleated at grain boundaries or plate surfaces in the bulk of the material and what we observe is the plate emerging from interior on the surface.

The majority of nucleation events were observed to take place during cooling to the holding temperature or at early stages of the isothermal holding at T=723 K (450 °C) (Fig. 7.3), T=773 K (500 °C) (Fig. 7.4) and T=823 K (550 °C) (Fig. 7.5), respectively. No new nucleation was observed during the later stages of the isothermal holding stage. In contrast, nucleation occurred only during the whole isothermal holding stage for holding at T=973 K (650 °C) (Fig. 7.6).

Although all the imaged grains in a particular sample by default were exposed to exactly the same thermal history, both the total number of bainite nucleation events per grain and the time window during which nucleation took place varied significantly between grains. For example, for the isothermal experiment at T=723 K (450 °C), (Fig. 7.3) 13 bainitic plates are formed within about 20 s in grain 4, but only 3 nucleation events in 22 s were recorded for grain 1. For the experiment at T=773 K (500 °C) (Fig. 7.4) 10 plates formed within 35s in grain 1 while only 1 plate formed in grain 8; For the experiment at T=923 K (550 °C) (Fig. 7.5) 8 plates nucleated over 45 s in grain 2, while only 2 plates nucleated over 20 s in grain 4 and 6 plates nucleated over 85 s in grain 3. For the experiment at T=1023 K (650 °C) (Fig. 7.6) 4 plates nucleated over 75 s in grain 1 while only 2 nucleated in 13 s in grain 2.

Both the total number of bainitic plates that nucleated in each experiment and the time window Δt of total nucleation events, i.e. the time difference between first and last nucleation event were found to depend on the degree of undercooling (ΔT). For the experiment at T=723 K (450 °C), nucleation of new bainitic plates stopped 28 s after formation of the first bainitic plate, while at T=923 K (650 °C) nucleation continued for about 75 s. In addition, the total number of nuclei formed in the different grains was higher at lower transformation temperatures, i.e. bainite formation is more rapid at higher degrees of undercooling.

7.3.2 Growth

The growth of individual bainitic plates was investigated through measuring the plate lengths from images separated by 1 s in time (i.e. only a fraction of all the images collected at a rate of 15 Hz was used). Fig. 7.7 a-c shows three individual images for the experiment at T=923 K (650 °C). The corresponding plate lengths as a function of time are shown in Fig. 7.7d. The plate growth rates are determined by linear regression and the corresponding fit lines are also plotted in Fig. 7.7d. It is observed that some plates grow at different rates at different stages of their evolution. In these cases, the velocities of distinct stages are obtained from piecewise linear regression. As shown in Fig. 7.7d, plate 4 (not contained in Fig. 7.7 a-c) first grew at 3.57 μm/s followed by a slower lengthening rate of 0.43 μm/s and then continued at a speed of 4.66 μm/s until it stopped growing abruptly.

The results of all plate lengthening measurements are reported in Fig. 7.8, Fig. 7.9, Fig. 7.10 and Fig. 7.11 for isothermal holding at 723 K, 773 K, 823K and 923 K (450 °C, 500 °C, 550 °C and 650 °C), respectively. In each figure the relevant stage of the time-temperature profiles is also plotted. Time is set to zero at the onset of isothermal holding. For each plate the length evolution is indicated by a line drawn through the data points taken at 1 second interval. The symbol at the start of the line indicates the type of nucleation site (GB, on a plate (OP) or internal with no clear initiation source (IN). The symbol at the end of the line section indicates the microstructural feature at which the plate stopped (GB, OP or IN where IN may also be a topological defect on the surface other than a grain boundary or bainitic plate).

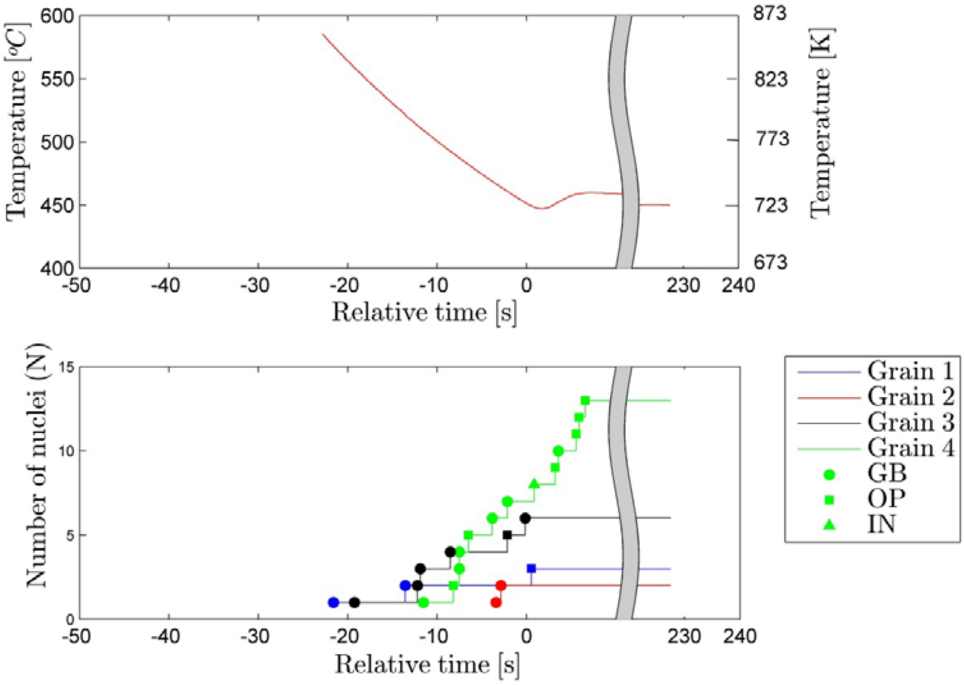

Fig. 7.3- Temperature and nucleation sequence versus time of bainitic ferrite plates in Fe-0.2C-1.5Mn-2.0Cr during isothermal holding treatment at 723 K (450 °C).

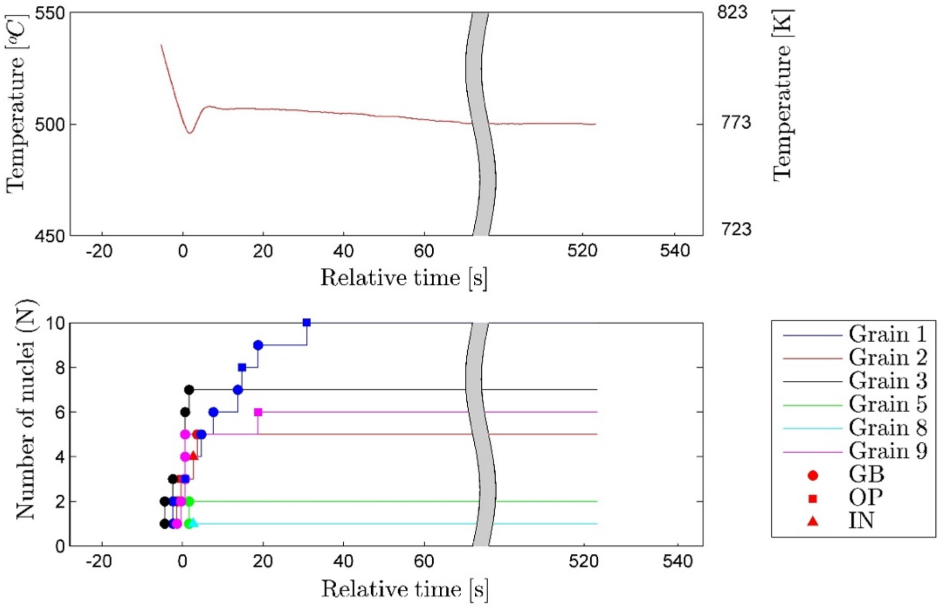

Fig. 7.4- Temperature and nucleation sequence versus time of bainitic ferrite plates in Fe-0.2C-1.5Mn-2.0Cr during isothermal holding treatment at 773 K (500 °C).

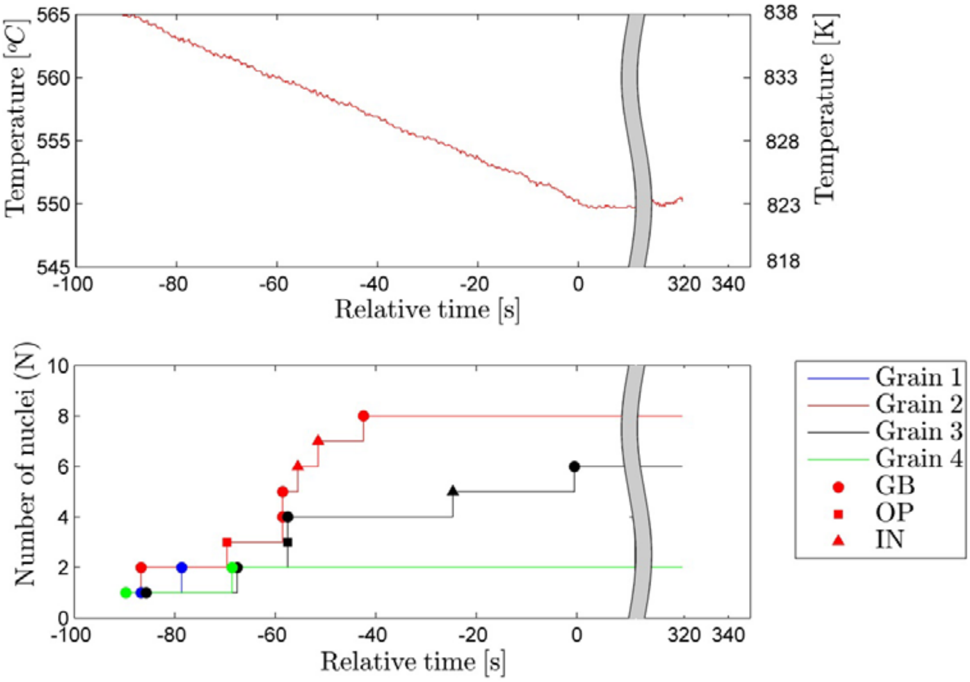

Fig. 7.5- Temperature and nucleation sequence versus time of bainitic ferrite plates in Fe-0.2C-1.5Mn-2.0Cr during isothermal holding treatment at 823 K (550 °C).

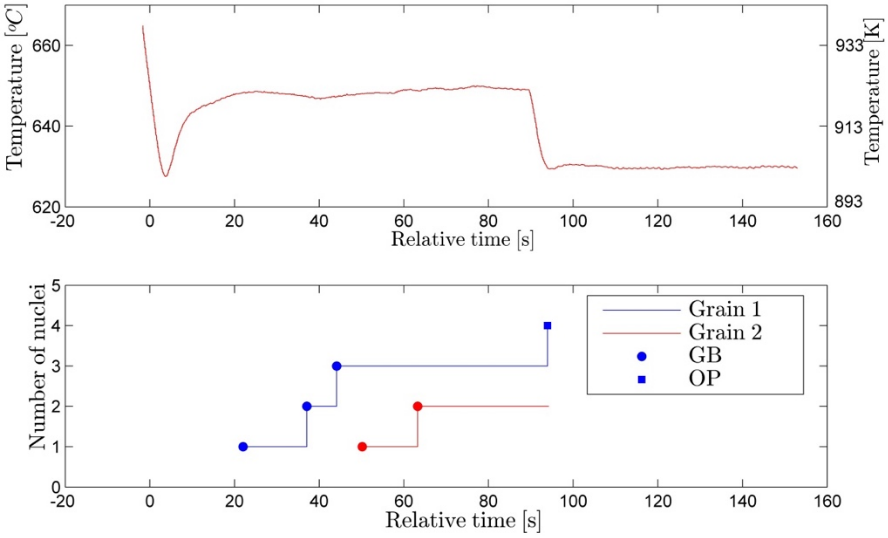

Fig. 7.6- Temperature and nucleation sequence versus time of bainitic ferrite plates in Fe-0.2C-1.5Mn-2.0Cr during isothermal holding treatment at 923 K (650 °C).

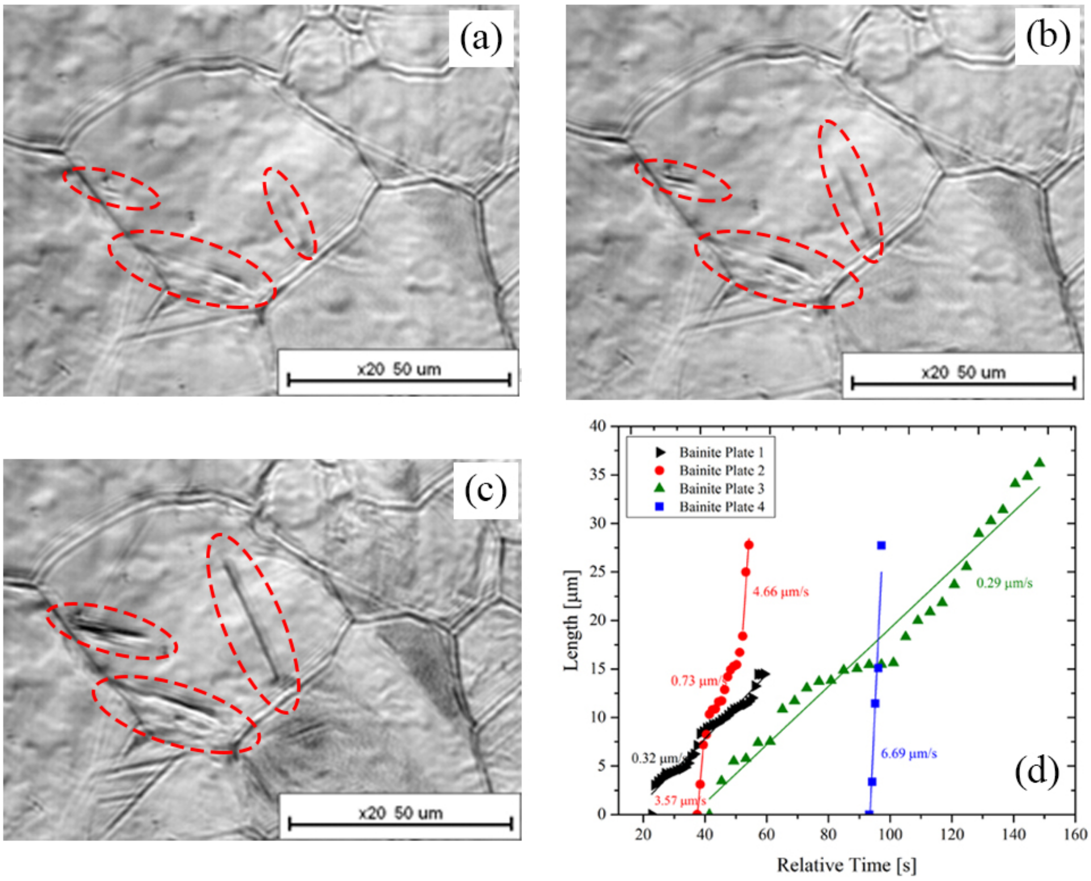

Fig. 7.7- (a), (b), (c) Micrographs showing growth of bainitic ferrite plates during holding at 923 K (650 °C) at various stages of isothermal holding time and (d) Length versus time plot of the corresponding plates and their lengthening rate.

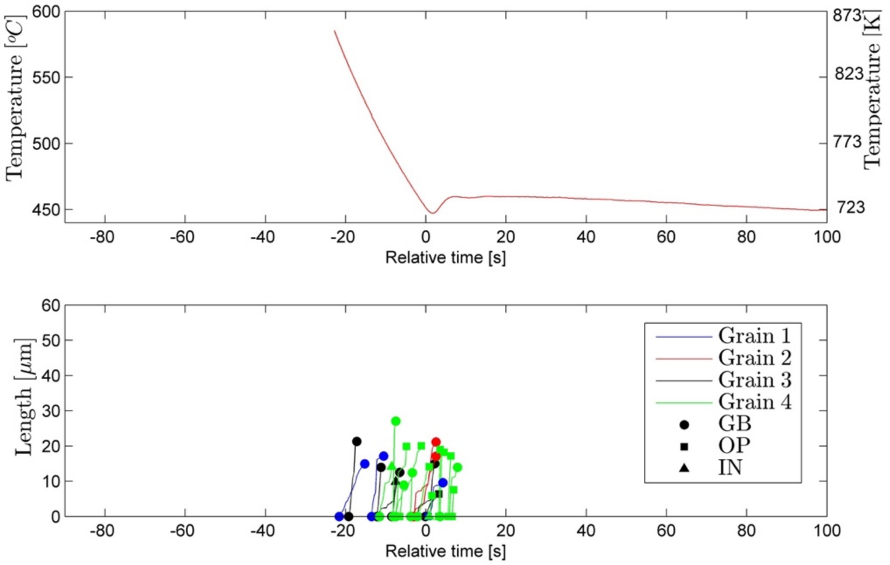

Fig. 7.8- Temperature versus time and temporal plate growth sequence of bainitic ferrite plates in Fe-0.2C-1.5Mn-2.0Cr during isothermal holding treatment at 723 K (450 °C).

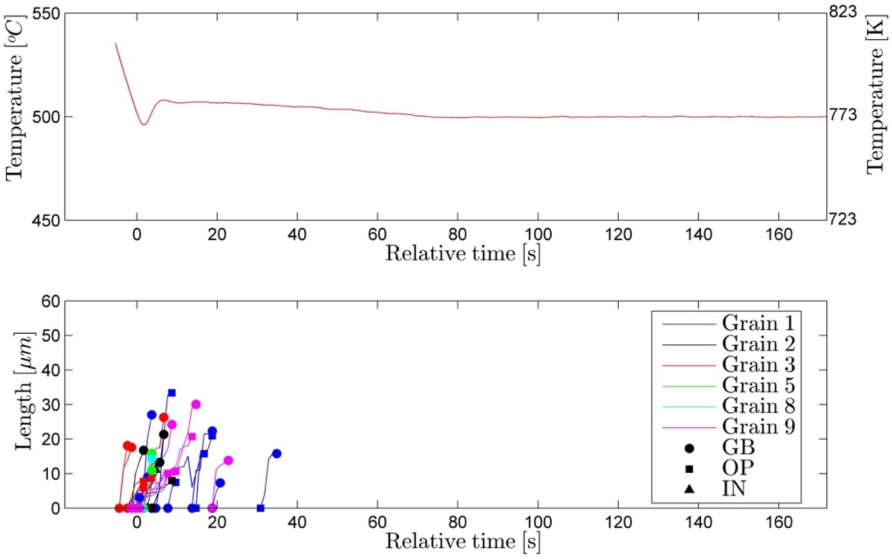

Fig. 7.9- Temperature versus time and temporal plate growth sequence of bainitic ferrite plates in Fe-0.2C-1.5Mn-2.0Cr during isothermal holding treatment at 773 K (500 °C).

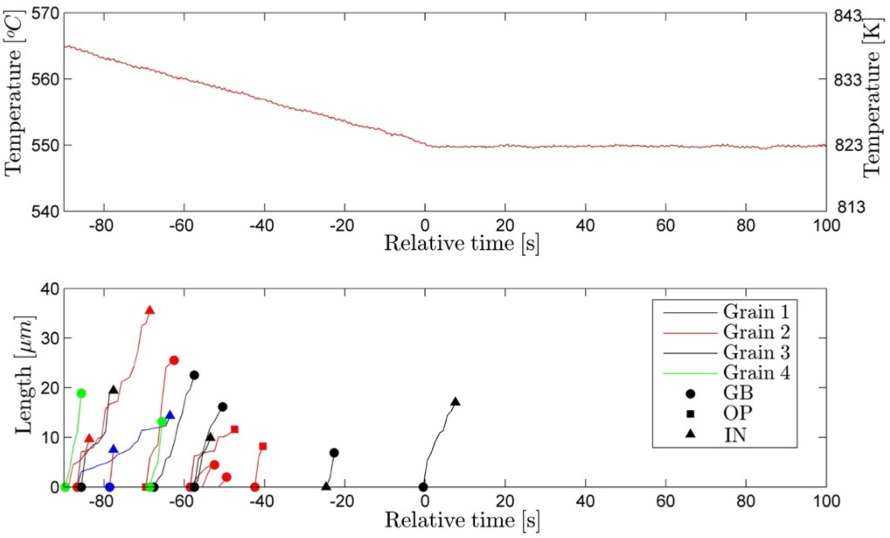

Fig. 7.10- Temperature versus time and temporal plate growth sequence of bainitic ferrite plates in Fe-0.2C-1.5Mn-2.0Cr during isothermal holding treatment at 823 K (550 °C).

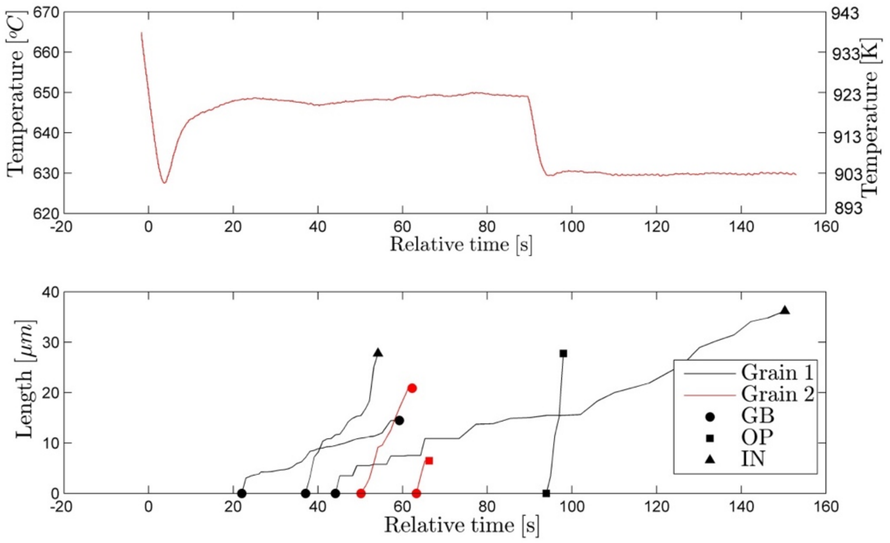

Fig. 7.11- Temperature versus time and temporal plate growth sequence of bainitic ferrite plates in Fe-0.2C-1.5Mn-2.0Cr during isothermal holding treatment at 923 K (650 °C).

Various combinations of type of nucleation site and termination site can be distinguished. Plates that formed at the initial stage of the transformation generally started from the grain boundary and grew until their growth was stopped by impingement with another segment of the grain boundary. Plates that started growing at later stages were also stopped due to previously formed plates and thus these plates grew to a shorter length than ones formed at initial stages. No cases of bainite growth continuing in the neighbouring grain after impacting a grain boundary were observed. As can also be seen from the Fig. 7.8, Fig. 7.9, Fig. 7.10 and Fig. 7.11, most plates stopped due to impingement with either a grain boundary or another bainitic plate. In only a very few cases the bainitic transformation stopped within a grain without any microscopically detectable reason. The plate thickening or widening rates were observed to be slower than the lengthening rates yet the kinetics could not be quantified due to the limited spatial resolution in the LSCM images and the less clearly defined boundary. There were no indications that the plate widening was also interrupted due to interactions with other local features or distortions in the microstructure.

The observed lengthening rate of individual plates in a particular experiment showed some variation from plate to plate and between different grains but overall the lengthening rates were found to be approximately in the same order of magnitude, see Fig. 7.8, Fig. 7.9 and Fig. 7.10. In contrast the lengthening rates scattered largely for the highest transformation temperature (Fig. 7.11). In general, a shorter time window for growth, Δt, and a higher lengthening rate is observed for lower transformation temperatures. Given the effect of transformation temperature on the nucleation rates (Fig. 7.3 to Fig. 7.6) and the growth rates (Fig. 7.8 to Fig. 7.11), one can expect a more rapid bainite transformation at higher undercooling as a cooperative result of both higher nucleation and lengthening rates.

7.4 Discussion

7.4.1 Nucleation

As described in the Results section, plates of bainitic ferrite were observed to nucleate at three different types of location. The total number of observed nucleation phenomena grouped by nucleation sites versus holding temperature is presented in Fig. 7.12. The total number of nucleation events increases by reducing transformation temperature, reaching its maximum at T=773 K (500 °C) and decreases for lower temperatures. Nuclei are mainly formed at grain boundaries. Nucleation inside the austenite grains is a rare event and were difficult to observe unambiguously by means of LSCM measurements. Such nucleation events were strongly outnumbered by nucleation events from grain boundaries or newly formed bainite plates. Nucleation on existing bainitic plates -autocatalytic nucleation- occurs at all transformation temperatures, and its fraction increases at lower transformation temperatures.

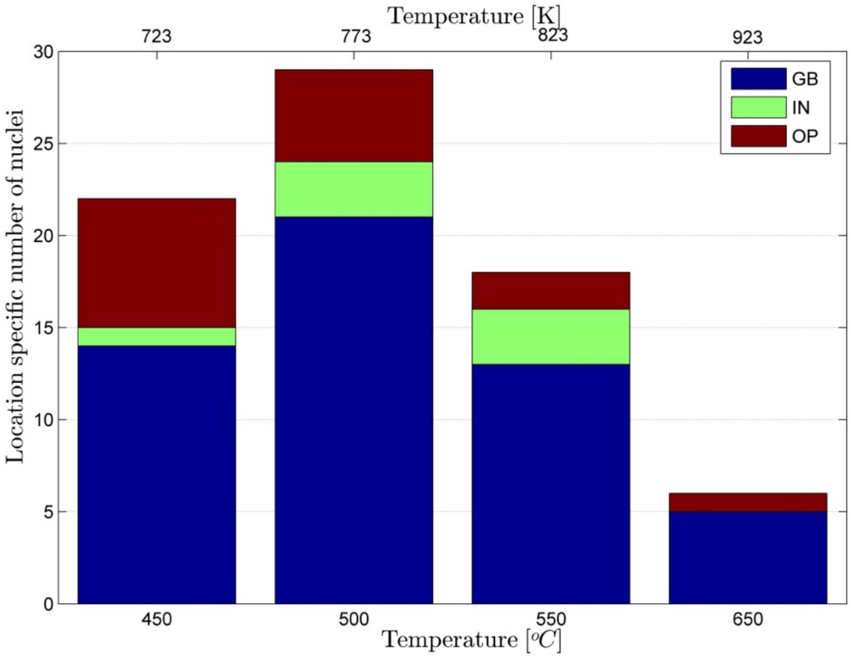

Fig. 7.12- Total number of observed nucleation events grouped by the observed nucleation sites versus the isothermal temperature of each experiment.

Fig. 7.3, Fig. 7.4, Fig. 7.5 and Fig. 7.6, as presented, provide only a 2D view of the nucleation rate in different grains and the differences in nucleation rate between the different grains is likely due to the orientation of the grain with respect to the observed surface. Due to complexity of the nucleation in 3D structures, there is no assumption-free method of quantitatively evaluating and comparing the overall nucleation rate per unit of volume from such 2D observations. The average nucleation rate per unit area versus the temperature range of observation is shown in Fig. 7.13. The average nucleation rate decreases upon increasing isothermal holding temperature from 723 K to 823 K (450 °C to 650 °C). The scatter in nucleation rates was more pronounced at lower transformation temperatures compared to higher temperatures.

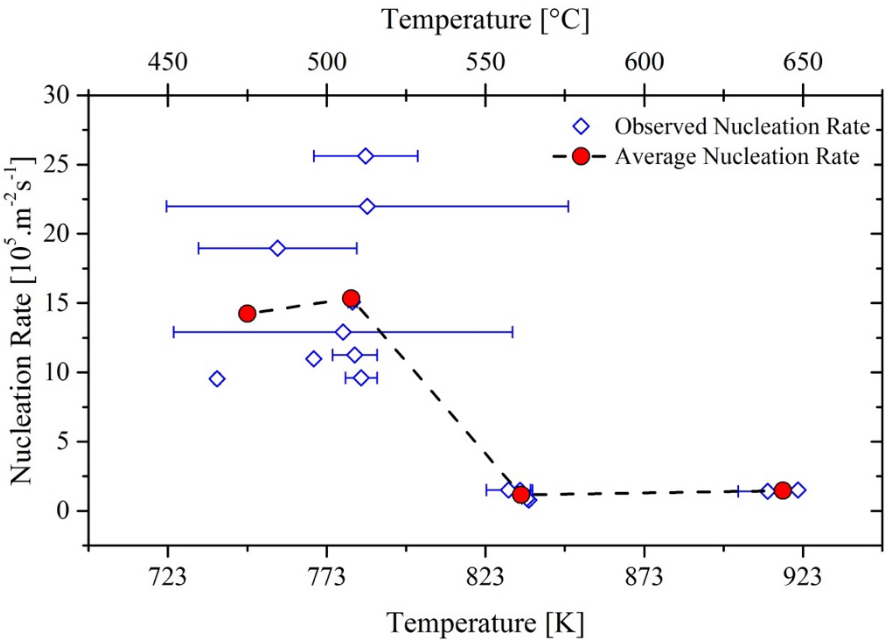

Fig. 7.13- Temperature dependence on the average nucleation rate per unit area.

Enhanced analysis of the observed nucleation behaviour can be done by comparing the averaged nucleation rates to those obtained by classical nucleation theory (CNT) [75,76]. According to CNT, the nucleation rate is expressed as a product of two exponential terms: one accounting for the number of stable nuclei n* being formed such that $n^* \propto exp\left(-\frac{\Delta G^*}{k_B T}\right)$ where ΔG* is the activation energy needed for nucleation of product phase from parent nuclei and kB is the Boltzmann constant. ΔG* can be in general written in as $\Delta G^* = {}^{\Psi}/_{\Delta g_v^2}$, where Δgv being changes in Gibbs energy of phases under para-equilibrium condition and factor Ψ accounts for geometry and interfacial energies between nucleus and original phase. The other term accounts for cluster dynamics or the frequency with which parent phase atoms attach themselves to product nuclei cluster, $v_d \propto exp\left(-\frac{Q_D}{k_B T}\right)$, where Q_D is the activation energy for diffusion of migrating atoms, so the total nucleation rate, $\dot{\mathrm{N}}$, would be product of these two factors as

$$\dot{\mathrm{N}} \propto \exp\left(-\frac{\Delta G^{*} + Q_D}{k_B T}\right) \tag{7.2}$$

The low nucleation rate at high undercooling is attributed to the high activation energy for diffusion at lower temperatures. At lower undercooling, or at higher transformation temperature, the driving force is too low to produce a perceptible nucleation rate. Using the driving force for nucleation calculated by Thermo-Calc software linked to TCFE8 data base [77], leading to equilibrium transformation start temperature of 1043 K (770 °C), a best fit of normalized experimental data to equation (7.2) when $Q_D=4.72\times10^{-19}$ J [78], gives $\Psi=1.2\times10^{-13}$ $\mathrm{J^3mol^{-2}}$ (with Δg_v in $\mathrm{Jmol^{-1}}$) which is orders of magnitude smaller than the values predicted for ferrite nucleation [79–81] *. The values of ΔG* using fitted parameter of Ψ, vary from $3.9k_BT$ to $47.5k_BT$ between 723 K (450 °C) to 923 K (650 °C), respectively. These values are higher than the predicted values by *Quidort* and *Bréchet* [82] for bainite nucleation in a 0.5 mass%. carbon steel varying from $1.1k_BT$ to $1.7k_BT$ between 648 K (375 °C) to 773 K (500 °C), very different from the value of $0.03k_BT$ predicted by van Dijk et al. [83] for barrier free heterogeneous nucleation of ferrite grains in C35 steel at T=1003 K (730 °C). The driving force Δg_v is plotted versus temperature in Fig. 7.14a. The nucleation energy barrier ΔG* and the activation energy Q_D as multiples of (k_BT) are linked to the normalized nucleation rate $\dot{\mathrm{N}}/\dot{\mathrm{N}}_{max}$ according to CNT and these quantities versus temperature are presented in Fig. 7.14b as best fit to the experimental data.

---

* After conversion of the units, $\Psi=1.2\times10^{-3}$ $\mathrm{J^3m^{-6}}$ which is orders of magnitude greater than the values fitted for the ferrite nucleation in references [79–81].

7.4.2 Growth

Results in Section 150 show the temporal evolution of plate lengths for different isothermal temperatures. The data analysis was done corresponding to a frequency of 1Hz, though the experimental data were recorded at 15 Hz. To check that the lower sampling frequency did not lead to loss of information, two bainite plate growth events were analysed both at the lower sampling frequency of 1 Hz and one at the actual data recording frequency of 15 Hz: one plate with a high growth rate and other one with a lower growth rate. The results of the four analyses are shown in Fig. 7.15 a-d. The figures demonstrate that the low frequency data analysis provides complete information with respect to plate growth and that, at the temporal and spatial resolution used, the plate growth is continuous without any jerkiness, while the error associated with low resolution measurements remains between 0.79-3.01 μm (equal to 3-13 pixels in 1024×1024 pixels images).

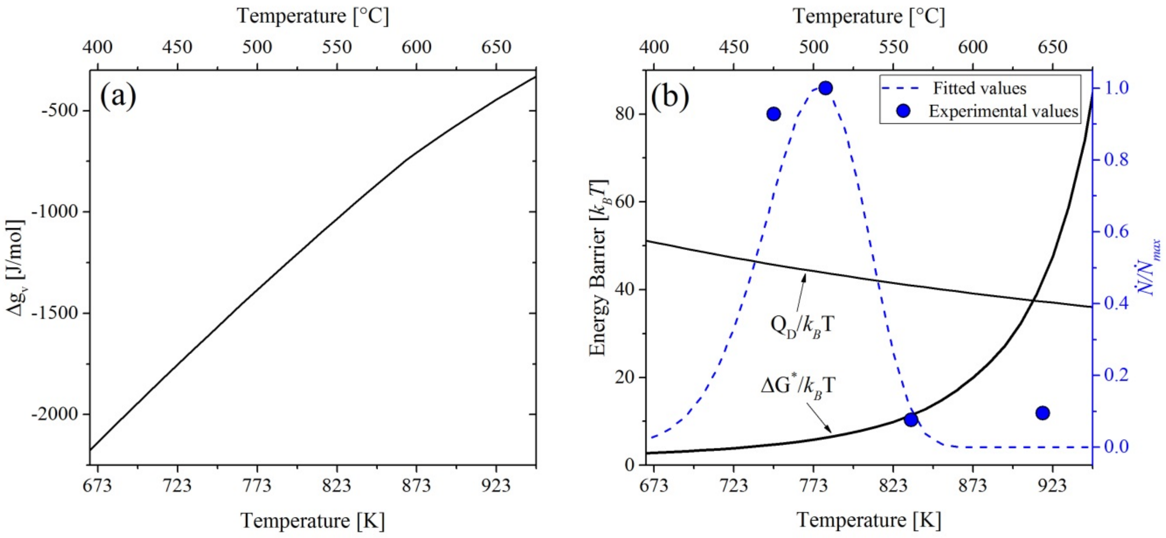

Fig. 7.14- (a) Nucleation driving force and (b) fitted energy barrier and nucleation rate according to classical nucleation theory.

Fig. 7.8, Fig. 7.9, Fig. 7.10 and Fig. 7.11 show the evolution of individual plates for the three transformation temperatures. Fig. 7.16 summarizes the average and range of measured lengthening rates during total transformation for bainite plates initiated at grain boundaries, within the grains and on preformed bainite plates for each experiment. Comparing all transformation temperatures, no clear relationship between nucleation site and lengthening rates of bainite plates is observed. However, the average and range of lengthening rate increases remarkably for lower transformation temperatures. In a similar LSCM study, Hu et al. [67] reported different bainite plate lengthening rates during cooling and isothermal holding. Such a difference was not observed in the current experiment.

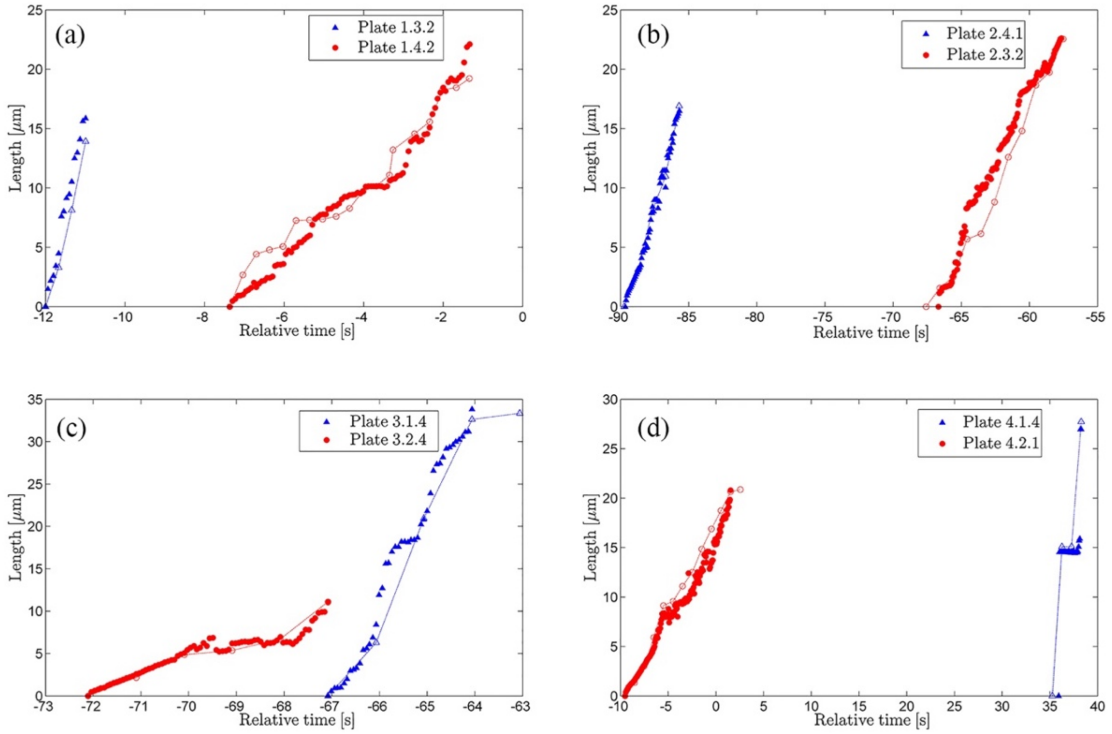

Fig. 7.15- High time resolution measurements on plates observed in Fe-0.2C-1.5Mn-2.0Cr at isothermal holding conditions: (a) T=723 K (450 °C) (b) T=773 K (500 °C) (c) T=823 K (550 °C) (d) T=923 K (650 °C).

Fig. 7.8, Fig. 7.9, Fig. 7.10 and Fig. 7.11 show the evolution of individual plates for the three transformation temperatures. Fig. 7.16 summarizes the average and range of measured lengthening rates during total transformation for bainite plates initiated at grain boundaries, within the grains and on preformed bainite plates for each experiment. Comparing all transformation temperatures, no clear relationship between nucleation site and lengthening rates of bainite plates is observed. However, the average and range of lengthening rate increases remarkably for lower transformation temperatures. In a similar LSCM study, Hu et al. [67] reported different bainite plate lengthening rates during cooling and isothermal holding. Such a difference was not observed in the current experiment.

Now the growth data are to be compared with the predictions by available models in the literature. The diffusionless hypothesis suggests that the lengthening rate of bainitic plates depends on the nucleation rate of bainite subunits. Due to complex dependence of the nucleation rate to different fitting parameters (discussed in [46,84]), which actually justifies the nucleation rate of subunit itself as a fitting parameter, the direct comparison of the experimental data can only be made with the diffusional model proposed for prediction of the maximum lengthening rate of bainitic plates.

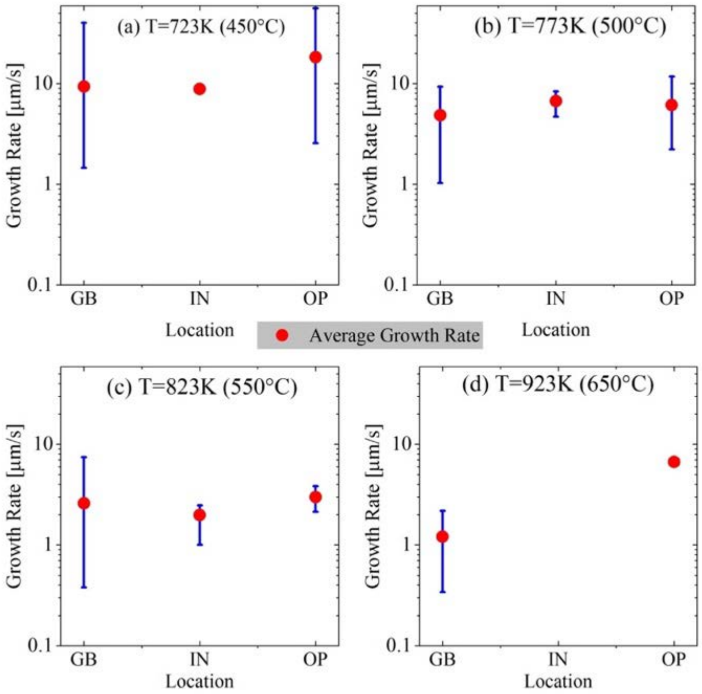

Fig. 7.16- Lengthening rates of bainite plates (in logarithmic scale) observed to nucleated and grow during cooling step and isothermal holding step on different locations namely grain boundary (GB), within the grain (IN) and on preformed bainite (OP) at (a) T=723 K (450 °C), (b) T=773 K (500 °C), (c) T=823 K (550 °C), (d) T=923 K (650 °C).

The diffusion controlled equation of lengthening known as *Zener-Hillert* model [68,69] has been recently improved by Leach et al. [85]. Upon removing the original simplifying approximations made by Zener [86], the lengthening rate, v, is described by:

$$v = \frac{D^{eff}\,(\Delta G_m^0 - B)/V_m}{2\sigma^{\alpha\gamma}} \cdot \frac{x^{\gamma/\alpha} - x_0^\gamma}{x_0^\gamma - x^{\alpha/\gamma}} \cdot \frac{\rho_{cr}}{\rho}. \tag{7.3}$$

where D^{eff} is the effective diffusion coefficient of carbon, ΔG_m^0 is the maximum driving force of transformation, B is the energy barrier of the transformation, V_m is molar volume, $\sigma^{\alpha\gamma}$ is the interface energy, $x^{\gamma/\alpha}$, $x^{\alpha/\gamma}$ and x_0^γ mole fraction of carbon at the austenitic side of interface, ferritic side of interface and in initial austenite phase; ρ is the radius of curvature of the plate tip and ρ_{cr} is the critical radius for which the growth rate is zero. The effective diffusion coefficient of carbon can be calculated by

$$D_C^{eff} = \int_{x_0^\gamma}^{x^{\gamma/\alpha}} \frac{D_C^\gamma(x_c)}{(x^{\gamma/\alpha} - x_0^\gamma)} dx_c \tag{7.4}$$

The dependency of carbon diffusivity in austenite to its mole fraction can be calculated by the following expression suggested by *Ågren* [87]:

$$\begin{aligned} D_C^\gamma = 4.53 \times 10^{-7} \left(1 + x_c(1 - x_c)\frac{8339.9}{T}\right) \exp[-(\frac{1}{T} - 2.221 \times 10^{-4})(17767 \\ - x_c 26436)] \end{aligned} \tag{7.5}$$

Equation (7.3) has been applied with parameters similar to those used in [88] for modelling the maximum growth rate of bainitic plates at different temperatures with assuming energy barrier B of 0 and 400 J/mol for growth. The equilibrium composition of austenite (Ae3 line) at low temperatures and transformation driving force have been calculated using Thermo-Calc software linked to TCFE8 data base [77]. The value for B= 400 J/mol is selected according to strain the energy barrier concept suggested by *Bhadeshia* [33,89] to accommodate the displacive nature of bainitic ferrite formation.

Fig. 7.17 shows the predicted maximum lengthening rates according to equation (7.3) for the two values for the energy barrier as well as the experimentally recorded growth data at the different temperatures. Equation (7.3) yields a typical C-type growth rate with a maximum shifting to a lower growth rate at a lower temperature upon introducing an energy barrier of 400 J/mol. In general, the correspondence between the calculated velocities and the experimental data is modest. The actual experimental growth rates at T=923 K (650 °C) are well captured by the model with B=400 J/mol. For T=823 K (550 °C), the measured lengthening rates are still in the range of the maximum growth rate predicted by the model. However, for lower temperatures, the predicted velocity grossly underestimates the actual values. This can be in-line with the other reports describing possibility of massive growth mechanism for bainitic plates at low temperatures [83]–[85].

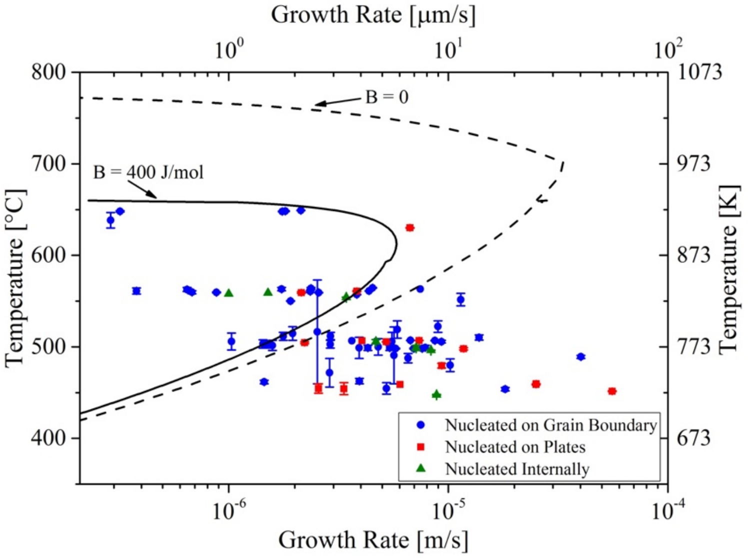

Fig. 7.17- Predicted maximum lengthening rates with equation (7.3) in logarithmic scale and the experimentally recorded growth data at different temperatures.

Given the composition of the samples studied an incomplete bainite transformation phenomenon [40,92–95] is expected to occur at the transformation temperatures imposed. As can be observed in Fig. of 8, 9, 10 and 11, (and in the supplementary information showing the original recordings of the isothermal transformation experiment at T=723 K (450 °C), the lengthening of the majority of bainite plates is independent of the nucleation time and location, terminates on geometrical obstacles of austenite grain boundaries or existing plates. However, widening of all the plates terminate within the austenite grains results in a limited width of the bainitic plates. This indicates that the transformation stasis can be caused by stasis in the widening of the bainitic plates, restricted by a growth limiting mechanism such as formation of Mn spike in front of the migrating interface, while the lengthening is assumed to be a massive transformation, i.e. no compositional changes in the bulk material but a carbon spike in front of the migrating interface. Such a mechanism for incomplete bainite transformation has been previously suggested in a modelling work by *Yang* et al. [96], where in ferrite transformation with plate-like morphology a complete transformation in the lengthening direction and incomplete growth in widening of the plates were predicted; proposing that the global stasis in ferrite formation with plate-like geometry is due to local stasis in widening of the previously nucleated plates and not in lengthening, while for an isotropic ferrite morphology the stasis occurs in all directions of growth.

7.5 Conclusions

In this study, isothermal bainite transformation in a C-Mn steel has been investigated using in-situ LSCM and image analysis. Assuming that the transformation features observed at the sample surface qualitatively reflect the features of the bainite formation in the bulk, the following conclusions are achieved:

1. The rate of nucleation (initiation) of bainitic plates is observed to be rather different in different austenite grains.

2. The majority of the bainitic plates nucleate on austenite grain boundaries.

3. The observed averaged nucleation rate for bainitic plates is found to be in qualitative agreement with the classical nucleation theory.

4. No special relationship is found between the lengthening rate of bainite plates and their nucleation site.

5. The predicted values of the maximum lengthening rate by means of an improved diffusional model considering 400 J/mol of growth barrier energy are in agreement with experimentally measured growth rates of bainite plates at high temperatures.

7.6 References

[1] H.K.D.H. Bhadeshia, R. Honeycombe, Steels: microstructure and properties: microstructure and properties, Elsevier, Butterworth-Heinemann, 2011. https://books.google.com/books?hl=en&lr=&id=6MtuBqok43MC&oi=fnd&pg=PP2&dq=bhadeshia+neural+networks&ots=zgmfvpqN6M&sig=Hh9U7P6VxYeYDULXe7bq-bWSS2s.

[2] H. Aydin, E. Essadiqi, I.H. Jung, S. Yue, Development of 3rd generation AHSS with medium Mn content alloying compositions, Mater. Sci. Eng. A. 564 (2013) 501–508. doi:10.1016/j.msea.2012.11.113.

[3] D.K. Matlock, J.G. Speer, Third Generation of AHSS: Microstructure Design Concepts, in: Microstruct. Texture Steels, Springer London, London, 2009: pp. 185–205. doi:10.1007/978-1-84882-454-6_11.

[4] C. Capdevila, J. Cornide, K. Tanaka, K. Nakanishi, E. Urones-Garrote, Kinetic transition during ferrite growth in Fe-C-Mn medium carbon steel, Metall. Mater. Trans. A Phys. Metall. Mater. Sci. 42 (2011) 3719–3728. doi:10.1007/s11661-011-0650-y.

[5] H. Luo, J. Shi, C. Wang, W. Cao, X. Sun, H. Dong, Experimental and numerical analysis on formation of stable austenite during the intercritical annealing of 5Mn steel, Acta Mater. 59 (2011) 4002–4014. doi:10.1016/j.actamat.2011.03.025.

[6] C. Wang, W. Cao, J. Shi, C. Huang, H. Dong, Deformation microstructures and strengthening mechanisms of an ultrafine grained duplex medium-Mn steel, Mater. Sci. Eng. A. 562 (2013) 89–95. doi:10.1016/j.msea.2012.11.044.

[7] R. Zhang, W.Q. Cao, Z.J. Peng, J. Shi, H. Dong, C.X. Huang, Intercritical rolling induced ultrafine microstructure and excellent mechanical properties of the medium-Mn steel, Mater. Sci. Eng. A. 583 (2013) 84–88. doi:10.1016/j.msea.2013.06.067.

[8] O. Bouaziz, S. Allain, C.P. Scott, P. Cugy, D. Barbier, High manganese austenitic twinning induced plasticity steels: A review of the microstructure properties relationships, Curr. Opin. Solid State Mater. Sci. 15 (2011) 141–168. doi:10.1016/j.cossms.2011.04.002.

[9] B.C. De Cooman, Structure-properties relationship in TRIP steels containing carbide-free bainite, Curr. Opin. Solid State Mater. Sci. 8 (2004) 285–303. doi:10.1016/j.cossms.2004.10.002.

[10] Y.K. Lee, C. Choi, Driving force for $\gamma \rightarrow \varepsilon$ martensitic transformation and stacking fault energy of γ in Fe-Mn binary system, Metall. Mater. Trans. A. 31 (2000) 355–360. doi:10.1007/s11661-000-0271-3.

[11] S. Zaefferer, J. Ohlert, W. Bleck, A study of microstructure, transformation mechanisms and correlation between microstructure and mechanical properties of a low alloyed TRIP steel, Acta Mater. 52 (2004) 2765–2778. doi:10.1016/j.actamat.2004.02.044.

[12] A. Grajcar, W. Zalecki, W. Burian, A. Kozłowska, Phase Equilibrium and Austenite Decomposition in Advanced High-Strength Medium-Mn Bainitic Steels, Metals (Basel). 6 (2016) 248. doi:10.3390/met6100248.

[13] A. Grajcar, K. Radwański, H.J. Krztoń, Microstructural Analysis of a Thermomechanically Processed Si-Al TRIP Steel Characterized by EBSD and X-Ray Techniques, Solid State Phenom. 203–204 (2013) 34–37. doi:10.4028/www.scientific.net/SSP.203-204.34.

[14] K. Radwański, A. Wrożyna, R. Kuziak, Role of the advanced microstructures characterization in modeling of mechanical properties of AHSS steels, Mater. Sci. Eng. A. 639 (2015) 567–574. doi:10.1016/J.MSEA.2015.05.071.

[15] H. Kamoutsi, E. Gioti, G.N. Haidemenopoulos, Z. Cai, H. Ding, Kinetics of Solute Partitioning During Intercritical Annealing of a Medium-Mn Steel, Metall. Mater. Trans. A. 46 (2015) 4841–4846. doi:10.1007/s11661-015-3118-7.

[16] K. Sugimoto, H. Tanino, J. Kobayashi, Impact Toughness of Medium-Mn Transformation-Induced Plasticity-Aided Steels, Steel Res. Int. 86 (2015) 1151–1160. doi:10.1002/srin.201400585.

[17] S. Lee, K. Lee, B.C. De Cooman, Observation of the TWIP + TRIP Plasticity-Enhancement Mechanism in Al-Added 6 Wt Pct Medium Mn Steel, Metall. Mater. Trans. A. 46 (2015) 2356–2363. doi:10.1007/s11661-015-2854-z.

[18] C. Garcia-Mateo, T. Sourmail, F.G. Caballero, C. Capdevila, C. García de Andrés, New approach for the bainite start temperature calculation in steels, Mater. Sci. Technol. 21 (2005) 934–940. doi:10.1179/174328405X51622.

[19] H. Farahani, W. Xu, S. van der Zwaag, Prediction and Validation of the Austenite Phase Fraction upon Intercritical Annealing of Medium Mn Steels, Metall. Mater. Trans. A. 46 (2015) 4978–4985. doi:10.1007/s11661-015-3081-3.

[20] A. Arlazarov, M. Gouné, O. Bouaziz, A. Hazotte, G. Petitgand, P. Barges, Evolution of microstructure and mechanical properties of medium Mn steels during double annealing, Mater. Sci. Eng. A. 542 (2012) 31–39. doi:10.1016/j.msea.2012.02.024.

[21] J. Lee, S.S. Sohn, S. Hong, B.-C. Suh, S.-K. Kim, B.-J. Lee, N.J. Kim, S. Lee, Effects of Mn Addition on Tensile and Charpy Impact Properties in Austenitic Fe-Mn-C-Al-Based Steels for Cryogenic Applications, Metall. Mater. Trans. A. 45 (2014) 5419–5430. doi:10.1007/s11661-014-2513-9.

[22] S.S. Sohn, S. Lee, B.-J. Lee, J.-H. Kwak, Microstructural Developments and Tensile Properties of Lean Fe-Mn-Al-C Lightweight Steels, JOM. 66 (2014) 1857–1867. doi:10.1007/s11837-014-1128-3.

[23] J. Han, S.-J. Lee, J.-G. Jung, Y.-K. Lee, The effects of the initial martensite microstructure on the microstructure and tensile properties of intercritically annealed Fe–9Mn–0.05C steel, Acta Mater. 78 (2014) 369–377. doi:10.1016/j.actamat.2014.07.005.

[24] I. Gutierrez-Urrutia, D. Raabe, Influence of Al content and precipitation state on the mechanical behavior of austenitic high-Mn low-density steels, Scr. Mater. 68 (2013) 343–347. doi:10.1016/j.scriptamat.2012.08.038.

[25] E. Davenport, E. Bain, Transformation of Austenite at Constant Subcritical Temperatures, Trans. AIME. 90 (1930) 117–144. doi:10.1007/BF03037891.

[26] H.W. Paxton, Commentary by: Transformation of austenite at constant subcritical temperatures, Metall. Trans. 1 (1970) 3479–3501. doi:10.1007/BF03037891.

[27] H.I. Aaronson, T. Furuhara, J.M. Rigsbee, W.T. Reynolds, J.M. Howe, Crystallographic and mechanistic aspects of growth by shear and by diffusional processes, Metall. Trans. A. 21 (1990) 2369–2409. doi:10.1007/BF02646984.

[28] M. Hillert, The Nature of Bainite., ISIJ Int. 35 (1995) 1134–1140. doi:10.2355/isijinternational.35.1134.

[29] M. Hillert, Diffusion in growth of bainite, Metall. Mater. Trans. A. 25 (1994) 1957–1966. doi:10.1007/BF02649044.

[30] G.R. Purdy, M. Hillert, Overview no. 38: On the nature of the bainite transformation in steels, Acta Metall. 32 (1984) 823–828. doi:10.1016/0001-6160(84)90018-X.

[31] M. Hillert, The growth of ferrite, bainite and martensite, in: Thermodyn. Phase Transform. Sel. Work. Mats Hillert, 2006: pp. 111–158.

[32] R.F. Hehemann, K.R. Kinsman, H.I. Aaronson, A debate on the bainite reaction, Metall. Trans. 3 (1972) 1077–1094. doi:10.1007/BF02642439.

[33] H.K.D.H. Bhadeshia, D.V. Edmonds, The mechanism of bainite formation in steels, Acta Metall. 28 (1980) 1265–1273. doi:10.1016/0001-6160(80)90082-6.

[34] W.T. Reynolds, F.Z. Li, C.K. Shui, H.I. Aaronson, The Incomplete transformation phenomenon in Fe-C-Mo alloys, Metall. Trans. A. 21 (1990) 1433–1463. doi:10.1007/BF02672561.

[35] W.T. Reynolds, S.K. Liu, F.Z. Li, S. Hartfield, H.I. Aaronson, An investigation of the generality of incomplete transformation to bainite in Fe-C-X alloys, Metall. Trans. A. 21 (1990) 1479–1491. doi:10.1007/BF02672563.

[36] D. Quidort, Y.J.M. Brechet, Isothermal growth kinetics of bainite in 0.5% C steels, Acta Mater. 49 (2001) 4161–4170. doi:10.1016/S1359-6454(01)00316-0.

[37] M. Hillert, L. Höglund, J. Ågren, Role of carbon and alloying elements in the formation of bainitic ferrite, Metall. Mater. Trans. A. 35 (2004) 3693–3700. doi:10.1007/s11661-004-0275-5.

[38] F.G. Caballero, H.K.D.H. Bhadeshia, Very strong bainite, Curr. Opin. Solid State Mater. Sci. 8 (2004) 251–257. doi:10.1016/j.cossms.2004.09.005.

[39] Z. Yang, H. Fang, An overview on bainite formation in steels, Curr. Opin. Solid State Mater. Sci. 9 (2005) 277–286. doi:10.1016/J.COSSMS.2006.06.005.

[40] H.I. Aaronson, W.T. Reynolds, G.R. Purdy, The incomplete transformation phenomenon in steel, Metall. Mater. Trans. A. 37 (2006) 1731–1745. doi:10.1007/s11661-006-0116-9.

[41] A. Borgenstam, M. Hillert, J. Agren, Metallographic evidence of carbon diffusion in the growth of bainite, Acta Mater. 57 (2009) 3242–3252. doi:10.1016/j.actamat.2009.03.026.

[42] F.G. Caballero, C. Garcia-Mateo, M.J. Santofimia, M.K. Miller, C. García de Andrés, New experimental evidence on the incomplete transformation phenomenon in steel, Acta Mater. 57 (2009) 8–17. doi:10.1016/j.actamat.2008.08.041.

[43] C. Liu, X. Di, C. Chen, X. Guo, Z. Xue, A bainite transformation kinetics model and its application to X70 pipeline steel, J. Mater. Sci. 50 (2015) 5079–5090. doi:10.1007/s10853-015-9060-7.

[44] W. Gong, Y. Tomota, S. Harjo, Y. Su, K. Aizawa, Effect of prior martensite on bainite transformation in nanobainite steel, Acta Mater. 85 (2015) 243–249. doi:10.1016/J.ACTAMAT.2014.11.029.

[45] L.S. Darken, R.M. Fisher, Decomposition of Austenite by Diffusional Processes, in: Proc. Symp. Philadelphia; Intersci. Publ. Bucks, UK, 1962: pp. 249–294.

[46] H. Matsuda, H.K.D.H. Bhadeshia, Kinetics of the bainite transformation, Proc. R. Soc. A Math. Phys. Eng. Sci. 460 (2004) 1707–1722. doi:10.1098/rspa.2003.1225.

[47] D. Quidort, Y. Bréchet, The role of carbon on the kinetics of bainite transformation in steels, Scr. Mater. 47 (2002) 151–156. doi:10.1016/S1359-6462(02)00121-5.

[48] G.I. Rees, H.K.D.H. Bhadeshia, Bainite transformation kinetics Part 2 Non-uniform distribution of carbon, Mater. Sci. Technol. 8 (1992) 994–1003. doi:10.1179/026708392790409815.

[49] M. Takahashi, Recent progress: kinetics of the bainite transformation in steels, Curr. Opin. Solid State Mater. Sci. 8 (2004) 213–217. doi:10.1016/j.cossms.2004.08.003.

[50] M.J. Santofimia, F.G. Caballero, C. Capdevila, C. García-Mateo, C.G. de Andrés, C. García-Mateo, C.G.D. Andrés, C. García-Mateo, C.G. de Andrés, Evaluation of Displacive Models for Bainite Transformation Kinetics in Steels, Mater. Trans. 47 (2006) 1492–1500. doi:10.2320/matertrans.47.1492.

[51] S.M.C. Van Bohemen, J. Sietsma, Modeling of isothermal bainite formation based on the nucleation kinetics, Int. J. Mater. Res. 99 (2008) 739–747. doi:10.3139/146.101695.

[52] A.M. Ravi, J. Sietsma, M.J. Santofimia, Exploring bainite formation kinetics distinguishing grain-boundary and autocatalytic nucleation in high and low-Si steels, Acta Mater. 105 (2016) 155–164. doi:10.1016/j.actamat.2015.11.044.

[53] H. Chen, S. van der Zwaag, Analysis of ferrite growth retardation induced by local Mn enrichment in austenite created by prior interface passages, Acta Mater. 61 (2013) 1338–1349. doi:10.1016/j.actamat.2012.11.011.

[54] H. Chen, K. Zhu, L. Zhao, S. Van Der Zwaag, Analysis of transformation stasis during the isothermal bainitic ferrite formation in Fe-C-Mn and Fe-C-Mn-Si alloys, Acta Mater. 61 (2013) 5458–5468. doi:10.1016/j.actamat.2013.05.034.

[55] H. Chen, A. Borgenstam, J. Odqvist, I. Zuazo, M. Goune, J. Ågren, S. van der Zwaag, Application of interrupted cooling experiments to study the mechanism of bainitic ferrite formation in steels, Acta Mater. 61 (2013) 4512–4523. doi:10.1016/j.actamat.2013.04.020.

[56] L.C. Chang, Microstructures and reaction kinetics of bainite transformation in Si-rich steels, Mater. Sci. Eng. A. 368 (2004) 175–182. doi:10.1016/J.MSEA.2003.10.297.

[57] S.. B. Singh, H.K.D.. H. Bhadeshia, Estimation of bainite plate-thickness in low-alloy steels, Mater. Sci. Eng. a-Structural Mater. Prop. Microstruct. Process. 245 (1998) 72–79. doi:10.1016/s0921-5093(97)00701-6.

[58] K.M. Wu, M. Kagayama, M. Enomoto, Kinetics of ferrite transformation in an Fe-0.28mass%C-3mass%Mo alloy, Mater. Sci. Eng. A. 343 (2003) 143–150. doi:10.1016/S0921-5093(02)00374-X.

[59] M. Enomoto, N. Maruyama, K.M. Wu, T. Tarui, Alloying element accumulation at ferrite/austenite boundaries below the time–temperature–transformation diagram bay in an

Fe–C–Mo Alloy, Mater. Sci. Eng. A. 343 (2003) 151–157. doi:10.1016/S0921-5093(02)00375-1.

[60] T. Ko, S.A. Cottrell, The formation of bainite, J. Iron Steel Inst. 172 (1952) 307.

[61] D. Zhang, H. Terasaki, Y. Komizo, In situ observation of phase transformation in Fe–0.15C binary alloy, J. Alloys Compd. 484 (2009) 929–933. doi:10.1016/j.jallcom.2009.05.074.

[62] P. Kolmskog, A. Borgenstam, M. Hillert, P. Hedström, S.S. Babu, H. Terasaki, Y.I. Komizo, Direct Observation that Bainite can Grow Below MS, Metall. Mater. Trans. A. 43 (2012) 4984.

[63] H. Yada, M. Enomoto, T. Sonoyama, Lengthening Kinetics of Bainitic Plates in Iron-Nickel-Carbon Alloys, ISIJ Int. 35 (1995). doi:10.2355/isijinternational.35.976.

[64] M. Kang, M.-X. Zhang, M. Zhu, In situ observation of bainite growth during isothermal holding, Acta Mater. 54 (2006) 2121–2129. doi:10.1016/j.actamat.2005.12.036.

[65] G. Xu, F. Liu, L. Wang, H. Hu, A new approach to quantitative analysis of bainitic transformation in a superbainite steel, Scr. Mater. 68 (2013) 833–836. doi:10.1016/j.scriptamat.2013.01.033.

[66] X.L. Wan, R. Wei, L. Cheng, M. Enomoto, Y. Adachi, Lengthening kinetics of ferrite plates in high-strength low-carbon low alloy steel, J. Mater. Sci. 48 (2013) 4345–4355. doi:10.1007/s10853-013-7250-8.

[67] Z. Hu, G. Xu, H. Hu, L. Wang, Z. Xue, In situ measured growth rates of bainite plates in an Fe-C-Mn-Si superbainitic steel, Int. J. Miner. Metall. Mater. 21 (2014) 371–378. doi:10.1007/s12613-014-0918-5.

[68] J.P. and G.P. J. Agren, Y. Brechet, C. Hutchinson, Thermodynamics and Phase transformations: The selected works of Mats Hillert, EDP Sciences, 2006. https://inis.iaea.org/search/search.aspx?orig_q=RN:38042210 (accessed September 26, 2017).

[69] M. Hillert, Role of interfacial energy during solid-state phase transformations, Jernkontorets Ann. 141 (1957) 757–789.

[70] R. Trivedi, G.M. Pound, Effect of Concentration-Dependent Diffusion Coefficient on the Migration of Interphase Boundaries, J. Appl. Phys. 38 (1967) 3569–3576. doi:10.1063/1.1710174.

[71] J. Tian, G. Xu, L. Wang, M. Zhou, H. Hu, In Situ Observation of the Lengthening Rate of Bainite Sheaves During Continuous Cooling Process in a Fe–C–Mn–Si Superbainitic Steel, Trans. Indian Inst. Met. (2017) 1–10. doi:10.1007/s12666-017-1151-5.

[72] H. Chen, E. Gamsjäger, S. Schider, H. Khanbareh, S. van der Zwaag, In situ observation of austenite–ferrite interface migration in a lean Mn steel during cyclic partial phase transformations, Acta Mater. 61 (2013) 2414–2424. doi:10.1016/j.actamat.2013.01.013.

[73] The Math Works Inc., MATLAB Image Processing Toolbox Realese 2015b; The Math Works Inc.: Natick, MA, USA, (2007). https://www.mathworks.com/products/image.html.

[74] J. Pak, D.W. Suh, H.K.D.H. Bhadeshia, Displacive Phase Transformation and Surface Effects Associated with Confocal Laser Scanning Microscopy, Metall. Mater. Trans. A. 43 (2012) 4520–4524. doi:10.1007/s11661-012-1264-8.

[75] V.I. Kalikmanov, Classical Nucleation Theory, in: Springer, Dordrecht, 2013: pp. 17–41. doi:10.1007/978-90-481-3643-8_3.

[76] W.D. Callister, Materials science and engineering: An introduction, 7th ed., John Wiley & Sons, 2007. doi:10.1016/0025-5416(87)90343-0.

[77] J.O. Andersson, T. Helander, L. Höglund, P. Shi, B. Sundman, Thermo-Calc & DICTRA, computational tools for materials science, Calphad. 26 (2002) 273–312. doi:10.1016/S0364-5916(02)00037-8.

[78] J. Kučera, K. Stránský, Diffusion in iron, iron solid solutions and steels, Mater. Sci. Eng. 52 (1982) 1–38. doi:10.1016/0025-5416(82)90067-2.

[79] S.E. Offerman, N.H. van Dijk, J. Sietsma, S. Grigull, E.M. Lauridsen, L. Margulies, H.F. Poulsen, M.T. Rekveldt, S. van der Zwaag, Grain Nucleation and Growth During Phase Transformations, Science (80). 298 (2002) 1003–1005. doi:10.1126/science.1076681.

[80] P. Clemm, J. Fisher, The influence of grain boundaries on the nucleation of secondary phases, Acta Metall. 3 (1955) 70–73. doi:10.1016/0001-6160(55)90014-6.

[81] W.F. Lange, M. Enomoto, H.I. Aaronson, The kinetics of ferrite nucleation at austenite grain boundaries in Fe-C alloys, Metall. Trans. A. 19 (1988) 427–440. doi:10.1007/BF02649256.

[82] D. Quidort, Y.J.M. Brechet, A Model of Isothermal and Non Isothermal Transformation Kinetics of Bainite in 0.5% C Steels., ISIJ Int. 42 (2002) 1010–1017. doi:10.2355/isijinternational.42.1010.

[83] N.H. van Dijk, S.E. Offerman, J. Sietsma, S. van der Zwaag, Barrier-free heterogeneous grain nucleation in polycrystalline materials: The austenite to ferrite phase transformation in steel, Acta Mater. 55 (2007) 4489–4498. doi:10.1016/j.actamat.2007.04.013.

[84] C. Liu, L. Shi, Y. Liu, C. Li, H. Li, Q. Guo, Acicular ferrite formation during isothermal holding in HSLA steel, J. Mater. Sci. 51 (2016) 3555–3563. doi:10.1007/s10853-015-9675-8.

[85] L. Leach, M. Hillert, A. Borgenstam, Modeling C-Curves for the Growth Rate of Widmanstätten and Bainitic Ferrite in Fe-C Alloys, Metall. Mater. Trans. A. 47 (2016) 19–25. doi:10.1007/s11661-015-3241-5.

[86] C. Zener, Kinetics of the decomposition of austenite, Trans. Aime. 167 (1946) 550–595.

[87] J. Ågren, A revised expression for the diffusivity of carbon in binary Fe-C austenite, Scr. Metall. 20 (1986) 1507–1510. doi:10.1016/0036-9748(86)90384-4.

[88] J. Yin, L. Leach, M. Hillert, A. Borgenstam, C-Curves for Lengthening of Widmanstätten and Bainitic Ferrite, Metall. Mater. Trans. A. 48 (2017) 3997–4005. doi:10.1007/s11661-017-4196-5.

[89] H. Bhadeshia, Bainite in Steels: Theory and Practice, 3rd ed., Maney Publishing, 2015. https://books.google.nl/books?id=kzjyrQEACAAJ (accessed February 19, 2016).

[90] M. Enomoto, T. Sonoyama, H. Yada, Kinetics of Austenite to Ferrite Transformation in 3 mass% Mn Low Carbon Steels, Mater. Trans. JIM. 39 (1998) 189–195. doi:10.2320/matertrans1989.39.189.

[91] J.M. Howe, Comparison of the atomic structure, composition, kinetics and mechanisms of interfacial motion in martensitic, bainitic, massive and precipitation face-centered cubic-hexagonal close-packed phase transformations, Mater. Sci. Eng. A. 438–440 (2006) 35–42. doi:10.1016/j.msea.2006.02.120.

[92] H. Chen, K. Zhu, L. Zhao, S. Van Der Zwaag, Analysis of transformation stasis during the isothermal bainitic ferrite formation in Fe–C–Mn and Fe–C–Mn–Si alloys, Acta Mater. 61 (2013) 5458–5468. doi:10.1016/j.actamat.2013.05.034.

[93] H. Chen, S. van der Zwaag, On the nature of the bainitic and ferritic transformation stasis in steels, in: PTM2015, Proc. Int. Conf. Solid-Solid Phase Transform. Inorg. Mater. 2015, International Conference on Solid-Solid Phase Transformations in Inorganic Materials 2015, 2015: pp. 37–44. https://www.scopus.com/record/display.uri?eid=2-s2.0-84962676257&origin=resultslist&sort=plf-f&src=s&sid=63360faf6ee7f77e57ff1c3ee52fd2f7&sot=autdocs&sdt=autdocs&sl=18&s=A

U-ID%2857188745139%29&relpos=18&citeCnt=0&searchTerm= (accessed September 27, 2017).

[94] H. Chen, Z. Yang, C. Zhang, K. Zhu, S. van der Zwaag, On the transition between grain boundary ferrite and bainitic ferrite in Fe–C–Mo and Fe–C–Mn alloys: The bay formation explained, Acta Mater. 104 (2016) 62–71. doi:10.1016/j.actamat.2015.11.012.

[95] H. Chen, S. Van Der Zwaag, An experimental study of the stagnant stage in bainite phase transformations starting from austenite-bainite mixtures, in: TMP 2012 - 4th Int. Conf. Thermomechanical Process. Steels, Sheffield, UK, 10–12 September, 2012. https://www.scopus.com/record/display.uri?eid=2-s2.0-84896891374&origin=resultslist&sort=plf-f&src=s&sid=1946a7bc694969cb3dc997da6da11cd7&sot=autdocs&sdt=autdocs&sl=18&s=AU-ID%2857188745139%29&relpos=33&citeCnt=0&searchTerm= (accessed September 27, 2017).

[96] Z.Z. Yang, W. Xu, Z.Z. Yang, C. Zhang, S. van der Zwaag, A 2D analysis of the competition between the equiaxed ferritic and the bainitic morphology based on a Gibbs Energy Balance approach, Acta Mater. 105 (2016) 317–327. doi:10.1016/j.actamat.2015.12.040.

Chapter 8 Predicting the cooperative effect of Mn-Si and Mn-Mo on the incomplete bainite formation in quaternary Fe-C alloys

This Chapter is based on

- H. Farahani, W. Xu , S. van der Zwaag, Predicting the cooperative effect of Mn-Si and Mn-Mo on the incomplete bainite formation in quaternary Fe-C alloys, *Philiosophical Magazine Letters*, DOI: 10.1080/09500839.2018.1515505.

ABSTRACT

Predicting the effect of alloying elements on the degree of incomplete austenite to bainite transformation in low carbon steels is of great industrial importance. This study introduces an extended Gibbs Energy Balance model which makes use of an additive approach to calculate the coupled effect of Mn, Si and Mo on the fraction of bainitic ferrite after the incomplete transformation in multicomponent steels. The model predicts significant effects of Mn and Mo and negligible effect of Si levels on the fraction of bainitic ferrite. This is attributed to the high value of dissipation of Gibbs energy caused by interfacial diffusion of Mn and Mo and low values caused by Si diffusion. The model predictions for quaternary Fe-C-Mn-Si system are comparable with the experimentally measured values of bainite fraction. For the Fe-C-Mn-Mo system, the agreement is less accurate, and the accuracy decreases with increasing Mo content, which is attributed a substantial carbide formation but interaction effects between Mn and Mo or a temperature dependent binding energy cannot be rules out.

8.1 Introduction

The effect of alloying elements on the incomplete transformation (ICT) phenomenon [1,2] during bainite formation in low carbon steels is of great technical importance. The simultaneous presence of alloying elements like Mn, Mo and Si in appropriate amounts enhances the mechanical properties achieved by bainitic microstructures obtained during quasi-isothermal annealing during industrial production; However, the addition of such alloying elements increases the degree of ICT and hence the fraction of untransformed austenite or unscheduled martensite formation. As the mechanical properties of the final microstructure of the alloy are strongly influenced by the bainite fraction, it is essential to predict the effect of alloying elements on the degree of ICT [3,4].

Two general theories have been proposed in the past to describe the mechanism of the bainite formation and consequently describe the effect of alloying elements on the ICT phenomenon in the bainite formation. The first theory assumes a non-diffusional and displacive growth mode for sheaves of bainitic ferrite [5–7]. According to this approach, the austenite to bainite transformation is stopped when the free energy of the supersaturated ferritic bainite equals the free energy of the untransformed austenite at the transformation temperature (T_0 model). Therefore, this theory models the effect of alloying elements on the ICT by predicting their effect on the total free energy of the supersaturated ferritic bainite and the austenite. In a later extension of the model a strain energy term compensating for the local elastic stresses due the bainite formation was added in order to improve the agreement between the experimental data and the model predictions. This model modification is called the T'_0 model. The second theory is based on a diffusion-controlled mechanism for the austenite to bainite transformation. In this theory, the effect of the alloying elements on the incomplete bainite formation is modelled by considering their effect on the migration velocity of the austenite/bainitic ferrite interface. Both schools have applied their models to predict the effect of alloying elements on the incomplete bainite formation and are able to describe the experimental observations to extent reasonable degree [8–10].

Recently, the Gibbs Energy Balance (GEB) model has been successfully introduced to predict the effect of alloying elements on the degree of the ICT in isothermal bainite transformation more accurately [11–13]. The GEB model, closest related to the diffusional theory, focusses on the solute drag effect of substitutional alloying elements at the migrating austenite/bainitic ferrite interface [14]. In this model, the velocity of migrating austenite/bainitic ferrite interface is calculated by matching the chemical driving force of the isothermal transformation as a function of the degree of transformation with the energy required to move the austenite-ferrite locally enriched by solute atoms trapped in the interface. The model assumes the carbon to partition to proceed with such a high speed that a mean field approximation can be applied. In the GEB model the bainite reaction will stop if the available energy is insufficient to drive the interface forward with a realistic velocity. For ternary, Fe-C-X alloys, it has been shown that the GEB model predictions of the degree of incomplete transformation as a function of the alloy composition and the transformation temperature are significantly better than those of the T'_0 model with a constant value for the strain energy contribution [13].

The present study introduces an extended Gibbs Energy Balance model. The extended GEB model makes use of a simple additive approach in the calculation of the Gibbs energy dissipation caused by interfacial diffusion of substitutional alloying elements in order to predict the cooperative effect of alloying elements on the bainitic ferrite fraction (f_α) in multicomponent steels and as function of the isothermal transformation temperature. The assumption of a simple additivity rule was prompted by the observation that the length of the stagnant stage during partially cyclic transformations, which is also related to the trapping of the interface by the local enrichment of the substitutional alloying element was found to depend on the linear sum of the concentrations of the alloying elements [15]. The predictions of f_α versus the critical concentrations of alloying elements in Fe-C-Mn-Si and Fe-C-Mn-Mo quaternary steels are presented, discussed and analysed and compared to experimental data reported in the literature as well as predictions by the T_0 and the T'_0 model.

8.2 Model

The GEB model as developed by *Chen* et al [16] is based on two fundamental components. The first component is the chemical driving force of the phase transformation, which is taken to be the Gibbs energy change for the transformation. The chemical driving force due to compositional and thermodynamic differences between the austenite and bainitic ferrite phases can be generally calculated using

$$\Delta G_m^{chem} = \sum_i^n x_i^0 (\mu_i^{\gamma/\alpha}(x_i^{\gamma/\alpha}) - \mu_i^{\alpha/\gamma}(x_i^{\alpha/\gamma})) \tag{8.1}$$

where ΔG_m^{chem} is the chemical driving force per mole atom, i is the element in the alloy, n is the total number of elements in the alloy, x_i^0 is the composition of material transferred over the interface, $\mu_i^{\alpha/\gamma}$ and $\mu_i^{\gamma/\alpha}$ are the chemical potential of the element i ferrite and austenite, and $x_i^{\alpha/\gamma}$ is the mole fraction of element i in ferritic side of interface and $x_i^{\gamma/\alpha}$ is the mole fraction at austenitic sides of interface [17]. For substitutional alloying elements, $x_i^{\alpha/\gamma}$ and $x_i^{\gamma/\alpha}$ are chosen according to the Negligible Partitioning Local Equilibrium (NPLE) thermodynamic model, but for carbon, being a fast diffusing interstitial alloying element, $x_C^{\alpha/\gamma}$ is assumed to be equal to the equilibrium concentrations of carbon in ferrite. $x_C^{\gamma/\alpha}$ is calculated from the *Zener-Hillert* equation [18]:

$$x_C^{\gamma/\alpha} = x_C^{\gamma} + \sqrt[2]{\frac{v x_C^{\gamma}}{25 \times 10^5 D_C^{\gamma} T}} \quad , \tag{8.2}$$

where x_C^{γ} is the average carbon concentration in austenite, v is the velocity of migrating austenite/ferritic bainite interface, D_C^{γ} is the diffusion coefficient of carbon in austenite and T is the temperature. The equilibrium carbon concentration in bainitic ferrite compared to carbon content of austenite is assumed to be negligible. As the carbon diffusion in austenite is much faster than of the substitutional alloying elements, the carbon content in the remaining austenite can be calculated using mean-field approximation leading to

$$x_c^\gamma = \frac{x_0^\gamma}{1-f_\alpha}\,. \tag{8.3}$$

where f_α is the fraction of bainitic ferrite and x_0^γ is the initial carbon concentration in austenite. Combining equation (8.2) and (8.3), $x_C^{\gamma/\alpha}$ can be calculated as a function f_α and migration rate of austenite/bainitic ferrite interface.

The second component of the GEB model is the dissipation of Gibbs energy due to interfacial diffusion of the substitutional alloying elements. As in the approach by *Purdy* and *Bréchet* [19] a triangular potential well inside the interface is assumed and the solute profile is calculated as a function of interface velocity. Based on the diffusion equation and the potential well and the solute profile inside the interface with width of 2δ at a given velocity, the dissipation of Gibbs energy due to diffusion inside interface can be calculated from

$$\Delta G_i^{diff} = -\int_{-\delta}^{+\delta} (x_i - x_i^0)\left(\frac{dE}{dz}\right)_i dz \qquad , \tag{8.4}$$

where ΔG_i^{diff} is the dissipation of Gibbs energy due to diffusion of substitutional alloying element of i inside the interface, x_i is the concentration of the element i at point z inside the interface, x_i^0 are the nominal concentration of the element i and $\frac{dE}{dz}$ is the gradient of the potential energy inside the interface. According to [19], $(\frac{dE}{dz})_i = \frac{(E_0 - |\Delta E|) - \mu_i^{\alpha/\gamma}}{\delta}$ in the ferritic side of the interface and $(\frac{dE}{dz})_i = \frac{\mu_i^{\gamma/\alpha} - (E_0 - |\Delta E|)}{\delta}$ in the austenitic side of the interface, where $\Delta E = \frac{(\mu_i^{\gamma/\alpha} - \mu_i^{\alpha/\gamma})}{2}$ and E_0 is the binding energy for atoms of alloy i inside the interface [17,19,20].

In the present model, the total dissipation of Gibbs energy caused by interfacial diffusion is calculated separately for each of the substitutional alloying elements present, and the total dissipation, ΔG_{total}^{diss}, is the summation of all contributions

$$\Delta G_{total}^{diss} = \sum_{i}^{m} \Delta G_i^{diff} \quad , \tag{8.5}$$

where m is the number of substitutional alloying elements.

As in the original GEB model, for a given composition and transformation temperature, in the simulations f_α is gradually increased and the interface velocity is calculated in a recursive loop establishing a balance between the components of the model described above. Once the interface velocity is calculated to be smaller than 0.1 $\mu m/s$, the condition for stagnant stage in bainite transformation is assumed to have been reached and the ferrite fraction at that state is taken to be the bainitic (stasis) fraction.

8.3 Results

In this section, the results of the GEB model in predicting the total fraction of isothermally formed bainitic ferrite in Fe-C-Mn-Si and Fe-C-Mn-Mo quaternary steels are presented. For both systems, the thickness of the interface, 2δ, is assumed to be 0.5 nm and independent of the transformation temperature and the degree of enrichment. Similar to the assumptions in previous studies [12,13], the binding energies for the substitutional alloying elements Mn, Si and Mo are taken as 9.9, 12.3 and 30.3 kJ/mol, respectively. The interfacial diffusion coefficient of these elements are again assumed to be the geometric average of the diffusion coefficients in austenite, in ferrite, and in the ferrite grain boundary [21]. Solute interaction terms or interactions between Carbon and the substitutional alloying elements are not considered.

Fig. 8.1 a-c displays the calculated bainite fractions at which the stasis occurs as a function of the Mn and Si concentration for three isothermal transformation temperatures T=450, 500 and 550 °C in Fe-0.1C-xMn-ySi system, where 0<x<3 mass% and 0<y<4 mass%. In each plot the iso-bainite fraction contours are plotted for the following bainitic stasis volume fractions fα=0.05, 0.25, 0.50, 0.75 and 0.95. The contours were determined on the basis of linear interpolations over the results of a large set of simulations. The curve of fα=0.05 specifies the concentrations above which bainite is predicted not to form. On the other side, the curve of fα=0.95 marks the domain below which the bainite formation is predicted to run close to the final thermodynamic fraction, i.e. bainitic stasis not to occur. The space between both curves is split up by the iso-bainite fraction contours. The results show that, more or less irrespective of the transformation temperature, the fraction of isothermally formed bainitic ferrite depends primarily on the Mn concentration, while the effect of Si content seems to be negligible. This is in agreement with previous experimental findings on Mn and Si quaternary alloys and steels that the ICT phenomenon critically depends on the composition of the alloy, in particular the Mn concentration [22]. The critical Mn concentration above which no bainite is predicted to form increases 3.0 to 3.25 mass% when the transformation temperature is lowered from 550 to 450 °C. For the fα=0.05 contour the critical Mn concentration increases slightly with the Si concentration, while the opposite trend is observed for the fα=0.95 contour.

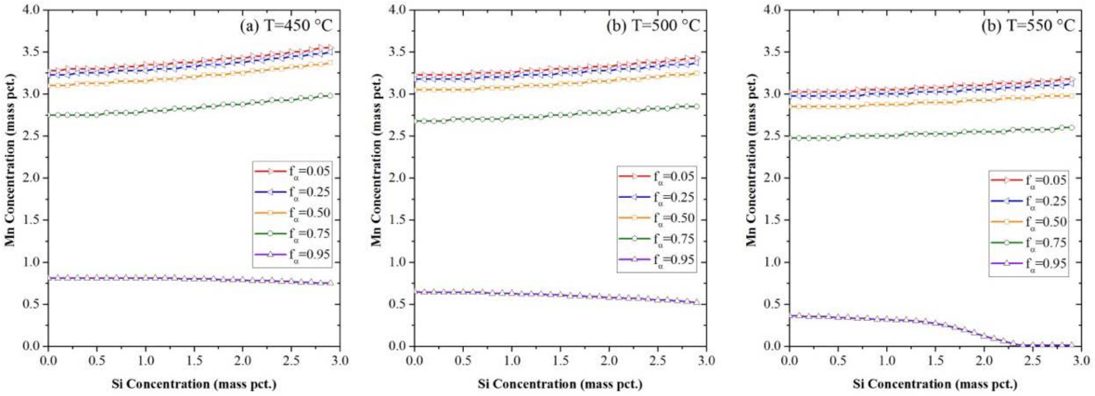

Fig. 8.1- The effect of Si and Mn addition on the volume fraction of bainitic ferrite calculated by GEB model at a) T = 450 °C, b) T = 500 °C and c) T = 550 °C in Fe-0.1C-xSi-yMn system (0<x<3 mass%, 0<y<4 mass%).

The calculated effect of the combinations of specific Mo and Mn levels on the total bainitic ferrite fractions for temperatures T=450, 500 and 550°C in Fe-0.1C-xMo-yMn system, where 0<x<3 mass% and 0<y<4 mass%, is shown in Fig. 8.2 a-c. It is immediately obvious that the dependence on elemental concentration is very different from that in the Si-Mn system. The model predicts a major effect of the Mo concentration on the degree of ICT. The critical Mn concentration for bainite formation drops from 3.25 mass% at 0 mass% Mo to about 0.1% for 2.5 mass% Mo. A lowering of the transformation temperature shifts the iso-bainite contours to lower Mn and Mo concentration levels.

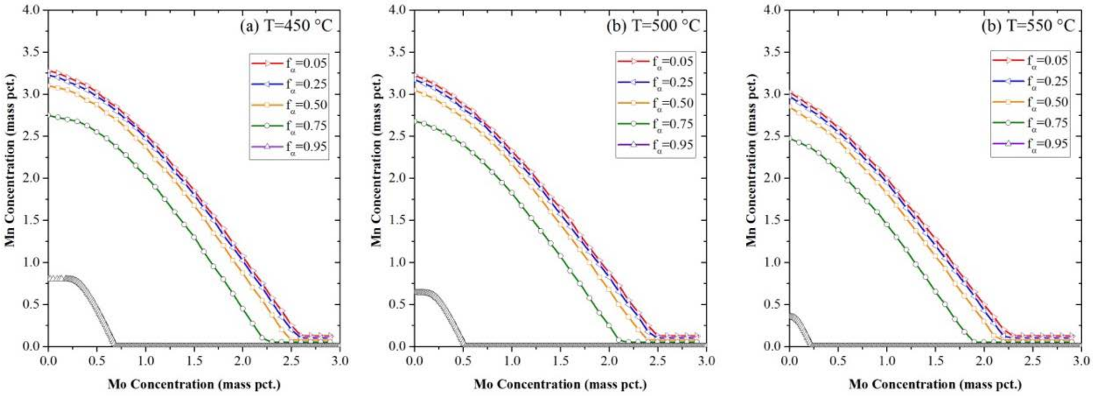

Fig. 8.2- The effect of Mo and Mn addition on the volume fraction of bainitic ferrite calculated by GEB model at a) T = 450 °C, b) T = 500 °C and c) T = 550 °C in Fe-0.1C-xMo-yMn system (0<x<3 mass%, 0<y<4 mass%).

8.4 Discussion

The present model on the cooperative effect of substitutional alloying elements on the degree of incomplete bainite phase transformation showed significant effects of Mn and Mo and negligible effect of Si addition on the degree of ICT. In this section, first the predictions of the GEB model for each system are discussed, followed by a more detailed analysis of model performance.

Fig. 8.3a shows the calculated dissipation of Gibbs energy caused by Mn and Si diffusion as a function of the interface velocity (in solid lines) and the calculated chemical driving force for the phase transformation for different bainitic ferrite fractions (in dashed lines) for the case of isothermal transformations in Fe-0.1C-1.0Mn-1.0Si quaternary system at T=550 °C at several stages of bainite formation. It is evident that the contribution of Si diffusion in the total dissipation of energy is negligible as the dissipation of energy by interfacial diffusion of Mn is much higher and the critical conditions for reaching the critical velocity, taken to represent the bainitic stasis, are barely affected by the Si level and for this combination of composition and temperature the transformation is predicted to run more or less to completion.

Fig. 8.3b illustrates the calculated dissipation (Solid lines) and driving force (dashed lines) in Fe-0.1C-1.0Mn-1.0Mo (all in mass%) quaternary system at T=550 °C. Contrary to Si, interfacial diffusion of Mo atoms generates huge dissipation of Gibbs energy and modifies the shape of the total dissipation curve and consequently shifts the intersection between the total dissipation curve and chemical driving force curves from v≈9μm/s for f_{α}=0.75 to v≈3nm/s for f_{α}=0.9. This sudden shift in migration rate of interface suggests that addition of Mo should be more effective than that of Mn in creating the transformation stasis. The predicted effect is supported by experimental observations of transformation stasis in Mo containing low-alloy low carbon steels. *Furuhara* et al. [23] reported complete bainitic transformations for transformations above T=550 °C for the Fe-0.15C-1.5Mn system but incomplete transformation for the alloy co-alloyed with 0.5 mass% Mo.

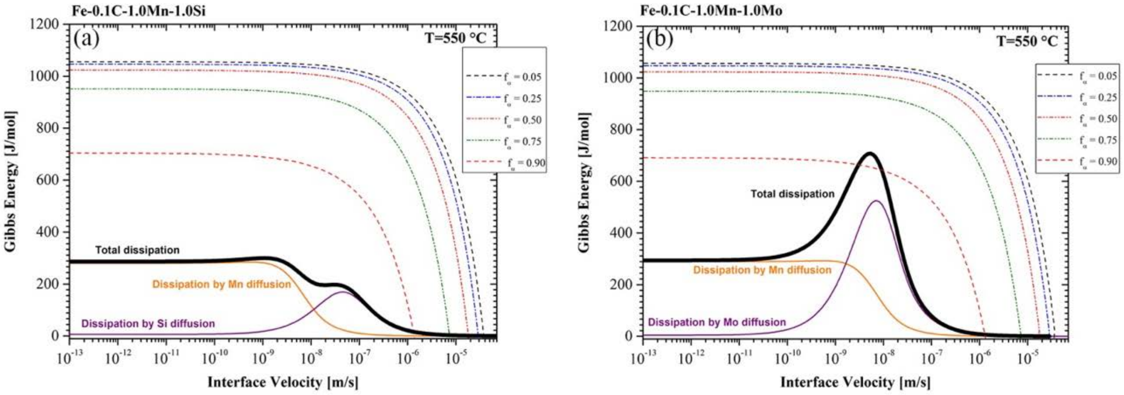

Fig. 8.3- The calculated dissipation of Gibbs energy (solid lines) and chemical driving force (dashed lines) for isothermal bainite transformation in a) Fe-0.1C-1.0Mn-1.0Si and b) Fe-0.1C-1.0Mn-1.0Mo systems at T=550°C.

In order to evaluate the performance of the GEB model for the multicomponent alloys, its predictions of the volume fraction of bainitic ferrite (f_{α}) are compared with experimentally reported values. Fig. 8.4 shows the comparison between prediction of the GEB model and experimental reports in Fe-0.1C-3.0Mn-1.5Si, Fe-0.1C-1.5Mn , Fe-0.1C-1.5Mn-0.3Mo, Fe-0.1C-1.5Mn-1Mo and Fe-0.2C-1.5Mn-1.5Si-xMo (x=0.2,1.5 and 3 mass%) alloys taken from [3,12,24]. In general, the agreement between both data sets is rather good for the quaternary Fe-C-Mn-Si system. However, in Fe-C-Mn-Mo and Fe-C-Mn-Si-Mo system there are discrepancies between predictions of the current GEB model and experimental data, which rise with increasing Mo content. In principle the value f_α predicted by the GEB model could have been corrected by adjusting the values of binding energy (E_0) for Mn or Mo as a function of the transformation temperature or the elemental concentration [12]; however, we could not find solid physical arguments which type of dependence to select. Instead, we may have a critical look at the general validity of the assumptions made in the GEB model.

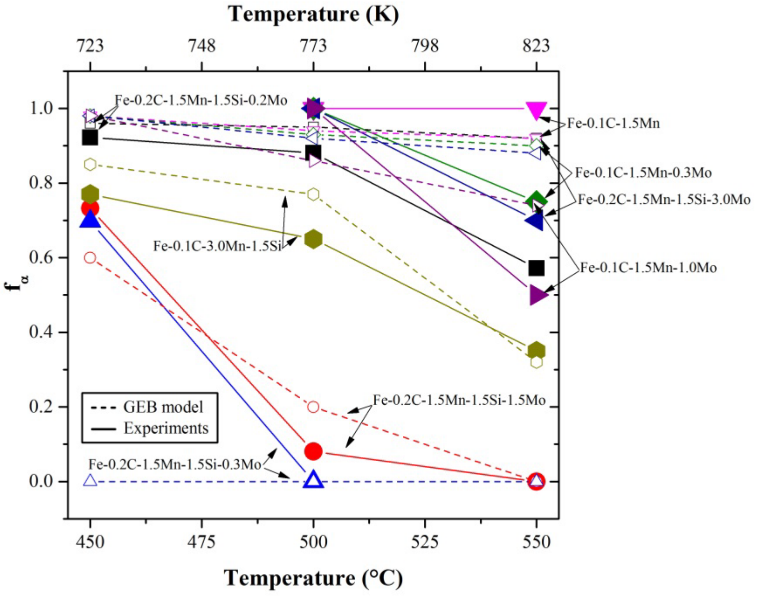

Fig. 8.4- Comparison between predicted values of fraction of bainitic ferrite (f_α) with the GEB model (shown with hollow symbols/dashed lines) and experimental reports (shown with solid symbols/lines) in Fe-0.1C-3.0Mn-1.5Si, , Fe-0.1C-1.5Mn, Fe-0.1C-1.5Mn-0.3Mo, Fe-0.1C-1.5Mn-1Mo alloys Fe-0.2C-1.5Mn-1.5Si-xMo (x=0.2,1.5,3.0 mass%) [3,12,24].

In the GEB model, the carbide formation during bainite transformation is taken to be zero and according to equation (8.3), it is assumed that during migration of the interface all of the carbon atoms are rejected to the austenite region making a flat profile. The accuracy of this assumptions can be investigated by comparing the carbon content in austenite at the transformation stasis stage (C^{γ}_{stasis}) predicted by the model and the experimentally measured data. Fig. 8.5 a-b compares values of C^{γ}_{stasis} as function of temperature, experimentally measured in Fe-0.43C-3.0Mn-2.12Si [5] and Fe-0.1C-1.5Mn-0.3Mo (all in mass%) [3] quaternary alloys and calculated by the GEB model, T_0 model and T_0' model predictions. In the T_0' model, additional deformation energies of 200 and 400 J/mol are assumed to take into account the shear deformation [25]. For Fe-0.43C-3.0Mn-2.12Si alloy, Fig. 8.5a, the experimental values of C^{γ}_{stasis} are close to the GEB model predictions but below the T_0' model assuming a strain energy of 400 J/mol. The high Si content in this system is known to suppress carbide formation [26,27], hence neglecting the carbide formation in the GEB model is an accurate assumption for this system. In Fe-0.1C-1.5Mn-0.3Mo alloy, Fig. 8.5b, the experimental values of C^{γ}_{stasis} are much lower than the predictions by the GEB model but correspond better to the predictions of the T_0 and T_0' model (assuming a strain energy of 200 J/mol) predictions. Neglecting the carbide formation the GEB model overestimates the carbon content in untransformed austenite, which has a major effect on the bainite formation in the presence of Mo [3].

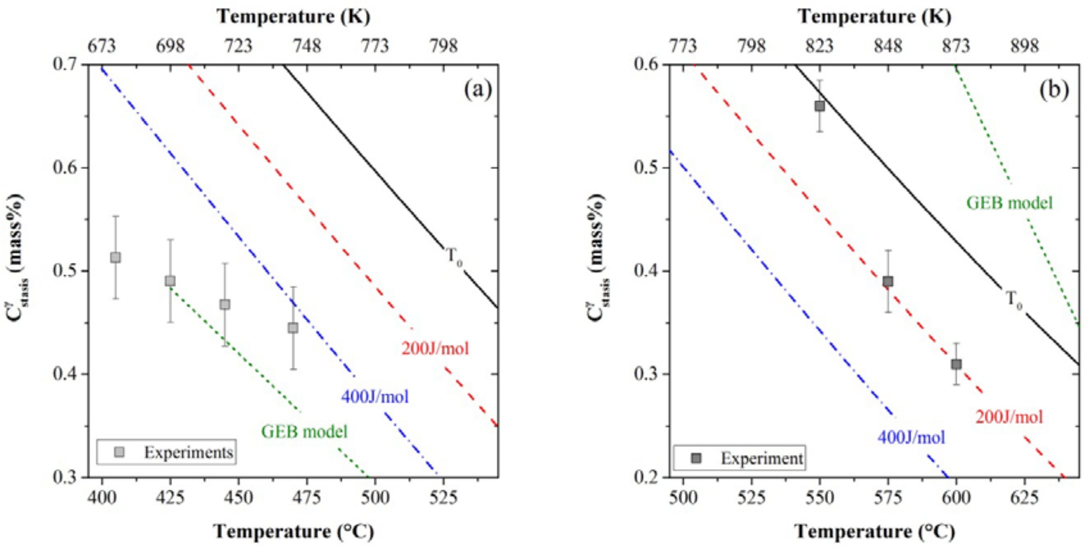

Fig. 8.5- Carbon concentration in austenite in the stasis stage calculated by the GEB model, T_0 and T_0' models and the experimentally measured values in a) Fe-0.43C-3Mn-2.12Si [5] and b) Fe-0.1C-1.5Mn-0.3Mo (mass%) [3] quaternary systems.

In addition to ignoring carbide formation [3], or in general the interaction between different alloying elements [24,28,29], the assumed mean field approximation of the carbon profile in austenite can limit the accuracy of the model predictions of the onset of transformation stasis [30]. Furthermore, the assumed perfect NPLE thermodynamic condition for calculation of the drag of substitutional elements during the whole transformation, may not be applicable under all conditions during the bainite formation. In general, bainite formation proceeds with transitions in partitioning mode of alloying elements at existing interfaces while concurrent nucleation of new bainitic plates and initiation of new interfaces takes place [11]. So, while the current model takes our understanding of the effect of alloying elements on bainite formation a little further, the need for more accurate models making fewer simplifying assumptions on the solute transport remains.

8.5 Conclusions

In this study, the original GEB model was extended in order to predict the coupled effect of Mn, Si and Mo on the fraction of bainitic ferrite after the incomplete transformation in multicomponent steels alloys and the following conclusions were made:

1. Addition of Si has a minor effect on the degree of incomplete bainite transformation via immobilizing migration of interfaces while addition of Mn and Mo significantly reduces fraction of isothermally formed bainite and these effects are qualitatively well captured in the extended GEB model.

2. The predicted minor effect of Si addition and major effect of Mn and Mo addition on the degree of incomplete bainite transformation are attributed to the high value of dissipation of Gibbs energy caused by interfacial diffusion of Mn and Mo and low values caused by Si diffusion.

3. Considering possible interaction between alloying elements, especially carbide formation in presence of Mo, can improve model prediction of the onset of transformation stasis, but also the option to make the binding energy for each element a function of other parameters, such as co-solutes and concentrations levels is to be explored.

8.6 References

[1] H.I. Aaronson, W.T. Reynolds, G.R. Purdy, The incomplete transformation phenomenon in steel, Metall. Mater. Trans. A. 37 (2006) 1731–1745. doi:10.1007/s11661-006-0116-9.

[2] F.G. Caballero, C. Garcia-Mateo, M.J. Santofimia, M.K. Miller, C. García de Andrés, New experimental evidence on the incomplete transformation phenomenon in steel, Acta Mater. 57 (2009) 8–17. doi:10.1016/j.actamat.2008.08.041.

[3] Y. Xia, G. Miyamoto, Z.G. Yang, C. Zhang, T. Furuhara, Direct measurement of carbon enrichment in the incomplete bainite transformation in Mo added low carbon steels, Acta Mater. 91 (2015) 10–18. doi:10.1016/j.actamat.2015.03.021.

[4] V. Biss, R.L. Cryderman, Martensite and retained austenite in hot-rolled, low-carbon bainitic steels, Metall. Mater. Trans. B. 2 (1971) 2267–2276. doi:10.1007/BF02917559.

[5] H.K.D.H. Bhadeshia, D.V. Edmonds, The mechanism of bainite formation in steels, Acta Metall. 28 (1980) 1265–1273. doi:10.1016/0001-6160(80)90082-6.

[6] H. Matsuda, H.K.D.H. Bhadeshia, Kinetics of the bainite transformation, Proc. R. Soc. A Math. Phys. Eng. Sci. 460 (2004) 1707–1722. doi:10.1098/rspa.2003.1225.

[7] H. Bhadeshia, Bainite in Steels: Theory and Practice, 3rd ed., Maney Publishing, 2015. https://books.google.nl/books?id=kzjyrQEACAAJ (accessed February 19, 2016).

[8] L.C.D. Fielding, The Bainite Controversy, Mater. Sci. Technol. 29 (2013) 383–399. doi:10.1179/1743284712Y.0000000157.

[9] M. Takahashi, Recent progress: kinetics of the bainite transformation in steels, Curr. Opin. Solid State Mater. Sci. 8 (2004) 213–217. doi:10.1016/j.cossms.2004.08.003.

[10] S.B. Singh, 10 - Mechanisms of bainite transformation in steels BT - Phase Transformations in Steels, in: Woodhead Publ. Ser. Met. Surf. Eng., Woodhead Publishing, 2012: pp. 385–416. doi:https://doi.org/10.1533/9780857096104.3.385.

[11] H. Chen, S. van der Zwaag, The Effect of Interfacial Element Partitioning on Ferrite and Bainite Formation, JOM. 68 (2016) 1320–1328. doi:10.1007/s11837-016-1848-7.

[12] H. Chen, S. van der Zwaag, Predicting the Effect of Mo, Ni, and Si on the Bainitic Stasis, Metall. Mater. Trans. A. 45 (2014) 3429–3437. doi:10.1007/s11661-014-2262-9.

[13] H. Chen, K. Zhu, L. Zhao, S. Van Der Zwaag, Analysis of transformation stasis during the isothermal bainitic ferrite formation in Fe–C–Mn and Fe–C–Mn–Si alloys, Acta Mater. 61 (2013) 5458–5468. doi:10.1016/j.actamat.2013.05.034.

[14] H. Chen, Z. Yang, C. Zhang, K. Zhu, S. van der Zwaag, On the transition between grain boundary ferrite and bainitic ferrite in Fe–C–Mo and Fe–C–Mn alloys: The bay formation explained, Acta Mater. 104 (2016) 62–71. doi:10.1016/j.actamat.2015.11.012.

[15] H. Chen, R. Kuziak, S. van der Zwaag, Experimental Evidence of the Effect of Alloying Additions on the Stagnant Stage Length During Cyclic Partial Phase Transformations, Metall. Mater. Trans. A. 44 (2013) 5617–5621. doi:10.1007/s11661-013-2040-0.

[16] H. Chen, A. Borgenstam, J. Odqvist, I. Zuazo, M. Goune, J. Ågren, S. van der Zwaag, Application of interrupted cooling experiments to study the mechanism of bainitic

ferrite formation in steels, Acta Mater. 61 (2013) 4512–4523. doi:10.1016/j.actamat.2013.04.020.

[17] M. Hillert, Phase Equilibria, Phase Diagrams and Phase Transformations: Their Thermodynamic Basis, Cambridge University Press, 2007. https://books.google.com/books?id=juk4cxteC1AC&pgis=1 (accessed February 20, 2016).

[18] M. Hillert, Diffusion in growth of bainite, Metall. Mater. Trans. A. 25 (1994) 1957–1966. doi:10.1007/BF02649044.

[19] G.R. Purdy, Y.J.M. Brechet, A solute drag treatment of the effects of alloying elements on the rate of the proeutectoid ferrite transformation in steels, Acta Metall. Mater. 43 (1995) 3763–3774. doi:10.1016/0956-7151(95)90160-4.

[20] J.W. Cahn, The impurity-drag effect in grain boundary motion, Acta Metall. 10 (1962) 789–798. doi:10.1016/0001-6160(62)90092-5.

[21] J. Fridberg, L. Torndhal, M. Hillert, Diffusion in iron, Jernkontorets Ann. 153 (1969) 263–276. http://www.scopus.com/inward/record.url?eid=2-s2.0-0014618161&partnerID=tZOtx3y1.

[22] W.T. Reynolds, S.K. Liu, F.Z. Li, S. Hartfield, H.I. Aaronson, An investigation of the generality of incomplete transformation to bainite in Fe-C-X alloys, Metall. Trans. A. 21 (1990) 1479–1491. doi:10.1007/BF02672563.

[23] T. Furuhara, K. Tsuzumi, G. Miyamoto, T. Amino, G. Shigesato, Characterization of Transformation Stasis in Low-Carbon Steels Microalloyed with B and Mo, Metall. Mater. Trans. A. 45 (2014) 5990–5996. doi:10.1007/s11661-014-2584-7.

[24] C. Zhang, H. Chen, K. Zhu, C. Zhang, Z. Yang, Effect of Mo Addition on the Transformation Stasis Phenomenon During the Isothermal Formation of Bainitic Ferrite, Metall. Mater. Trans. A. 47 (2016) 5670–5674. doi:10.1007/s11661-016-3797-8.

[25] H.K.D.H. Bhadeshia, A rationalisation of shear transformations in steels, Acta Metall. 29 (1981) 1117–1130. doi:10.1016/0001-6160(81)90063-8.

[26] E. Kozeschnik, H.K.D.H. Bhadeshia, Influence of silicon on cementite precipitation in steels, Mater. Sci. Technol. 24 (2013) 343–347. doi:10.1179/174328408X275973.

[27] B. Kim, C. Celada, D. San Martín, T. Sourmail, P.E.J. Rivera-Díaz-del-Castillo, The effect of silicon on the nanoprecipitation of cementite, Acta Mater. 61 (2013) 6983–6992. doi:10.1016/j.actamat.2013.08.012.

[28] H.P. Van Landeghem, B. Langelier, D. Panahi, G.R. Purdy, C.R. Hutchinson, G.A. Botton, H.S. Zurob, Solute Segregation During Ferrite Growth: Solute/Interphase and

Substitutional/Interstitial Interactions, JOM. 68 (2016) 1329–1334. doi:10.1007/s11837-016-1852-y.

[29] F. Danoix, X. Sauvage, D. Huin, L. Germain, M. Gouné, A direct evidence of solute interactions with a moving ferrite/austenite interface in a model Fe-C-Mn alloy, Scr. Mater. 121 (2016) 61–65. doi:10.1016/j.scriptamat.2016.04.038.

[30] W.W. Sun, H.S. Zurob, C.R. Hutchinson, Coupled solute drag and transformation stasis during ferrite formation in Fe-C-Mn-Mo, Acta Mater. 139 (2017) 62–74. doi:10.1016/J.ACTAMAT.2017.08.010.

Appendix A

HT in-situ EBSD maps

Creator/Director: H. Farahani, G. Zijlstra, V. Ocelík, J. Th. M. De Hosson, S. van der Zwaag

Description:

This video shows the in-situ high temperature Electron Backscatter Diffraction measurements during cyclic partial phase transformations in an Fe-0.056C-2.0Mn (all in mass%) alloy. The video includes the recorded OIM maps and the time and temperature for each measurement. This experiment has been conducted in the Zernike Institute for Advanced Materials, University of Groningen, the Netherlands.

DOI: **https://doi.org/10.4121/uuid:a390e8d4-d2dc-4f5c-9e41-03df0e5252bd**

Appendix B

3D Phase Field Simulation

Creator/Director: H. Farahani, M. G. Mecozzi, S. van der Zwaag

Description:

This video shows results of 3D Phase Field simulation of cyclic partial phase transformation using MICRESS software. Back and Forth migration of austenite/ferrite interfaces during partial transformations are explicitly visible in this video. This simulation has been conducted in Delft University of Technology, the Netherlands.

DOI: **https://doi.org/10.4121/uuid:327a72a5-51cd-42d5-b6b4-8b6dc6467894**

Appendix C

Two different sections of a 3D Phase Field Simulations

Creator/Director: H. Farahani, M. G. Mecozzi, S. van der Zwaag

Description:

This video shows results of 3D Phase Field simulation of cyclic partial phase transformation at two different 2D sections. The interfaces show different behaviors at these two different 2D sections. This simulation has been conducted in Delft University of Technology, the Netherlands.

DOI: **https://doi.org/10.4121/uuid:5bef9e0d-bb44-4186-ab70-f4c72b9b9e7a**

Appendix D

Isothermal bainite transformation at 723 K

Creator/Director: H. Farahani, E. Gamsjäger, S. van der Zwaag

Description:

This video shows in-situ bainite formation in Fe-0.2C-1.5Mn-2Cr (all in mass%) steel at T= 723 K (450 ℃) recorded using high temperature Confocal Laser Scanning Microscopy Method. This experiment has been conducted in the Montanuniversität Leoben, Austria.

DOI: **https://doi.org/10.4121/uuid:f5d8a28a-9f53-4a29-bd36-8560584eb6aa**

Acknowledgment

PhD is a process through which a freshly trained user of science, successfully evolves into a fresh contributor to development of science. For me, this evolution was a mission impossible without continuous support from several people at different levels and occasions.

First and foremost, thank you Sybrand. Words are not capable of expressing my sincere gratitude to you. In short, with no doubt I won the jackpot of life having you as my promotor during the PhD. What I learnt from you, both scientific and others, are numberless.

Thank you Wei. It was of a great opportunity to work on such a novel level under your supervision.

Thank you Farideh. In indeed, I hit the jackpot twice, and meeting you were the first one. You have been the inimitable source of courage and motivation during the last decade of my life.

I had no clue how lucky I am when I was admitted as a PhD candidate in NovAM. Thank you all the NovAMers: Shanta, Wouter P, Wouter V, Jimmy, Nikhil, Ruben, Maarten, Pim, Atsushi, Santiago, Frans, Mina, Jimmy, Zeljka, Martino, Silvia, Vincent, Sima, Hao, Petter, Casper, Michael, Christian, Hamideh, Nikodem, Amber, Gokul, Antonio, Daniella, Taylor, Marianella, Arijana, Ranjita, Nikolas, Max, Frederik, Jibran, Georgios, Kevin, Zenan, Xiaojun, Michiel, Vincenzo, Paul, Satya, Cleopatra, Hongli, Nan, Abhishek, Reza, Johan, Francesco, Marlies, Tadhg, Haixing, Rosério, Mariana, Yifan, Tian, Hugo, Anton, Cong, Lishuai, Shuai, Huifang, Theo, Balaji, Linda and all the NovAM refugees.

It’s of a unique opportunity to thank all who have supported me during the PhD at TU Delft. Thank you Jilt, Javier and all my colleagues from 3ME. I do acknowledge all the scientific collaborators from different universities world-wide, Hatem from the Hamilton, Ernst from Leoben, Jeff, Vasek and Gerrit from Groningen Salil from Linköping and Chris from Melbourne. And also, all the members of the ALEMI community.

I would like to acknowledge all the composers who made my time -inside and outside of the office- happier during the last 4 years: Yann Tiersen, Mohsen Namjoo, Gerorge Winston, Ludovico Einaudi, Ibrahim Maalouf, Steven Wilson, Sohrab Pournazeri, Milad Derakhshani, Habib Mohebbian, Reza Yazdani, Moselm Rasouli, Eric Clapton, Fariborz Lachini, David Nevue, B-Band, King Raam and Steve Reich.

A big thank to all my family members and friends; specially my parents, without their endless continuous flow of support I could have ended up a homeless street visual artist, but never at such an academic level. Thank you all my organised and non-organised friends over years: from FPS to DISSA.

At the end, I would also like to acknowledge the ArcelorMittal research centre in Metz, France for the financial support of my project. And I thank all the committee members who have kindly read and commented my dissertation.

The thesis pages are too short to acknowledge all the people who have positively supported me throughout PhD and also in my life. I’ll keep them forever in my heart.

List of Publications

International peer-reviewed journals

1. H. Farahani, G. Zijlstra, M. G. Mecozzi, V. Ocelík, J. Th. M. De Hosson, S. van der Zwaag, In-situ high-temperature EBSD and 3D Phase Field studies of the austenite-ferrite transformation in a medium Mn steel, submitted to *Microscopy and Microanalysis*.

2. H. Farahani, W. Xu, S. van der Zwaag, Determination of mode switching in cyclic partial phase transformation in Fe-0.1C-xMn alloys as a function of the Mn concentration, submitted to *JOM*.

3. H. Farahani, W. Xu , S. van der Zwaag, Predicting the cooperative effect of Mn-Si and Mn-Mo on the incomplete bainite formation in quaternary Fe-C alloys, *Phliosophical Magazine Letters*, DOI: 10.1080/09500839.2018.1515505.

4. S. Sainis, H. Farahani, E. Gamsjäger, S. van der Zwaag, An in-situ LSCM study on bainite Formation in a Fe-0.2C-1.5Mn-2.0Cr Alloy, *Metals*, Volume 8, Issue 7, July 2018, Article number 498.

5. H. Farahani, W. Xu, S. van der Zwaag, A Novel Approach for Controlling the Band Formation in Medium Mn Steels, *Metallurgical and Materials Transactions A*, Volume 49, Issue 6, 1 June 2018, Pages 1998-2010.

6. H. Farahani, H. Zurob, C.R. Hutchinson S. van der Zwaag, Effect of C and N and their absence on the kinetics of austenite-ferrite phase transformations in Fe-0.5Mn alloy, *Acta Materialia*, Volume 150, 15 May 2018, Pages 224-235.

7. H. Farahani, W. Xu, S. van der Zwaag, Prediction and Validation of the Austenite Phase Fraction upon Intercritical Annealing of Medium Mn Steels, Metallurgical and Materials Transactions A, Volume 46, Issue 11, 1 November 2015, Pages 4978-4985.

International Conferences

1. Farahani, H., Xu, W., van der Zwaag, S., “Modelling of Continuous Transitions in the Partitioning Mode of Alloying Elements during Isothermal Ferrite and Bainite Formation”, Euromat 2017, Thessaloniki, Greece, September, 2017.

2. Farahani, H., Xu, W., van der Zwaag, S., “Analysis of the Critical Effect of Mn Concentration on Transformation Kinetics in Fe-C-Mn Steels using Cyclic Partial Phase Transformations”, FiMPART 2017, Frontiers in Materials Processing Applications, Research and Technology, Bordeaux, France, July 2017.

3. Farahani, H., Zurob. H, van der Zwaag, S., “Indirect Evidence of Mn Interaction with the Interface in Presence and Absence of Interstitial Elements in Fe-0.5Mn Alloy “, 16th ALEMI Workshop, Tsinghua University, Beijing, China, June 2017.

4. Farahani, H., Xu, W., van der Zwaag, S., “An Interface Controlled Transformation Model Predicting the Kinetics for Isothermal Bainite Formation in Medium Mn Steels”, 2017 TMS Annual Meeting & Exhibition, San Diego, USA, February-March 2017.

5. Farahani, H., Xu, W., van der Zwaag, S., “The effect of alloying element partitioning on the interface velocity during the isothermal bainite formation”, PTM 2015 - Proceedings of the International Conference on Solid-Solid Phase Transformations in Inorganic Materials 2015 pp. 925-926.

6. Farahani, H., Xu, W., van der Zwaag, S., “A Study of the Effect of Composition on Bainite Stasis”, MSE 2014: International Conference Materials Science Engineering, Darmstadt, Germany, September 2014.

7. Farahani, H., Xu, W., van der Zwaag, S., “Predicting the microstructure upon intercritical annealing as a function of initial microstructure and Mn concentration”, HMNS2014, 2nd International Conference on High Mn Steels, Aachen, Germany, September 2014.

8. Farahani, H., Xu, W., Chen, H., van der Zwaag, S., “Predicting the Phase Fractions after Intercritical Annealing in Medium Mn Steels using Different Equilibrium Assumptions and Different starting microstructures”, ALEMI 2014.

9. M. Moshref-Javadi, A. Nasiri, Hussein Farahani, et al., “Hydrogen Storage in Carbonic Nanomaterials”, 2nd International Congress on New and Advanced Materials (NAMIC 2013), Isfahan, Iran, 13-15 Aug. 2013.

10. M. Moshref-Javadi, Hussein Farahani, “Molecular Dynamics Simulation of Solidification of Ni Nanoparticles”, 4th International Conference on Ultrafine Grained and Nano-Structured Materials, Nov. 2013.

About the Author

Hussein Farahani

Born on November 15 1985, Tehran, Iran

Education:

2014-2018	PhD candidate, Novel Aerospace Materials Group, Faculty of Aerospace Engineering, Delft.

t University of Technology, The Netherlands.

2011-2014	M.Sc. in Computational Material Science, Technical University Bergakademie Freiberg, Germany.
2008-2011	M.Sc. in Material Science & Engineering, Iran University of Science and Technology, Tehran, Iran.
2004-2008	B.Sc. in Material Science & Engineering, University of Tehran, Iran.

Professional Experience:

From Feb. 2018	Postdoc researcher, Department of Materials Science and Engineering, TU Delft, the Netherlands.
Feb.2014- Feb.2018	PhD researcher, TU Delft, the Netherlands.
May 2013-Jan. 2014	Research assistant, ICAMS, Ruhr-University Bochum, Germany.
2008-2010	Engineering expert, Valafan co., Tehran. Iran.
2005-2008	English language instructor, Tehran, Iran.